mesostructured porous materials: pore and surface engineering towards bio-inspired synthesis of heterogeneous copper catalysts

Kun Zhang

▶ To cite this version:

Kun Zhang. mesostructured porous materials: pore and surface engineering towards bio-inspired synthesis of heterogeneous copper catalysts. Chemical Sciences. Ecole normale supérieure de lyon - ENS LYON, 2008. English. NNT : . tel-00310153

HAL Id: tel-00310153
https://theses.hal.science/tel-00310153

Submitted on 8 Aug 2008

N° d'ordre :

N° attribué par la bibliothèque :

THESE

en vue d'obtenir le grade de

Docteur de l'Université de Lyon – Ecole Normale Supérieure de Lyon

Spécialité : Chimie

Laboratoire de Chimie

École Doctorale de Chimie de Lyon

présentée et soutenue publiquement le 30 Juillet 2008

par Monsieur Kun ZHANG

Titre :

MESOSTRUCTURED POROUS MATERIALS: PORE AND SURFACE ENGINEERING TOWARDS BIO-INSPIRED SYNTHESIS OF HETEROGENEOUS COPPER CATALYSTS

Directeur de thèse : *Monsieur Laurent BONNEVIOT*

Co-directeur de thèse : *Monsieur Mingyuan HE*

Après avis de : *Monsieur Peng WU, Rapporteur,*
Monsieur Jean-Luc BLIN, Rapporteur,

Devant la Commission d'Examen formée des membres suivants :
Monsieur Peng WU, Rapporteur,
Monsieur Jean-Luc BLIN, Rapporteur,
Monsieur Joël PATARIN, Membre
Monsieur Jean-Marie HERRMANN,
Monsieur Mingyuan HE, Membre,
Membre Monsieur Laurent BONNEVIOT, Membre

Adventure journey in MCM-41 channel

'In one's life, there are only several key steps' Chinese great writer, Ai Qing said "Going abroad to study is always my dream". In 2005, I was so lucky and happy to be a PhD student co-directed by Prof. Laurent Bonneviot and Prof. Ming-Yuan He, two world famous experts in catalysis and green chemistry. Due to their choices, my dream was realized. Despite the different nationalities, but the truth-seeking, pragmatic and innovative scientific concept of two instructors is the same, which will deeply affect my scientific career. I take this opportunity to express my intense reverence towards them for bringing me into the science hall, and into the research frontier on catalysis and green chemistry, which is closely related to economy and society. My deepest personal regards are due for them forever.

In the past three years, almost every day, I was able to learn something new under the guidance of my two instructors. They let me know how to do research, how to do systematic and in-depth scientific research independently. If some problems were encountered during the experiment, at any time, I could enter their rooms for help and discussed with each other for a resolution. To solve a problem, we searched the internet, studied the literature and check the chemical handbook till late in the day when a phone call from home was interrupting us. On this occasion, I want to say sorry to their families, because I took a lot of their time away from their families. I also like to work with them, even to repair ovens, washed EPR tubes, and changed gas bottles and so on learning from them everyday experiment skills. During this course, a lot of research keywords: "chain reactions on paper", "boss's eye", "patience", "details" and "why not" etc. were heard and remembered. In addition to do research, both instructors also regard directing students and sharing their knowledge with students as fun. Moreover, I had the priviledge to attend an international conference with them. To give beautiful presentations and explain our ideas, numerous efforts were devoted to prepare posters and oral presentations to bring attention from other researchers on your work, then discuss with us and create opportunities for possible collaboration. For me, the most impressive memory was that they told me a lot of wonderful stories, for instance, on how papers may received sometimes mixed feeling and resistence from referees before acceptance and then found a large success in the research community. Understanding these interesting stories, I know how to do the innovative research.

Through the channel, after experiencing the darkness, we could enjoy the beautiful scenery inside. Obviously, like catalysts that accelerates the transformation of reactant to final product my both instructors has propulse my vision of the world and my personnel skills in science to a level I could not dare to imagine at the beginning of my thesis.

Now where is my next dream? To be a professor like them will be the best return for their rewards.

Kun Zhang

张坤

May 2008

Abstract

Advanced control of the surface structure and chemistry in confined space has been developed here in mesostructured porous silicas of MCM-41 type to design novel metal supported catalysts combining confinement, hydrophobicity and site specificity using the inspiring model of metalloproteins. First, it is demonstrated that the surface of such a type of materials usually seen as smooth has indeed an alveolar structure generated by the imprint of the ammonium surfactant head groups used here as directing agent. Increasing hydrothermal temperatures is shown first to enlarge the pore size by mere surface smoothing followed by a decrease explained by wall thickening. In addition, conditions were found to generate hybrid materials with hierarchical micro- and mesoporority. Finally, both rough and smooth surfaces were found amenable for multifonctionnalization using molecular stencil patterning technique and compared for isolation of bidentate aminoethyleaminopropyl tethers by trimethylsilyl grafted hydrophobic groups. Then copper (II) can easily be retained by complexation to these bidentate tethers inside the nanochannels of the material.

Résumé

Le contrôle fin de la structure et de la chimie de surface en milieu confiné a été développé dans des silices poreuses mésostucturées de type MCM-41 pour synthétiser des catalyseurs hétérogènes combinant confinement moléculaire, hydrophobicité et spécificité de sites à l’instar des métalloprotéines. La surface considérée comme lisse a en fait une rugosité de type alvéolaire due à l’empreinte de la tête ammonium du tensioactif de synthèse. Pour des températures croissantes du traitement hydrothermal, la taille des mésopores augmente par érosion de cette rugosité puis diminue par épaississement des parois. On a aussi trouvé des conditions de synthèse de zéolihes mésoporeuses avec une micro- et mésoporosité hiérarchisée. Ces surfaces sont polyfonctionnalisées grâce à la technique de pochoir moléculaire pour isoler des fonctions bidentatés aminoéthylaminopropyles par des groupements hydrophobes triméthylsimyles. Les ions cuivriques sont alors retenus dans le matériau par complexation à ces fonctions diamino.

CONTENTS

Chapter 1 General introduction

1.1 Introduction

When beginning to write something, especially like PhD these, one always find that it is so difficulty to start. Throughout society in general, we see rapid development of Science and Technology that affects many aspects of day-to-day living positively. Concomitantly, numerous questions are raised, for example, air and water pollution resulted by over-emissions of the waste form chemical industries. At some point during the early 70s the world started to become aware of the impacts that industry had on the environment, partially sparked off by Rachel Carson's book “Silent Spring”. This new trend of thought gave birth to the discipline of environmental catalysis, also called “green chemistry” [1].

To realize green chemistry and chemical processes is really a great challenge. But nature always gives us many good lessons. As said by Prof. George Whitesides, pioneer in soft nanolithography, “**Nature** ‘s full of amazing things, the basic process of just going and seeing what's there, sticking your nose under that rock and seeing what happens to be there, is unbelievably interesting? What's there in ***Science*** [2]? In one word, nature makes, man reshapes. Two typical examples are cited in the following.

1.2 Enzymology study toward recoverable catalysts

Metallobiomolecules are natural products that in their essence are highly elaborated metal complexes equipped with the necessary protein structure for complementarities and all other aspects of function.[3] We are especially interested in Cu-containing enzymes that activate O_2 function as dioxygenases, monooxygenases, and oxidases.[4] Because hemocyanin is the only Cu protein that is crystallographically characterized in both reduced (redHc) and oxygenated (oxyHc) forms (see figure 1.1). The coordination environments of

Cu in these enzymes provide important insights into the structural attributes that are required to operate properly.[5] However, despite relatively high turnover numbers achieved by enzymes, all natural machinery is subject to degradation and must be regenerated by biosynthesis. This poses to chemists the irresistible challenge of trying to do better than Nature and create "immortal" catalysts that do not deactivate and can be recovered with efficiencies of 100%. While valiant attempts to realize this unattainable goal are being made to asymptotically approach it, using different support, such as polymer and microporous zeolite.[6]

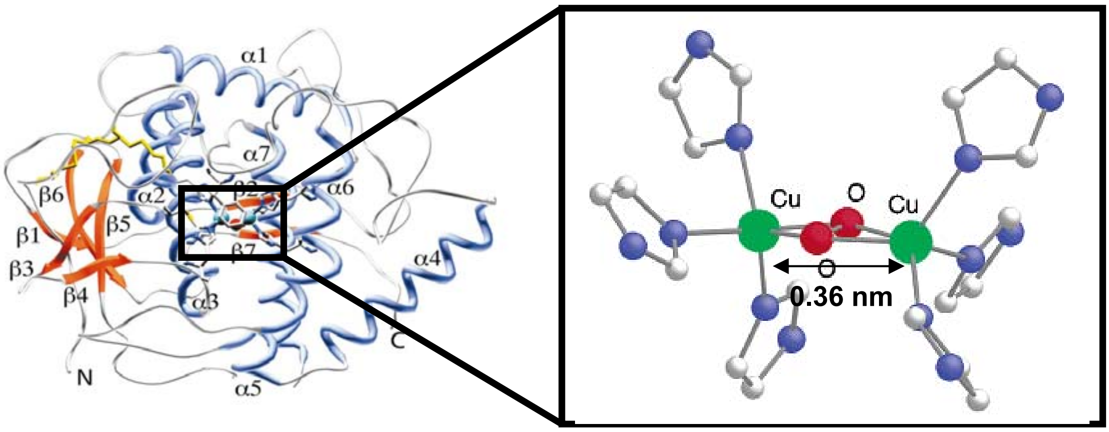

Figure 1.1 hemocyanin structure from crystallographic characterization, on the right, zoom of metal active center.

1.3 Surfactant template mesoporous materials: from inorganic to hybrid

Nevertheless the major drawbacks of the systems above mentioned concern both their mechanical, chemical stabilities and diffusion limitations. Because the nature of the support plays a vital role to improve the selectivity and activity of catalysts, the production of new materials with desired structures and compositions is, therefore, of great importance.[7]

As revealed by biominerallization processes, another fascinating example of mimicking nature, organic amphiphlic molecules are capable of self-assembling in the presence of growing inorganic solids and, mold their shape and porosity.[8] Such organic-inorganic self-assembling properties has allowed the synthesis of a new family of mesoporous materials with controlled porosity, structures and compositions, namely, the M41S familly. Over the past decade, research on mesoporous materials has led to advances in the control of pore structure and morphology, the tailoring of pore surface chemistry, and the design of framework composition. Such materials with unique properties, such as high specific surface area of at least 700 m^2/g, pore volume larger than 0.7 ml/g, narrow size distribution, etc., seems the best candidate for the rational design of bio-inspired catalyst.

1.4 Best of two worlds

Indeed, using mesoporous silica as a host matrix is an interesting idea to design supported metal complex in well defined pore size and hydrophobic environment as encountered in the enzyme cavity. A balanced combination of both properties paves the road to the rational synthesis of novel multifunctional heterogeneous catalysts.

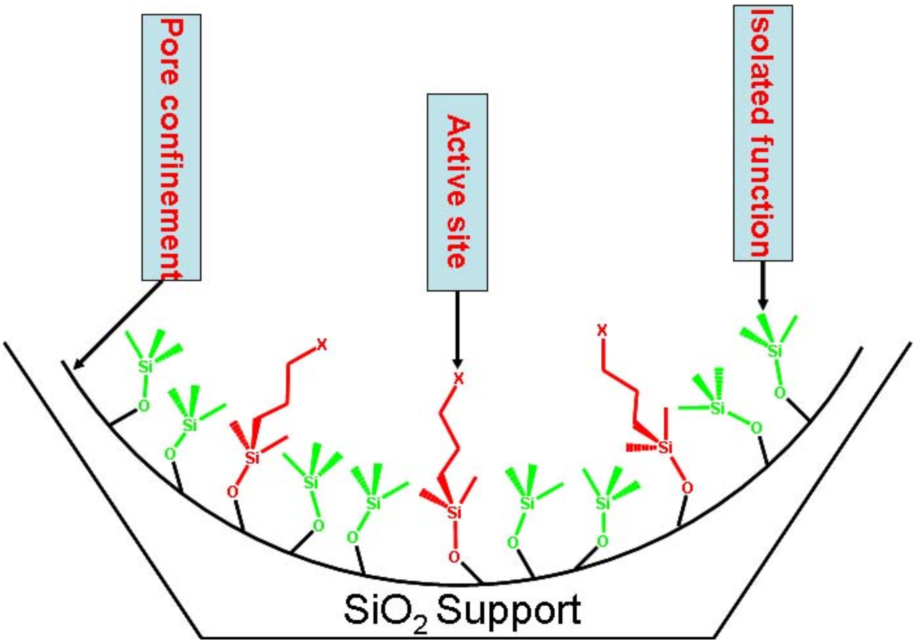

Figure 1.2 Scheme of bio-inspired catalyst prepared according to “Molecular stencil patterning” technique

The main objective of this thesis is to develop a novel, general and effective technique to synthesize highly selective and active multifunctional catalyst according to this approach. For this purpose, a variant of the so-called "molecular stencil patterning" developped by our laboratory is developped here to generate site dispersion and hyrophobization of mesostructured porous materials with different surface rugosity (figure 1.2).[9] This technique makes use of the $CTMA^+$ surfactant present in the as-made material as protecting agent of surface silanol the density of which is controlled by partial extraction.[10] Mutual electrostatic repulsion ensures the patterning effect during the grafting of the first function here trimethylsimyl that dilute the second function grafted after removal of the protecting surfactant (figure 1.2). The first variation concerns here the replacement of the surfactant by a smaller molecule, tetrametylamonium ions (TMA^+) introduced by cation exchange of $CTMA^+$ to decrease the steric hindrance during the grafting of the diluting function. The second variation concerns the diluting function itself that is replaced by octylsilyl (OS) or 2,2,5,5-tetramethyl-2,5-disilasilyl (TMDSS) groups. These modifications are tested to disperse a second function, i.e., N-[3-(trimethoxysilyl) propyl] ethylenediamine (AEPTMS). In the last step, Cu (II) is used as probe to investigate the spatial distribution between the grafted ethylenediamine. We find that, most of functions grafted in the first place are effectively retained during the second grafting step. The pore size, the surface topology, the type of organosilane, and even the counterion of the copper salt are of paramount importance for defining the distribution of functional groups. Very interesting results about Cu (II) coordination environment are reported. Though the concept seems to apply, optimization is still needed for a better control on O_2 activation and a better analogy with metalloenzymes.

1.5 Outline of thesis

Based on the main objective mentioned above, the thesis will be presented in six chapters, a brief summary of which is given below.

Chapter 1 briefly describes how our original ideas for bio-inspired catalyst come about, and presents the outline of this thesis.

Chapter 2 presents a brief historical development of porous materials, with a particular emphasis on mesoporous silica (type MCM-41). Based the thesis proposal, new trends concerning MCM-41 are presented in two parts. The first one is devoted to synthesis and mechanism with specific attention on surface engineering for control of pore size, morphology, hydrophobicity and functionalization. The second reports on designed synthesis of novel heterogeneous catalysts based on the structural and the functional model of metalloenzymes. The main objectives, features and contributions of the present work are outlined at the end of this part.

Chapter 3 is based on the discovery that the pore surface of the MCM-41 type of silicas have a “egg-box” type of shape controlled by gel ageing or hydrothermal post-synthesis treatment. Pore size and surface engineering is then developped according to a novel mechanism of pore size enlargement proposed here. Pore enlargement provoked is then interpreted as the erosion of this surface rugosity. Different structured mesoporous silicas with tailored pore size, surface properties and stability are synthesized according to these observations. A panel of techniques are used to characterize the properties of interest namely, nitrogen adsorption-desorption profile for the pore volume, and the pore size, the XRD powder diffraction to get the structure, Scanning Electron microscopy and Transition Electron Microscopy. Chemical analysis, solid state NMR, FTIR spectroscopies had also performed to check the organic modification of the surface.

Chapter 4 Inspired by several important conclusions in chapter 3, a new synthetic strategy is proposed to create ordered micropores in the mesopore network leading to “hybrid materials” with hirarchechical porosity. Hydrothermal temperature compatible with zeolite formation is applied on siliceous gel in the presence of surfactant and tetrapropylammonium (TPA). The formation of the zeolite form mesoporous silica occurs apparently through a solid-solid transformation mechanism (SST). Ti-containing MFI zeolite with hierarchical micro- and mesopores is synthesized through this non-conventional mechanism starting from clear solutions and from a dense system. The synthesis principle developed in this present work offers interesting keys to experimentally bridge the gap between microporous and mesoporous materials.

Chapter 5 focuses on the designed synthesis of bio-inspired catalyst using mesoporous silicas synthesized above. Organic modifications of the solid are also at stake using the "*molecular stencil patterning*" technique (MSP) developed by another student of our group. A variation of this technique is proposed where the positively charged surfactant are quantitatively exchanged by tetramethylammonium cations that, in its turn, can be used as a patterning agent for the MSP technique. Another variation proposed by us included the test for other hydrophobic organosilanes which are found more stable or effective than the trimethylsilane for site isolation (copper was used as an EPR probe for this characterization). The synthesis methods for immobilization and in-depth characterization of the bio-inspired catalysts are described and monitored thanks to XRD, N_2 adsorption, FTIR, ^{13}C CP MAS NMR, EPR and UV-visible techniques. It is found that Cu(II) coordinated by the grafted ethenediamine function is a good candidate for the activation of O_2.

Chapter 6 summarizes the results obtained and the basic findings of the present work. The perspective for future work is also discussed at the end of this chapter.

1.6 References

(1) Lindström, B.; Pettersson, L. J. *Cat. Tech.* **2003**, 7, 130, feature article.

(2) Whitesides, G.; Weiss, P. S. *ACS Nano* **2007**, 1, 73, conversation.

(3) Holm, R. H.; Solomon, E. I. *Chem. Rev.* **1996**, 96(7), special volume for *bioinorganic enzymology*.

(4) Eicken,C.; Krebs, B.; Sacchettini, J. C. *Curr. Opin. Struc. Bio.* **1999**, *9*, 677.

(5) Mirica, L. M.; Ottenwaelder, X.; Stack, D. P. *Chem. Rev.* **2004**, 104, 1013.

(6) Gladysz, J. A. *Chem. Rev.* **2002**, 102(10), special volume for *recoverable catalyst and reagent—perspective and prospective.*

(7) Lu, Y. F. *Angew. Chem. Int. Ed.* **2006**, 45, 7664, highlights.

(8) Choi,M.; Ryoo, R. et al, *Nature Mater.* **2006,** 5, 718.

(9) Abry, A.; Alebela, B.; Bonneviot, L. C. R. Chimie, 2005, 8, 741.

(10) Bonneviot, L.; Morin, M.; Badiei, A. Patent WO 01/55031 A1, 2001.

Chapter 2 General introduction and literature survey

An overall review about the most important development conncerning MCM-41 and mesostructured porous silicas is presented here in two parts: one is devoted to the synthesis and the formation mechanism of the mesoporous silica family, with an emphasis on surface engineering for the control of pore size and the mesophase topology; the other part reports on the design and thhe synthesis of novel heterogeneous catalysts based on the structural and the functional model of metalloenzymes. Then, UV-visible and EPR spectroscopies are shortly introduced in connection with their utility in classifying the active sites in copper protein. Finally，the scope and the objective of this thesis is described.

2.1 Background

In virtually every arena and every aspect of the material life—transportation, communication, clothing, shelter etc. — chemistry has resulted in an improvement, not merely in the trappings of life, but also in the quality of living of billions of individuals who now inhabit the planet. However, these amazing achievements have come at a price, which is the toll that the manufacture, use, and disposal of the synthetic chemicals have taken on human health and the environment.[1]

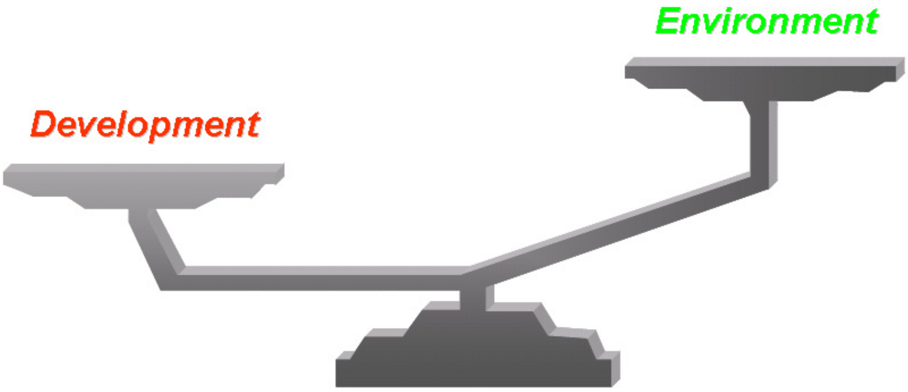

Figure 2.1 Unbalance between industry development and respect of environment.

At some point during the early 60s the world started to become aware of the impacts that economy development had on the environment, partially spared off by Rachel Carson's book "silent spring". This new trend of thought gave birth to the discipline of green chemistry. [2] Green chemistry is an approach that provides a fundamental methodology for changing the intrinsic nature of a chemical product or process so that it is inherently of less risk to human health and the environment. Chemists have always striven for efficiency in their synthetic methodologies. Now the concept of "atom economy" has replaced the time-honored metric of 'yield' as a standard by which to measure the quality of a synthetic methodology.[1] It means that the substrate can transfer into the product in 100% without any byproducts.

To realize this elegant objective, environmental catalysis was the first step towards the modern chemical industry where catalysis is applied to almost every process, including the production of fine chemicals for pharmaceutical applications to the production of bulk chemicals and exhaust gas catalysts.[2] It should be importantly mentioned that the innovative source of new catalyst and chemical process is to search for the novel catalytic materials.

2. 2 Synthesis and formation mechanism of Mesoporous Silica

2. 2.1. A Brief history of Mesoporous Silica

Many fascinating materials in nature are composed of ordinary building components that are precisely defined with unique functions and properties. For instance, zeolites, also called "boiling stones" are the most widely used catalysts in industry. So far, above 100 types of artificial zeolites has been synthesized. Figure 2.2 shows some typical examples of stones containing natural zeolites and some artificial zeolites with different topological symmetries.

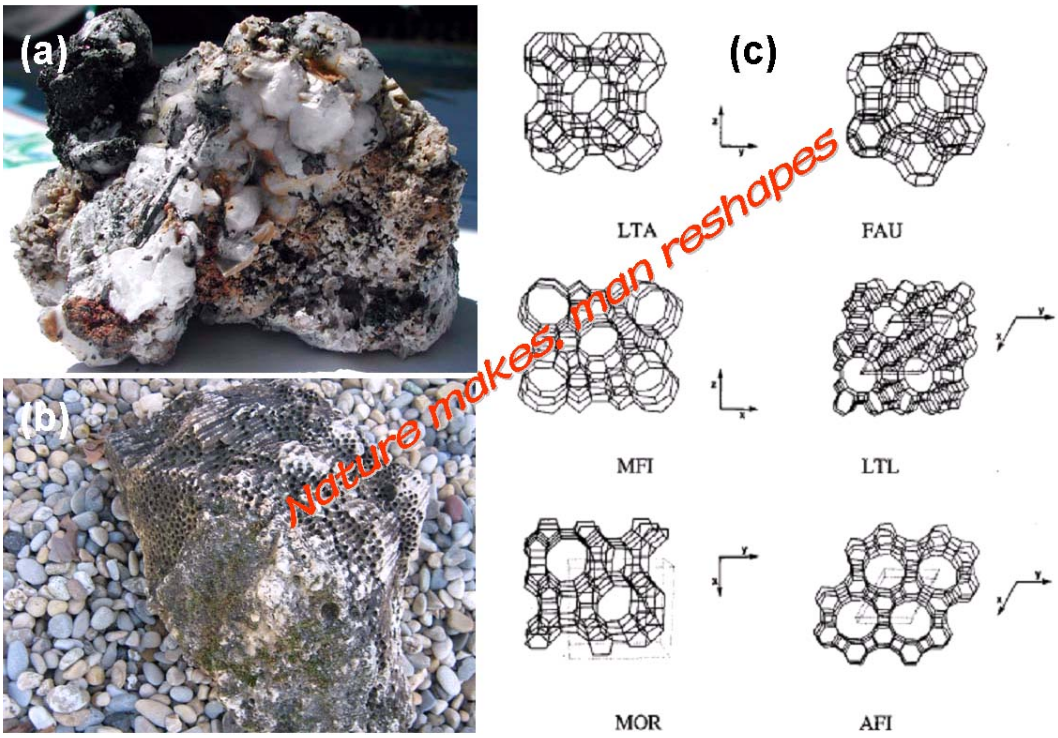

Figure 2.2 (a) and (b), stone in nature, (c), and zeolite structures. LTA, zeolite A (pore size 4.1 Å for the Na$^+$ form); FAU, zeolite X or Y (faujasite structures with different Si/Al ratios, pore size 7.4 Å); MFI, ZSM-5 (aluminosilicate) or silicalite 1 (pure silica form) (pore sizes 5.3 5.6 and 5.1 5.5 Å); LTL, zeolite L (pore size 7.1 Å); MOR, mordenite (main pore size 6.5 7.0 Å); AFI, $AlPO_4$-5 (an aluminophosphate, pore size 7.3 Å). Lines represent oxygen bridges; nodes represent tetrahedral framework atoms such as Si or Al (reference source 3).

Zeolites are crystalline aluminosilicate materials that are technologically important for their applications in catalysis (for gasoline production), radioactive ion sequestration, purification systems (for water softening) and many more. In catalytic processes, they typically offer high activities, but their nanoporous structures (pores approximately 1 nm in diameter) rather limit their uses to reactions involving bulky reactants and products.[4, 5]

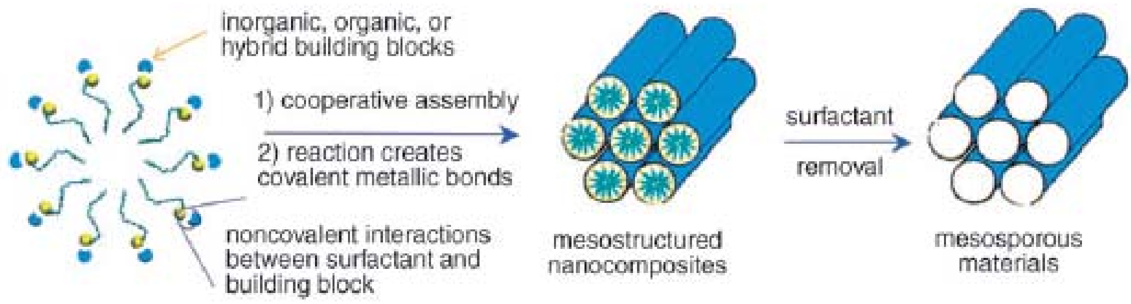

Figure 2.3 Synthetic strategies of mesoporous materials by cooperative self-assembly. [6]

To overcome this pore size limitation, a great deal of effort has been devoted to synthesize porous inorganic solids with high surface area and pore in the mesoscopic regime (about 2-50 nm). The most cited over the past decade are probably the surfactant-directed mesostructured materials discovered by Mobil scientists in 1992. The cooperative assembly of surfactants with silicates led to the synthesis of MCM-41 and the M41S family of mesoporous materials.[7] This discovery sparked a decade of extensive research on surfactant-directed assembly, the use of surfactant to direct and assemble building blocks into mesoscopically ordered structures. More specifically, noncovalent interactions between the self-assembling surfactant and building inorganic blocks drive their spatial organization (Figure 2.3). Simultaneous or subsequent reactions (for example, a condensation of the inorganic blocks) create covalent bonds among the building blocks, resulting in a mesostructured nanocomposite that can be seen as the results of the mineralization of the surfactant liquid-crystal. The removal of the surfactant by calcination or solvent extraction creates a mesoporous material with a templated pore structure.[6] Then, the size, shape, and intermolecular interactions of the mesoporous material can be tuned to produce hexagonal, cubic, lamellar, and other mesostructures (figure 2.4).[8]

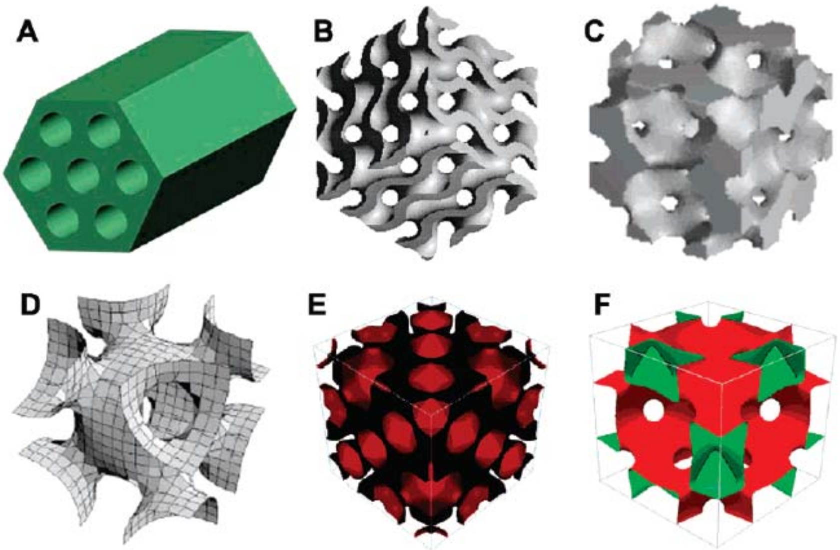

Figure 2.4 Pore models of mesostructures with different symmetries of (A) *p*6*mm*, (B) *Ia*3h*d*, (C) *Pm*3h*n*, (D) *Im*3h*m*, (E) *Fd*3h*m*, and (F) *Fm*3h*m.* [8-12]

2. 2.2. Formation mechanism

Many models have been proposed to explain the formation process of mesoporous materials according to various synthesis routes.[13-25] All these models are based on the structure directing role of the surfactants during the nucleation-growth of the material. The surfactants have a hydrophilic head group and a long chain hydrophobic tail group within the same molecule, which will aggregate and self-organize in such a way so as to minimize the contact between the incompatible ends in solution.[14] Herein, two well known models for mesophase formation are described below: the liquid crystal templating mechanism and the charge density matching mechanism.

2.2.2.1. Liquid crystal templating mechanism

The liquid crystal templating (LCT) mechanism was first proposed by the researchers of Mobil Co., based on the similarity between the structures of both liquid crystalline surfactant assemblies (i.e., lyotropic phases) and M41S family. [7] Accordingly, the long chain ammonium amphiphile molecules, $CnH_{2n+1}(CH_3)_3N^+$, organize into lyotropic liquid crystal phase and serve as template for the formation of the mesophase. The example is the hexagonal MCM-41 structure of scheme 2.1. The surfactant micelles aggregate into a hexagonal array of rods, followed by interaction of silicate or aluminate anions present in the reaction mixture with the surfactant cationic head groups. Thereafter condensation of the silicate species occurs, leading to the formation of an inorganic polymeric species. It was argued after that this pathway 1 do not take place because the surfactant concentration used is far below the critical micelle concentration (CMC) required for hexagonal LC formation.[15]

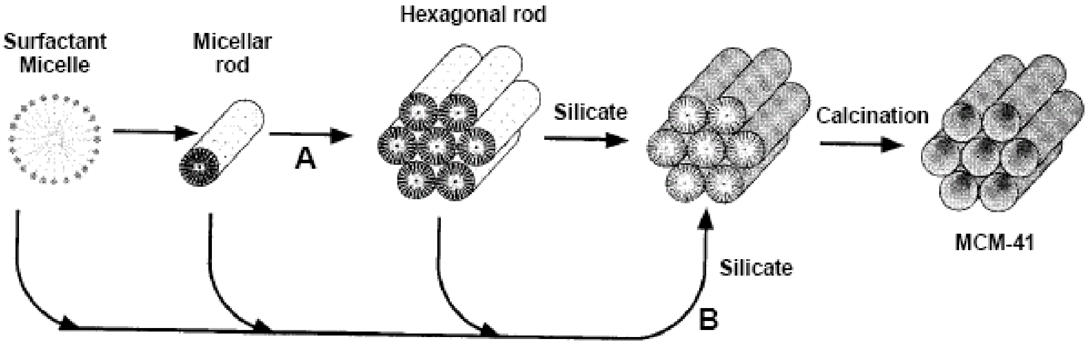

Scheme 2.1 Liquid crystal templating (LCT) mechanism proposed for the formation of MCM-41; (A) liquid crystal phase initiated and (B) silicate anion initiated. [Adapted from Ref. 7]

The second mechanistic pathway of LCT was also suggested as a cooperative self-assembly of the ammonium surfactant and the silicate precursor species below the CMC. It has been known that no preformed LC phase was necessary for MCM-41 formation but, now, the actual details of MCM-41 formation is still under investigation by several groups.

2.2.2.2. Charge density matching mechanism

A "charge density matching" mechanism was suggested by Monnier et al.[18] and Stucky et al.[19] and showed that MCM-41 could be derived from a lamellar phase. The initial phase of the synthesis mixture was layered (as detected by

X-ray diffractometry (XRD)), and was formed from the electrostatic attraction between the anionic silicates and the cationic surfactant head groups (Scheme 2.2). As the silicate species began to condense, the charge density was reduced. Accompanying this process, curvature was introduced into the layers to maintain the charge density balance with the surfactant head groups, which transformed the lamellar mesostructure into the hexagonal mesostructure.

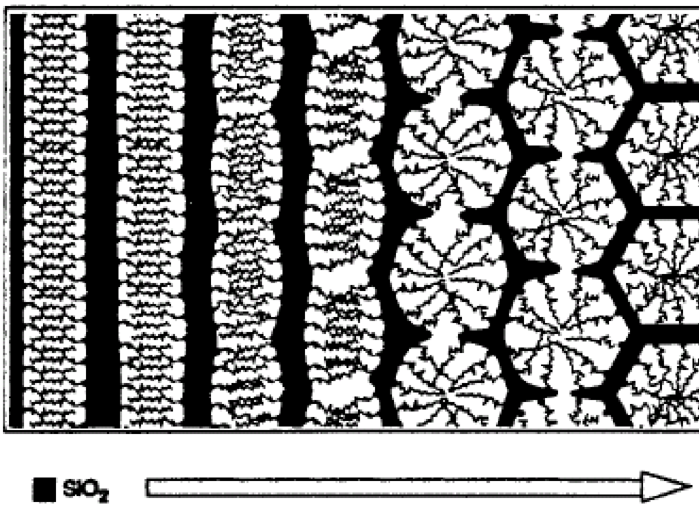

Scheme 2.2 Curvature induced by charge density matching, the arrow indicates the reaction coordinate.

It is worth noticing that the g parameter can help to explain the phase transformation.[18] g $=V_s/(al)$, where V_s is the surfactant volume, *a* is the head-silica interfacial area and the surfactant length, *l*, is a sum of the effective tail length. Hydrothermal treatment of composites drives surfactant packing changes. Specifically, the surfactant tail volume expands, but its radial length shrinks. The pie wedge (scheme 2.3a) is used to depict such changes. Upon heating, it expands and becomes truncated. Because of this, heating a pore with uniform tail density may give rise to a low tail density center (scheme 2.3b). This pore center can be modeled with an average zero tail density. This modeling captures basic aspects of surfactant packing in the composites and aids in understanding the phase transition.[26-27]

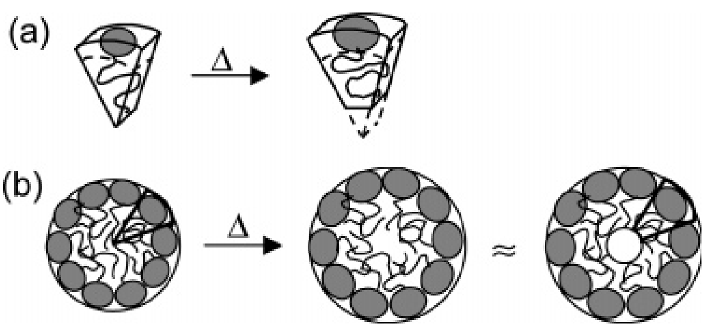

Scheme 2.3 Effect of hydrothermal treatment on curvature: a) volume occupancy by single surfactant (hydrophilic head in gray, head size increases while dynamic length of hydrophobic chain decreases); b) micelle expansion with temperature. [26]

A generalized mechanism of formation based on the specific type of electrostatic interaction between a given inorganic precursor I and surfactant head group S was proposed by Huo and co-workers.[28, 29] Based on the nomenclature, pathway 2 of the original LCT mechanism (Scheme 2.1), which involved anionic silicate species and cationic quaternary ammonium surfactant, could be categorized as the S^+I^- pathway. By extension, the other charge-interaction pathways are S^-I^+, $S^+X^-I^+$ (X^- is a counterion) and $S^-M^+I^-$ (M is a metal atom).

2.2.3. Proposed wall structure for MCM-41

There are two interrelated key questions about the MCM-41 channels which our and other experiments raise. First, are the channel walls smooth or rough? [30-31] Second how does the center of the channel move relative to the hexagonal unit cell as we move down the channel? White and coworkers postulated several extreme models to explain the data collected by X-Ray diffraction: (1) a straight channel in which the walls of a narrow channel are lined with a thick layer of finely divided, extremely fluffy, silica; (2) an almost 3-dimensional channel system related to MCM-48 in which the walls of a meandering wide channel are smooth. As a variant of (2), we can postulate (3) a straight channel system in which there are smooth walls but the channel width varies dramatically. The X-ray data and neutron scattering from H_2 adsorbed in MCM-41 exclude (4) the conventional model of straight, wide, smooth walled, cylindrical channels (Figure 2.5 (a)). Finally, a three-region hole-fluffy silica-solid pore wall model was proposed in figure 2.5 (b). In this model, there are two regions of different silicate densities around the hexagonally packed channel with R_2, the hole radius of ca. 7 Å and R_1, the radius to a denser projection of ca. 21 Å. $2R_3$ represents in this model the hexagonal lattice unit cell of 48 Å. The region inside, radius R_2, is called the "central hole", between R_2 and R_1 the "lining" and outside R1, the rest, the densest part called the "wall".[32-33] It should be herein mentioned that the central pore size was only 7 Å that is clearly wrong, because numerous experiments have proved that the large molecule (molecular diameter larger than 1 nm) can easily diffuse in and out the channel. Based on the large quantity of experimental data obtained during this present thesis, we propose that MCM-41 mesoporous channel is covered by surface open micropores of about 7 Å in diameter in scheme 3 (c). Using this new model, the physical properties evidenced in this thesis and the literatures can be rationalized including the apparent mismatch between N_2 adsorption, pore surface area and total pore volume.

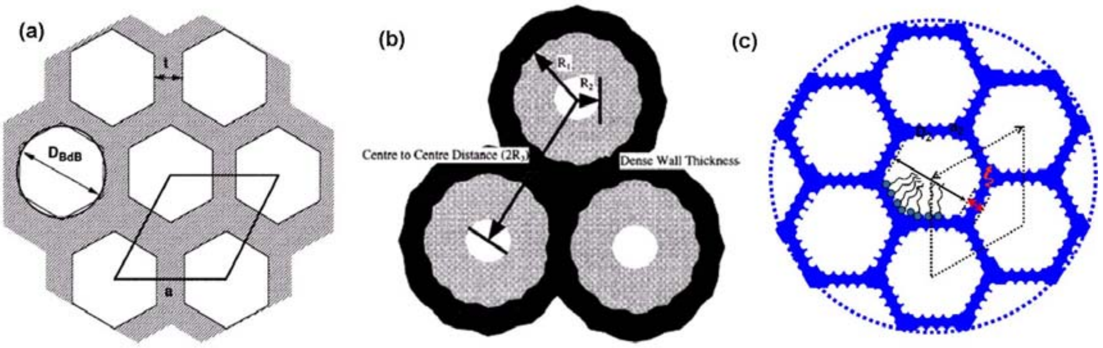

Figure 2.5 Scheme of MCM-41 structure, (a), conventional hexagonal model assuming smooth walled straight channel, (b) Edler model assuming three region of different density (dense wall-fluffy silica-central hole)[32,33] (c) packing hexagonal channel edging micropores

Our model is inspired by the model propose for SBA-15 materials templated by non-ionic surfactants SBA-15.[34-42] One of the differences lies in the connection of the mesopores of SBA-15 through micropores, which do not exist for MCM-41. The amount of micropores decreases with the increase of the hydrothermal temperature, to end up with no micropores for synthesis close to 130 °C (figure 2.6, right). The micropores are formed due to the interactions of PEO chains between different micelles. When the synthesis temperature increases, the PEO chains are dehydrated, the pore sizes increase, and progressively PEO chains no longer interact with the other PEO chains of the other micelles (figure 2.6).

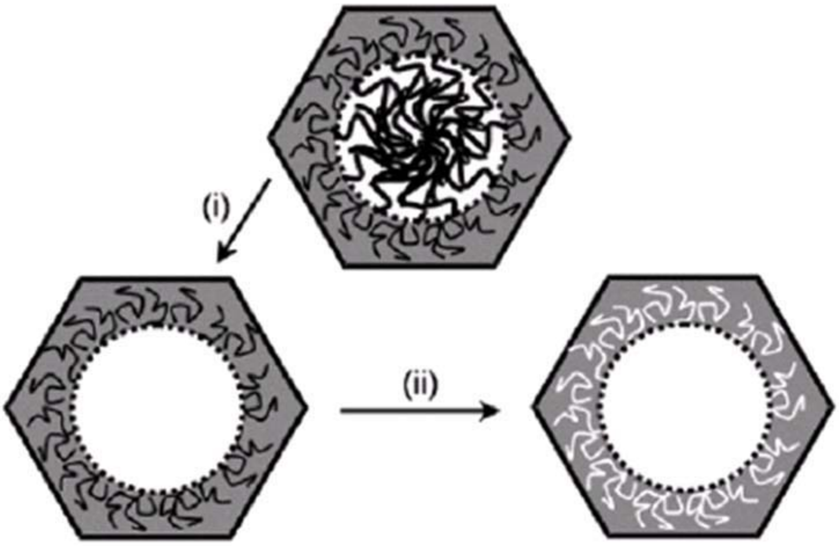

Figure 2.6 Scheme of different states of SBA-15 with PEO surfactant (top), after extraction of surfactants (left) and after calcination (right) [34]

2.2.3. The pore size control of MCM-41

A remarkable feature of MCM-41 materials is the possibility to tune their pore size in a wide range from about 2 to 10 nm.[43] Custom-tailoring the surface properties of siliceous supports may require introduction of high coverages of relatively large ligands, which results in a substantial decrease of the pore diameter as seen in this presnt work. Under such conditions, large-pore supports may be beneficial. Application of either unmodified or organic-modified MCM-41 or related porous materials as stationary phase for gaz phase or liquid-phase chromatography or as mere adsorbents, pore diameters larger than 4.5 nm would be highly desirable. For instance, large pore (5.5 nm) MCM-41 with chemically bonded cross-linked mercaptopropylsilane ligands was recently shown to be a highly efficient adsorbent for the removal of heavy metal ions from water. Recently developed synthetic methods for large pore MCM-41 are listed in table 2.1.

Table 2.1 Recently developed methods for synthesis of silicas with tailored narrow pore-size distributions

Pore size nm	methods	Reference
2-5	use of surfactants with different chain lengths as templates: charged (usually alkyltrimethylammonium) neutral (usually amines)	7, 27 44
4-10	use of charged surfactants and expanders: aromatic hydrocarbons alkanes trialkylamines alkyldimethylamines	7, 27, 45 46 47, 48 48
4-7	hydrothermal postsynthesis treatment: in mother liquor in water	49, 50 27
2.5-6.6	high-temp synthesis	51-53
4-11	water-amine postsynthesis treatment	48
2-30	use of oligomers and polymers as templates	54-57
>50	emulsion templating	58
>200	colloidal crystallization	59

Because high temperature post-synthesis treatment is an environmentally benign chemical synthetic strategy, many research groups investigated the relation between pore size expansion and experimental conditions. Literature shows that the most important parameters of the synthesis in order to control the pore opening are the following: [7, 27, 44-59]

(1) Silica source : TEOS, sodium silicate, fumed silica are preferred, especially for hydrothemal stability and thermal stability

(2) Addition of auxiliary salt: NaX (X is an halogenide) and quaternary ammonium cation (TMA^+,TEA^+), cosurfactant (ethanol), etc.

(3) Reaction (or crystallization) time and temperature

However, the explanation of the pore enlargment differs from one author to the other and there is no clear understanding of it. First, Khushalani and Ozin (1995), [49] proposed that pore enlargement is due to water penetration when crystallization is performed at increasing temperature. Then Klinowski et al (1995 & 1996) propose that decomposition of the surfactant occurs and produce swelling molecules that should expand the templating micelles. A neutral long chain dimethylalkylamine (CDMA from CTMA) that is a good candidate as swelling agent has been identified.[51] TMA^+ as also been proposed by Corma et al in 1997 as a promoter for swelling the micelles and expand the pore size.[52] In this thesis a comprehensive mechanism for pore size expansion is proposed.

2.2.4. Structure geometry control of mesoporous silica

Besides the pore size effect, the mesophase geometry also affects the molecular diffusion and therefore the chemical reactivity. Huo et al carefully examined how the molecular shapes of covalent organosilanes, quaternary ammonium surfactants and, mixture of surfactants in various synthesis conditions can be used to prepare silica-based mesophase of various structures such as MCM-41 (2d hexagonal, *p*6*m*), MCM-48 (cubic *Ia*3*d*), MCM-50 (lamellar), SBA-1 (cubic *Pm*3*n*), SBA-2 (3d hexagonal $P6_3/mmc$), and SBA-3 (hexagonal *p*6*m* from acidic synthesis media).[27] The structural function of surfactants in mesophase formation can to a first approximation be related to that of classical surfactants in water or other solvents with parallel roles for organic additives. The effective surfactant ion pair packing parameter, $g = V/a_0l$, remains a useful molecular structure-directing index to characterize the geometry of the mesophase products, and phase transitions may be viewed as a variation of *g* inside the liquid-crystal-like solid phase. Solvent and cosolvent structure direction can be effectively used by varying polarity, hydrophobic/hydrophilic properties and functionalizing the surfactant molecule, for example with hydroxy group or variable charge. Surfactants (Table 5.2) and synthesis conditions can be chosen to controlled the desired silica-based mesophases.[27]

Then, such ordered mesoporosity of tunable size and geometry in the nanoscale range of distances provides an unpreceeding opportunity to control the diffusion of large molecules and also to create tunable confined environment with a defined polarity by organic modification. Surface and interfacial engineering at the molecular scale with the possibility to introduce different chemical functions may allow us to approah the properties of biological counterparts such as enzymes for instance.[60]

2.3 Design synthesis toward the bioinspired catalyst

Green oxidation reactions will, of course, necessitate the use and the generation of little or no hazardous substances, with maximum efficiency of atom incorporation at low temperature to avoid energy loss.[61] The use of highly selective catalysts working in water would be ideal. Nature does that routinely using enzymes that often contains catalytically active metal centers. An enzyme-catalyzed reaction is usually very specific and very rapid, even under mild reaction conditions. Their high activity and selectivity are related to a complex combination of functional groups covering their internal surfaces in a very specific spatial arrangement. Synthetic catalyst are usually much more simple with only one or two functional groups and also much less selective.

Table 5.2 often used cationic surfactants

Name	Example Structure
Alkyltrimethyammonium $C_nTMA = C_nH_{2n+1}N(CH_3)_3$ n=10, 12-16, 18, 20, 22	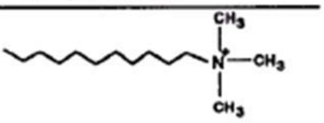
Gemini ammonium C_{m-s-m} = $C_mH_{2m+1}N(CH_3)_2(CH_2)_sN(CH_3)_2C_mH_{2m+1}$ m = 12,14,16,18,20,22; s = 2-12	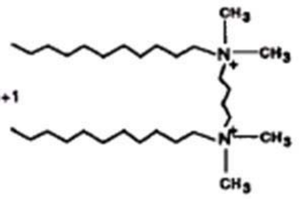
Divalent surfactant C_{n-s-1} = $C_nH_{2n+1}N(CH_3)_2(CH_2)_sN(CH_3)_3$ n=12,14,16,18,20,22; s=2,3,6	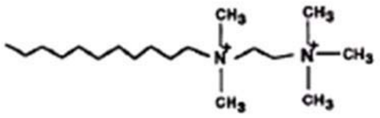
Organosilane $C_nH_{2n+1}N(CH_3)_2(CH_2)_3Si(OCH_3)_3$ n=14	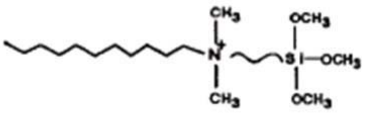

2.3 Design synthesis toward the bioinspired catalyst

Since complexity may rapidely be a nightmare use enzyme as a structural guide to design catalyst is very attractive. A first approach would be to merely reconstruct the site and investigate its properties to understand how the catalytic site of enzyme work, this is the so-called biomimetic approach.[60] Since copying migh generate difficulties and unnecessary constrains, a second approach that consists in taking more freedom and transpose the structural and reactivity concept of enzyme to develop novel artificial catalytic site that may depart from the their natural counterpart, this is the bio-inspired approach. Along this reasoning in both cases, structure resolution and spectroscopy characterization of metalloenzyme pave a road to rationally design the multifunctional bio-inspired catalysts. Several examples will be presented in the next section.

2.3.1 Dioxygen and metalloproteins

Transport, activation, and metabolism of dioxygen are very important processes in most living organisms. These functions are often realized by metalloproteins containing copper or iron.[62] In this review, we focus on the presentation of copper proteins which are abondant in the nature and exhibit a wide range of catalytic and electron-transfer properties. According to their spectroscopic properties, the protein-bound copper centers are classified as type I, type II and type III.

Type I copper proteins, also called blue copper proteins, exhibit an intense blue color relatively to that of inorganic copper complexes and, unusually small hyperfine couping constants characterized by electron paramagnetic resonance (EPR) in their oxidized state. Type I copper can be found in a wide range of electron –transfer proteins, including amicyanin and azurin in bacteria, and also plastocyanin in plants. The copper coordination sphere in type I cupredoxins typically consists of three strong equatorial ligands, two N-donor ligand rpovided by two histidine residues (His) and on S-donor lignand from cystein (Cys), forming a trigonal plane plus an additional axial ligand, usually provided by a methionin residue (Met).[63] The importance of the latter position has been evidenced by Mathews and coworkers using site-directed mutagenesis.[64] When this axial ligand is missing the protein undergoes a reversible switch in ligation geometry when going from the aqueous to the frozen state. The rationale is the profound influence of this axial ligand that affects not only the uptake specificity for copper, the active site geometry and properties but also the protein stability.

The most studied type II copper protein is methanotroph methylosinus trichosporium OB3b that oxidizes methane to methanol in methanotrophic bacteria (also called methane monooxygenase, pMMO). Unfortunately, the nature of pMMO active site and the overall metal content are controversial, with spectroscopic and crystallographic data suggesting the presence of a mononuclear copper center, a dinuclear copper center, a trinuclear center, and a diiron center or combinations thereof. Based on the investigation by EPR and extended X-ray absorption fine structure (EXAFS), Rosenzweig and coworkers reported that purified *M. trichosporium OB3b pMMO* contains two distinct species. They show that are two copper at a distance Cu···Cu of 2.52 Å similar to that observed previously in crystal structure of *M. capsulatus* (Bath) *pMMO*. However, there are significant differences between the *pMMO* structures both organisms: a mononuclear copper center present in *M. capsulatus* (Bath) *pMMO* is absent in *M. trichosporium OB3b pMMO*.[65] In the present thesis, similar EPR characteristics have been observed depending one the preparation conditions.

Type III copper proteins contain two paired copper centers that behave cooperatively. Such sites are found in hemocyanins (Hcs) that have been identified as the oxygen transporting protein of mollusks and arthropods. It is also present in catechol oxidases (*COs*) that exhibit catalytic properties in the oxidation of *o*-diphenols to *o*-quinones in the presence of oxygen. Recently, the crystal structures of both oxidized and reduced forms of *COs* of sweet potatoes were determined. The oxidized *COs* contain the dinuclear *met* form, [Cu^{II}-OH-Cu^{II}], and each copper center is coordinated by three nitrogen atoms from histidine residues. The Cu(II) centers contain a hydroxide bridge completing the four coordinated trigonal pyramidal coordination sphere with a Cu···Cu distance of 2.9 Å (Figure 2.7).[66] Interestingly, similar dinuclear copper centers connected by a bridging ligand are observed in the materials synthesized in this thesis.

In summery, structure resolution of 3 types of Cu protein showed that the relatively subtle changes in the nature of the ligands or in the molecular vicinity of the potential ligands, even in the absence of significant change of the overall protein structure, may play a critical role in the assembly and the metal properties of the protein. This provides interesting insights for the design of bio-inspired catalyst.

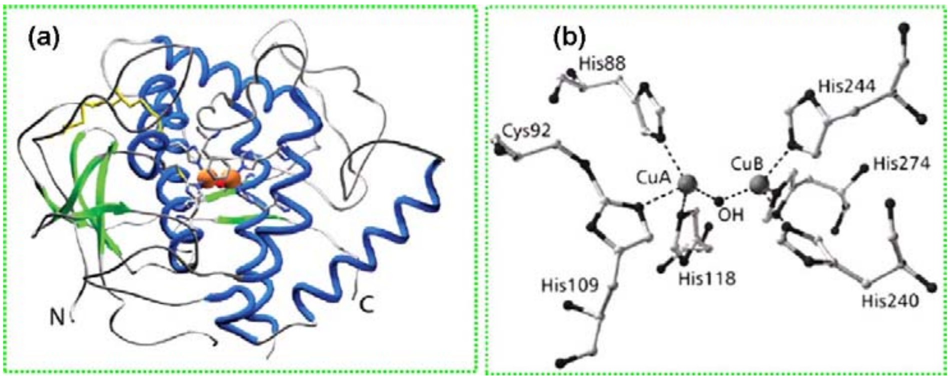

Figure 2.7 Crystal structure of sweet potato *CO enzyme*,[66] (a), Overall structure of *ibCO* (copper atoms are shown in orange, R helices in blue, β sheets in green, and disulfide bonds in yellow), (b), coordination sphere of the dinuclear copper center in the met state.

In summery, structure resolution of 3 types of Cu protein showed that the relatively subtle changes in the nature of the ligands or in the molecular vicinity of the potential ligands, even in the absence of significant change of the overall protein structure, may play a critical role in the assembly and the metal properties of the protein. This provides interesting insights for the design of bio-inspired catalyst.

The catalytic mechanism of *TYR* (tyrosinase, type III copper protein) was first studied in detail by Solomon and co-workers.[67-69] Solomon proposed a mechanism for both the cresolase and catecholase activities of *TYR* (Figure 2.8).[67] This mechanism suggests that the *oxy* state is the starting state of the cresolase activity. This state is present in the resting form of *TYR* in a proportion of about 15% (85% *met* state). A monophenol substrate binds to the *oxy* state and is monooxygenated to *o*-diphenol. This diphenol stays linked to the copper pair in a bidentate bridging mode producing the *metD-TYR* form the structure determined by analogy with the spectral properties of a model compound.[70] Oxidation of the diphenol substrate leads to the reduced state of the dinuclear copper center. Reoxidation of the reduced state to the *oxy* state occurs by attack of dioxygen and closes the catalytic cycle. The mechanism of catecholase activity starts from the *oxy* and *met* states. For example, a diphenol substrate binds to the *met* state, followed by the oxidation of the substrate to the first quinone and the formation of the reduced state of the enzyme. Binding of dioxygen leads to the *oxy* state, which is subsequently attacked by the second diphenol molecule. Oxidation of the second quinone forms the *met* state again and closes the catalytic cycle.

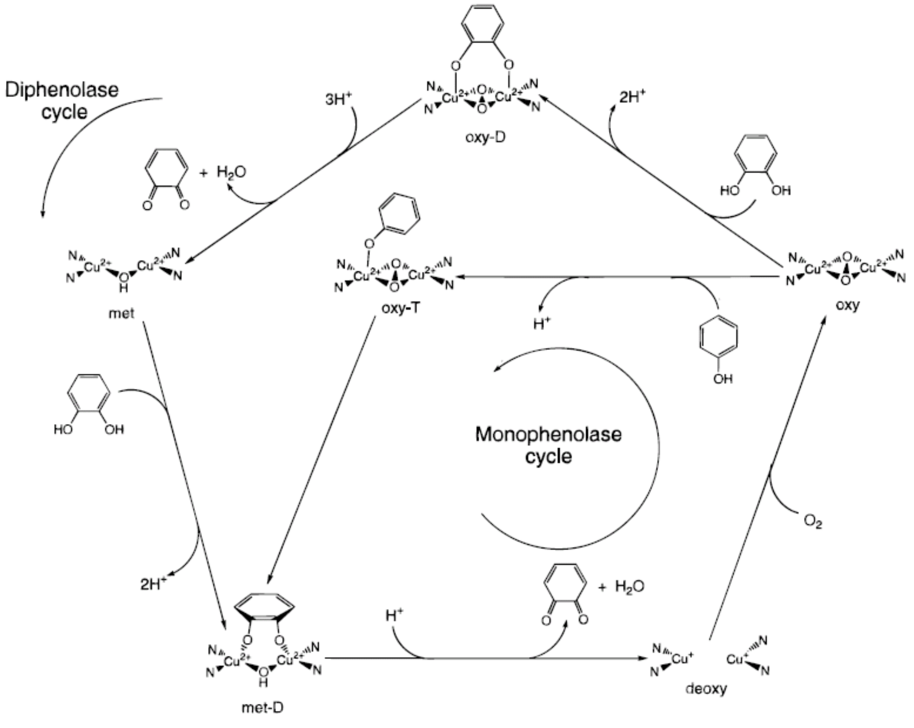

Figure 2.8 Catalytic cycle for the monooxygenation of monophenols and the oxidation of *o*-diphenols to *o*-quinones by tyrosinase (adapted from ref 71). Axial ligands at Cu not included for clarity. T = tyrosine and D = DOPA bound forms.

The elucidation of reaction mechanism further confirmed that the catalytic activilty and selectivity strongly depend on the Cu coordination environment and Cu···Cu interaction distance.

2.3.2 Synthetic approach of homogeneous catalyst

According to the information obtained from the metalloproteins, numerous artificial analogues were synthesized. Stack and coworkers' reviewed in details the features structure and optical adsorption of the Cu complexes. The oxidation of Cu (I) by O_2 in homogeneous solutions is a deceptively simple reaction. The lability of Cu (I) and Cu (II) ions makes the role of ligation paramount in controlling which species form and how stable they are. Seemingly minor ligand alterations can dramatically affect the oxygenation reactions, thus providing an incisive mechanistic probe if ligand variation is systematic.[72-73] It is important to note that the ligands should reproduce particular active site geometries, yet retain some flexibility to accommodate the multiple oxidation states of the metal and, control the distance between coupling Cu···Cu pairs as metelloprotein already does.

Herein copper coordination chemistry of westiellaide (H_3L^{wa}) and its imidazole (H_3L^1), oxazole (H_3L^2), and thiazole (H_3L^3) analogues are presented to show the influence of both ligand type and pH on Cu coordination.[74] Compounds H_3L^{wa}, H_3L^1, H_3L^2 and H_3L^3 have in common a macrocyclic backbone similar to an alternating sequence of heterocyclic nitrogen lone pairs of peptide nitrogen donors in a highly preorganized arrangement inside a protein. X-band EPR spectra of the Cu complexes in figure 2.9 evidences the change of Cu coordination, depending on the deprotonation degree that is closely related to Cu concentration and pH. The coordination sphere in $[Cu\text{-}(H_2L^{wa})(OHCH_3)]^+$ differs from those in the synthetic analogues. Dinuclear copper (II) complexes ($[Cu^{II}_2(HL)(\mu\text{-}X)]^+$; $X=OCH_3$, OH; $L=L^1$, L^2, L^3 and L^{wa}) are observed in the mass spectra. While a dipole-dipole coupled EPR spectrum is observed for the dinuclear copper (II) complexe of H_3L^3, the corresponding complexes with H_3L ($L=L^1$, L^2 and L^{wa}) are EPR silent. It was concluded that the protonation of nitrogen can affect the exchange of different copper species with different coordination geometry. Similar experimental observations are also made on the materials synthesized in this thesis.

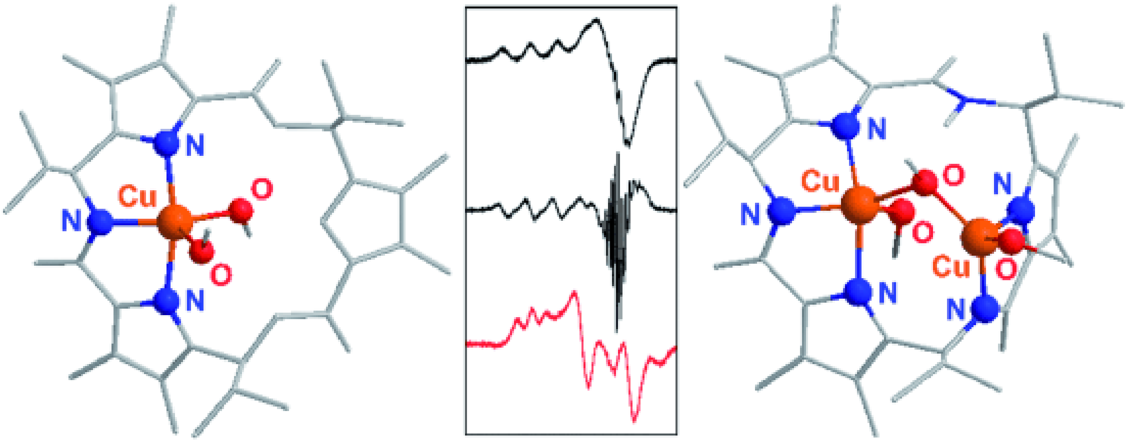

Figure 2.9 Stable copper (II) complexes: The copper (II) coordination chemistry of the [18]azacrown-6 macrocycle westiellamide, as well as of its imidazole, oxazole, and thiazole analogues (adapted from ref. 74)

Although authors claimed that this series of Cu complexes is very stable, the synthesis of [18] azacrown-6 macrocycle westiellamide and its analogues is tedious and time consuming.[74] In addition, from the application standpoint, the separation and reuse of homogeneous catalyst are not easy. Thus, recoverable heterogeneous catalysts and reagents are becoming a very exciting subject and are attracting increasing attentions.[75]

2.3.3 Synthetic approach of biomimic or bioinspired catalyst using mesoporous silicas as a support

Silicon-containing catalyst supports play prominent roles in the design of heterogeneous catalyst.[75] For example, Duchateau reviews the use of incompletely condensed silsesquioxanes as platforms for immobilized olefin polymerization catalysts. Lu, Lindner, and Mayer describe the fascinating concept of interphase catalysis, with a focus on sol-gel-derived microenvironments. Kakkar covers thin film methodologies for the heterogenization of homogeneous catalysts. These include Langmuir-Blodgett films, and the direct functionalization of glass, quartz, and single crystal silicon. Further investigations are expanded to the treatment of inorganic oxide catalyst supports. Wight and Davis review strategy and design in the preparation of hybrid organic-inorganic catalysts, where the latter derives from a porous inorganic oxide (amorphous silica, zeolites). In a complementary tractate, De Vos, Dams, Sels, and Jacobs describe a number of organic reactions catalyzed by metal fragments immobilized on zeolites or ordered mesoporous molecular sieves. Herein, it should be mentioned that the transition metal complexes are mainly encapsulated in zeolites by the electrostatic interaction and pore confinement, thus functional molecules are readily leached in the chemical reaction.[76] Finally, it is worthy to note that the design of bio-inspired or biomimic catalyst is becoming more and more complicated. For example, bulky functional groups with multidentate ligands were incorporated into the mesoporous channel to obtained improved chemical reactivity. In the homogeneous system, Cu coordination sphere can be modified by selecting the different ligands. However, in some cases, the catalytic activity of heterogenized Cu complexe is significantly smaller than expected, suggesting that the Cu coordination has been modified due to confinement or also to reaction with surface functions. One plus one is not always equal to two and the synergy if any might not be positive.

To overcome these difficulties, mesoporous organic–inorganic hybrid materials, a new class of materials characterized by large specific surface areas and pore sizes between 2 and 15 nm, have been obtained by coupling inorganic and organic components and templated synthesis. There are three possibilities to incorporate functionalities in the templated porous systems i) by covalent attachment of organic components onto a pure silica matrix, this is the grafting or post-synthesis treatment, ii) by simultaneous co-condensation of inorganic silica precursors and condensable organomonosilane, that is the one-pot synthesis route, and iii) by incorporation of condensable organodisilane inside the pore wall of the porous mesophase that lead to periodic mesoporous organosilicas (PMOs). In all the cases, the functional groups are covalently bonded to silica framework in this new class of materials, which significantly improves the stability of functional molecule and moieties. It should be mentioned that the co-condensation synthesis often caused the loss of ordering structure of mesoporous silica. To design metal supported catalysts combining molecular confinement, hydrophobicity and site specificity using the inspiring model of metalloproteins, in this thesis we focus on the sequential grafting methods, as depicted in figure 2.10.[77]

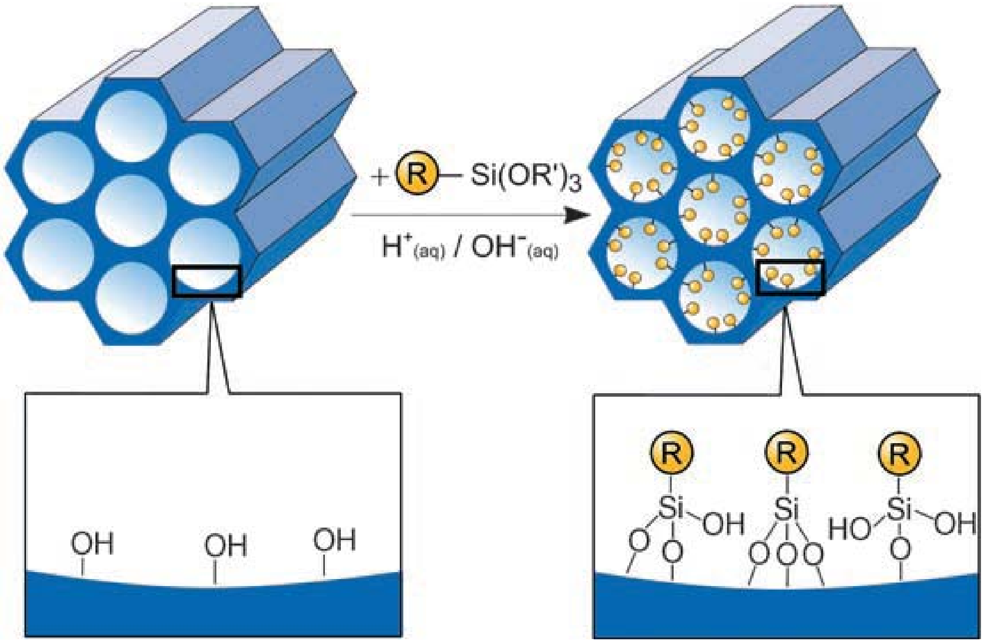

Figure 2.10 Grafting (postsynthetic functionalization) for organic modification of mesoporous pure silica phases with terminal organosilanes of type (R'O)$_3$SiR. R'=organic functional group

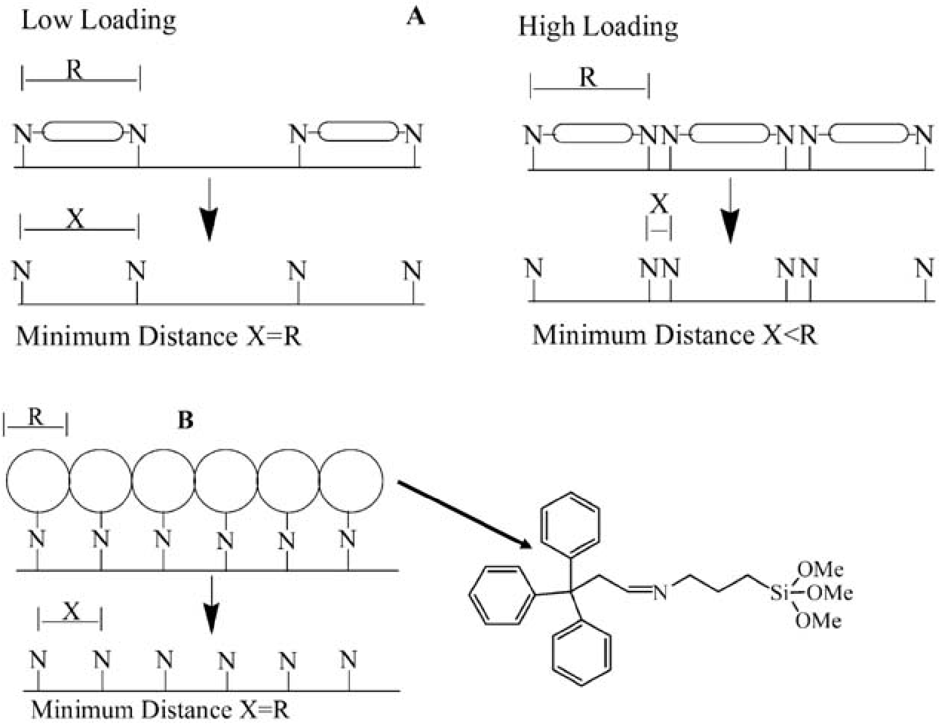

Scheme 2.4 “molecular imprinting” strategy used to synthesize heterogeneous catalyst with isolated active site: A, according to Wulf et al.[78, 79,] and B, according to Jones et al,[84 85]

Because the objective of thesis is to design the multifunctional heterogeneous catalyst using MCM-41 silicas as support, herein we will review the different approaches reported in literatures that describe both site-isolation and controlled distance between sites. Wulff et al. have demonstrated that it is possible to graft two aminopropyltriethoxysilane at a specific distance one to each other as long as, they are connected by an organic spacer before their grafting on the surface of an amorphous silica. Then, the recovery of the aminogroup is obtained by hydrolysis under mild conditions to remove the spacer (Scheme 2.4 (A)).[78-79] Sasaki et al. used a similar procedure to position three amines using different types of tripod templates also on a silica-gel surface.[80-81] This approach was extended later by Shin et al. to position two or three amines (dipod or tripod, respectively) on mesostructured porous silica (SBA-15), according to Scheme 2.5.[60, 82] Very interestingly, the formation of the grafted function monolayer is described as stepwise due to the surface roughness (Scheme 2.6).[60] A similar interpretation was made by Katz and Davis who fixed three amine groups at a specific distance one to each other using a direct synthesis to imprinted amorphous silica.[80] In all of these cases, the distance between these vicinal functions is controlled a low loading only (<1 molecule nm^{-2}) to avoid short distance bewwen tow pairs or triades of functions as depicted in scheme 2.4 (top right). In order to have higher loading, a molecular patterning technique can be used as described by McKittrick and Jones.[84-85] A voluminous aldehide is reacted with the aminopropyl group before gafting. The bulky imine produces a spacing by steric hindrance working specifically at high coverage (Scheme 2.4(B)).

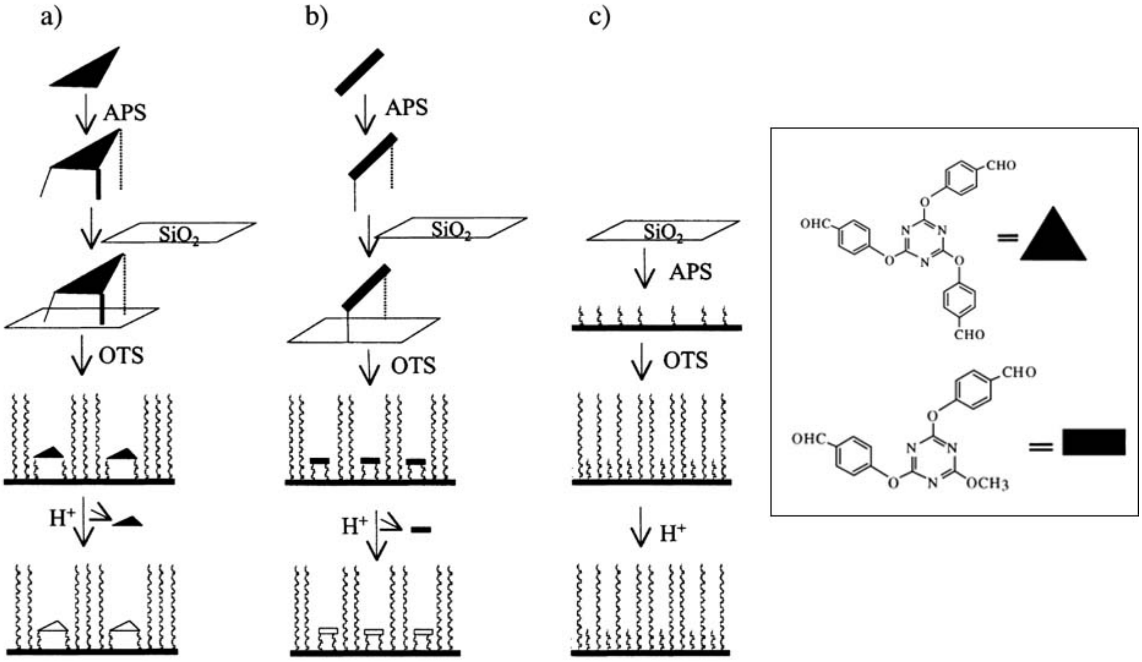

Scheme 2.5 Developed “molecular imprinting” process,.[60, 82-83]

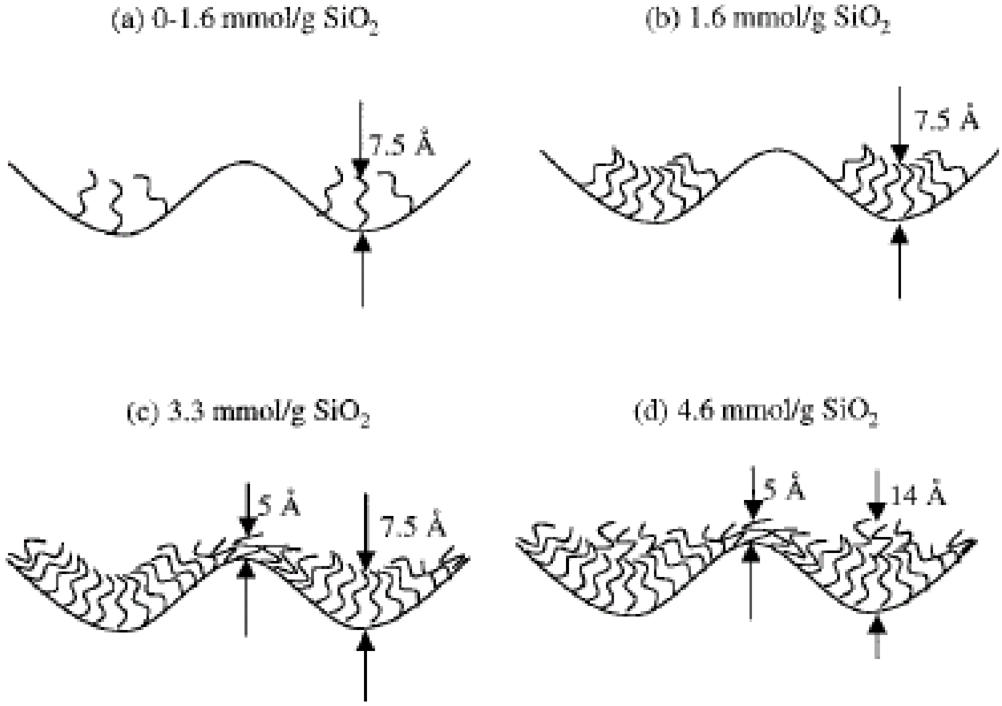

Scheme 2.6 Stepwise formation of grafted function monolayer on rough surface. [60]

However, in the first strategy a statistical distribution of the sites is obtained while in the second, deprotecting theamino group necessitate strong acidic condition leading to function degrafting. A new strategy developed in the laboratory consists to take advantage of the presence of the positively charged surfactant in the as-made silica, the positioning of which is ruled by electrostatic repulsion. In fact, one of us has proved that it is possible to graft trimethylsilyl (TMS) groups while maintaining most of the surfactant inside the channels.[86] Then, the remaining surfactant can be displaced by cation exchange or acid treatment prior introduction of the second function. The surfactant molecules act in both cases as protecting groups homogeneously distributed onto the surface. This is a novel approach based on the use of a so-called 'molecular stencil pattern'. The surfactant plays here two roles: (i) patterning due to the coulombic repulsion and, (ii) stencil from surface protection-deprotection (Scheme 2.7).[87]

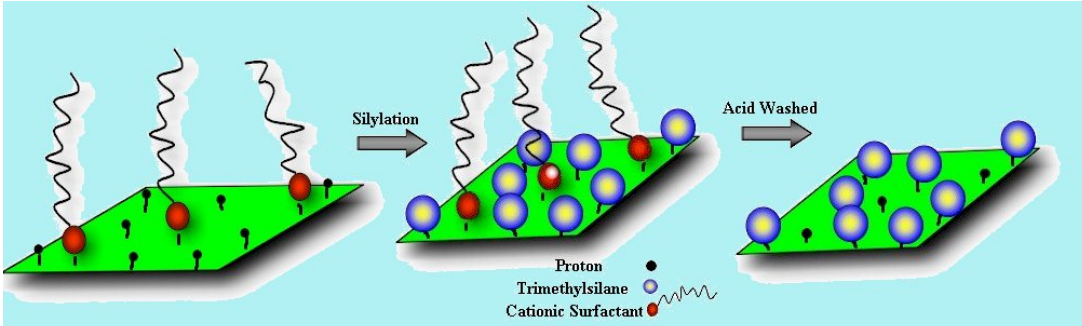

Scheme 2.7 So-called “molecular stencil patterning” technique: on the left, surface with controlled surfactant density, middle, silylated surface with surfactant, on the right, surface free of surfactant retaining grafted trimethylsilyl groups.

When bulkier functions have to be introduced in step 1 of this process, the surfactant molecules acting as a surface protecting molecule will also block their diffusion in between the aliphatic chains partially occulting the channel. Pore clogging and bad dispersion may results from such a trial. To circumvent this problem an alternative strategy is developed in this thesis based on the use of TMA^+ ions to replace the CTA^+ structure directing agent. Compared to CTA^+, TMA^+ is a much smaller and is expected to favor molecule diffusion inside the channels. It also undergoes self-electrostatic repulsion but do not have chains entanglement that may affect the dispersion homogeneity all over the surface like it may occur in the case of CTA^+. This is a variation of the “molecular stencil patterning” technique that we will try to prove usefull to isolate functional sites at high surface coverage.

2.4 EPR and absorption features: characterization of copper species

These spectroscopic classifications are based upon the oxidized (i.e. cupric) state of copper which has a d^9 open shell configuration and is thus amenable to study by a variety of spectroscopic methods.[88]

2.4.1. Electronic paramagnetic resonance of copper(II)

Copper(II) complexes are generally found to have a tetragonal geometry, due to the Jahn-Teller effect, with four tightly bound equatorial ligands and either none, one, or two weakly bound axial ligands (Figure 2.11A). This ligand field splits the d orbitals such that the $d_{x^2-y^2}$ is the highest energy half-occupied orbital. It has its lobes pointed at the four equatorial ligands and is thus involved in a strong antibonding interaction with these ligands. The unpaired electron in the $d_{x^2-y^2}$ orbital produces a characteristic $S = 1/2$ EPR signal with $g_{//} > g_{\infty} > 2.0023$ (Figure 2.11B). Note that the EPR spectrum presented is the first derivative of a powder or frozen solution of a copper(II) complex and has a peak present at a magnetic field associated with g ($= h\nu/\beta H = 0.71448\nu(\mathrm{MHz})/H(\mathrm{G})$) and an intense derivative shaped feature with its crossover point at a magnetic field associated with $g_{\square}$ (the Zeeman splitting of the $S = 1/2$ ground state for a magnetic field oriented perpendicular to the z axis, therefore in the equatorial plane). The two naturally occurring isotopes ^{63}Cu and ^{65}Cu (abundance of 69% and 31%, respectively) have a nuclear spin I of 3/2 which couples to the electron spin to produce a $2I+1$ line, that is here a 4 line hyperfine splitting of the EPR signal. As shown in Figure 2.11B (bottom), the parallel hyperfine splitting, $A_{//}$, observed for normal tetragonal Cu(II) complexes is generally large, in the range of $150\text{-}250\ X\ 10^{-4}$ cm^{-1}, while the A_{∞} splitting is much smaller, $<35\ X\ 10^{-4}$ cm^{-1}.[67]

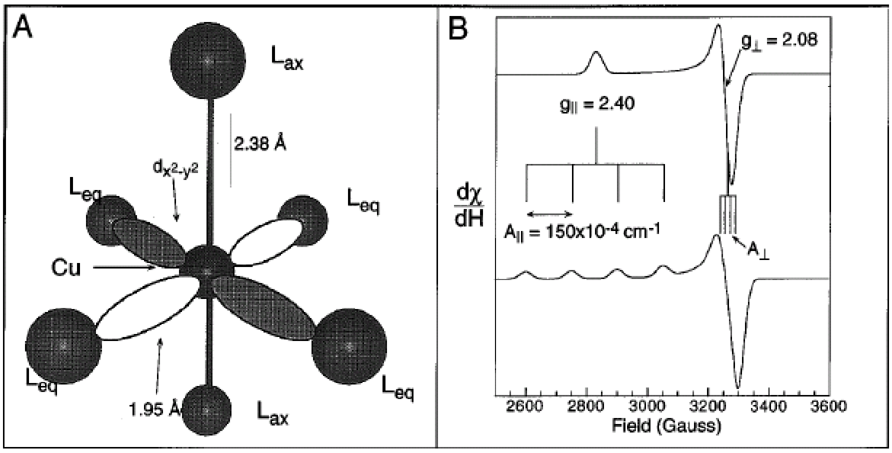

Figure 2.11 Geometry and EPR spectrum of a normal copper complex, (A) Geometry of the Jahn-Teller tetragonally distorted $Cu(H_2O)_6^{2+}$ ion with the $d_{x^2-y^2}$ orbital overlaid on the Cu(II) center. (B) Simulated EPR spectrum of $Cu(H_2O)_6^{2+}$ without (upper) and with (lower) the copper hyperfine splitting (at X-band, v = 9.50 GHz).[67]

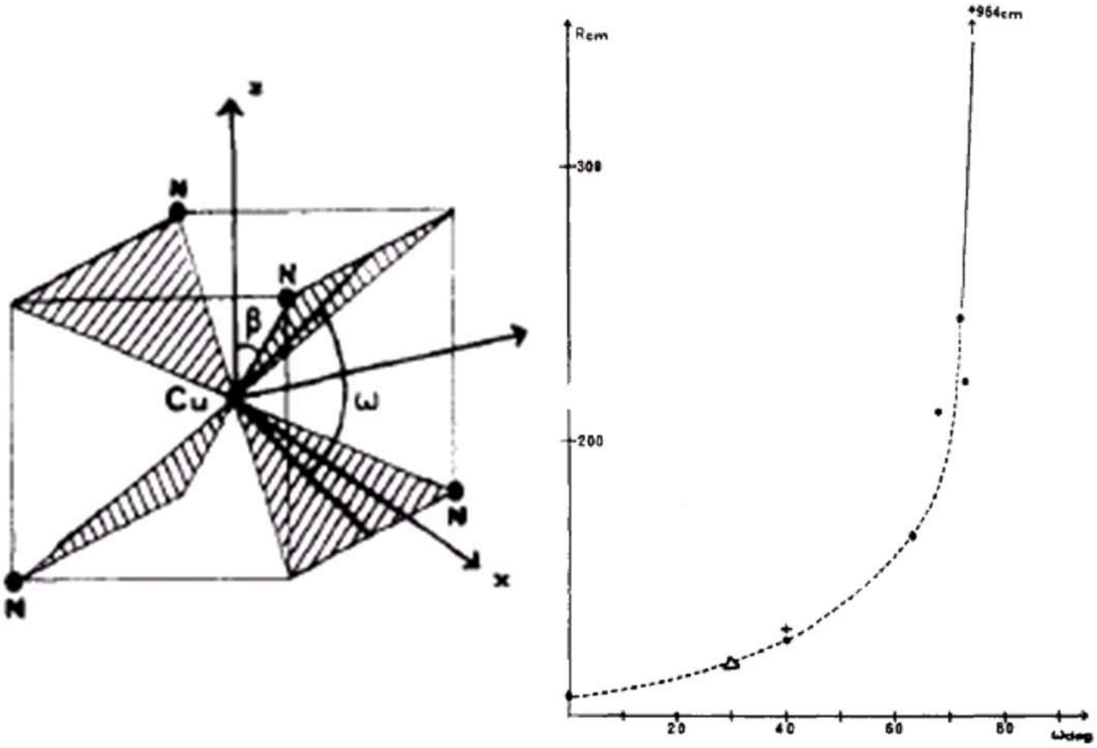

Figure 2.12 Variation curve of $R = G_{//}/A_{//}$ versus ω value (in left panel, ω and β is defined) (adapted from ref 90)

To investigate the Cu coordination environment, two angles, denoted as ω and β, are generally used to estimate the deviation from pure tetrahedral or square planar geometry in copper (II) complexes.[89-90] The ω is the dihedral angle between the two N_2Cu planes (Figure 2.12, left). It varies from 0° in square-planar to 90° in tetrahedral geometry. β varies from 90° in square-planar to 54.7° in tetrahedral geometry. Using the plot of $R = G_{//}/A_{//}$ versus ω value, the Cu conformation geometry can be easily deduced (Figure 2.12, right).

2.4.2. UV-visible characterization

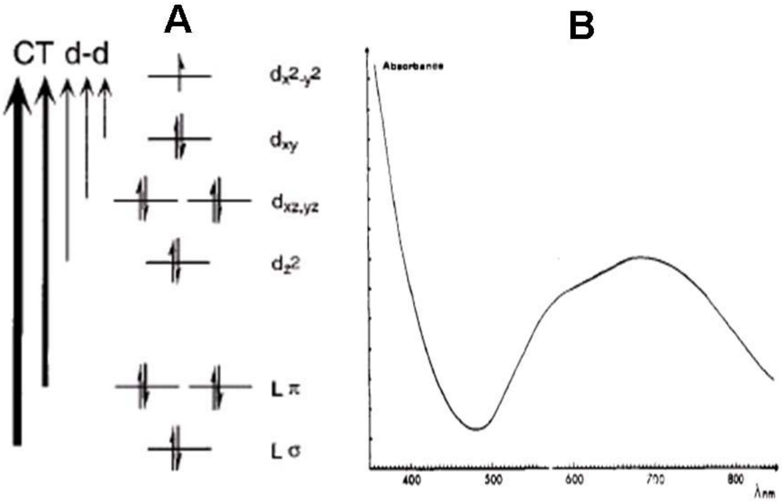

Figure 2.13 Electronic transitions of a normal copper complex. (A) Molecular orbital energy level diagram. The intense, electric dipole-allowed LMCT transitions are the bold arrows, the weak, electric dipole-forbidden d→d transitions are light arrows.[67, 91] (B) UV-visible absorption of the tetrakis (cyclohexylamine) copper (II) nitrate in the d→d (adapted from ref 90).

The low-energy region of the absorption spectrum of a Cu (II) complex will be dominated by transitions from the filled d orbitals to the half-occupied $d_{x^2-y^2}$ orbital. Since these d orbitals are split in energy by the ligand field at the metal center (Figure 2.13A), the associated d→d transitions are sensitive probes of the ligand geometry. Tetragonal Cu(II) complexes exhibit d→d transitions in the

~500 nm to 1 μm region, while copper(II) sites constrained by ligation to be close to tetrahedral exhibit d→d transitions in the 1-2μm region. These transitions are electric dipole forbidden and thus generally appear as weak features in the absorption spectrum, $\varepsilon < 200$ M^{-1} cm^{-1}. Of higher energy in the absorption spectrum are the electric dipole allowed, hence intense, ligand-to-metal charge transfer (LMCT) transitions. The intensity of these transitions reflects the overlap of the ligand and metal orbitals involved in the charge transfer, and their energy splitting reflects differences in π and σ ligand-metal bonding interactions.[67, 88] Therefore, the energy and intensity of charge transfer transitions are very useful probes of the bonding interactions of the ligand with the cupric center.

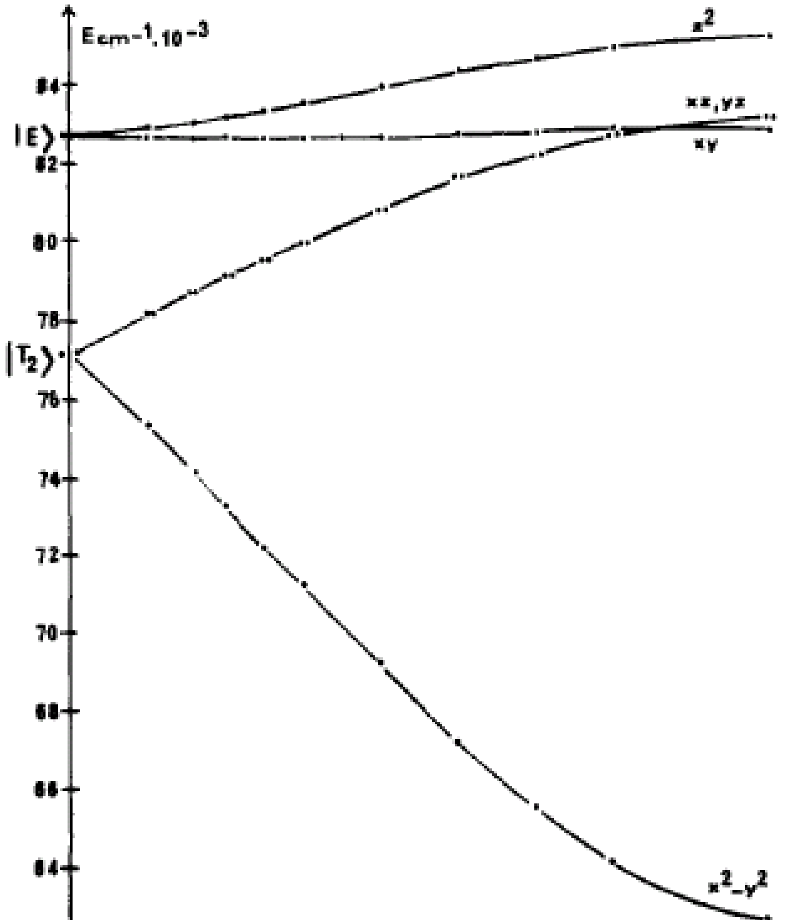

Figure 2.14 energy of d level with respect to ω value(adapted from ref 90)

Moreover, in some Cu homologous series, it has been shown that d→d transition bands are a good indication of the distortion magnitude. Figure 2.14 exhibited the energy of d level with respect to ω value. Thus, using optical characterization, Cu coordination geometry can be deduced.[90]

2.5. Scope and objective of this thesis

Copper-containing proteins have taken part in many enzymatic activities, such as dioxygen transport and activation, electron transfer, reduction of nitrogen oxides, and hydrolytic chemistry.[92, 93] More recently, the crystal structure of catechol oxidase revealed new insight into the functional properties of type-III copper proteins.[66] Many model compounds were synthesized to simulate the properties of type-III copper centers.[72-73, 94-97] They are important for the elucidation of the binding mode of dioxygen to the copper center in the oxy state. The study of model complexes such as the H-BPMP type [2,6-bis[{bis(2-pyridylmethyl)amino}methyl]-4-methylphenol],[97-101] the Hbbp type [1,3-bis(2-benzimidazolyl)-2-propanol],[102-105] or macrocyclic Schiff base ligands,[106-107] have been widely investigated.

Based on these studies, **a model compound of the *met* state of dinuclear copper complex containing only a single hydroxo bridge would be desirable for mimicking the structure of enzyme *COs*,** due to the less steric hindrance, which makes the substrate (for example, catechol) easliy approach the dinuclear active site during the oxidation reaction. A steric match between both hydroxyl oxygen atoms of catechol and the dinuclear copper center would facilitate the electron transfer between them.[92]

Literature showed that immobilizing catalytic centers in a solid support can simulate the natural occurring enzymes, where the solid support could provide both the proper geometry and distance for catalytic

centers, and enhance the stability of metal centers.[108-112] **The simple ligands are promised the prime candidate.**

In this thesis, we firstly investigated the influence of synthesis conditions on pore size, structure and morphology. Mesoporous silica with tuned pore size, more or less smooth surface and high hydrothermal stability are synthesized according to a *high temperature* post-synthesis treatment. Then, dual functionalization on the surface of a mesoporous silica is investigated using a novel approach based on the use of so-called “molecular stencil patterning”. The choice herein is AAPTMS ((3-aminoethyl)-amino-propyltrimethoxysilane) the complexing properties are probed by Cu(II) ion. Finally preliminary study on oxygen activation is reported.

Departure from regular square-planar coordination of the EPR active copper and Cu-Cu pair formation connected by exogenous bridging ligand, hydroxide(OH^-) is discussed with the help of the met form of COs (catechol oxidase) bio-inspired models cited above. Reference to AAPTMS forms stable 1:1 and 2:1 complexes with Cu^{2+} ($[Cu(AAP\text{-}Si\equiv)]^{2+}$ and $[Cu(AAP\text{-}Si\equiv)_2]^{2+}$, respectively) on the surface of fumed silica is also made.[89] Temperature dependent equilibrium between different Cu coordination environment is investigated based on the chemical element analysis, IR, UV-visible and EPR spectrum. Influence of pore size, surface morphology and hydrophobicity on the copper coordination chemistry is discussed.

2.6. Reference

(1) Anastas, P. T.; Warner, J. C. In Green chemistry: Theory and Practice; Oxford University Press, Oxford, New York, Tokyo, 1998, p1-2.
(2) Lindström, B.; Pettersson, L. J. *Cat. Tech.* **2003**, 7, 130, feature article.
(3) Bein, T. *Chem. Mater.* **1996,** *8,* 1636.
(4) Chmelka, B. F. *Nature*, **2006**, *5*, 681.
(5) Corma, A., *chem. Rev.* **1997**, *97*, 2773.
(6) Lu, Y. F. *Angew. Chem. Int. Ed.* **2006**, 45, 7664, highlights.

(7) Beck, J. S.; Vartuli, J. C.; Roth, W. J.; Leonowicz, M. E.; Kresge,C. T.; Schmitt, K. D.; Chu, C. T. W.; Olson, D. H.; Sheppard, E. W.; McCullen, S. B.; Higgins, J. B.; Schlenker, J. L. *J. Am. Chem. Soc.* **1992**, *114*, 10834.

(8) Wan, Y.; Zhao, D. Y. *Chem. Rev. 2007*, 10.1021/cr068020s.

(9) Sakamoto, Y.; Kaneda, M.; Terasaki, O.; Zhao, D. Y.; Kim, J. M.; Stucky, G.; Shim, H. J.; Ryoo, R. *Nature* **2000**, *408*, 449.

(10) Garcia-Bennett, A. E.; Miyasaka, K.; Terasaki, O.; Che, S. N. *Chem. Mater.* **2004**, *16*, 3597.

(11) Kaneda, M.; Tsubakiyama, T.; Carlsson, A.; Sakamoto, Y.; Ohsuna, T.; Terasaki, O.; Joo, S. H.; Ryoo, R. *J. Phys. Chem. B* **2002**, *106*, 1256.

(12) Yu, T.; Zhang, H.; Yan, X. W.; Chen, Z. X.; Zou, X. D.; Oleynikov, P.; Zhao, D. Y. *J. Phys. Chem. B* **2006**, *110*, 21467.

(13) Ying, J. Y.; Mehnert, C. P.; Wong, M. S. *chem. Rev.* **1999**, *38*, 67.

(14) J. S. Beck, J. C. Vartuli, G. J. Kennedy, C. T. Kresge, W. J. Roth, S. E. Schramm, *Chem. Mater.* **1994**, *6*, 1816.

(15) J. C. Vartuli, C. T. Kresge, M. E. Leonowicz, A. S. Chu, S. B. McCullen, I. D. Johnson, E. W. Sheppard, *Chem. Mater*. **1994**, *6*, 2070.

(16) C.-Y. Chen, S. L. Burkett, H.-X. Li, M. E. Davis, *Microporous Mater.* **1993**, *2*, 27.

(17) Steel, S. W. Carr, M. W. Anderson, *J. Chem. Soc. Chem. Commun.* **1994**, 1571.

(18) A. Monnier, F. Schüth, Q. Huo, D. Kumar, D. Margolese, R. S. Maxwell, G. D. Stucky, M. Krishnamurty, P. Petroff, A. Firouzi, M. Janicke, B. F. Chmelka, *Science* **1993**, *261*, 1299.

(19) G. D. Stucky, A. Monnier, F. Schüth,Q. Huo, D. Margolese, D. Kumar, M. Krishamurty, P. Petroff, A. Firouzi, M. Janicke, B. F. Chmelka, *Mol. Cryst. Liq. Cryst.* **1994**, *240*, 187.

(20) a) T. Yanagisawa, T. Shimizu, K. Kuroda, C. Kato, *Bull. Chem. Soc. Jpn.* **1990**, *63*, 988; b) S. Inagaki, Y. Fukushima, K. Kuroda, J. Chem. Soc. Chem. Commun. **1993**, 680; c) Y. Fukushima, S. Inagaki, *Mater. Sci. Eng. A* **1996**, *217 - 218*, 116.

(21) A. Firouzi, D. Kumar, L. M. Bull, T. Besier, P. Sieger, Q. Huo, S. A. Walker, J. A. Zasadzinski, C. Glinka, J. Nicol, D. Margolese, G. D. Stucky, B. F. Chmelka, *Science* **1995**, *267*, 1138.

(22) S. Ikeda in Surfactants in Solution, Vol. 2 (Eds.: K. L. Mittal, B. Lindman), Plenum, New York, 1984, pp. 825.

(23) A. Firouzi, F. Atef, A. G. Oertli, G. D. Stucky, B. F. Chmelka, J. Am.Chem. Soc. 1997, 119, 3596.

(24) C. A. Fyfe, G. Fu, J. Am. Chem. Soc. 1995, 117, 9709.

(25) O. Regev, Langmuir 1996, 12, 4940.

(26) Lapen, A. M.; Gross, A. F.; Tolbert, S. H. Langmuir 2005, 21, 470-480

(27) Huo, Q. S.; Margolese, D. I.; Stucky, G. D. *Chem. Mater.* **1996**, *8*, 1147.

(28) Q. Huo, D. I. Margolese, U. Ciesla, P. Feng, T. E. Gier, P. Sieger, R. Leon, P. M. Petroff, F. Schüth, G. D. Stucky, *Nature* **1994,** *368*, 317.

(29) Q. Huo, D. I. Margolese, U. Ciesla, D. G. Demuth, P. Feng, T. E. Gier, P. Sieger, A. Firouzi, B. F. Chmelka, F. Schüth, G. D. Stucky, *Chem. Mater.* **1994**, *6*, 1176.

(30) Galarneau, A.; Desplantier-Giscard, D; Di Renzo, F.; Fajula, F. *Catal. Today* **2001**, *68*, 191.

(31) Springerguel-Huet, M. A.; Sun, K.; Fraissard, J. *Microporous Mesoporous Mater.***1999**, *33*, 89.

(32) Edler, K. J.; Reynolds, P. A.; White, J. W.; Cookson, D. *J. Chem. Soc., Faraday Trans.* **1997**, *93*, 199.

(33) Edler, K. J.; Reynolds, P. A.; White, J. W. *J. Phys. Chem. B* **1998**, *102*, 3676.

(34) Yang, C. M.; Zibrowius, B.; Schmidt, W.; Schuth, F. *Chem. Mater.* **2003**, *15*, 3739.

(35) Galarneau, A.; Cambon, H.; Di Renzo, F.; Fajula, F. *Langmuir* **2001**, *17*, 8328.

(36) Galarneau, A.; Nader, M.; Guenneau, F.; Di Renzo, F.; Gedeon, A. *J. Phys. Chem. C* 10.1021/jp068526e

(37) Melosh, N. A.; Davidson, P.; Chmelka, B. F. *J. Am. Chem. Soc.* **2000**, *122*, 823.

(38) Melosh, N. A.; Davidson, P.; Feng, P.; Pine, D. J.; Chmelka, B. F. *J. Am. Chem. Soc.* **2001**, *123*, 1240.

(39) Liu, Z.; Terasaki, O.; Ohsuna, T.; Hiraga, K.; Shin, H. J.; Ryoo, R. *Chem. Phys. Chem.* **2001**, *4*, 229.

(40) R. Ryoo, C.H. Ko, M. Kruk, V. Antochshuk, M. Jaroniec, *J. Phys. Chem. B* **2000**, *104*, 11465.

(41) Sun, Y. Y.; Han, Y.; Yuan, L.; Ma, S. Q.; Jiang, D. H.; Xiao, F. S. *J. Phys. Chem. B* **2003**, *107*, 1853.

(42) Liu, J.; Zhang, X.; Han, Y.; Xiao, F. S. *Chem. Mater.* **2002**, *14*, 2536.

(43) Kruk, M.; Jaroniec, M.; Sayari, A. *Langmuir*, *J. Phys. Chem. B* **1999**, *103*, 4590.

(44) Tanev, P. T.; Pinnavaia, T. J. *Science* **1995**, *267*, 865.

(45) Namba, S.; Mochizuki, A. *Res. Chem. Intermed.* **1998**, *24*, 561.

(46) Ulagappan, N.; Rao, C. N. R. *Chem. Commun.* **1996**, 2759.

(47) Dong, J.-X.; Liu, G.-H.; Xu, H.; Gao, Z.-Q. In *Abstracts of International Symposium on Zeolites and Microporous Crystals*; Tokyo, Japan, 1997; Poster P155.

(48) Sayari, A.; Kruk, M.; Jaroniec, M.; Moudrakovski, I. L. *Adv. Mater.* **1998**, *10*, 1376.

(49) Khushalani, D.; Kuperman, A.; Ozin, G. A.; Tanaka, K.; Garces, J.; Olken, M. M.; Coombs, N. *Adv. Mater.* **1995**, *7*, 842.

(50) Sayari, A.; Liu, P.; Kruk, M.; Jaroniec, M. *Chem. Mater.* **1997**, *9*, 2499.

(51) Cheng, C.-F.; Zhou, W.; Park, D. H.; Klinowski, J.; Hargreaves, M.; Gladden, L. F. *J. Chem. Soc., Faraday Trans.* **1997**, *93*, 359.

(52) Corma, A.; Kan, Q.; Navarro, M. T.; Perez-Pariente, J.; Rey, F. *Chem. Mater.* **1997**, *9*, 2123.

(53) Bagshaw, S. A.; Prouzet, E.; Pinnavaia, T. J. *Science* **1995**, *269*,1242.

(54) Attard, S. G.; Glyde, J. C.; Goltner, C. G. *Nature* **1995**, *378*, 366.

(55) Goltner, C. G.; Henke, S.; Weissenberger, M. C.; Antonietti, M. *Angew. Chem., Int. Ed. Engl.* **1998**, *37*, 613.

(56) Zhao, D.; Feng, J.; Huo, Q.; Melosh, N.; Fredrickson, G. H.; Chmelka, B. F.; Stucky, G. D. *Science* **1998**, *279*, 548.

(57) Zhao, D.; Huo, Q.; Feng, J.; Chmelka, B. F.; Stucky, G. D. *J. Am. Chem. Soc.* **1998**, *120*, 6024.

(58) Imhof, A.; Pine, D. J. *Nature* **1997**, *389*, 948.

(59) Velev, O. D.; Jede, T. A.; Lobo, R. F.; Lenhoff, A. M. *Nature*, **1997**, *389*, 447.

(60) Liu, J. ; Shin, Y. S. ; Nie, Z. M.; Chang, J. H.; Wang, L. Q.; Fryxell, G. E.; Samuels, W. D.; Exarhos, G. J. *J. Phys. Chem. A* **2000**, *104*, 8328. Feature article

(61) Anastas, P. T.; Warner, J. C. In Green chemistry: Theory and Practice; Oxford University Press, Oxford, New York, Tokyo, 1998, p116.

(62) Holm, R. H.; Solomon, E. I. *Chem. Rev.* **1996**, 96(7), special volume for *bioinorganic enzymology*.

(63) Adman, E. T. *Adv. Protein Chem.* **1991**, *42*, 145.

(64) Carrel, C. J.; Ma, J. K.; Antholine, W. E.; Hosler, J. P.; Mathews, F. S.; Davidson, V. L. Biochemstry, **2007**, *46*, 1900.

(65) Hakemian, A. S.; Kondapalli, K. C.; Hoffman, B. M.; Stemmler, T. L.; Rosenzweig, A. C. **2008**, DOI: 10.1021/bi800598h.

(66) Gerdemann, C.; Eicken, C.; Krebs, B. *Acc. Chem. Res.* **2002**, *35*, 183.

(67) Solomon, E. I.; Sundaram, U. M.; Machonkin, T. E. *Chem. Rev.* **1996**, *96*, 2563-2605.

(68) Sanchez-Ferrer, A.; Rodriguez-Lopez, J. N.; Garcıa-Canovas, F.; Garcıa-Carmona, F. Biochim. *Biophys. Acta* **1995**, *1247*, 1-11.

(69) Eicken,C.; Krebs, B.; Sacchettini, J. C. *Curr. Opin. Struc. Bio.* **1999**, *9*, 677.

(70) Karlin, K. D.; Kaderli, S.; Zuberbu¨ hler, A. D. *Acc. Chem. Res.* **1997**, *1997*, 139.

(71) Wilcox, D. E.; Porras, A. G.; Hwang, Y. T.; Lerch' K.; Winkler, M. E.; Solomon, E. I. J. Am. Chem. Soc. **1985**, 107, 4015

(72) Mirica, L. M.; Ottenwaelder, X.; Stack, D. P. Chem. Rev. 2004, 104, 1013.

(73) Stack, D. P. Dalton Trans. 2003, 1881. Perspective article

(74) Comba, P.; Gahan, L. R.; Haberhauer, G.; Hanson, G. R.; Noble, C. J.; Seibold, B.; Van den brenk, A.L.; *Chem. Eur. J.* 2**008**, *14*, 4393..

(75) Gladysz, J. A. Chem. Rev. 2002, 102(10), special volume for recoverable catalyst and reagent—perspective and prospective.

(76) Sreinivas, D.; Sivasanker, S. *Catal. Surv. Asia* **2003**, *7*, 121.

(77) Hoffmann, F.; Cornelius, M.; Morell, J. Froba, M. *Angew. Chem. Int. Ed.* **2006**, *45*, 3216.

(78) Wulff, G.; Heide, B.; Helfmeier, G. *J. Am. Chem. Soc.* **1986,** *108*, 1089.

(79) Wulff, G.; Heide, B.; Helfmeier, G. *React. Polym.* **1987**, *6*, 299.

(80) Tahmassebi, D. C.; Sasaki, T. *J. Org. Chem.* **1994**, *59*, 679.

(81) Hwang, K.-O.; Yakura, Y.; Ohuchi, F. S.; Sasaki, T. *Mater. Sci. Eng. C* **1995**, *3*, 137.

(82) Shin, Y.; Liu, J.; Wang, L.-Q.; Nie, Z.; Samuels, W.D., Fryxell, G. E.; Exarhos, G.J. *Angew. Chem. Int. Ed. Engl.* **2000**, *39*, 2702.

(83) Katz, A.; Davis, M. E. *Nature* **2000**, *403*, 286.

(84) McKittrick, M.W., Jones, C. *Chem. Mater.* **2003**, *15*, 1132.

(85) Hicks, J. C.; Jones, C. *Langmuir* **2006**, *22*, 2676.

(86) Bonneviot, L.; Badiei, A.; Crowther, N. Patent WO 0216267, 2002.

(87) Abry, S.; Albela, B.; Bonneviot, L. *C. R. Chimie* **2005**, *8*, 741–752.

(88) Solomon, E. I. *Commun. Inorg. Chem.* **1984**, *3*, 225.

(89) De Monredon, S.; Pottier, A.; Maquet, J. ; Babonneau, F. ; Sanchez, C. *New J. Chem.* **2006**, *30*, 797.

(90) Gouteron, J.; Jeannin, S.; Jeannin, Y.; Livage, J. ; Sanchez, C. *Inorg. Chem.* **1984**, *23*, 3387.

(91) Pantoliano, M. W. ; Valentine, J. S.; Nafie, L. A. *J. Am. Chem. Soc.* **1982**, *104*, 6310.

(92) Lee, C. H.; Wong, S. T.; Lin, T. S.; Mou, C. Y. *J. Phys. Chem. B* **2005**, *109*, 775.

(93) Wong, S. T.; Lee, C. H.; Lin, T. S.; Mou, C. Y. *J. Catal.* **2004**, *228*, 1.

(94) Kitajima, N.; Moro-oka, Y. *Chem. Rev.* **1994**, *94*, 737.

(95) Kodera, M.; Katayama, K.; Tachi, Y.; Kano, K.; Hirota, S.; Fujinami, S.; Suzuki, M. *J. Am. Chem. Soc.* **1999**, *121*, 11006.

(96) Monzani, E.; Battaini, G.; Perotti, A.; Casella, L.; Gullotti, M.; Santagostini, L.; Nardin, G.; Randaccio, L.; Geremia, S.; Zanello, P.; Opromolla, G. *Inorg. Chem.* **1999**, *38*, 5359.

(97) Latour, J. M.; Le Pape, L.; Luneau, D. *Inorg. Chem.* **2000**, *39*, 3526.

(98) Belle, C.; Beguin, C.; Gautier-Luneau, I.; Hamman, S.; Philouze, C.; Pierre, J. L.; Thomas, F.; Torelli,

S. *Inorg. Chem.* **2002**, *41*, 479.

(99) Torelli, S.; Belle, C.; Hamman, S.; Pierre, J. L. *Inorg. Chem.* **2002**, *41*, 3983.

(100) Reim, J.; Krebs, B. *J. Chem. Soc., Dalton Trans.* **1997**, 3793.

(101) Mukherjee, J.; Mukherjj, R. *Inorg. Chim. Acta* **2002**, *337*, 429.

(102) Zippel, F.; Ahlers, F.; Werner, R.; Haase, W.; Nolting, H.-F.; Krebs, B. *Inorg. Chem.* **1996**, *35*, 3409.

(103) Neves, A.; Rossi, L. M.; Bortoluzzi, A. J.; Szpoganicz, B.; Wiezbicki, C.; Schwingel, E.; Haase, W.; Ostrovsky, S. *Inorg. Chem.* **2002**, *41*, 1788.

(104) Fernandes, C.; Neves, A.; Bortoluzzi, A. J.; Mangrich, A. S.; Rentschler, E.; Szpoganicz, B.; Schwingel, E. *Inorg. Chim. Acta* **2001**, *320*, 12.

(105) Gentschev, P.; Moller, N.; Krebs, B. *Inorg. Chim. Acta* **2000**, *300*,442.

(106) Rockcliffe, D. A.; Martell, A. E. *J. Mol. Catal., A* **1996**, *106*, 211.

(107) Louloudi, M.; Mitopoulou, K.; Evaggelou, E.; Deligiannakis, Y.; Hadjiliadis, N. *J. Mol. Catal. A Chem.* **2003**, *198*, 231.

(108) Robert, R.; Patnasamy, P. *J. Mol. Catal. A Chem.* **1995**, *100*, 93.

(109) Ganesan, R.; Viswanathan, B. *J. Mol. Catal. A Chem.* **2002**, *181*, 99.

(110) Viana Rosa, I. L.; Manso, C. M. C. P.; Serra, O. A.; Iamamoto, Y. *J. Mol. Catal. A Chem.* **2000**, *160*, 199.

(111) Seelan, S.; Sinha, A. K. *Appl. Catal. A: Gen.* **2003**, *238*, 201.

(112) Karandikar, P.; Dhanya, K. C.; Deshpande, S.; Chandwadkar, A. J.; Sivasanker, S.; Agashe, M. *Catal. Commun.* **2004**, *5*, 69.

Chapter 3 Surface and pore size engineering using high-temperature postsynthesis treatment

3.1 *Understanding the microporosity of classical MCM-41 silica*

3.1.1 Introduction

Since the discovery of M41S family silica in 1992,[1] numerous studies focused on the synthesis, characterization and applications.[2-4] Mesoporous silica materials still face a great challenge for water involved reactions under severe conditions, such as high temperature and pressure because of inherent amorphous nature of the pore wall. Though SBA-15 silica was claimed to be very stable due to much thicker pore wall than that of MCM-41 silica,[5, 6] Galarneau and coworkers reported that SBA-15 mesoporous silica was not as stable in water even at room temperature as expected because of the existence of microporosity in the pore walls for synthesis temperature below 110°C.[7] Moreover, the calcined MCM-41 silica Is kown to loose its mesostructure when it is exposed under atmospheric conditions for several months due to a narrow wall thickness of ca. 1,0 to 1,5 nm.[8]

More recently, the surface area and pore volume of primary mesopore of SBA-15 were found overestimated due to the presence of surface microporosity, [9] which was proved by N_2 adsoption-desoption isotherms [10] and comparison plots,[9, 11-13] characterization of platinum and carbon replicas [14-17] and laser hyperpolarized ^{129}Xe NMR data, [7, 18, 19] Several studies on microporosity of conventional mesoporous silicas, such as MCM-41 (hexagonal geometry, basic synthetic condition at high temperature), [20] SBA-3 (hexagonal geometry, acidic synthetic condition) [21-23] and MCM-48 (cubic simmetry) [24] were also reported. No convincing evidences provided the existence of microporosity in MCM-41 silica synthesized under basic conditions at low reaction temperature, Some results, can not be easily understood only based on the simple hole-pore wall structure, i.e., well-accepted cylindrical geometry model.[28] These results for MCM-41 silicas include the overestimated surface area and pore volume of primary mesopores and silica density (2.2 cm^3g^{-1}) of pore wall,[25] the larger nitrogen uptake at very low relative pressure in a range of 0-0.01,[26] negative intercept value from t-plot, higher thermal and hydrothermal stability and low pore expansion efficiency below 1 nm after high temperature post-synthesis treatment.[25, 27]

To explain the local silica density between 0.8 and 1.5 cm^3g^{-1} observed by small-angle neutron scattering and synchrotron X-ray diffraction, White et al. proposed a new model for MCM-41: [29, 30] a straight channel in which the walls of narrow channel are lined with a thick layer (density 0.99 cm^3g^{-1}) of finely divided extremely fluffy silica (0.87cm^3g^{-1}), significantly different from the conventionally assumed smooth walled linear cylindrical channels passing though silica of essentially bulk density. However, the primary mesopore size derived from this model was only 0.7 nm, which was obviously not right.

In this study, the data of X-ray diffraction (XRD) patterns, nitrogen adsorption isotherm, laser hyperpolarized ^{129}Xe nuclear magnetic resonance (NMR) and X-Ray photoelectron (XPS) spectrum, combined with geometrical calculation, have been to evidence the presence of the open micropores on the channel surface. It will be shown that the surface is alveolus, i.e., made of small cavities or pits, such as a honey comb cells or tooth sockets in a jaw bone. To evidence the presence of these alveoli, CTA^+ surfactant molecules were ion exchanged by tetramethyl ammonium ions, according to conditions that have been tuned to keep as much as possible the morphology of the surface and all the physical properties characterizing the porosity. Note that TMA^+ was chasen because it has the same kinetic diameter than the hydrophilic head of CTA^+ that is ca. 0.67nm. It was impossible to keep the structure intact using smaller cations as lithium, sodium or caesium. In addition, the exchange yield was quantitatively monitored using both FT-IR and chemical analysis.

Nitrogen adsorption-desorption data analyses according to various methods including the Broekhoff-de Boer method (BDB[32]) shows that the microporosity depends on drastically on the silica source, the ageing temperature and time and the autoclaving temperature and time. The presence of the microporosity is detected from the anomalies of the adorption at low pressure from a “normal” silica surface and the much too large specific surface area for a perfectly smooth surface of hexagonal or cylindrical channel has usually depicted. The TMA exchange mesoporous silica does not show micropores, is characterized by a consistent set of value for surface area, pore volume and mesoporous channel diameter. This very same sample reitrives the anomalies due to the microporosity after calcination. More directly, polarized ^{129}Xe NMR spectrum exhibits features that can be consistently interpreted with the other set of data assuming that TMA^+ cations fit perfectly into the micropores. The data described in detailed in the following will prove that this microporosity is reversibly accessible by TMA cation the size of which correspounds to the size of these micropores of about 0,7 nm diameter. The surface can be depicted as shown on Figure 3.1.

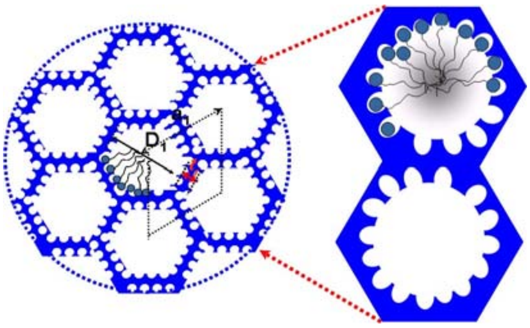

Figure 3.1 Scheme of proposed wall structure for MCM-41 type of silica with open micropores around the hexagonally packed channel (on the right, zoom of two channels).

3.1.2 Experimental section

3.1.2.1 Synthesis of C16-MCM-41: C16-MCM-41 was prepared as follows:[33] Ludox (15.5 g, 0.26 mol) was added to sodium hydroxide (2 g, 5 $\times 10^{-2}$ mol) in deionised water (50 ml), then stirred at 313 K until clear (about 24 h). A second solution of hexadecyltrimethylammonium *p*-toluenesulfonate (CTATos) (2.5 g, 5.5 $\times$ 10^{-3} mol) (> 99% Merck) in deionised water (90 ml) was stirred for 1 h at 60°C. The first solution was added dropwise to the second one, and then stirred at 60°C for 2 h. The resulting mixture was heated in an autoclave at 130°C for 20 h. After filtration and washing with deionised water, the as-synthesized solid was dried at 80°C.

3.1.2.2 Synthesis of C12-MCM-41: C12-MCM-41 was synthesized using dodecyltrimethylammonium *p*-toluenesulfonate (DTATos, about synthesis see the report of Michel Morin) as template modified recipe was as follows: 6.58 g DTATos was dissolved in 120 ml of water and stirred for 1 hour at 60°C. 22.82 g 1.0M tetramethylammonium hydroxide (TMAOH) aqueous solution was added into 107 ml water, followed by addition of 10.79 g fumed silica under vigorous agitation. After stirring for 1 hour at 60°C, the silicate solution was then added drop by drop into CTATos solution. The molar composition of the final mixture was SiO_2: 0.09 DTATos: 0.35 $TMAOH^-$: 79.9 H_2O. The mixture was stirred for 2 hours at 60°C and then transferred into a 250 ml Teflon-lined steel autoclave. The final mixture was heated in autoclave under static condition at 130°C for 20 hours.

3.1.2.3 Synthesis of TMA-C_x-MCM-41 molecular sieve: Ion exchange of C_X-MCM-41 molecular sieve was performed in a 100 mL two neck bottom-round flask in the following way: 1.0 g as-made MCM-41 silica was mixed with 0.67 g TMABr (3 equi. to surfactant) in 40 ml 95% ethanol, and the mixture was stirred for 15 min at 40°C. The solid was filtrated and washed two times by ethanol (95%) and then acetone, and dried at 80°C over night. This process repeated 3 times, and surfactant could be fully exchanged. It should be mentioned that exchange in water lead to complete destruction of the structure.[34]

3.1.2.4 Full Trimethylsilylation of MCM-41: As-made silica (3.0 g) first was extracted by 1M HCl in 120 ml ethanol (1.2 equiv. to surfactant) at 40°C for 30 min, and the surfactants were completely removed after repeating this process. The recovered solid was dried at 80°C for 12h. After the obtained solid was activated for 5 h under vacuum at 130°C, and cooled down to room temperature under Ar protection, hexamethyldisiloxane (HMDSO, 98% Acros)(12.5 ml, 5.9×10^{-2} mol) and chlorotrimethylsilane (CTMS) (98% Acros) (7.5 ml, 5.9×10^{-2} mol) were added under nitrogen. The mixture was stirred 1 h at room temperature and then refluxed for 15 h. The obtained solid, C16-MCM-41, was finally washed with ethanol and acetone (about 100 ml) and dried at 80°C.[35]

3.1.3 Characterization

Low-angle X-ray powder diffraction experiments have been carried out using a Bruker (Siemens) D5005 diffractometer using Cu Kα monochromatic radiation. Nitrogen adsorption isotherms were measured at 77 K using an ASAP 2010 volumetric adsorption analyzer (Micromeritics, Norcross, GA). Before the measurements, samples were outgassed for 6 h at desired temperature in the degas port of the adsorption analyzer. Laser hyperpolarized ^{129}Xe NMR measurements were collected at 110.688 MHz on a Bruker spectrometer at room temperature. The samples were evacuated at desired temperatures overnight before xenon was adsorbed at 296 K in a pressure range of 8-1000 Torr. A π/2 pulse (c. 10 μs) was used. Typically, 1000–50 000 scans were recorded to obtain a sufficiently high signal-to-noise ratio. The repetition time was 1 s. The chemical shift reference (0 ppm) is the shift of gaseous xenon extrapolated to zero pressure.[36] X-ray photoelectron spectroscopy measurements were done in equipment ESCALAB MKII de VG, source Al Ka with energy (hv =1486.6 eV), under pressure of 10^{-8} mbar. C1s was taken as reference at 284.6 eV.

3.1.4 Results and discussion

3.1.4.1 XRD patterns: Small angle XRD patterns in figure 3.2 show typical hexagonal structure of MCM-41 silicas. Note that the d_{100} value of C16-MCM-41 (4.05 nm) is larger than that of C12-MCM-41 (3.46 nm). This is consistent with the larger chain lengh for the C-16 surfactant and the difference of 0.4 nm matches well the expectation.[1]

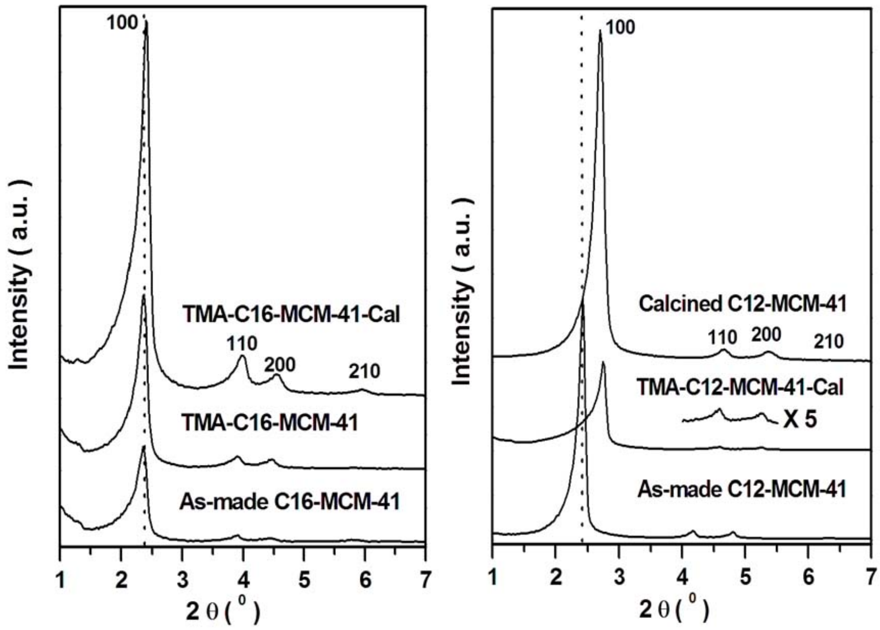

Figure 3.2 XRD patterns of C16-MCM-41 samples:bottom, as-made samples, middle, after TMA ion exchange and top calcined after TMA exchange; on the right, C12-MCM-41: bottom, as-made samples, middle, calcined after TMA exchange and top, directly calcined sample with C12 surfactant.

The small angle XRD profile for the TMA exchanged sample also exhibited high quality MCM-41 structure. The XRD peaks are within the measurement precision at the same place after TMA exchange and calcination for the material templated with the C-16 surfactant. In addition, the intensity increases after TMA exchange consistently with the removal of matter in the channel (no more filling by the C-16 alkyl chains), calcination that removes TMA provokes a further increase of the contrast.

The evolution is not as straiforward for the material templated with the C-12 surfactant. The XRD peaks shifts notably toward high angles, i. e., lower d spacing after TMA exchange. In addition, the peak intensity decreases, showing that there is morelikely some structure loss that will be confirmed latter by the chemisorption data.

Table 3.1 Elemental analysis of C16-MCM-41 samples

Sample	C/%	H/%	N/%	S/%	C : N[d]	N/Si[e]
C16-MCM-41[a]	33.0	6.7	1.9	0.35	**20.0 (19.0)**	**0.16**
TMA-MCM-41[b]	8.6	3.2	2.3	<0.1	**4.4 (4.0)**	**0.14**
TMS-MCM-41[c]	11.5	3.0	-	<0.1	**-**	**(0.27)**[f]

Note: a, as-made sample with surfactants; b, sample exchanged by TMA; c, full silylated sample; d, atom number ration of C and N, the value in parenthesis from Surfactant or tetramethyl ammonium (TMA); e, molar ratio of N/Si; f, molar ratio of TMS/Si_{in}.

3.1.4.2 elemental and thermalgravimetric analysis: TGA of both materials are qualitatively equivalent with a weight loss of 5 % below 120°C that corresponds to water desorbtion. Between 150 and 380 °C, there is the decomposition of the surfactant. Between 380 and 650°C the main loss is due to silanol condensation. The residual mass is 52 and 58 % for the C-16 and C-12 surfactant templated materials. From this data, it appears on the latter that the proportion of silica is higther. Note that a wall of the same thickness for both materials would results in a higher proportion of silica for a smaller pore diameter as observed here. Indeed, the calculated N/Si ratio decrease from 0.16 to 0.14. The C/N ratio should be close to the theoretical value obtained from the molecular formula of the surfactant, which is 19 for the C-16 surfactant and 4 for the TMA exchanged materials (given in parenthesis in table 3.1).

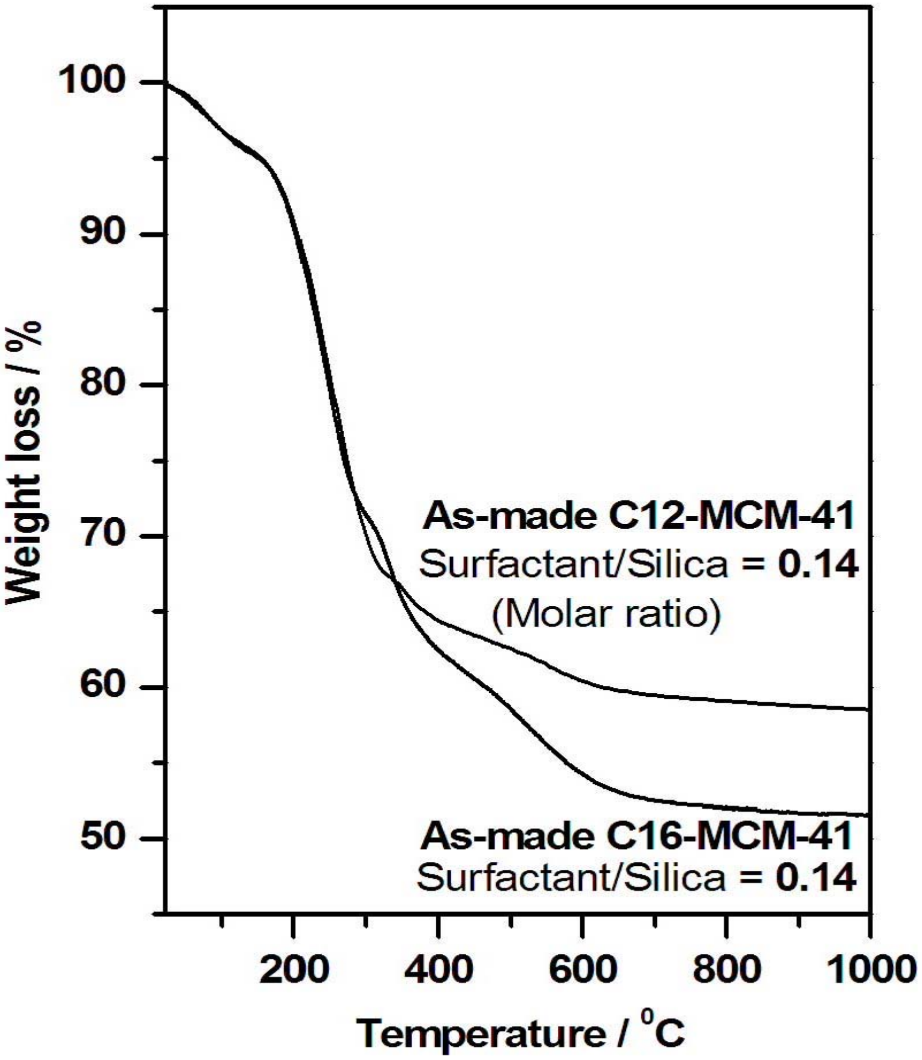

Figure 3.3 Thermal gravimetric analysis (TGA) for the samples C16-MCM-41 and C12-MCM-41.

Note that the surfactant counterion is a tosylate that contains 1 sulfur for 7 carbon atoms per molecular formula. Some anions are obviously remaining in the solid as attested by the presence of 0.35% by weight of sulfur. This accounts for as 0,08 S atom per nitrogen or ca. 0.6 carbon atoms per nitrogen. So, for the overall 20 carbon atoms per nitrogen atoms, 0.6 are from the tosylate and 19.4 corresponds to the surfactant, which is rather good carbon balance. When the CTA is ion exchanged by TMA one count 4.4 C per N which is again within 10% in good agreement with an effective ion exchange of most of the CTA^+ ions. The C/Si that allows to calculate of the trimethylsilyl loading provides 0,27 TMS function per silicon, which again compares well with 0.24-0.23 reported earlier.[33,35]

It is worth to calculate the total volume occupies by the surfactant, the volume occupied by its hydrophilic heads only and the surface covered by the head assuming to be equal to its projected surface. In this approximation, the covered surface is the same both for TMA and CTA. Calculation of the volume occupied by 0.16 surfactant per Si can be performed using molecular density, $\rho_{surfactant} = 0.77\ cm^3g^{-1}$ and leads to *ca.* $V_{total\ (micelle\ volume)}$ of $1.02\ cm^3g^{-1}$.[28] this is a rough estimation since the density is known only for the surfactant salt that includes the counterion, and that the actual packing in the liquid and in the templating micelle in the solid is unknown. The following calculation is based on the molecule dimension taken from the Van der Waals (VdW) radius. The VdW diameter of TMA^+, $D_{TMA,}$ is 0.43 nm and will be taken also as the size of the surfactant head. The projected projected surface head ($\pi D_{TMA}^2/4$) is 0,148 nm^2 and the occupied volume ($\pi D_{TMA}^3/6$) is 0,065 nm^3. This leads for 0.16 surfactant per Si to a surface covered of 232 m^2/g and a volume occupied of 0,067 cm^3/g. The same calculation for the material prepare with the C12 surfactant leads to 210 m^2/g and 0,06 cm^3/g, respectively. This figures will be worth to compare with the value obtained for the materials using nitrogen chemisorption.

3.1.4.3 N_2 adsorption isotherm: N_2 adsorption-desorption isotherm (Figure 3.4, left) exhibits the typical type IV isotherm of MCM-41 silica, and the capillary condensation pressure shifted to higher value as exhibited in the pore size distribution plot by BJH method from desorption branch (Figure 3.4, right). For mere comparison, the adorption desorption profile of a material synthesized at much higher temperature (175°C) that contains zeolitic microporosity is represented also in figure 3.4. The adsorption profiles of the TMA exchanged materials are compared also with the calcined materials in Figure 3.5. Figure 3.6 depicts t-plot, α-plot, β-plot and very low pressure range plotted as V_{ads} vs $\log(P/P_o)$ used to analyze the data. The reason for exploiting such diversity of analyses is motivated by the feeling that non of them are fully satisfying because of the connectivity between both micro- and mesopore systems. All the quantitative information is gathered in Table 3.2.

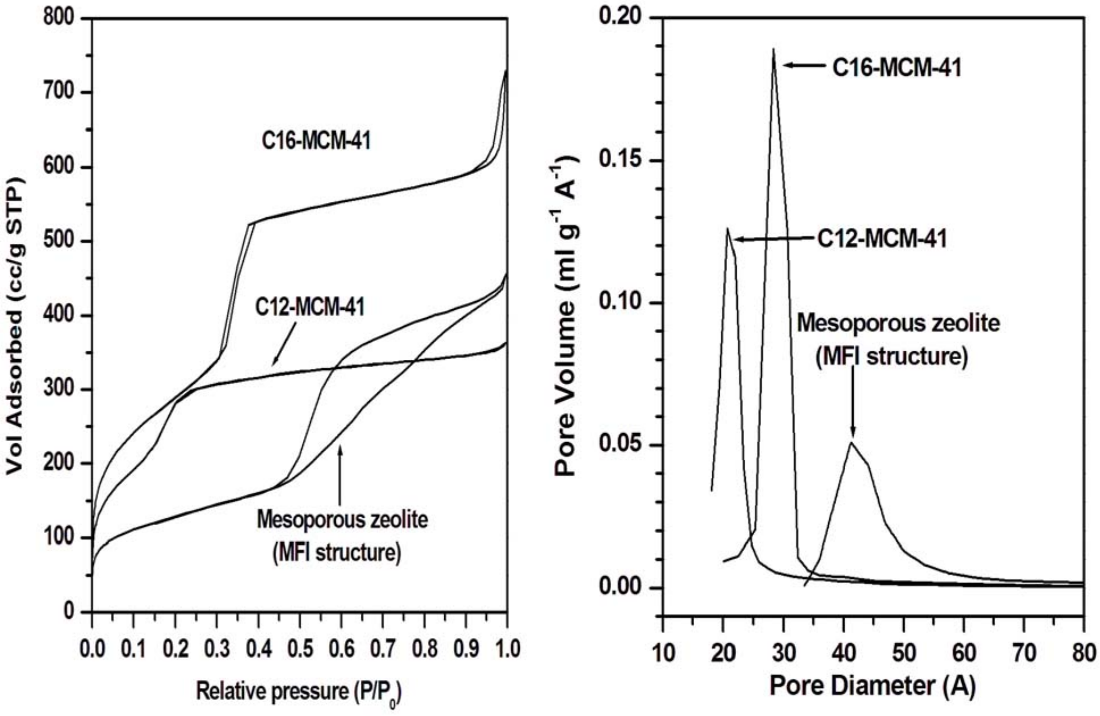

Figure 3.4 Nitrogen adsorption-desorption isotherm (left) and BJH mesopore size distribution (right) from desorption branch of MCM-41 silicas with different pore size.

For the normal calcined material obtained from C-16 surfactant, C16-MCM-41, the total pore volume of 0,97 cm^3g^{-1} and 1060 m^2g^{-1} BET surface area for templated silica is typical of MCM-41 type of silica. The pore volume is consistent with the estimation of the volume of micelle contained in the material. From capillary condensation unsing BJH or DBD methods, the pore size is 3.1 nm for the former or 3.7 nm respectively, as expected for such a material. From α- or β-plots, a value of 3.2 nm is found. In comparison, the uncalcined TMA exchanged material, C16-MCM-a, exhibits a decreased pore volume and surface area down to 0.73 cm^3g^{-1} and 800 m^2g^{-1}, respectively. The missing volume matches well the volume of the surfactant ammoniun head, 0.25 cm^3g^{-1} calculated above. This would be consistent with TMA^+ cations occupying the same surface location as the CTA^+ cations, from which it has been substituted by ion exchange. Consistently, the remaining pore volume corresponds to the volume of the alkyl chains that are now absent in this material. In parallel, the mesoporous pore size diameter is unchanged whatever the technique used for its measurement. In addition, when TMA is removed by calcination the mesoporous size is still the same. This shows that the TMA exchange reaction has preserved the porosity whatever its nature. TMA obviously occupies a volume, which is not the mesopore volume.

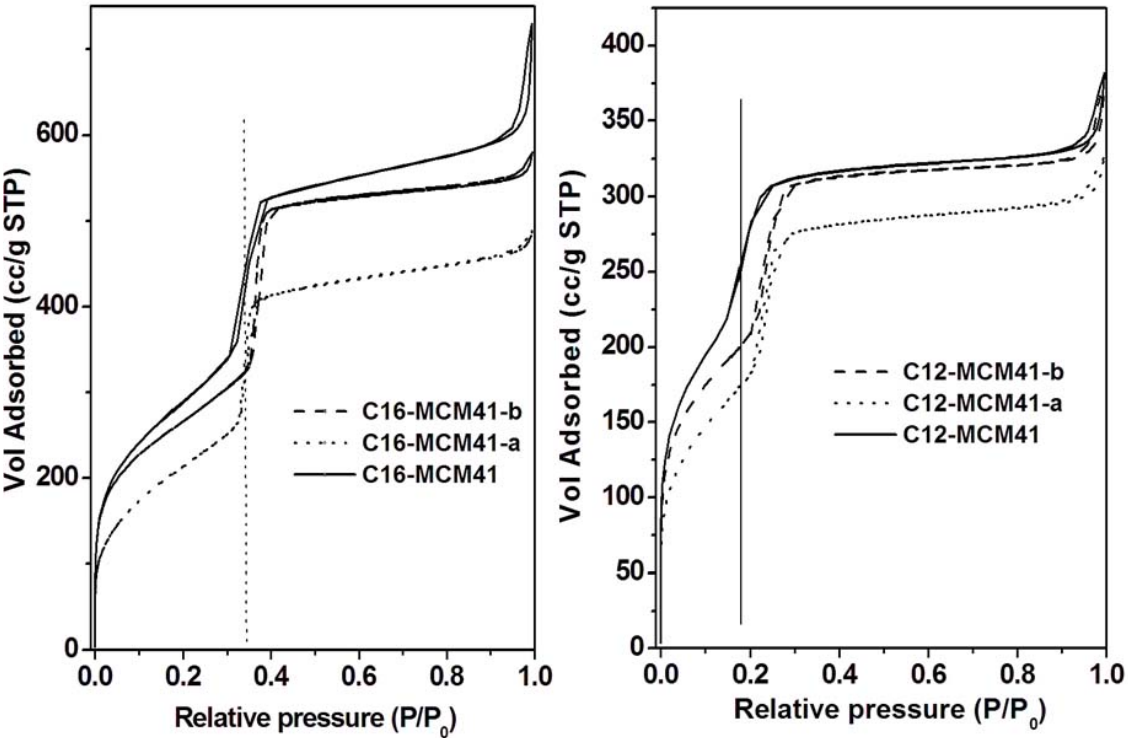

Figure 3.5 N_2 adsorption-desorption isotherms of mesoporous materials exchanged by TMA or silylated by TMS: C16-MCM41 (left) and C12-MCM-41 (right).

It is legitimate to think that TMA occupies the microporous portion of the surface that is not involved in either the formation of the adsorption layers nor to the capillary condensation mechanism. Another surprising observation concerns the effect of capping the OH by trimethylsilylation using TMSCl (Figure 3.6, left).

The material C-16-MCM41-c, which is fully silylated according to the TMS coverage of 0,27 TMS/Si for 1060 m^2g^{-1}, exhibits as the three previous materials, virtually no change of unit cell parameter (the variation lies within range of incertainty ± 0.1 nm). Note that TMS groups are slightly bulkier than TMA by *ca.* 15% (diameter of 0.70 for 0.67 nm from the VdW radius and volume of 0.180 for 0.157 nm^3, respectively) and the quantity incorporated is nearly double, 0,27 TMS/Si for 0,14TMA/Si, in comparison with material C16-MCM-a. The total pore volume occupied by TMS moieties is *ca*. 0.49 cm^3/g. The volume decreasing down to 0.31 cm^3g^{-1} indicates that there is an incomplete filling with about 0.48 cm^3g^{-1} of empty space.

Table 3.2 Summary of the pore characteristics of mesoporous materials

Sample Name	a_0[d] (nm)	S_{BET}[e] ($m^2 g^{-1}$)	V_{total}[e] ($cm^3 g^{-1}$)	$V_{mic+mes}$[f] ($cm^3 g^{-1}$)	D_{BDB}[e] (nm)	$D_{as\text{-}plot}$[g] (nm)	$D_{\beta\text{-}plot}$[f] (nm)
C16-MCM41	4.6	**1060**	**0.92**	0.77	**3.7**	3.2	3.2
C16-MCM41-a[a]	4.7	**800**	**0.71**	0.67	**3.7**	3.0	3.1
C16-MCM41-b[b]	4.7	**960**	**0.85**	0.80	**3.9**	3.5	3.7
C16-MCM41-c[c]	4.8	300	0.28	0.18	3.4	2.0	2.0
C12-MCM41	3.8	920	0.54	0.50	**2.6**	2.7	2.2
C12-MCM41-a	4.0	660	0.46	0.42	**2.9**	2.7	2.4
C12-MCM41-b	3.8	760	0.50	0.48	**2.9**	2.9	2.6

a) TMA exchanged not calcined b) as a and calcined, c) fully silylated materials,d) $a_0 = d_{100}*2/1.732$, hexagonal lattice parameter calculated from XRD, e) S_{BET} and V_{total} determined using a micromerttics ASAP2010 porosimeter, BET surface areas calculated using the relative pressure range of $0.05 \leq P/P_0 \leq 0.16$, V_{total} is single point pore volume at

P/P_0=0.92, f)internal volume obtained by extrapolation of the plateau in α-plot, g) D_{BDB}, $D_{\alpha\text{-plot}}$ and $D_{\beta\text{-plot}}$ determined using BDB method from the desorption branch also and the 4V/S from the adsorption branch using α-plot and β-plot (C_{ref}=2.20 [13]), respectively.

The drop of surface area down to 300 m^2g^{-1} corresponds to a 3,5 fold decrease (1060 m^2g^{-1}/300 m^2g^{-1}). The BJH method leads to an inconsistent increase and is obviously off by far. On the other hand, the BDB method leads to a slight decrease down to 3.4 nm (-0.3 nm) while both methods based on α– and β-plots give a much smaller value of 2.0 nm.

A coverage of 0,27 TMS/Si on a surface of 1060 m^2g^{-1} corresponds to a dense layer of grafted function.[33, 36] The thickness of such a layer on a smooth surface is equal to the size of the molecule, which is for a TMS, *ca.* 0,7 nm. Accordingly, the pore diameter should decrease by twice this size, *ca.* 1.4 nm, for a smooth cylindrical or a hexagonal channel. From the BDB pore diameter the actual diameter should be about 2.3 nm or from the α– or β-plots about 1.8 nm. For a 1D smooth channel, this decrease should generate surface drop down to 650 m^2g^{-1} instead of to 300 m^2g^{-1} measured and a volume drop down to 0.33 cm^3g^{-1} while 0.31 cm^3g^{-1}. Again this shows that evolution of volume are consistent while surface does not follows the expected trend of a smooth channel.

Similar trends were also performed on the C-12 templated silica, C12-MCM41 (Figure 3.4-3.6 and Table 3.2). The calcined form exhibits a relatively low pore volume of 0.55 cm^3g^{-1} for a high surface area of 920 m^2g^{-1} in comparison to its C16 templated analogue. The loss of volume due to the presence of TMA is smaller and the recovery of the structure after calcinations of the TMA exchange sample is really obtained. This may indicate the presence of more microporosity, a higher surface rugosity and a more fragile surface. Comparing material generated from C12 and C16 does not appear obvious at this stage and necessitate a better description of the microporosity.

3.1.4.4 Comparison plots: To characterize the micropore volume, nitrogen adsorption isotherm such as comparison plots (t-plot, α_s-plot and β-plot) and low pressure regions 10^{-7}-0.01 of the adsorption isotherms were carefully analyzed in figure 3.6. On β-plot, the first strike point is the negative intercept of the linear extrapolation of the adsorption curve at low pressure for both C_{12}- and C_{16}-MCM-41 calcined silica. Though not obvious on the t-plot as it is reported on figure 3.6 all the intercept are negative indicating that the reference amorphous silica is not correct for the present materials. The results obtained from comparison plots implied that the routine physisoption methods using nonporous silica as references are not suitable to precisely extrapolate the pore volume and surface area of primary mesopores in the presence of micropores; this is a known fact.[26] However, when micropores are present, their filling should occur at very low relative pressure ($p/p_0<0.01$). They involve pores with diameters comparable to the size of the gas molecules used, which implies a primary filling mechanism highly sensitive to the surface morphology and affinity with the surface as claimed by Sing et al.[38] In our case, the negative intercept indicates that, at very low pressure, nitrogen adsorption is retarded in comparison with a silica having no micropores or large micropores in comparison of the molecular size. The hindered formation of the first layer in the present material is due to very small micropores. This is also observed for the mesozeolite, the pore size of which is about 0.56 nm. The close examnation of the very low present range (Figure 3.6d) indicates a ghange of adsorption rate at about $p/p_0 = 10^{-5}$ where both adsorption curves merges for C_{12}- and C_{16}-MCM-41 materials. This change is seen at $p/p_0 = 10^{-4,5}$ in the mesozeolite. Above, it seems that the adsorption occurs in a rather “normal way”. The latter refers to the secondary pore filling process involving adsorbent-adsorbate as well as adsorbate-adsorbate interaction.[38] This mechanism leads to the formation of multiple adsorbed layers known to be well defined in the pressure range of $0.01<p/p_0<0.2$ where micropore should be filled. To minimize adsorption pecularities of nitrogen, it is recommended to use argon adsorption.[26] All these results show why the mesoporous templated silica provides use a great challenge for the characterization of microporosity in presence of mesoporosity both intellectually and experimentaly.[10, 18]

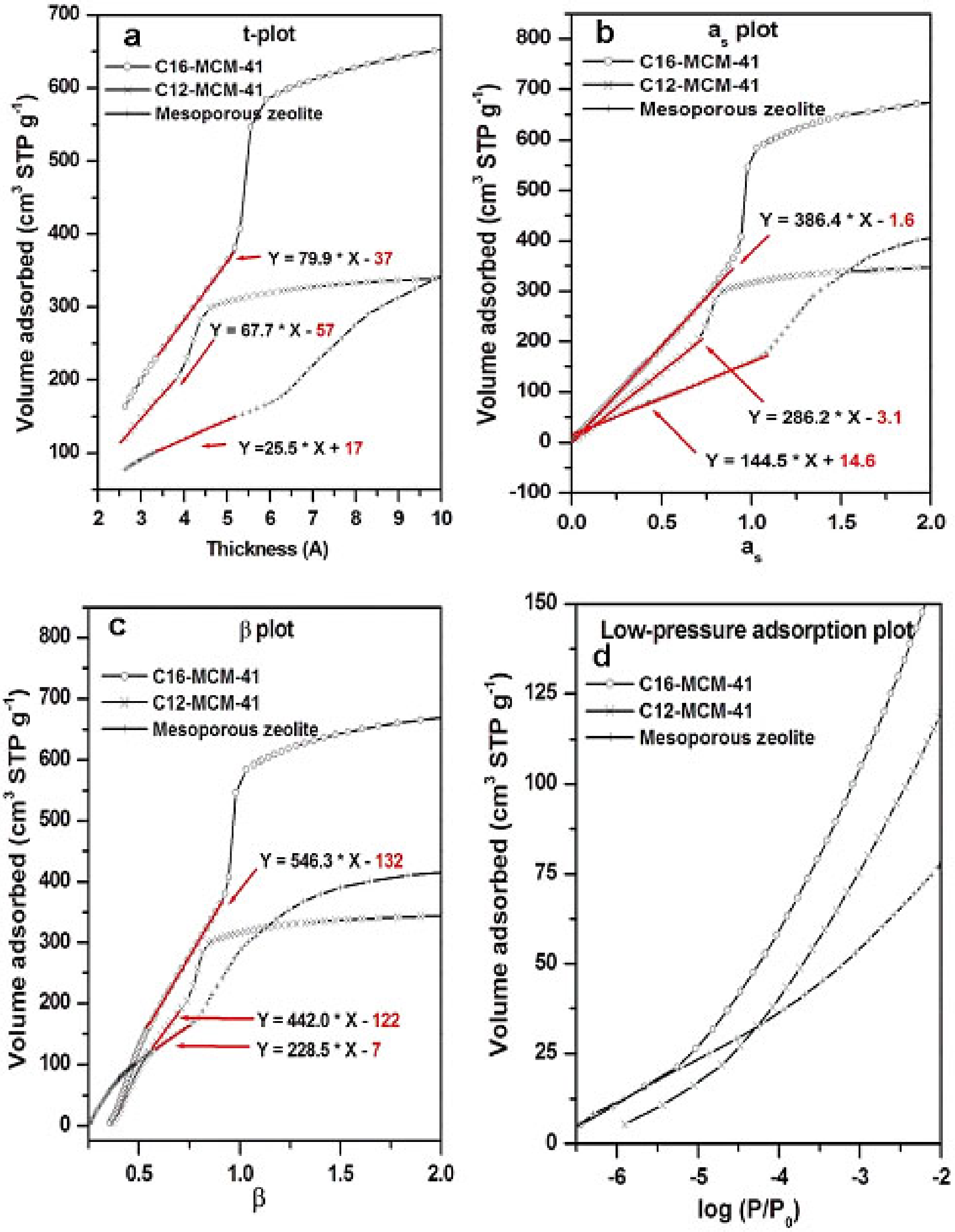

Figure 3.6 Nitrogen adsorption isotherms of MCM-41 silicas using different comparision methods including t-plot (a), a_s-plot (b), beta-plot (c), and low pressure adsorption plot (d).

3.1.4.5 ^{129}Xe NMR measurements: To further characterize the microporosity, NMR measurements were performed using laser hyperpolarized ^{129}Xe adsorbed in the materials (Figure 3.7). The measurement were performed at various pressure from 10 to 840 Torrs. On the right hand side of Figure 3.8, the material contains TMA as described before. All NMR signals exhibit a narrow intense peak at 0 ppm assigned to gaseous Xenon taken as reference for chemical shifts. Another signal arises at *ca.* 50 ppm whatever the pressure, which appears relatively large. It may present a shoulder on its left at about 70 ppm, quite large and difficult to distinguish from the noise at 125 Torrs or below. On the calcined material that does not contain TMA, there is two well defined pressure dependent signals. One of them is relatively large and arises at 58 pmm for a pressure of 10 Torrs. It gradually shifts down to 40 ppm at 700 Torrs. Except the pressure dependant spectral shift, this signal seems similar to the signal of the material containing TMA. The second signal hardly seens at 10 Torrs, grows faster with pressure than the first one. Between 143 and 700 Torrs, its position moves from 70 to 64 ppm. The NMR data were collected in the same conditions with the same data accumulation. A five time higher signal to noise ratio at 10 Torrs in absence of TMA indicates a much higher pore occupancy of about the same ratio. This shows that removing TMA liberates places where Xe atoms can over concentrate. This is consistent with the presence of small micropores trapping Xe. To explain the peak position one has to remind some features of the ^{129}Xe NMR.

The chemical shift measures the shielding due to the electrons on the nucleus.^{129}Xe does not built any durable bonds, therefore the chemical shift is an average value of the electronic interaction occuring at each shock between Xe atoms in the gas, and between Xe and the solid palissade. The number of shocks affects the chemical shift and depends on the pressure (average mean free path) in the gas. In the presence of a porous solid, this depends on the exposed surface area and on the polarity of the surface. The intensity depends on the statistics and the position on the relative number of shocks of different types. Eventually, only one single signal should be seen at an average chemical shift. Fortunately, when the exchange rate between two probed locations is longer than the measurement time then two signals can be seen. However, the relative position depends on the exchange rate between two sites. The chemical shift displacement with pressure is a mark of the connectivity and exchange rate between to sites.

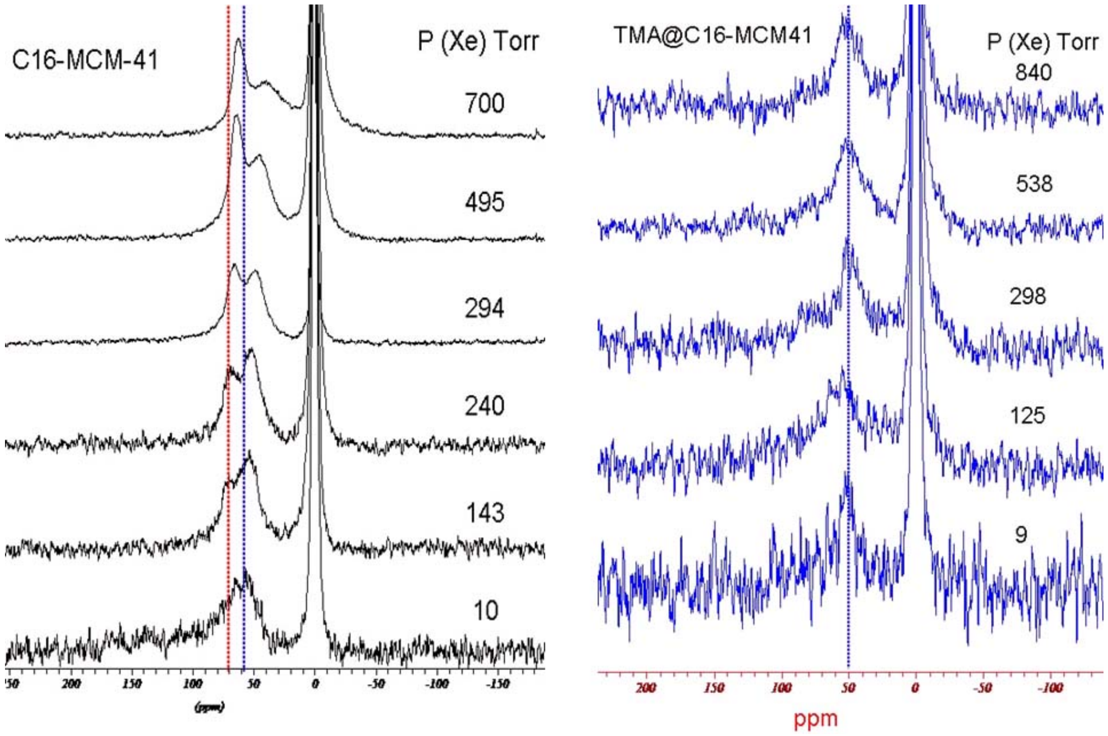

Figure 3.7 ^{129}Xe NMR spectra as function of Xe pressure given in Torr (1 Torr≈132 Pa): calcined sample (left) and sample exchanged by TMA molecule (right)

Note that the pore occupancy depends on the adsorption pressure and in small pores the statistics for Xe-wall interactions are much larger than in large pores leading to larger chemical shift for the former than for the latter.[37]

Accordingly, it seems reasonable to assigned the signal at about 50 ppm to Xe probing both the voids between fibers and the mesoporous volume, with a rapid exchange process between them. The absence of pressure dependant shift for TMA containing material may be due to a perfect compensation of the pressure effect in mesopores and in the voids in comparison with the gas phase. This compensation is broken in the presence of micropore that over concentrate Xe in the mesopores that explains the pressure dependence in the presence of micropores of C16-MCM-41 empty material.

The ^{129}Xe NMR experiments further proves that TMA in the exchanged materials and, therefore, CTA in the as-made materials occupies which a good match with the volume of the micropores in MCM-41 type of materials.

3.1.4.6 XPS measurements: To further explore the specific properties of the surface, XPS has been performed on as-made material C16-MCM41, TMA exchanged C16-MCM41 and the C12 analogues (see table 3.3). C1s is used as an internal reference, both Si2p and O1s lines were investigated to understand the structure of the surface.

Table 3.3 Characteristics of Si2p and O1s XPS lines of as-made and TMA exchanged mesoporous silica of MCM-41 type of structure.

Sample Name	Si^a (eV)	Si^b (eV)	O^a	O^b	$O^a/(O^a+O^b)$	$Si^a/(Si^a+Si^b)$
C16-MCM41	101.4	102.6	530.0	532.1	**12%**	**9%**
TMA@C16-MCM41	101.4	102.7	530.0	532.1	**8%**	**5%**
C12-MCM41	101.3	102.5	529.7	532.1	**7%**	**3%**
TMA@C16-MCM41	101.4	102.7	529.8	532.1	**7%**	**4%**

* Each line are deconvoluted to extract the peak position and the relative intensityies of each components, a) assigned to SiO_4 tetrahedron located above the charge lines in the rough pore wall, b) assigned to bulk SiO_4 tetrahedron in between the charge lines inside the pore wall.

All the materials are characterized by strong peaks typical of SiO_2 at binding energies of 102.6 ± 0.1 and 532.1 ± 0.1 eV for the Si2p and O1s lines respectively. The striking point is the presence for both lines of a shoulder at lower binding energies by -1.2 and -1.1 eV, respectively for C16-MCM41 and TMA@C16-MCM41. Same shifts are seen on the Si2p lines for C12-MCM41 and TMA@C12-MCM41. The C12 material differs from their C16 analogues on the O1s lines with a larger shift of -1.4 and -1.3 eV with or without TMA, respectively.

Not reported here, there are other results in of the group concerning C16-MCM41 from which the surfactant has been chemically extracted using mild HCl condition. These materials exhibits also a high surface area like the calcined sample and should have the same surface topology. For such materials like other conventional amorphous silicas, there is not such a shoulder on the Si2p and O1s lines as described here. So the presence of these shoulders are related to the presence of charges but the number of Si or O species involved in these signals does not match the number of silanolate species, ($\equiv SiO^-$) that is closed to the number of surfactant or TMA exchanged species.[35]

Generally, the difference of electron binding energy is assigned to different environment. For as–made MCM-41 silica, Si atom is present in two forms, siloxane (Si-O-Si) and silanote ($\equiv SiO^-$) groups.[35] If the difference of binding energy results from the chemical environment, after TMA ion exchange, the SiO^-/SiO_2 ratio should be the same. However, here also there is no correlation between the number of SiO^- and the shouders intensity which decreases slightly for C16-MCM41 and stay basically constant for C12-MCM-41. In addition, the difference of such a ratio in C16 and C12 material does not fit an assignement to silanolate species. Finally for solid synthesized at higher autoclaving temperature and with very little microporosity (smooth surface), these shoulders are not seen despite the necessary presence of the silanolate groups that retain the surfactants in the solid.

These observations leads to the conclusion that the shift of binding energy is related to a physical effect that is effective on rough surfaces only as far the presence of surface charges only. Therefore, it is believed this is the position of the Si and O ions relative to the plane of charges that determines their binding energies. The difference will be driven by different electrostatic extraction work function. Obviously, most of these atoms that belong to the pore wall are located in between the double layers of charges developed on both sides of the wall between adjacent channels. These atoms should be electrostatically equivalent. However, for high roughness some of the Si and O atoms can be located outside the charges lines. Since the inorganic SiO_2 matter is the location of the negative charges, some of the SiO_4 terahedral species are located "above" negative charges on the channel side (Figure 3.8). The electrostatic work of electron extraction is then expected to be easier.

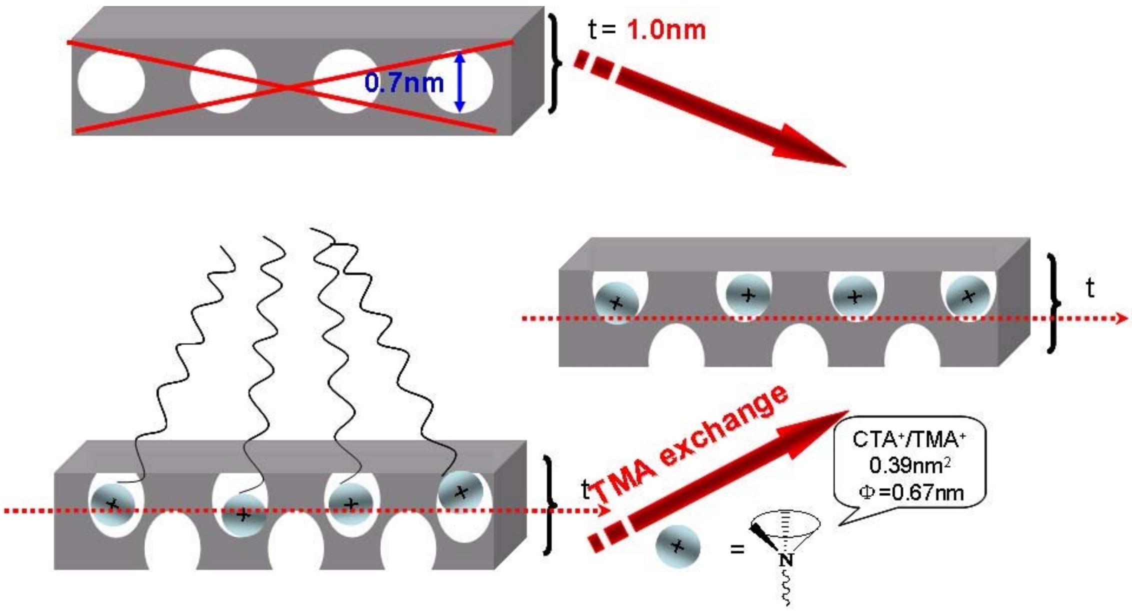

Figure 3.8 Schematic representations for the proposed model of MCM-41 with open microporosity.

3.1.4.7 Modelisation of the microporous pore wall : To further document the the model of the pore structure schematized in Figure 3.8, a geometric model is simulated assuming that the microporosity is created exclusively by the imprint of the surfactant head in the pore wall creating after its elimination either chemically or by calcinations micropores of the diameter of the surfactant ammonium head, that is 0,67 nm the penetration depth is yet to be evaluated. This model should provide the penetration depth of the head in the wall, the distance between the heads on the templated surface and the distance between the heads across the wall.

The model is based on parameters that are the less questionable, which are, the distance between the channel center obtained from the XRD lattice parameter a_0, the density of bulk amorphous silica, 2.2, and the total pore volume (not model dependent), V_{total}. The pore diameter is an important parameter chosen here as the experimental diameter obtained from the BDB method. It is model dependent but apparently the most reliable measurement according to common acceptation. It matches value obtained by the DFT calculation method developed by Niemark et al. The other parameters are the VdW size of the surfactant heads (diameter of 0.67 nm, projected surface of 0,352 nm^2, volume of 0,157 nm^3) that allows the calculation of both heads volume of 0,253 cm^3/g and the projected surface of 566 m^2/g in the C16-MCM41. 0,229 cm^3/g and 513 m^2/g is obtained for C12-MCM41 material. The surface developed by the ammonium heads defines the number of pits in the mesopore wall and therefore the distance between pits, $d_{pit\text{-}pit}$. The adopted mesopore geometry is hexagonal (Figure 3.1). A trial with cylindrical shape of channel leads to thicker wall of irrealistic density by almost a factor of 2 lower than the hexagonal channel shape. The geometry for micropores is cylindrical pits with a hemispherical bottom. The pit diameter is equal to the VdW diameter of the ammonium head, i.e., 0.67 nm. Trials with larger pits provides unsatisfying results. Pits are distributed according to an hexagonal pattern on the wall palissade.

Then, the wall density is a variable adjusted to fit the total pore volume. The experimental surface area has not been taken as reference and is imposed by the model constrains given above. A single self-consistent set of data is obtained in each case and reported in table 3.3.

Table 3.3 Theorical pore characteristics according to a muffin tin surface model using pit with a spherical bottom and a cylindrical edge.

Sample Name	T_w[d] (nm)	d_w[e] (nm)	V_{mes}[f] (cm^3 g^{-1})	V_{mic}[f] (cm^3 g^{-1})	$V_{mes+mic}$[f] (cm^3 g^{-1})	S_{mes}[g] (m^2 g^{-1})	S_{mic}[g] (m^2 g^{-1})	$d_{pit-ppit}$[h] (nm)	d_{pit}[h] (nm)
C16-MCM41	0.9	**0.85**	0.76	**0.16**	0.92	780	1356	0.75	**0.45**
C16-MCM41-a[a]	1.0	**≤0.81**	0.73	**≥0.00**	≤0.73	**≥690**	_	0.76	**_**
C16-MCM41-b[b]	0.8	**0.92**	0.75	**0.10**	0.85	821	820	0.77	**0.36**
C16-MCM41-c[c]	0.9	**1.60**	0.28	**0.00**	0.31	490	-	-	**-**
C12-MCM41	1.2	**1.38**	0.34	**0.21**	0.55	140	1680	0.72	**0.54**
C12-MCM41-a[a]	1.1	**1.60**	0.25	**0.14**	0.47	120	1190	0.71	**0.42**
C12-MCM41-b[b]	0.9	**1.37**	0.43	**0.09**	0.52	423	1030	0.86	**0.29**

a) TMA exchanged not calcined b) as a and calcined, c) fully silylated materials,d) T_w wall thickness, e) d_w apparent wall density, f) V_{total} experimental total pore volume, V_{mic} volume of pits associated to micropores, V_{meso} volume of the hexagonal clearance, g) S_{meso} surface of the matter exposed in the hexagonal channel, S_{mic} surface developed by the pit hole, h) $d_{pit-pit}$ distance at the hexagonal surface, d_{pit} dip depth using the gylinder length varying from 0 to 34 in the above examples. An overall hexagonal array of hexagonal channel of sizes fixed by a_0 and $D_{BDB.}$. Are also fixed: TMA and surfactant diameter 0,67 nm, pit diameter 0,67 nm, silica density of 2.2, Surfatant/Si = 0,160 and 0,145 for C12 andC16 surfactants, respectively, according to experimental data. $d_{pit-pit}$ distance calculated from the ratio of the surface covered by the surfactant and the surface of the hexagonal channel for the original material, this ratio in kept constant for the derived materials (TMA exchanged, calcined and TMS capped). The hexagonal surface is obtained from the adjustement of d_w to fit the experimental total pore volume V_{tot}.

The data can be analysed first in terms of volume and then in terms of surface but first the wall density needs some comments. The C16-MCM41 is characterized by density of about 0.9 and 1.1 in a very good agreement with the data of Edler and White obtained from SAXS measurements.[29,30] The depth penetration of the surfactant head is about the size of the ammonium head. The data for TMA@C16-MCM41 assuming no microporosity leads to a wall density of *ca*. 0.8 that is surprisingly smaller than the empty wall of C16-MCM41. This may be due to the lattice expansion and wall expansion.

The calcined TMA exchange material shows basically the same characteristics with a slight loss of microporosity rendered by a smaller penetration depth of the ammonium heads. The microporous volume consistenly corresponds to the volume of the ammonium heads. The distance between pits is 0.90 nm and is about the same as the distance between pits across the wall (*ca*. 0.93 nm) not reported in the table.

The mesoporous surface provided in the table is the geometric available matter at the mesoporous pore wall. This surface is 566 m^2/g larger if one counts the surface of the pore aperture. So the overall mesopore surface is 780 + 566 = 1446 m^2/g. Since the mesopores are filled after the micropores, the mesopore are filled with opturated windows and should give the overall surface of 1446 m^2/g. It is not yet understood why the mesopore experimental measurment is about 400 m^2/g below the theorical mesopore surface. This pecularity is also observed for TMA@C16MCM experimental with an effective surface of 730 + 566 = 1296 m^2/g to compare with 800 m^2/g measured. The same is true for calcined TMA@C16MCM41. The plane of positive charges is then 0.31 nm inside the wall and the percentage of silica pointing outside the wall above this line is *ca*. 16 %. This figure compares well with 12 and 9 % of Si and O atoms with a lower binding energy obtained from the XPS measurments.

The TMS capped materials fully covered develop a relatively low surface calculated to be 490 m^2/g which correspond to half the coverage capacity of the grafted TMS functions. This figure has to be compared with the experimental value of 300 m^2/g. yhe discrepancy might be due to an imperfect model for the adsorption process used for its measurements. Nevertheless, the tren is there. This corresponds to half of the function engaged in the micropores and half close packed on an upper layer. This is in agreement with the view of Liu et al. for the distribution of TMSover a rough surface (Figure 2.6).[40]

The same model applied to C12-MCM41 allows a consistent interpretation of the data and an explanation of the difference between both sets of materials. The main difference is due to a higher pore wall density of 1.4 that increases to 1.6 when the micropores are filled with TMA. The penetration depth is smaller 0.54 instead of 0.65 nm and the pit-to-pit distance is much smaller, 0.71 instead of 0.90 nm. The latter indicates that there is a very narrow separation of only 0.04 nm instead of 0.27 nm between the heads, respectively. The surface looks more like an eggbox for the C12-MCM41 than a muffin tin surface for the C16-MCM41. This more fragile topology may explain why it was difficult to recover this morphologie after exchange and TMA calcinations.

3.1.5 Conclusions

From N_2 adorption-desorption experiments, laser hyperpolarized ^{129}Xe experiments and XPS measurements a novel model for MCM-41 type of material is proposed to explain the origin of the mysterious microporous character that has been puzzling the scientific community for more than 10 years. This is indeed a model close to the model proposed for SBA-15 few years ago. The main difficulty is the strong connectivity of these micropore with the mesopores that strongly affects the adsorption properties. The presence of such open micropores is due to the imprint of the surfactant heads in the wall that generate pits of ca. 0.67 nm diameter for an equivalent depth. These alveoli most likely generates a pattern due to the ammonium self-repulsion. The surface topology may compared to muffin tin or an eggbox for the C16- and the C12-MCM41 material. The fragility of the MCM-41 silica towards water is understandable and one may anticipate that high temperature hydrothermal post-synthesis and organsilylation can effective improve this stability in minimazing this surface roughness.

New insight into pore expansion mechanism during ageing and hydrothermal post synthesis to explain our data and the literature data[39] will be discussed in the next section using this muffin tin or eggbox surface morphology of the mesopore wall surface.

3.2 New insights into high-temperature unit-cell and pore size expansion in MCM-41 mesoporous silica

3.2.1 Introduction

The capacity to manipulate both surface topology and interfacial chemistry in the mesoporous confined environment with various organosilanes containing relatively large ligand led to much more sophisticated materials, such as multifunctional catalysts (i.e., enzyme-mimic or biomimic catalyst) and hierarchical size-and-shape selective adsorbent [41, 36]. Due to pore blocking, classical MCM-41 silica with pore size less than 3.7 nm cannot satisfy above requests. Thus, the synthesis of larger pore MCM-41 (above 4.5 nm in diameter) and other larger pore ordered mesoporous materials has attracted considerable and still growing attention [1, 5, 9, 25, 27, 28, 39, 40, 42-48].

Many new methods aimed to synthesize silica with narrow pore-size distribution and tailored pore sizes were developed using cetyltrimethylammonium (CTA^+) as a template. [1, 25, 27, 28, 39, 40, 42-48] First, good quality MCM-41 with pore diameter below 4.5 nm could be easily prepared using surfactants of long chain,[1] but when the carbon number of surfactant tail is larger than 20, the ordering significantly decreases and leading to a single broad peak XRD fingerprint.[42] Then, scientists from Mobile firstly proposed that mesitylene as swelling agent could be used to synthesize lager pore MCM-41 with pore diameter up to 10 nm, and this method was developed using other auxiliary organics as swelling agents by other research group.[1, 6, 46-48] These materials exhibits a modest quality of ordering and the introduction of large amounts of organics is not an environmentally friendly solution. Later, Ozin et al. firstly reported the synthesis of MCM-41 with tunable pore size without introducing organic swelling agents via post-synthesis approach.[40] Despite minor increment in the pore size (7 Å), as observed by Klinowski et al.[39, 44], this simple and one-pot synthetic strategy was further explored by other research group because of the environment friendly characteristic.[25, 27,45] Corma et al. directly synthesized large pore MCM-41 with pore diameter up to 6.6 nm (a pore size increment of 3.0 nm).[45]

To explain the significant difference of pore size increment, Jaroniec et al proposed an unified interpretation of high-temperature pore size expansion process in MCM-41 mesoporous silica[25] with concommitant degradation of the surfactant producing *N,N*-dimethylhexadecylamine (DMHA) acting as a swelling agent. Based on this model, pore size expansion at high temperature above 165ºC could be easily understood due to the swelling action of decomposition species from surfactants, but it could not be used to explain why the pore size could also be enlarged by extending the crystallization time at low temperature below 155 ºC where the surfactants could not be decomposed, and why pore could be effectively swelled in the presence of tetrametylammonium (TMA^+).[25, 27, 39, 44-46] In the previous section, we discovered the presence of micropores of *ca.* 7 Å regularly distributed on the mesopore surface as open pits generating muffin tin or eggbox types of morphology. Herein the maximun pore expension is about the pore size of open micropores and matches well the limitation observed by Ozin et al.[40]

Based on the above-mentioned model of surface morphology, a comprehensive mechanism of high-temperature pore size expansion in MCM-41 mesoporous silica is proposed here. At modest synthetic temperature (<155 ℃), the pore enlargement is explained by erosion of the surface rugosity during gel ageing combined with increasing autoclaving treatments. At higher temperature (>155 ℃), both swelling effect of degradation products of the surfactants and erosion of the surface rugosity are thought to contributed together to the pore size expansion. Most importabtly, we suggest a possible mechanism for the role of TMA^+ ions in pore enlargement: first, TMA^+ ions is acting as the counterions for charge compensation to maintain the structure ordering of initially formed MCM-silica and, secondly, as a promoter to accelerate the dissolution and deposition of local silica near the micropores with its capacity to engage a dynamic ion exchange with the templating CTA^+ ions. It should be mentioned that this comprehensive mechanism is based on a hypothesis that the expansion process does not involve any appreciable reconstruction of the silicate framework of MCM-41.

3.2.2 Experimental section

3.2.2.1 Synthesis: Different silica precursors, base sources (NaOH or TMAOH), surfactant counterion (Br^- or tosylate), aging step (35 ℃ for 3 days or 60 ℃ for 1 day) and hydrothermal temperature (100 to 175 ℃) were used (listed in Table 3.4). In a typical synthesis procedure of FS-AT-35-130-1, 3.70 g CTATos was dissolved in 120 ml water and stirred for 1 hour at 60 ℃. 22.79 g 25% tetramethylammonium hydroxide (TMAOH) aqueous solution was added into 107 ml water, followed by addition of 10.78 g fumed silica under vigorous agitation. Fumed silica solution was stirred for 1 hour at 60 ℃ and then added into CTATos solution drop by drop. The obtained gel composition was SiO_2: 0.045 CTATos: 0.35 TMAOH: 79.9 H_2O. The mixture was stirred continuously for 2 hours at 60 ℃ and then loaded into a 250 ml Teflon-lined steel autoclave where the gel mixture was pre-aged for 3 days at 35 ℃. The final mixture was heated in autoclave under static condition at 130 ℃ for 20 hours. Solid obtained was fully washed by water, and then was dried at 80 ℃ in the oven overnight. For comparisons, LUS-1 [33] with gel composition SiO_2: 0.045 CTATos: 0.52 NaOH: 79.9 H_2O and classical MCM-41 [39] with gel composition SiO_2: 0.27 CTABr: 0.19 TMAOH: 40H_2O were also synthesized. All experiment parameters were listed in table 3.4, for Example: FS-AT-35-155-2 means mesoporous silica prepared from fumed silics using TMAOH as base source, tosylate as surfactant counterion, gel aged at 35 ℃ for 3 days, autoclaving 155 ℃ for 48h.

Table 3.4 Nomenclature of samples

Silica source	Base source	Surfactant conterion	Aging Temp & Time	Autoclaving Temp & Time
Fumed silica = FS	NaOH = N	Br = B	35^{0}C-3days = 35	130^{0}C = 130 & 20h = 1
Ludox = LX	TMAOH = A	Tosylate = T	60^{0}C -1days =60	165^{0}C = 165 & 48h = 2

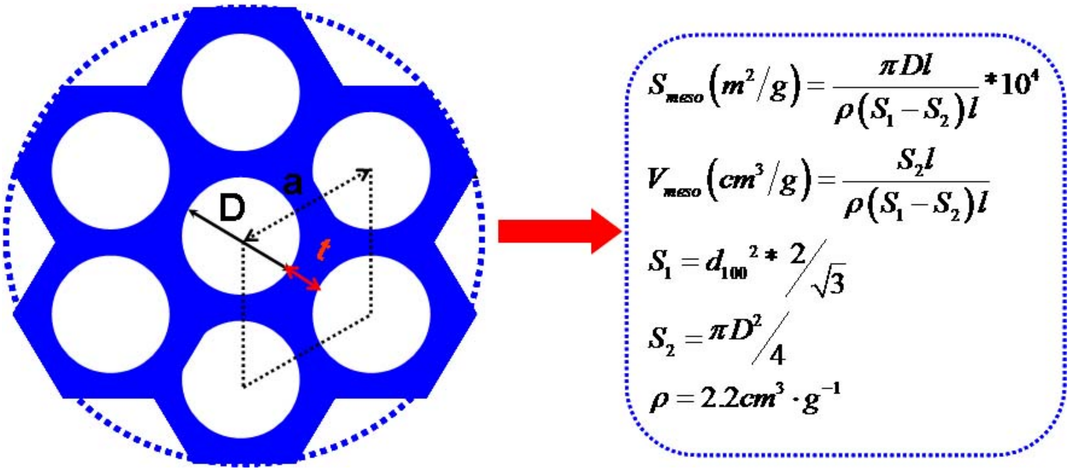

Figure 3.10 Cylindrical geometrical model and related calculation formulas

3.2.2.2 Characterization: Powder X-ray diffraction (XRD) data were obtained on a Bruker AXS D8 diffractometer by using Cu Kα radiation and a Ni filter. The adsorption-desorption isotherms of nitrogen at 77 K were measured using a Micromeritics ASAP 2010 instrument. Each sample was outgassed at 200°C until a stable static vacuum of 3×10^{-3} Torr was reached. The BET surface area, S_{BET}, was calculated in the domain of validity of the BET equation, that is, between $0.1 < p/p_0 < 0.3$. Pore diameters, *D*, were evaluated from the nitrogen desorption branch according to the BJH method and the Broekhoff and de Boer method, and latter was validated as one of the most accurate methods to evaluate mesopore size. Moreover the cylinder pore arranging pattern was used to geometrical model calculation (figure 3.10). ^{13}C and CPMAS solid NMR measurements were collected on a Bruker DSXv400 spectrometer (for both crosspolarisation (CP) was used) and at 100.6 MHz, a 6 μs ($h = p/2$) pulse was used with a repetition time of 3 s. The spinning rate of the rotor was about 5 kHz and the number of scans was 10000. The morphology of MCM-41 samples was observed with scanning electron microscopy (SEM, JEOL JSM-7401F) at 3.0 kV. The transmission electron microscopy (TEM) micrographs were recorded digitally with a Gatan slow-scan charge-coupled device (CCD) camera on a JEOL 2010 electron microscope operating at 200 kV.

3.2.3 Result and discussion

3.2.3.1The influence of aging process: Inspired by the study on the preparation of a water-resistant siliceous MCM-41 sample through the improvement of crystallinity reported by Kuroda et al. [50], before high temperature hydrothermal treatment, the silica-surfactant gel was aged at 35ºC for 3 days or 60ºC for 1 day to improve the hydrothermal stability of mesoporous silica in this thesis.

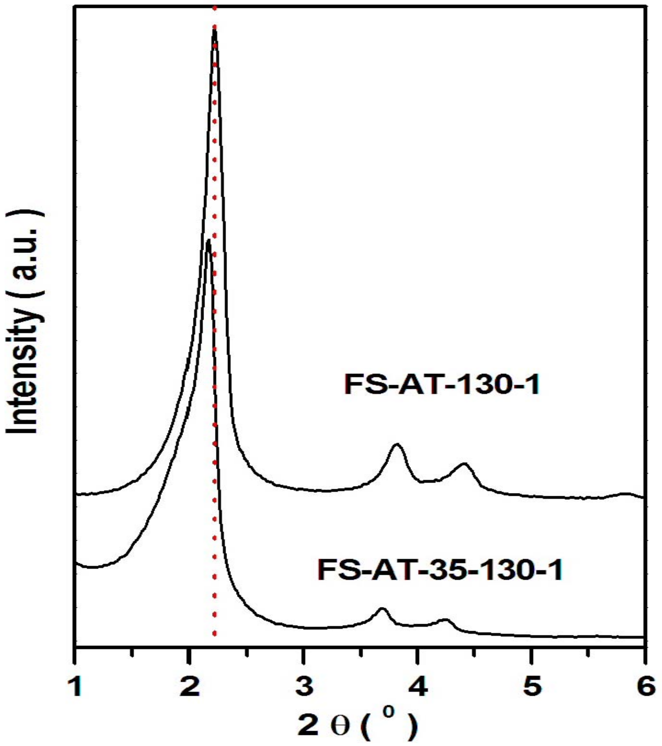

Figure 3.11 XRD patterns of sample FS-AT-130-1 and FS-AT-35-130-1

The XRD patterns of sample FS-AT-130-1 in Figure 3.11 exhibited four well-resolved peaks indexed as (100), (110), (200), and (210) reflections, indicating a high-quality MCM-41 with *p*6*mm* symmetry [1]. The sample FS-AT-35-130-1 only showed three reflections and the (100) reflection band was broader, which indicated a slight decrease of mesostructure ordering. N_2 adsorption (see figure 3.12) showed the typical IV isotherm of mesoporous silica, implying the good maintenance of the uniform mesoporous. The observation of SEM (see Figure 3.13) further supported that the mesoporous silica did not involve an intensive framework restructuring, because both samples exhibited the similar fiber–like morphology of mesoporous silica. The most interesting aspect of as-made sample FS-AT-35-130-1 was that, ^{29}Si MAS NMR spectrum (Figure 3.14) gave a broad band at -108 ppm, together with a faint shoulder at -98 ppm, however, sample FS-AT-130-1 showed a definite shoulder. These two bands could be assigned to Q^4 silicon species, ($Si(OSi)_4$) and to Q^3 silicon species ($HOSi(OSi)_3$) [51, 52].

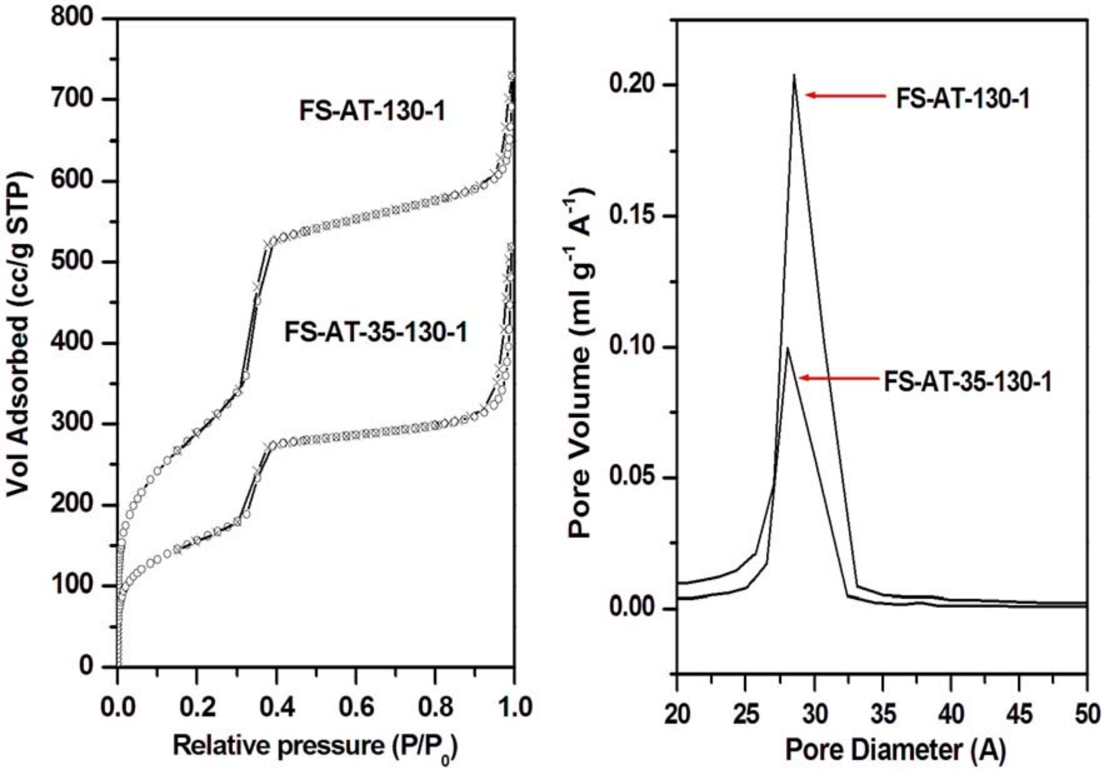

Figure 3.12 N_2 adsorption isotherms (left) and BJH mesopore size distribution (right) from adsorption branch of sample FS-AT-130-1 and FS-AT-35-130-1

Figure 3.13 Morphology evolution observed by SEM for sample FS-AT-130-1 and FS-AT-35-130-1

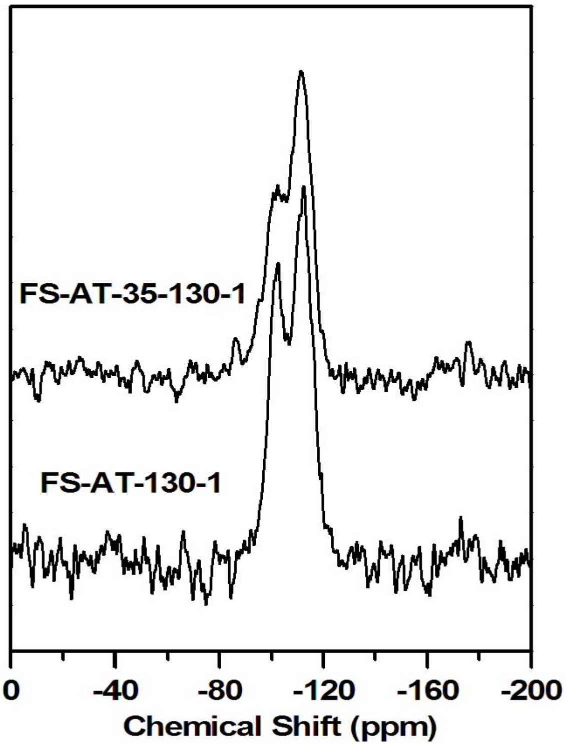

Figure 3.14 ^{29}Si MAS NMR spectra of sample FS-AT-130-1 and FS-AT-35-130-1.

Table 3.5 Effect of aging on texture properties of MCM-41 mesophase

Sample Name	d_{100} (nm)	S_{BET} ($m^2 g^{-1}$)	V ($cm^3 g^{-1}$)	D_{BJH} (nm)	D_{BDB} (nm)	t_{BJH} (nm)	t_{BDB} (nm)	S_{meso} ($m^2 g^{-1}$)	V_{meso} ($cm^3 g^{-1}$)
FS-AT-130-1	3.98	1061	0.97	3.72	3.67	0.88	0.93	786	0.76
FS-AT-35-130-1	4.07	558	0.56	5.16	3.74	-	1.10	569	0.51
FS-AT-60-130-1	3.97	584	0.55	4.49	3.67	-	1.06	593	0.52
LX-NT-130-1	4.16	920	0.80	3.03	3.52	1.77	1.28	490	0.43
LX-NT-35-130-1	3.87	449	0.92	11.8	9.7	-	-	-	-
LX-NT-60-130-1	3.78	1080	0.95	3.18	3.74	1.18	0.62	967	0.90
LX-AT-130-1	4.17	1148	1.10	3.48	3.81	1.34	1.01	626	0.60
LX-AT-60-130-1	4.00	955	0.98	3.32	3.81	1.30	0.81	768	0.73

Note: t is the mean pore wall thickness, and D is pore size calculated from BDB and BJH theoretical model, respectively, S_{meso} and V_{meso} are primary surface area and pore volume of primary mesopores using cylindrical model calculation.

The small Q_3/Q_4 ratio for sample FS-AT-35-130-1 indicates a more condensed silica framework and thus high hydrothermal stability. This is the reason that the MCM-41 silica exhibited the strong water-resistence by Kuroda et al [50].

Moreover, it should be mentioned that, although the primary mesopore size from BDB calculation was kept unchanged, the BET surface area and pore volume significantly decreased (Table 3.5). The origin for these observations will be discussed in details later.

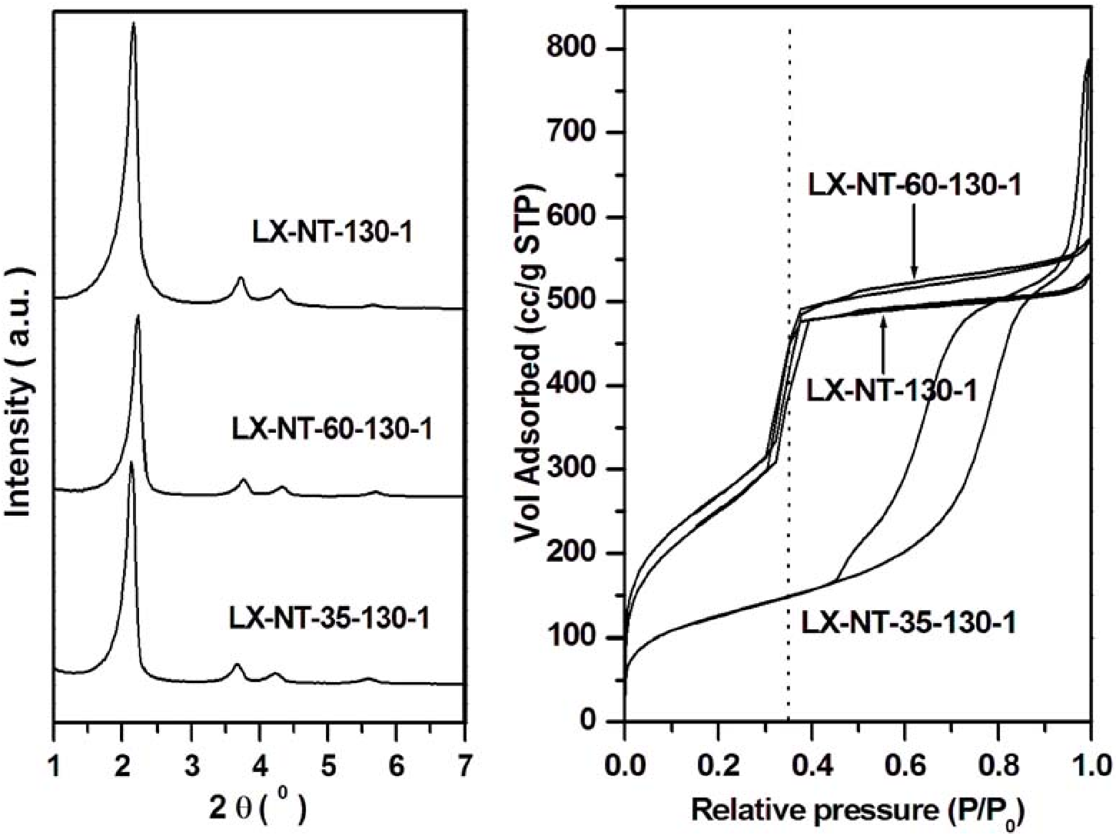

Figure 3.15 XRD patterns (left) and N_2 adsorption-desorption isotherms of samples LX-NT-130-1, LX-NT-60-130-1, and LX-NT-35-130-1 (right).

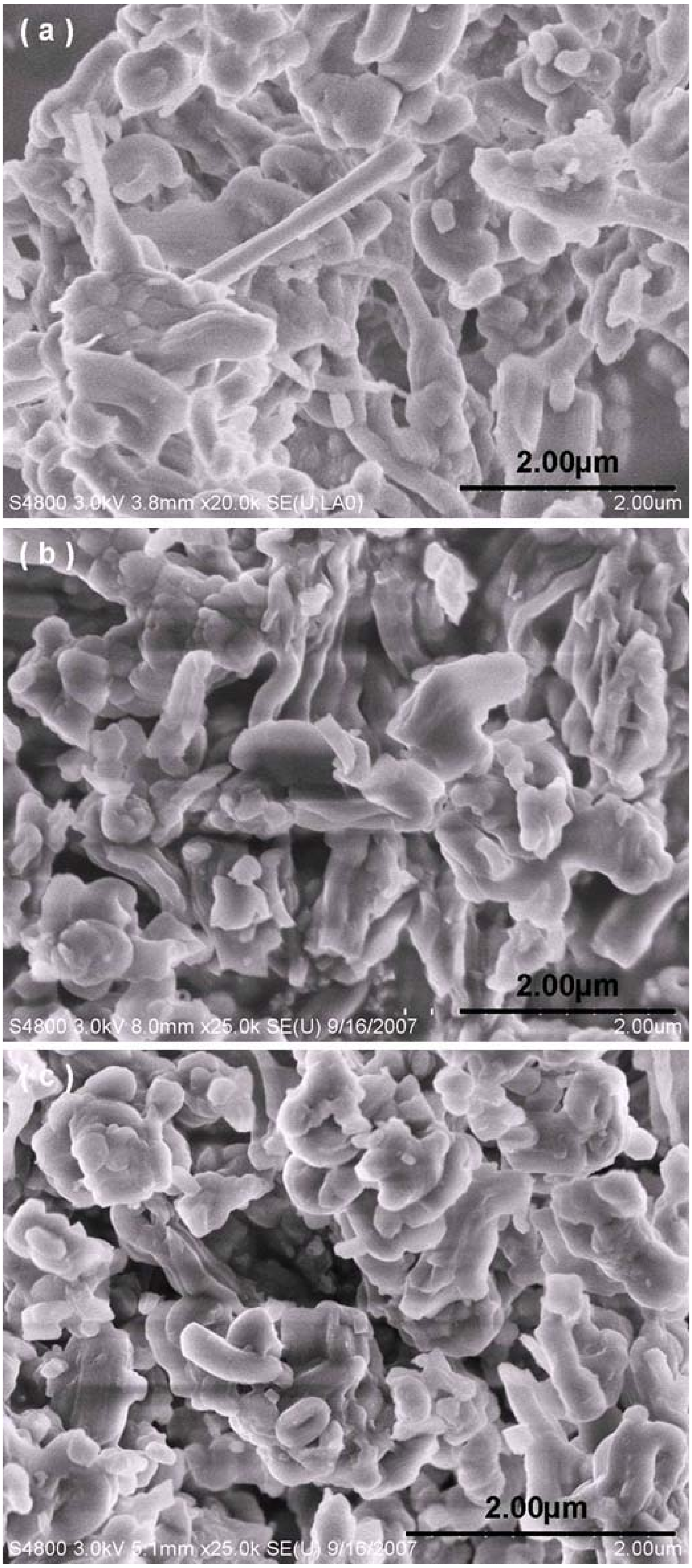

Figure 3.16 Morphology evolution observed by SEM for samples (a) LX-NT-130-1, (b) LX-NT-60-130-1, and (c) LX-NT-35-130-1.

The same procedure was applied to other system to further understand the influence of aging on the pore structure and stability of mesoporous silica. To our surprises, MCM-41 silica synthesized under different experimental conditions, showed completely different chemical behaviors. The XRD patterns of the as-made LX-NT series in figure 3.15 (left) exhibited typical MCM-41 structure, indicating the higher ordering, while the adsorption of N_2 showed remarkable difference (figure 3.15, right): if aging was proceeded at 60ºC for 1 day, the sharp step centered at around relative pressure 0.35 in the adsorption isotherm was similar; when the gel was aged at 35ºC for 3 days, the jump of N_2 uptakes for sample LX-NT-35-130-1 shifted to higher relative pressure (about 0.70) with typical H1 hysteresis like that of SBA-15 [5, 9].

In addition, at high relative pressure, a secondary hysteresis loop was observed on the sample LX-NT-35-130-1 due to the presence of the void of particle packing. Its BET surface area (449 m^2/g) was only a half of that of MCM-41 silica without aging, while the total pore volume was remained. It was importantly noted that SEM micrographs did not showed the significant morphology change (See figure 3.16). Moreover, the pore size of this sample was 9.7 nm calculated by BDB method, however, d_{100} value from the XRD pattern was only about 4.0 nm. This information indicated that the channels of mesoporous silica were possible interconnected by some defects in the pore wall. To our best knowledge, this was the largest pore size for MCM-41 silica with good quality synthesized under the base condition using CTA^+ as a template without swelling agents at mild-temperature. It was interesting to note that only this sample aged at 35ºC for 3 days showed the significant pore enlargment unexpectedly, indicating the synthesis of the mesoporous silica was very sensitive to the hydrothermal treatment conditions. At some point during the post-synthesis treatment, the most fragile part, such as the boundary between the open micropores as shown in figure 3.9, was attacked by OH^- , the siloxane bond was then broken in current case, thus, some holes was produced, which led to the interconnection between the channels due to the disordered distribution of large holes. Furthermore, it was important to note that, when the aging was preceded at 60ºC for 1day, only thinning of pore wall thickness was observed for both sample LX-NT-60-130-1 and sample LX-AT-60-130-1; when the crystallization temperature was increased to 165ºC, the pore size was centered at the intermediate between sample LX-NT-130-1 and LX-NT-35-130-1, this interesting pore size evolution will be discussed later.

The results briefly outlined here not only provided us with a new method for an alternatively synthetic strategy to rationally fabricate novel porous materials with custom-tailored properties, but also gain the better understanding for the surface structure of the MCM-41 silica. The originality of current approach resides in the combination of gel ageing to strengthen the wall before high-temperature postsynthesis treatment for pore expansion. To further understanding the common mechanism for the unit-cell and the pore size enlargement, the crystallization temperature was varied to synthesize the large pore size MCM-41 silica with the improved hydrothermal and mechanical stability.

3.2.3.2 Pore size tailoring by controlling hydrothermal temperature

3.2.3.2.1 XRD patterns: The XRD patterns of the calcined samples FS-AT-35-X-2 in figure 3.17 (left) showed the typical hexagonal close packing structure of MCM-41 silica with high ordering, and the d_{100} spacing in calcined samples FS-AT-35-X-2 increased from 4.12 to 5.50 nm with the temperature increasing from 100 to 175ºC when the duration of the synthesis was kept for 2 days (table 3.6). Furthermore, these samples contracted much less after calcination at 550 ºC for 6 hours as shown in figure 3.17 (right), which further proved that the hydrothermal stability of MCM-41 silica was greatly improved due to the higher pore wall thickness. Most interestingly, after 130 ºC, the rate of lattice uint expansion was significantly increased as reported by Klinowski et al [39, 44].

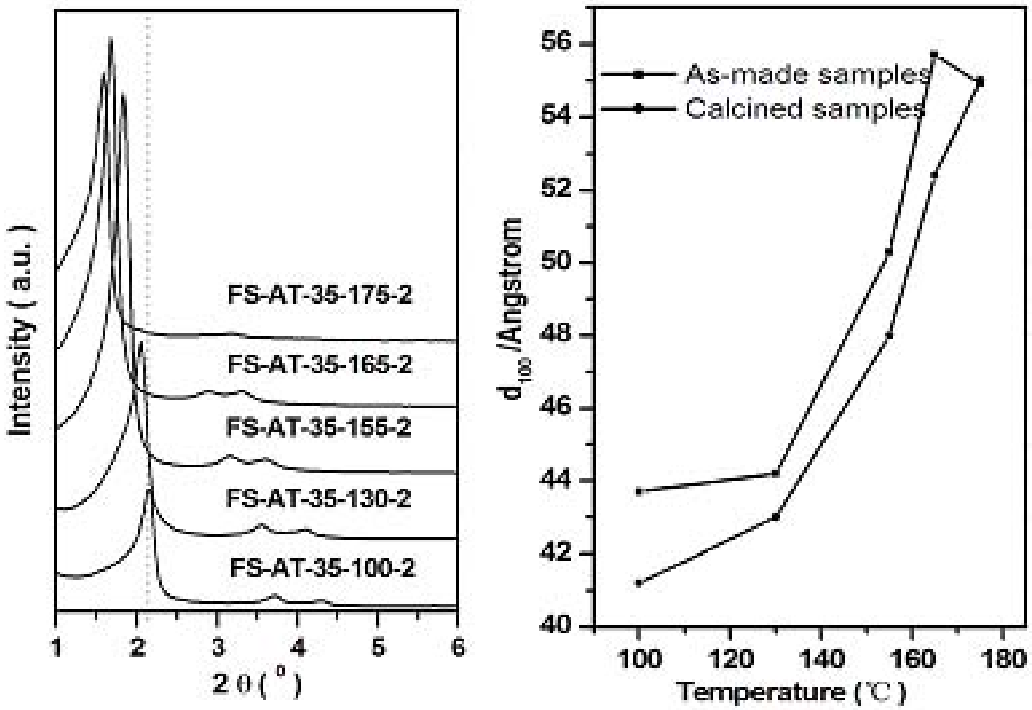

Figure 3.17 XRD patterns (left) and d_{100} spacing evolution (right) of series of FS-AT-35-X-2 silica synthesized in temperature range x = 100-175 °C.

Table 3.6 Effect of hydrothermal temperature on texture properties of MCM-41 mesophase

Sample Name	d_{100} (nm)	S_{BET} (m^2 g^{-1})	V (cm^3 g^{-1})	D_{BJH} (nm)	D_{BDB} (nm)	t_{BJH} (nm)	t_{BDB} (nm)	S_{meso} (m^2 g^{-1})	V_{meso} (cm^3 g^{-1})
FS-AT-35-100-2	4.12	605	0.67	5.57	3.59	-	1.17	540	0.48
FS-AT-35-130-2	4.30	578	0.58	4.26	3.74	0.71	1.23	515	0.48
FS-AT-35-155-2	4.80	528	0.51	3.70	4.13	1.84	1.41	446	0.46
FS-AT-35-165-2	5.24	446	0.44	3.81	4.31	2.24	1.74	359	0.39
FS-AT-35-175-2	5.50	305	0.29	3.75	3.13	2.60	2.22	274	0.28

3.2.3.2.2 N_2 adsorption and TEM: N_2 adsorption-desorption measurements showed in figure 3.18 (left). Firstly capillary condensation of N_2 adsorption shifted to higher relative pressure value with the hydothermal temperature increase. If temperature was above 165ºC, this value became smaller, indicated the decrease of mesopore size, which was supported by the calculation of BJH method using adsorption branch in figure 3.18 (right). The same trend was observed by TEM (see figure 3.19). Even sample synthesized at 165ºC, showed the honey comb packing of channels, implying the well defined MCM-41 structure.

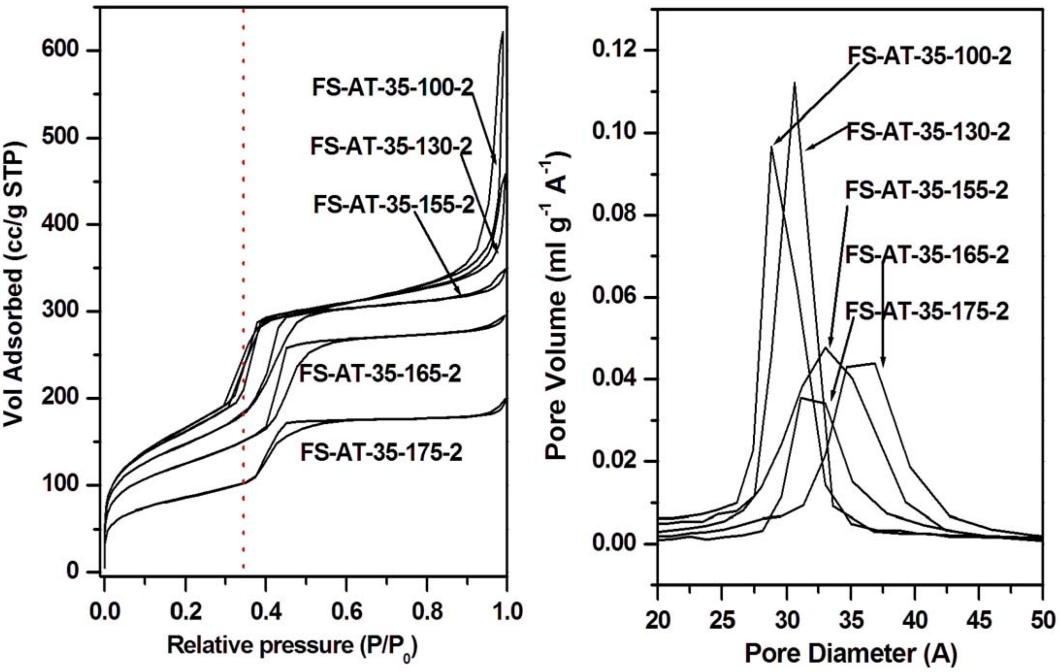

Figure 3.18 N_2 adsorption isotherm (left) and BJH mesopore size distribution (right) from adsorption branch of FS-AT-35-X-2 silicas (see figure 3.17).

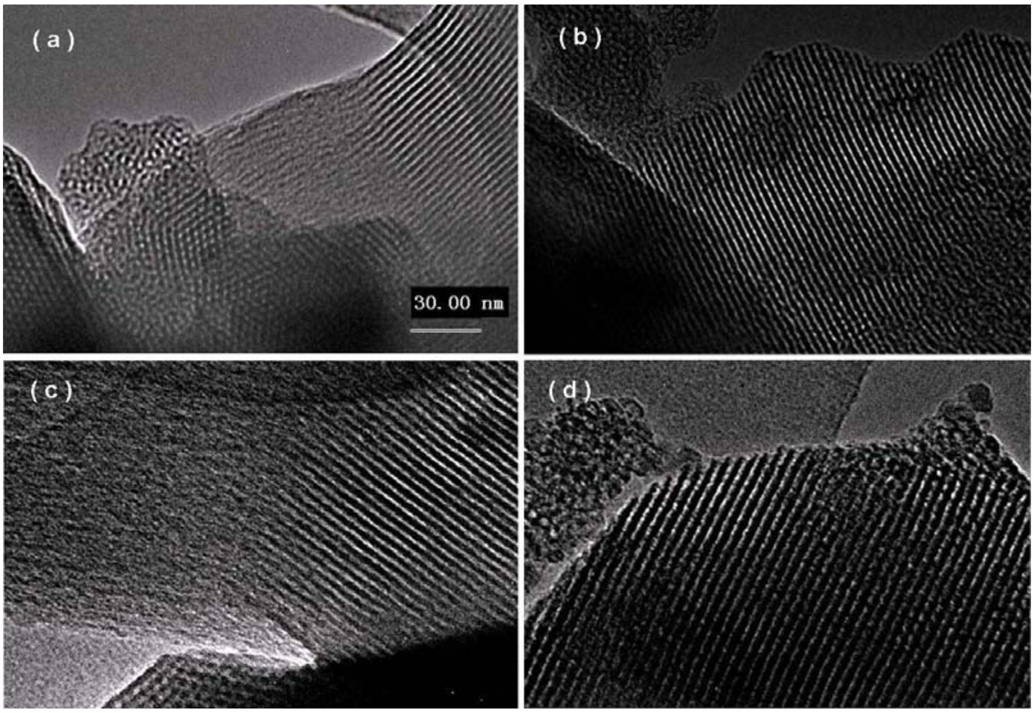

Figure 3.19 TEM observation for sample FS-AT-130-1(a and b) and FS-AT-35-165-2 (c and d, scale is the same for these two samples)

The pore size from BDB method was thought as the most reliable evaluation method for calculating the mesopore size [28, 47]. The wall thickness calculated by subtracting the pore size evaluated by BDB method from the unit-cell parameter strongly depended on the hydrothermal temperature (see figure 3.20). The pore size first increased, after the maximum value of 4.3 nm in diameter at 165ºC, pore size began to decrease, as exhibited by N_2 adsorption characterizations in figure 3.18. However, wall thickness monotonically increased as a function of hydrothermal temperature, up to about 2.2 nm at 175ºC, similar result with pore size 2.6 nm using BJH calculationwas reported by Klinowski et al [39, 44].

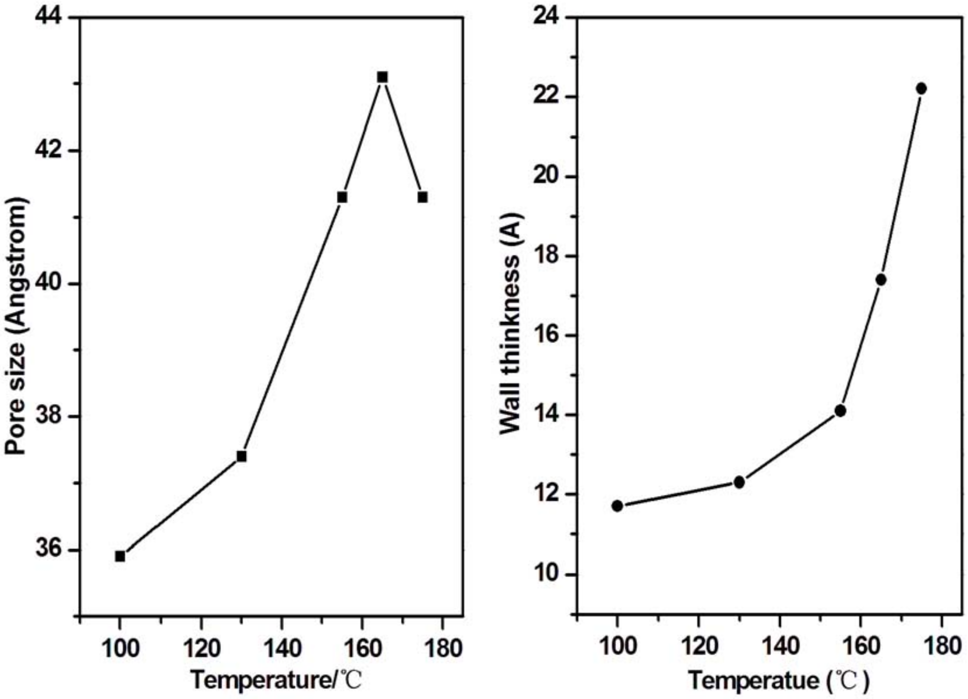

Figure 3.20 Evolutions of pore size (left) and pore wall thickness calculated using BDB method from desorption branch (right) of FS-AT-35-X-2 silicas.

The specific surface area and pore volume of mesopores calculated using geometrical model were listed in the table 3.6. The surface area and pore volume versus hydrothermal temperature from both model calculation and experimental measurements was plotted in figure 3.21. We found that, with the increasing of reaction temperature, the experimental values of specific surface area and pore volume are gradually close to the geometrical calculated ones, which indicated that the open micropores were slowly eroded. Consequently, the negative value derived from β-plot (figure 3. 22) became neglect.

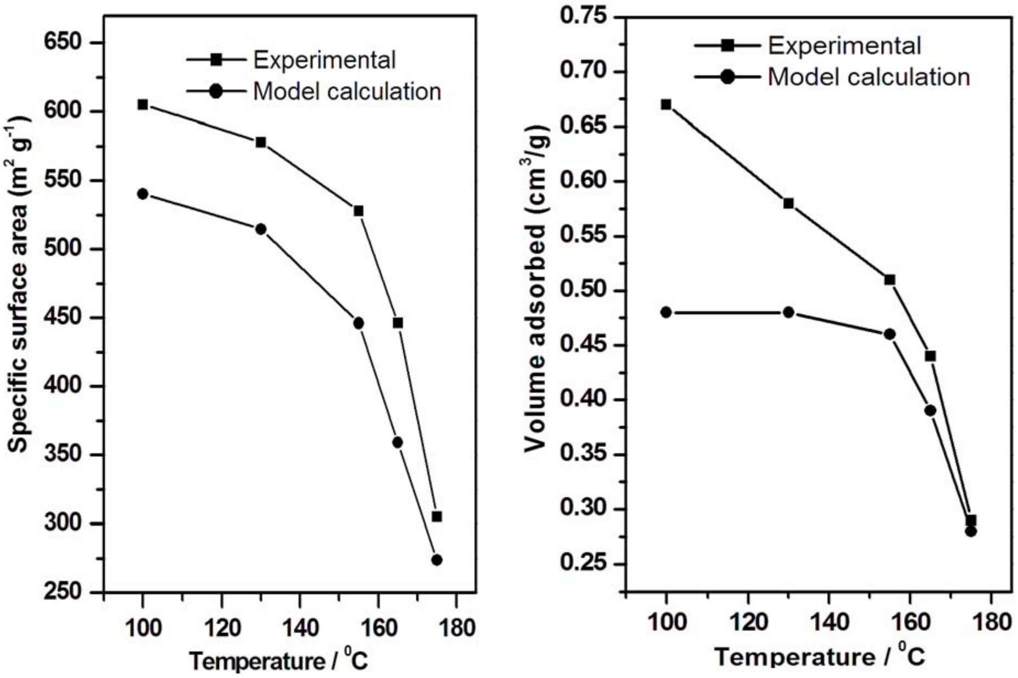

Figure 3.21 Influence of hydrothermal temperature on specific surface area (left) and pore volume (right) of FS-AT-35-X-2 silicas.

3.2.3.2.3 C_{BET} value: Most strikingly, the C_{BET} values for the serial FS-AT-35-X-2 samples increased with the hydrothermal temperature increasing as showed in figure 3.23. In case of silica and alumina, most common used as mesoporous or macroporous adsorbents, C_{BET} for nitrogen adsorption at 77K are in a range 80-150, for example, the typical value of a nonmicroporous calcined silica is 100 [9, 53], which is very close to the ones of our series sample. C value calculated from BET is characteristic of adsorbent-adsorbate interactions, and a higher value evidences stronger interaction of nitrogen molecules with the silanol groups on the silica surface, indicating more hydrophilic surface.

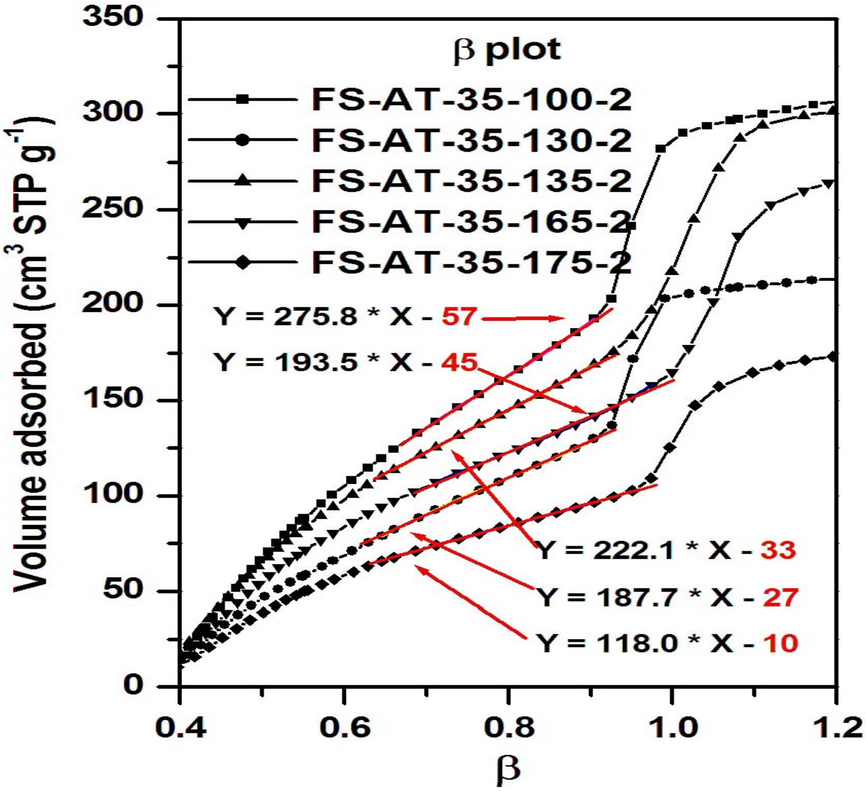

Figure 3.22 β-plots of FS-AT-35-X-2 silicas

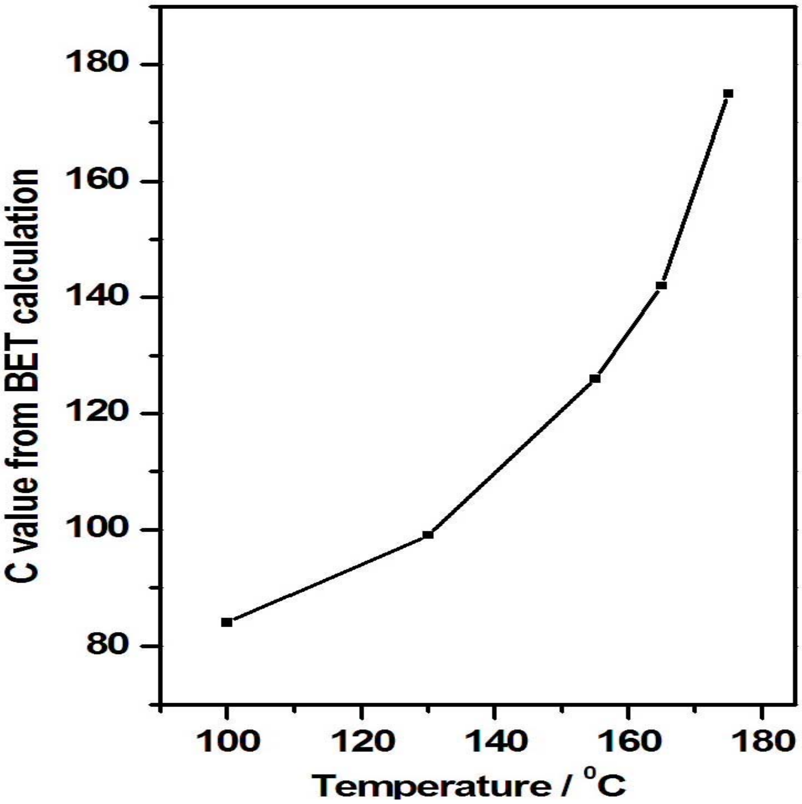

Figure 3.23 Evolution with temperature of C parameter from BET equation of FS-AT-35-X-2 silicas.

3.2.3.2.4 Solid ^{29}Si MAS NMR spectrum: Contrast to the C value, the ^{29}Si MAS NMR spectrum in figure 3.24 showed the surface became more and more hydrophobic with temperature increase, because the percentage of Q^3/Q^4 significantly decreased (table 3.7). It should be mentioned that the C_{BET} value of sample FS-AT-35-175-2 equal to be 175 was much lager than 76 of FS-AT-130-1. This could be attributed to the change of channel surface morphology. At high temperature, although the density of silanol groups dramatically decreased with temperature, the surface became smoother, which led to the strong interaction between nitrogen and silanol groups. Concern with this factor, the peculiarity of C_{BET} evolution could be easily understood. Besides the hydrophilic and hydrophibic properties of surface, C_{BET} value in fact reflects the surface roughness degree of silica. This interesting phenomenon due to the presence of open micropores was very similar to the superhydrophobicity of lotus leaf surface, which resulted from the regular distribution of clusters in μm scale [54]. This answered why N_2 physisorption methods are not suitable for the characterization of micro- and mesoporous composite materials.

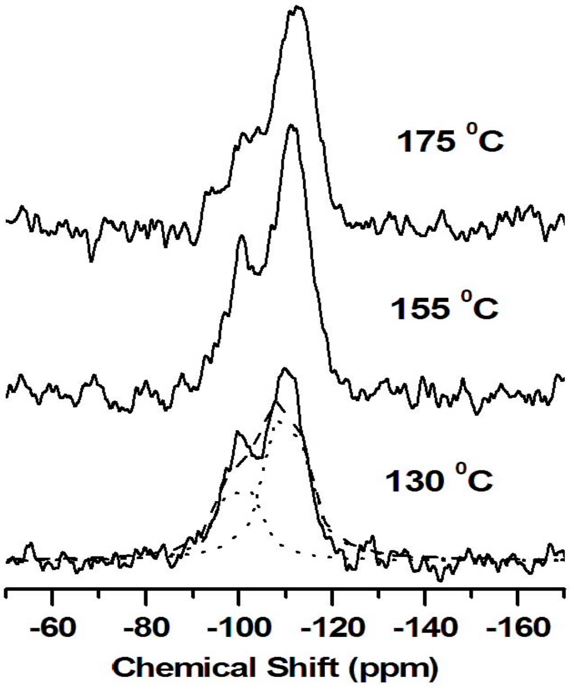

Figure 3.24 ^{29}Si MAS NMR spectra of FS-AT-35-X-2 silicas synthesized at different temperatures (x = 130, 155 and 175 °C).

Table 3.7 Relative concentration of Q^n species from signal deconvolution of Solid-state ^{29}NMR spectra of FS-AT-35-X-2 silicas (x = 130, 155 and 175 °C).

Sample Name	Q^3 (ppm)	Q^4 (ppm)	$Q^3/(Q^4+Q^3)$ (%)	$Q^4/(Q^4+Q^3)$ (%)
FS-AT-35-130-2	-99.9	-111.7	**33.6**	66.4
FS-AT-35-155-2	-100.6	-111.3	**27.3**	72.3
FS-AT-35-175-2	-101.5	-112.1	**20.9**	79.1

Herein we correlated the pore size expansion with the erosion of the open micropores in the mesopore during the postsynthesis treatment. The same mechanism was applied to elucidate the pore size expansion of SBA-15, while the unit-cell size kept constant. This process can answer a lot of problems encountered in literatures, such as over evaluated specific surface area and pore volume [24, 55], low efficiency of pore size expansion within 1.5 nm [39, 40, 44], negative intercepts evaluated by comparison methods including t-plot, α_S-plot and β-plot [10, 13, 37].

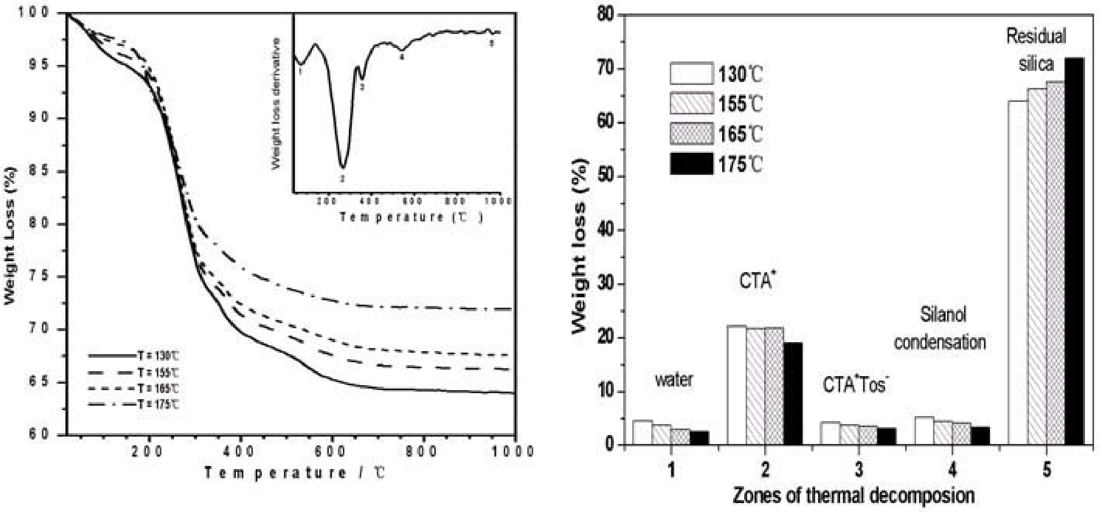

Figure 3.25 TG-DTG analysis of FS-AT-35-X-2 silicas; hydrothermal temperature, x, in a range 100-175 °C.

3.2.3.2.5 Surfactant/silica mass ratio: The significant increase of the pore wall thickness with hydrothermal temperature increase required the much more soluble silica species which must be transported into the channel from the mother liquor as reported by Klinowski [39]. Thermogravimetric studies (figure 3.25) further supported our conclusion, because the surfactant/silica mass ratio significantly increased with hydrothermal temperature, differing from the observation by other research groups [25, 27, 39, 44-46].

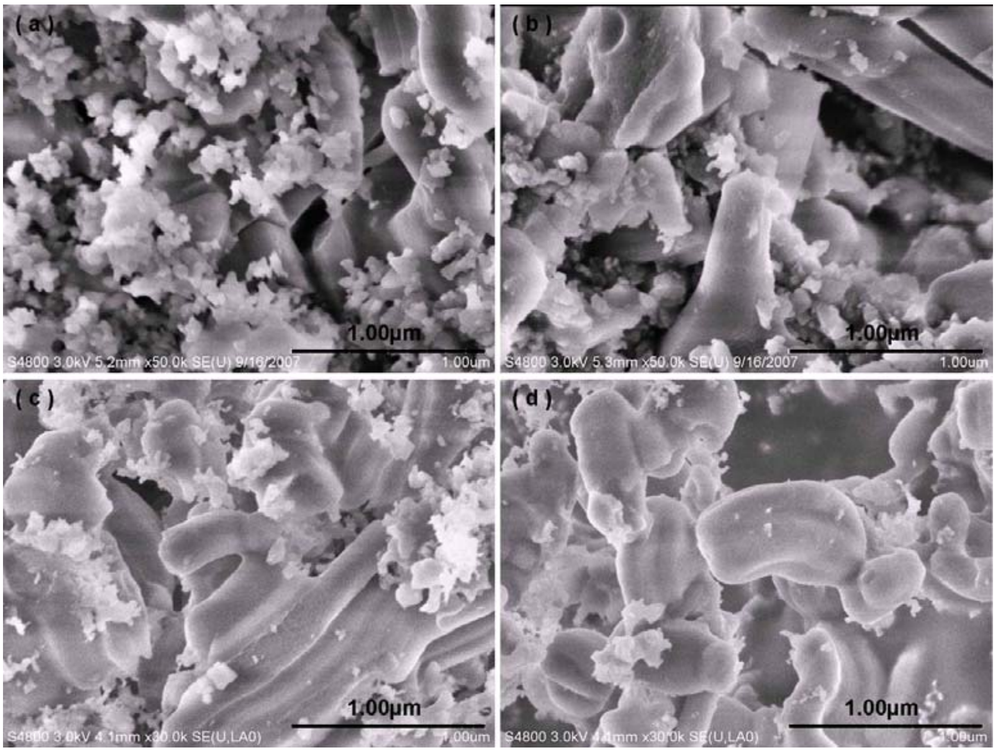

Figure 3.26 SEM pictures of FS-AT-35-X-2 series synthesized at at different temperatures: (a), 130ºC, (b), 155ºC, c, (c), 165ºC, (d), 175ºC

3.2.3.2.6 SEM observation: SEM is an effective tool to investigate the morphology evolution and formation mechanism of mesoporous silica. With the temperature increase, the particles did not exhibited the distinct morphology change in figure 3.26, indicateing the extensive restructuring was not happed, as repoted by other research groups [7-12].The careful examination found that, when the hydrothermal temperature increased, the crystalinity significantly improved, because the quantity of the armorphous silica like snow flower was dramatically reduced, implying high temperature posttreatment accelerated the dissolution and redeposition of small particles. This also answered that the ratio of silica/surfactant was significantly increased as exhibited by TG analysis in figure 3.25.

3.2.3.2.7 Elemental analysis and ^{13}C CPMAS NMR spectrum: TMA$^+$/CTA$^+$ molar ratio after calculation was listed in table 3.8. When temperature increased, this value remained almost the same. It was importantly noted that, in current gel composition, even 8% TMA$^+$/CTA$^+$ molar ratio was much larger than those reported by literatures [7-12]. Moreover, the ^{13}C CPMAS NMR (figure 3.27, right) easily identified the presence of TMA$^+$ ions. However, the TMA$^+$ ion exchange process seemed not to happen for the FS-AB-X-2 series based on the characterization of the ^{13}C CPMAS NMR.

Table 3.8 Elemental Analysis of as-made MCM-41 silica

Sample	C/%	H/%	N/%	S/%	C:N	TMA/%
FS-AT-130-1	31.37	6.69	1.86	0.22	19.31	**8.0**
FS-AT-35-130-1	22.19	4.83	1.55	0.15	16.40	**20.0**
FS-AT-35-155-2	21.73	4.82	1.55	<0.1	16.16	20.0
FS-AT-35-165-2	21.02	4.54	1.52	<0.1	15.93	20.0
FS-AT-35-175-2	18.03	3.90	1.32	<0.1	15.71	22.0
FS-AB-130-1	38.46	8.02	2.32	-	**19.30**	-
FS-AB-165-2	34.84	7.05	2.13	-	**19.08**	-

Now we can clearly understand the role of TMA$^+$ ions. First, TMA$^+$ ion was used as a promoter to accelerate the dissolution and deposition of local silica near the micropores, when exchange process between TMA$^+$ and CTA$^+$ ions happened, which led indirectly to the pore expansion. At higher hydrothermal temperature, much more soluble silicate species migrated into the channel and subsequent deposition significantly increased the pore wall thickness. This is the reason that mesoporous silica involved by TMA$^+$ ion generally showed higher thermal stability. Concurrently, the neutral long chain amine, a product from the decomposition of the CTA$^+$ was solublized into the micelle, leading to the pore size expansion. The other functions of TMA$^+$ ions were used as the counterions for charge compensation to maintain the structure ordering of initially formed MCM-41 silica, as proposed by Jaroniec et al [25].

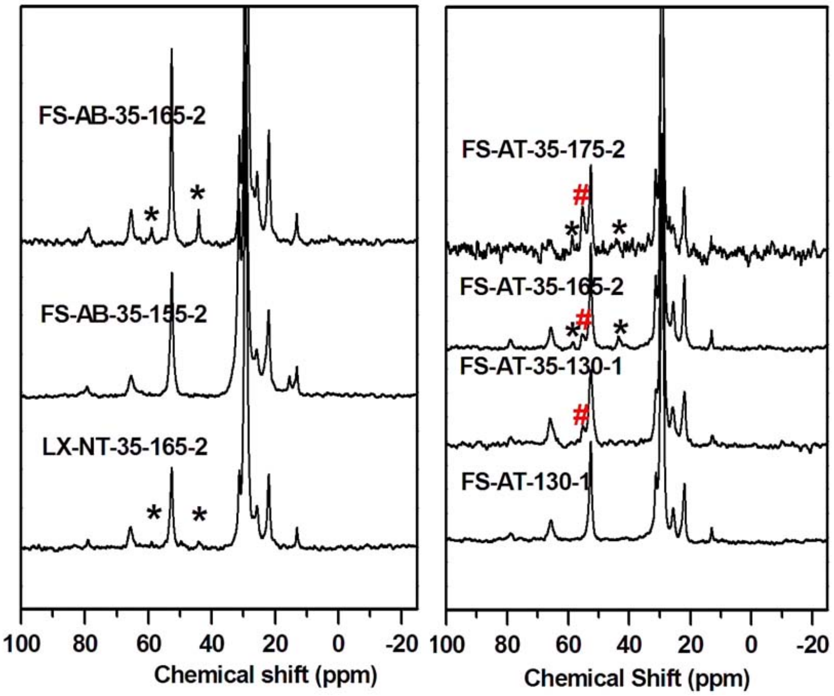

Figure 3.27 ^{13}C CP MAS NMR spectra of FS-AB-35-X-2 and LX-NT-35-165-2 (left), FS-AT-X (right); (*) Chemical shift of speciesgenerated by decomposition of surfactants, (#) chemical shift of TMA.

To further investigate the structure changes during unit-cell enlargement, several type of MCM-41 silicas were synthesized using the different gel compositions at the hydrothermal temperature 165ºC, because the restructuring of mesoporous silica synthesized via the higher temperature postsynthesis treatment is still in debate.

3.2.3.3 Structure change during the unit-cell enlargement at 165ºC

3.2.3.3.1 XRD patterns: The FS-AT series of samples showed the high ordering of typical MCM-41 hexagonal structure as exhibited by XRD patterns. However, for other three series of samples, whether the aging was adopted or not, the pore structure properties of samples such as specific surface area and pore volume showed the same characteristics with that of FS-AT-165-2, as exhibited in figure 3.28. At low temperature 130ºC, XRD patterns showed the good quality of mesoporous silica, except that sample FS-AB-135-2 exhibited a small fraction of lamellar phase marked by star. But at high hydrothermal temperature 165ºC, this sample showed the best quality among these samples. The rest of samples including LX-AT-60-165-2 and LX-NT-35-165-2 showed much broader d_{100} reflection band, indicating partial structure ordering was lost during the high temperature hydrothermal treatment (figure 3.29).

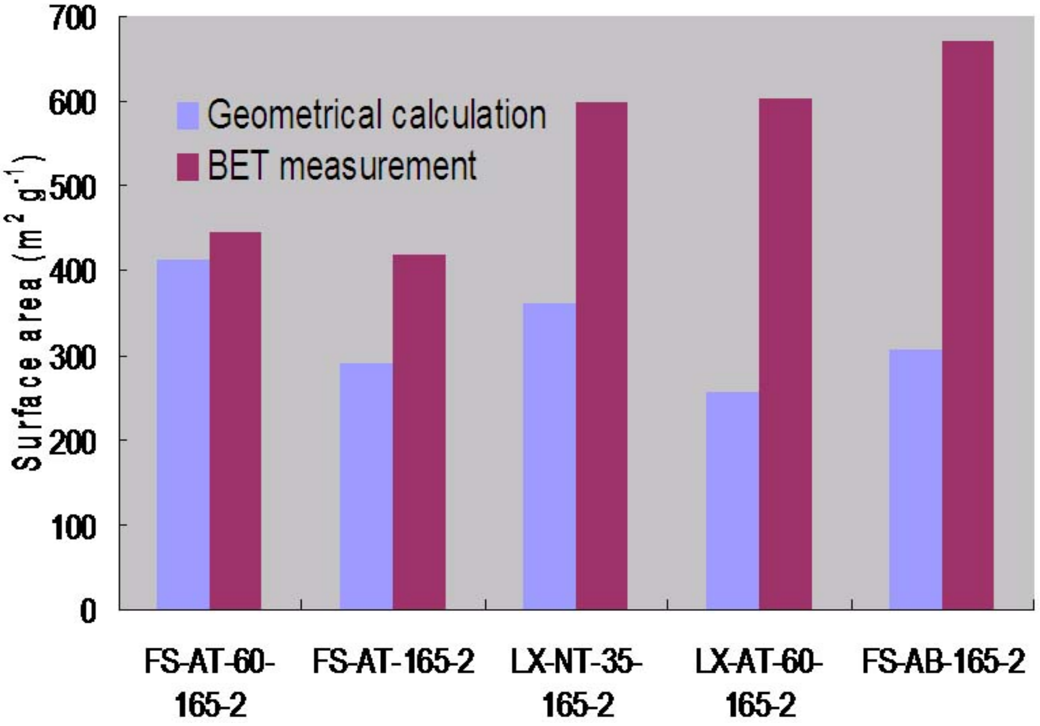

Figure 3.28 Comparison of surface areas obtained from geometrical calculation and BET measurement for samples synthesized at 165ºC

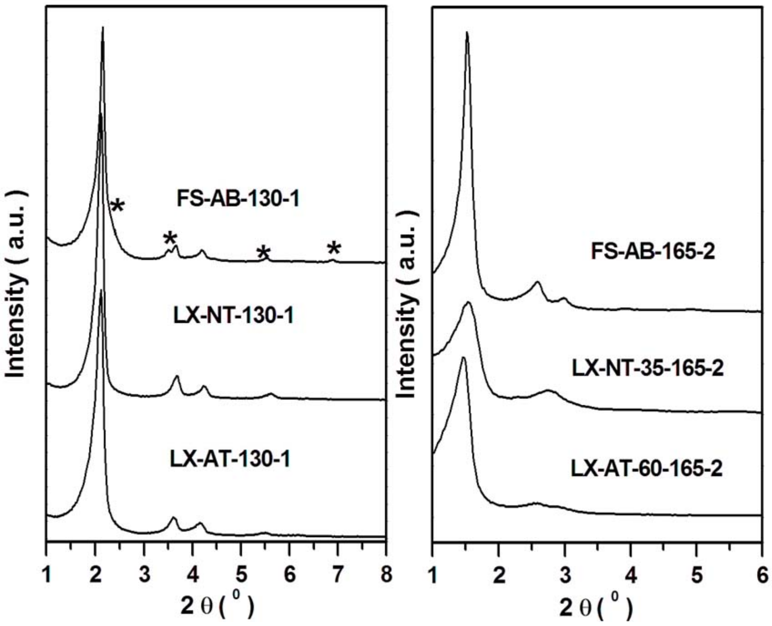

Figure 3.29 XRD patterns of as-made MCM-41 silicas synthesized using different gel composition and different autoclaving temperatures; (*) means lamellar phase.

3.2.3.3.2 N_2 adsorption: For all the samples, N_2 adsorption measurement exhibited typical IV adsorption isotherm with H1 hysteresis loop centered at relative pressure about 0.45 (figure 3.30, left), and BJH adsorption branch showed narrow pore size distribution (figure 3.30, right). The textural properties of all the samples were listed in table 3.9. For FS-AT series after ageing process, the calculated specific surface area and mesopore volume are very close to the experimental ones. However if there is no aging process, the values calculated are much less than the value measured by N_2 adsorption isotherm, indicating the contribution of micropores. For others series samples, the large discrepancy between experimental value and geometrical model calculation up to 50% is observed, indicating high temperature postsynthesis did not affect the structure of surface micropores. Jaroniec et al. supposed the presence of micropores or constraints on the pore channel, which has been proved using α_s-plot method [20]. The presence of micropores after high temperature treatment showed two possibilities: one is that the considerable restructuring did not happened, only solouable silicate species migrated into thannel and consequently deposited on the edge of micropores; the other one is that a complete restructuring took place, micropore was produced. To answer this quention, the SEM observation was carried out.

Table 3.9 Effect of aging temperature and gel composition on texture properties of MCM-41 mesophase

Sample Name	d_{100} (nm)	S_{BET} (m^2 g^{-1})	V (cm^3 g^{-1})	D_{BJH} (nm)	D_{BDB} (nm)	t_{BJH} (nm)	t_{BDB} (nm)	S_{meso} (m^2 g^{-1})	V_{meso} (cm^3 g^{-1})
FS-AT-165-2	5.57	419	0.42	3.86	4.31	2.57	2.12	290	0.31
FS-AT-60-165-2	5.21	445	0.48	3.97	4.49	2.05	1.53	413	0.46
FS-AB-165-2	5.81	672	0.76	4.65	4.68	2.06	2.03	307	0.36
LX-AT-60-165-2	5.94	604	0.68	4.44	4.49	2.42	2.37	257	0.29
LX-NT-35-165-2	5.56	598	0.74	4.93	4.68	1.49	1.74	361	0.42
LX-NT-60-165-2	5.72	648	0.78	5.05	4.68	1.55	1.92	324	0.38

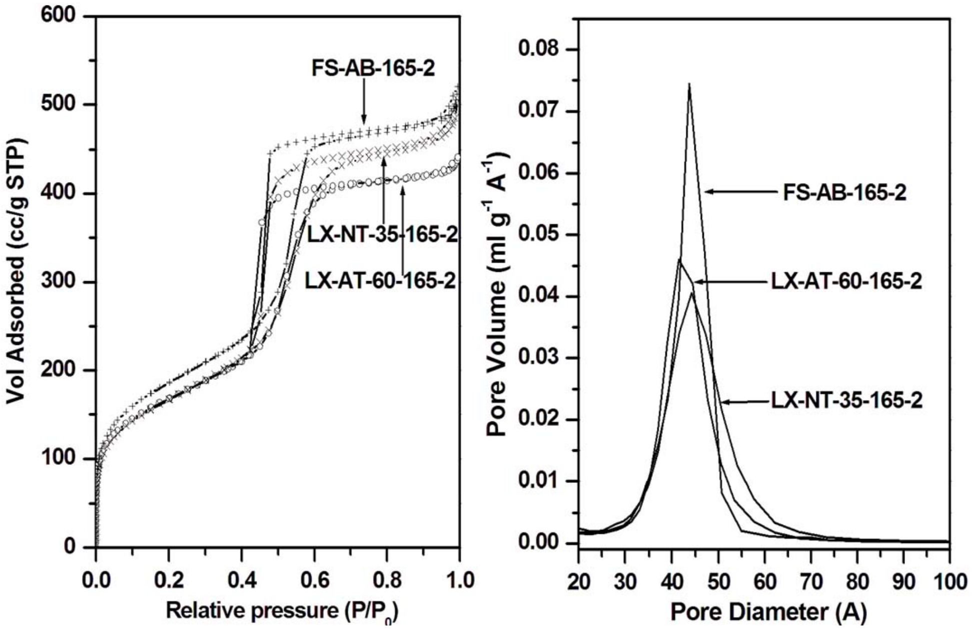

Figure 3.30 N_2 adsorption isotherms of as-made MCM-41 silicas synthesized using different gel composition and aging temperature; (*) lamellar phase.

3.2.3.3.3 SEM observation: If assumed that the unit-cell expansion did not experience the full restructuring, the morphology should be remained after high temperature postsynthesis treatment. For FS-AB series, samples did not show the distinct the morphology change, indicating mesoporous structure was maintained during the postsynthesis treatment. It should be mentioned although no obvious morphology evolution was observed, but for this series of samples, the large quantity of amorphous silica like snow was significantly decreased similar to FS-AT-35 series. Large pore makes the solouble silicate species easily migrate into the pore channel, consequent deposition led to the thicker pore wall. In contrast, the morphology of other two samples exhibited much more difference after high temperature postsynthesis treatment, especially for series LX-NT sample, the particles transferring from fiber morphology into spherical form, implying the complete restructure took place during the pore expansion at high temperatue. Literature showed that, in the presence of Na^+, mesoporous silica generally exhibited the lower stability, consitent with cuurent observation. Now we returned to the sample LX-NT-35-130-1 to further understand the formation MCM-41 silica with superlarge pores. Even at mild reaction conditions, mesopore structure covered by open micropores could be easily local restructured due to the very thin pore wall. At the initial work of Stucky research group, they reported that MCM-41 was formed by complicated solid-solid phase transformation mechanism [56], which means that even morphology was not changed, the restructuring of mesoporous silica was possible under relatively severe reaction conditions.

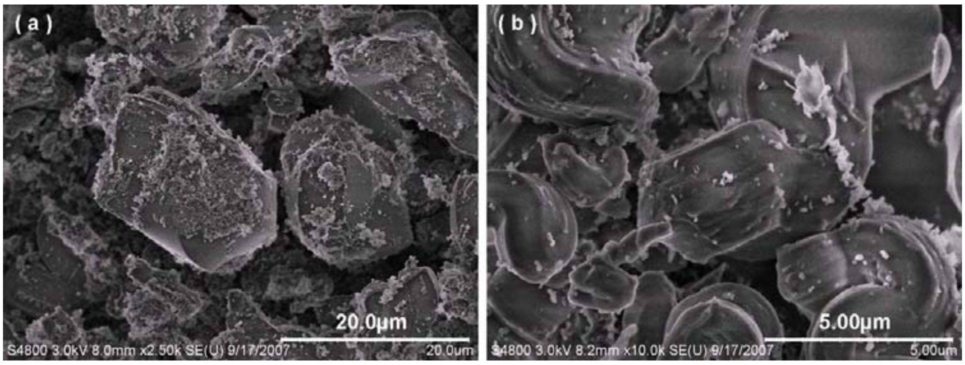

Figure 3.31 SEM images of FS-AB-130-1 and FS-AB-165-2.

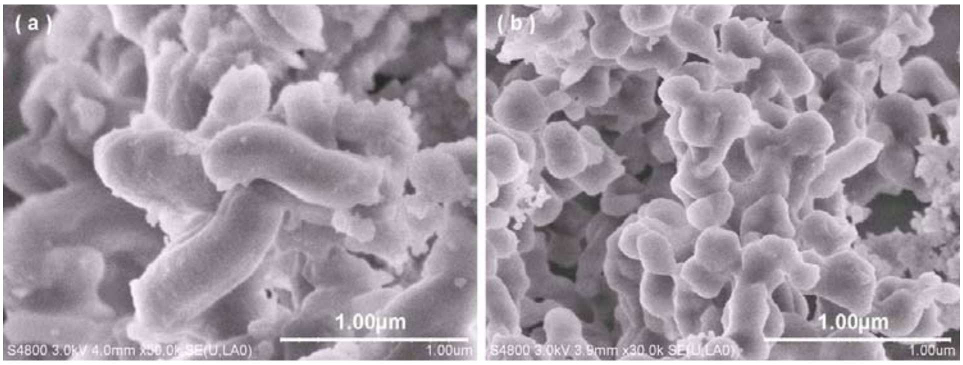

Figure 3.32 SEM images of LX-AT-130-1 and LX-AT-60-165-2.

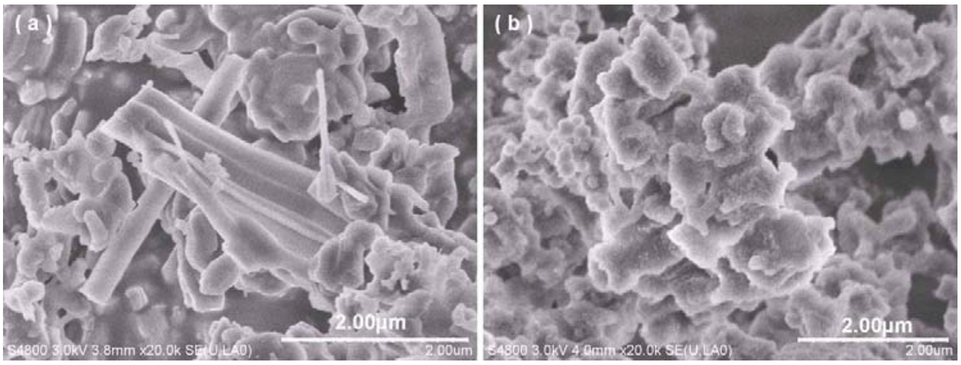

Figure 3.33 SEM images of LX-NT-130-1 and LX-NT-35-165-2.

3.2.4 Conclusion

In a summary, depending on the experimental parameters, pore size and unit-cell expansion of MCM-41 silica is found to be a very complicated process as depicted in figure 3.34. The red arrow indicates routes using high temperature and prolongated time of treatment producing unit-cell lattice expansion with extensive dissolution-redeposition of initially formed silica framework and in situ generation of DMHA; swelling action is the main driving force. The blue arrow indicates a more controlled process were pore size and unit-cell lattice expansion is the result of a cooperative interaction mechanism due to erosion of the surface rugosity and the swelling action of micelle. At low temperature, the erosion mechanism, i.e., the local dissolution-redeposition process of silica at the surface open micropores in the channel, is the dominant process, while, at higher temperature, the swelling action of decomposition species from surfactants enters also in action. This proposed comprehensive description of both pore size and unit-cell expansion mechanisms explains previous literature data and also strengthens our understanding of the formation mechanism of MCM-41 silica.

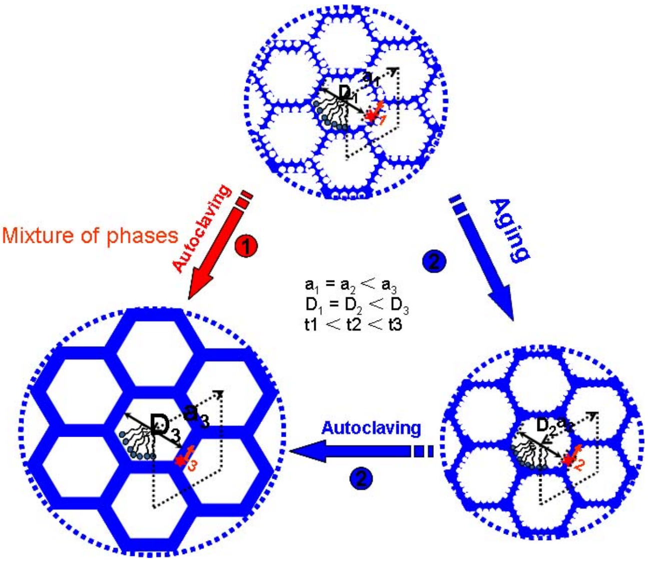

Figure 3.34 schematic representation of pore evolution in the presence of microporosity in the pore wall.

3.3 General conclusion and perspective

3.3.1 Understanding the microporosity of classical MCM-41 silica: Calcined MCM-41 silica and TMA exchanged MCM-41 were investigated to confirm the presence of open micropores with pore size of *ca*. 7 Å on the channel surface, using a panel of complementary characterization techniques, such as X-ray diffraction (XRD) patterns, nitrogen adsorption isotherm including comparison plot (t-plot, α_s-plot and β-plot) and low pressure regions 10^{-7}-0.01 of the adsorption isotherms, laser hyperpolarized ^{129}Xe nuclear magnetic resonance (NMR) and X-Ray photoelectron (XPS) spectrum. This new model allows us describe and quantify the true mesoporosity of MCM-41 silicas, to understand better why MCM-41 silicas are so fragile, to explain how both pore and structure can expand and, to propose novel synthesis conditions to improve thermal and hydrothermal stability. The presence of open micropores strongly connected to the mesopores leads to unreliable determination of the surface area and micropore volume using either t-plot, α_s-plot, β-plot, or very low pressure region of nitrogen adsorption. Combined with the BDB method to analyze pore size of cylindrical pores, a geometrical model permits the calculation of true surface area, both micropore and mesopore volumes, the wall thickness and the wall density.

3.3.2 New insights into high-temperature unit-cell and pore size expansion in MCM-41 mesoporous silica: The most striking aspect of MCM-41 silicas with improved crystalinity synthesized via high-temperature autoclaving treatment in the presence of cetyltrimethylammonium (CTA^+) surfactant was the possibility of engineering their pore size. A panel of experimental techniques, such as XRD, N_2 adsorption measurement, solid NMR (^{13}C CPMAS and ^{29}Si MAS), SEM and TEM, etc., combined by the geometrical model calculation, was used to describe the true picture for unit-cell and pore enlargements using high-temperature postsynthesis treatment. Besides the swelling effect of decomposition species from surfactants at high temperature, the role of

TMA^+ ions to facilitate the rugosity erosion was tentatively explained. The action of TMA was associated with its capacity to cation exchange with CTA^+ and to accelarate the dynamics of site-to-site exchange then, producing an increased exposure of the silica walls to OH^- erosion. In fact, combining the effects of different experimental parameters including surfactant concentration, type and concentration of base, even silicon source, time and temperature etc., conditions for full restructurion of the silica framework was possible, even though the external morphology of particles was not significantly changed.

3.3.3 Perspectives: Although the hydrothermal stability of MCM-41 silica after high-temperature postsynthesis treatment was significantly improved, the amorphous nature of pore wall, i.e., was still preserved. Therefore, crystallization of the pore wall and generation of true zeolitic pore, remains a challange. To achieve this objective, two necessary requirements must be satisfied: A minimum pore wall thickness of 2.0 nm is necessary to grow the primary unit cell of a zeolite, obviously high-temperature postsynthesis is a requirement for this goal. However, during the crystallization process, the templating role of surfactant should be maintained. Up to now, well accepted solution-mediated mechanism have not been successful for synthesizing mesoporous materials with crystalline pore walls. Current works provide an innovative alternative, via solid-solid transformation, the design synthesis of hybrid materials can be realized using dual template as structure directing agent. Because of the paramount importance of such a material in petroleum chemistry, this project has been treated and reported in separate chapter, that follows.

3.4 References

(1) Beck, J. S.; Vartuli, J. C.; Roth, W. J.; Leonowicz, M. E.; Kresge, C. T.; Schmitt, K. D.; Chu, C. T.-W.; Olson, D. H.; Sheppard, E. W.; McCullen, S. B.; Higgins, J. B.; Schlenker, J. L. *J. Am. Chem. Soc.* **1992**, *114*, 10834.

(2) Corma, A. *Chem.Rev.* **1997**, 97, 2373.

(3) Ciesla, U.; Schüth, F. *Microporous Mesoporous Mater.* **2005**, *77*, 1.

(4) Hoffmann, F.; Cornelius, M; Morell, J.; Fröba, M. *Angew. Chem. Int. Ed.* **2006**, 45, 3216.

(5) Zhao, D. Y.; Feng, J. L.; Huo, Q. S.; Melosh, N.; Fredrickson, G. H.; Chmelka, B. F.; Stucky, G. D. *Science* **1998**, *279*, 548.

(6) Zhao, D. Y.; Huo, Q. S.; Feng, J. L.; Chmelka, B. F.; Stucky, G. D. *J. Am. Chem. Soc*. **1998**, *120*, 6024.

(7) Galarneau, A.; Nader, M.; Guenneau, F.; Di Renzo, F.; Gedeon, A. *J. Phys. Chem. C* 10.1021/jp068526e

(8) Selvam, P.; Bhatia, S. K.; Sonwane, C. G. *Ind. Eng. Chem. Res.* **2001**, *40*, 3237.

(9) Galarneau, A.; Cambon, H.; Di Renzo, F.; Fajula, F. *Langmuir* **2001**, *17*, 8328.

(10) Groen, J. C. ; Peffer, L. A. A. ; Ramirez, J. P. *Microporous Mesoporous Mater.* **2003**, *60*, 1.

(11) Kruk, M.; Jaroniec, M.; Ko, C. H.; Ryoo, R. *Chem. Mater.* **2000**, *12*, 1961.

(12) Albouy, P. A.; Ayral, A. *Chem. Mater.* **2002**, *14*, 3391.

(13) Lukens, W. W.; Schmidt-Winkel, P.; Zhao, D. Y.; Feng, J. L.; Stucky, G. D. *Langmuir* **1999**, *15*, 5403.

(14) Liu, Z.; Terasaki, O.; Ohsuna, T.; Hiraga, K.; Shin, H. J.; Ryoo, R. *Chem. Phys. Chem.* **2001**, *4*, 229.

(15) R. Ryoo, C.H. Ko, M. Kruk, V. Antochshuk, M. Jaroniec, *J. Phys. Chem. B* **2000**, *104*, 11465.

(16) Sun, Y. Y.; Han, Y.; Yuan, L.; Ma, S. Q.; Jiang, D. H.; Xiao, F. S. *J. Phys. Chem. B* **2003**, *107*, 1853.

(17) Liu, J.; Zhang, X.; Han, Y.; Xiao, F. S. *Chem. Mater.* **2002**, *14*, 2536.

(18) Haddad, N. E.; Guenneau, F.; Galarneau, A., Di Renzo, F.; Fajula, F; Gedeon, A. *J. Phys. Chem. B* **2003**, *107*, 12456.

(19) Davidson, A.; Berthault, P.; Desvaux, H. J. Phys. Chem. B **2003**, *107*, 14388.

(20) Jaroniec, M.; Kruk, M.; Olivier, J. P. *Langmuir*, **1999**, *15*, 5410.

(21) Albouy, P. A.; Ayral, A. *Chem. Mater.* **2002**, *14*, 3391.

(22) Lee, J. S.; Joo, S. H.; Ryoo, R. *J. Am. Chem. Soc.* **2002**, *124,* 1156.

(23) Chen, F. X.; Xu, X. J.; Shen, S. C.; Kawi, S.; Hidajat, K. *Microporous Mesoporous Mater.* **2004**, *75*, 231.

(24) Kremer, S. P. B. ; Krischock, C. E. A.; Aerts, A.; Aerts, C. A.; Houthoofd, K. J.; Grobet, P. J.; Jacobs, P. A.; Lebedev, O. I.; Tendello, G. V. ; Martens, J. A. *Solid State Sciences* **2005**, *7*, 861.

(25) Kruk, M.; Jaroniec, M.; Sayari, A. *Langmuir*, *J. Phys. Chem. B* **1999**, *103*, 4590.

(26) Storck, S.; Bretinger, H.; Maier, W. F. *Appl. Catal. A* **1998**, *174*, 137.

(27) Kruk, M.; Jaroniec, M.; Sayari, A. *Microporous Mesoporous Mater.* **1999**, *27*, 217.

(28) Galarneau, A.; Desplantier-Giscard, D; Di Renzo, F.; Fajula, F. *Catal. Today* **2001**, *68*, 191.

(29) Edler, K. J.; Reynolds, P. A.; White, J. W.; Cookson, D. *J. Chem. Soc., Faraday Trans.* **1997**, *93*, 199.

(30) Edler, K. J.; Reynolds, P. A.; White, J. W. *J. Phys. Chem. B* **1998**, *102*, 3676.

(31) Han, S. H.; Xu, J.; Hou, W. G.; Yu, X. M.; wang, Y. S. *J. Phys. Chem. B* **2004**, *108*, 15043.

(32) Broekhoff. J. C.P. ; de Boer, J. H. *J. Catal*. **1967**, *9*, 8.

(33) Bonneviot, L.; Morin, M.; Badiei, A. Patent WO 01/55031 A1, **2001.**

(34) Martins, L.; Bonagamba, T. J.; de Azevedo, E. R.; Bargiela, P.; Cardoso, D. *Appl. Catal. A* **2006**, *312*, 77.

(35) Abry, S.; Albela, B.; Bonneviot, L. *C. R. Chimie* **2005**, *8*, 741–752

(36) Springerguel-Huet, M. A.; Sun, K.; Fraissard, J. *Microporous Mesoporous Mater.***1999**, *33*, 89.

(37) K.S.W. Sing, J. Rouquerol, in: G. Ertel, H. Knözinger, J. Weitkamp (Eds.), Handbook of Heterogeneous Catalysis, vol. 1, VCH, Weinheim, 1997, p. 427.

(38) Cheng, C. F.; Zhou, W.; Klinowski, J. *Chem. Phys. Lett.* **1996**, *263*, 247.

(39) Khushalani, D.; Kuperman, A.; Ozin, G. A.; Tanaka, K.; Garces, J.; Olken, M. M.; Coombs, N. *Adv. Mater.* **1995**, *7*, 842.

(40) Liu, J. ; Shin, Y. S. ; Nie, Z. M.; Chang, J. H.; Wang, L. Q.; Fryxell, G. E.; Samuels, W. D.; Exarhos, G. J. *J. Phys. Chem. A* **2000**, *104*, 8328.

(41) Huo, Q. S.; Margolese, D. I.; Stucky, G. D. *Chem. Mater.* **1996**, *8*, 1147.

(42) Ulagappan, N.; Rao, C. N. R. *Chem. Commun.* **1996**, 2759.

(43) Zhou, W. Z. ; Klinowski, J. *Chem. Phys. Lett.* **1998**, *292*, 207.

(44) Corma, A.; Kan, Q.; Navarro, M. T.; Perez-Pariente, J.; Rey, F. *Chem. Mater.* **1997**, *9*, 2123.

(45) Sayari, A.; Kruk, M.; Jaroniec, M.; Moudrakovski, I. L. *Adv. Mater.* **1998**, *10*, 1376.

(46) Galarneau, A.; Desplantier, D.; Dutartre, R.; Di Renzo, F. *Microporous Mesoporous Mater.* **1999**, *27*, 297.

(47) Lefèvre, B.; Galarneau, A.; Iapichella, J.; Petitto, C.; Di Renzo, F.; Fajula, F. *Chem. Mater.* **2005**, *17*, 601.

(48) Zhu, H. Y.; Zhao, X. S.; Lu, G. Q.; On, D, T. *Langmuir*, **1996**, *12*, 6513.

Mori, T.; Kuroda, Y.; Yoshikawa, Y.; Nagao, M.; Kittaka, S. **2002**, *18*, 1595.

(49) Zhao, X. S.; Lu, G. Q.; Whittaker, A. K.; Millar, G. J.; Zhu, H. Y. *J. Phys. Chem. B* **1997**, *101*, 6525.

(50) Ishikawa, T.; Matsuda, M.; Kandori, K.; Inagaki, S.; Fukushima, T.; Kondo, S. *J. Chem. Soc., Faraday Trans.* **1996**, *92*, 1985.

(51) Rouquerol, F.; Rouquerol, J.; Sing, K. *Adsorption by powders &porous solids*: *principles, methodology and applications*; Academic

Press: San Diego, CA, 1999.

(52) Zheng, Q. S.; Yu, Y.; Zhao, Z. H. *Langmuir* **2005**, *21*, 12207.

(53) Chen, F. X.; Xu, X. J.; Shen, S. C.; Kawi, S.; Hidajat, K. *Microporous Mesoporous Mater.* **2004**, *75*, 231.

(54) Monnier, A.; Schuth, F.; Huo, Q.; Kumar, D.; Margolese, D.;Maxwell, R. S.; Stucky, G. D.; Krishnamurty, M.; Petroff, P.; Firouzi, A.; Janicke, M.; Chmelka, B. F. *Science* **1993**, *261*, 1299.

(55) Ogura, M.; Miyoshi, H.; Naik, S. P.; Okubo, T. *J. Am. Chem. Soc.* **2004**, *126*, 10937.

Chapter 4 Design synthesis of hybrid mesoporous-microporous materials

4.1 Introduction

Although the high-temperature post-synthesis treatment could increase pore wall thickness and thus significantly improved the hydrothermal stability, the amorphous nature of pore wall was is still a weakness of such materials. Indeed, extensive research efforts have been already devoted to the synthesis of hybrid materials in order to reduce the diffusion limitation and take full advantage of the catalytic activities of the crystallized microporous zeolite.[1, 2]

Recently, two main synthetic strategies, hard casting and soft template techniques,[3, 4] were proposed. The latter directly using surfactant or polymer as templates is intrinsically appealing.[5-8] Unfortunately, because dual-templates system worked in a competitive, rather than a cooperative manner based on conventional solution-mediated transformation (SMT),[9] rational design of mesoporous materials with crystalline framework like zeolite in most cases remains a pipe dream. Most recently, two new types of hierarchical materials, denoted as zeogrids and zeotiles were developed by modifying the ordering of the building units through addition of surfactants and polymers in the zeogrid hardware aboard the International Space Station.[10] Inspired by this new synthetic concept, Ryoo [11] and Pinnavaia [12] claimed that crystalline hybrid materials were synthesized using a rationally designed silane-functionalized surfactant and polymer as templates, respectively. Obviously, the sophisticated synthesis of the silane-functionalized surfactant and polymer was tedious, low yield and, costly.

One of important conclusions out of chapter 3 is that TMA^+ ions can be incorporated into the mesopores to balance the surface charge between silicate anions and CTA$^+$ cations. Since TMA$^+$ can enter into the pore why TEA$^+$ and TPA$^+$ should not do it? This is important to investigate because they are efficient structure directing agent (SDA) in the synthesis of conventional microporous zeolites. The other observation is that many mesophases with different geometry structure, such as SBA-8, MCM-48, and MCM-50, could be synthesized via the solid-solid transformation mechanism (not shown here). That is to say, during phase transformation, surfactant was retained in the channel, thus, the templating function of surfactants was maintained.

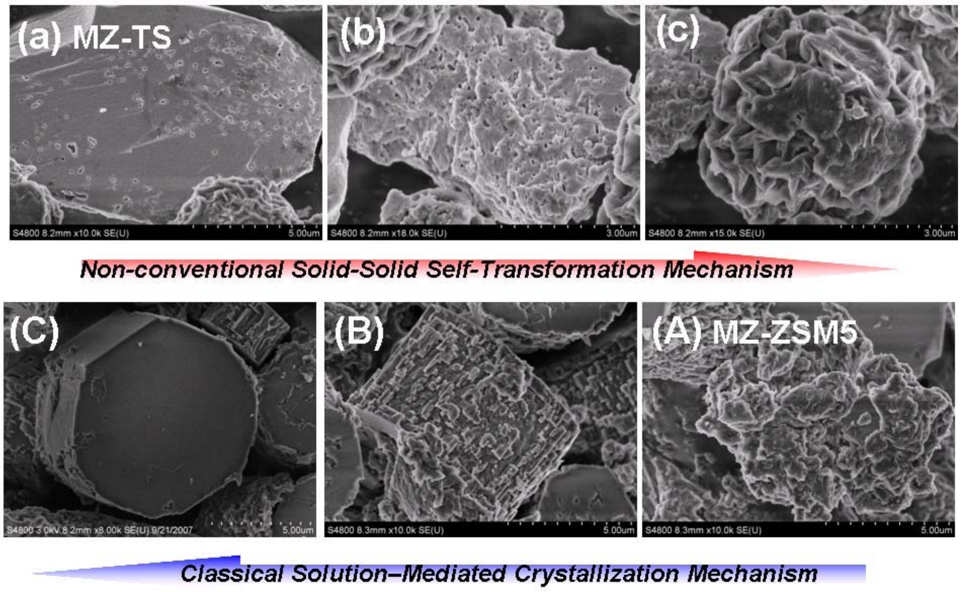

Scheme 4.1 Formation mechanism of crystalline hybrid materials using CTA$^+$ using TPA$^+$ as co-template in the present work.

Inspired by these important discoveries above, a novel synthetic strategy was proposed to prepare the crystalline hybrid materials via solid-solid transformation mechanism using dual templates as structure directing agents, instead of well-accepted solution-mediated transformation mechanism (Scheme 4.1). The synthesis approach was based on the idea that the molecular templates, for example, TPA$^+$, could direct zeolite crystallization in the mesopore wall, while mesoporous structure was maintained according to the supramolecular templating mechanism of the surfactant micelles due to soild-solid transformation. It should be mentioned that the formation of hybrid materials necessitated two requirements.[13, 14] The pore wall thickness should be lager than 2.0 nm to satisfy the growth of primary structure unit of zeolite, on the other hand, the crystallization temperature, generally, should be higher than 165℃. At this temperature, however, the structure of most of MCM-41silica should collapse according to the literature but hope is permitted in the view of previous chapters.

For the synthesis of crystalline hybrid materials, another challenge was what type of zeolite was selected as a prime candidate to illustrate our new approach. To realize the synthesis of hybrid materials, a temperature of 175℃ was set to carry out this series of experiments.

4.2. Experimental section

4.2.1 Synthesis of metal free materials

The synthesis recipe was similar with that described in the previous chapters. Crystallization temperature was set 175 or 185℃, and base was changed to TEAOH or TPAOH if necessary. A typical synthesis was as follows: 3.70 g CTATos was dissolved in 120 ml water and stirred for 1 hour at 60°C. 63ml of 1.0M tetramethylammonium hydroxide (TMAOH) aqueous solution was added into 107 ml of water, followed by addition of 10.78 g fumed silica under vigorous agitation. After stirring for 1 hour at 60 °C, the silicate solution was then added into CTATos solution drop by drop. Obtained gel composition was SiO_2: 0.09 CTATos: 0.35 TMAOH: 79.9 H_2O. The mixture was stirred continually for 2 hours at 60 °C and then loaded into a 250 ml Teflon-lined steel autoclave where the gel mixture was pre-aged for 2 days at 35 °C. The final mixture was heated in autoclave under static condition at 175 ℃ for 2 days. Collected sample was named FS-TMA-175-2 (175 is crystallization temperature, 2 means crystallization time, 2 days), the same nomenclature in this chapter was used.

4.2. 2 Synthesis of the hybrid materials containing Ti atom The solid was synthesized from clear silicate solutions (TPAOH used as not only base source, also structure directing agent of zeolite) using the hexadecyltrimethyl-ammonium-p-toluene-sulfonate (CTATos) as a template for mesoporous silica. In a typical synthesis procedure, 3.70 g CTATos was dissolved in 120 ml water and stirred for 1 hour at 60 °C. 63ml of 1.0M tetrapropylammonium hydroxide (TPAOH) aqueous solution was added into 107 ml of water, followed by addition of 10.78 g fumed silica under vigorous agitation. After stirring for 1 hour at 60°C, the silicate solution was cooled to ice temperature, 1.36 g Titanium(VI) ethoxide ($Ti(OC_2H_5)_4$ was added slowly and continued to stir for 30 min at 0 °C, then this solution was heated to 60 °C, and continued to stir for 10 min. It should be noted that the preparation of the raw materials via sol-gel methods resulted in a stabilization of the Ti atoms by dispersion in isolated positions of the amorphous SiO_2 network at ice temperature, which avoided the formation of undesired TiO_2 phase during both gel and crystallization process. The above obtained solution was dropwise added into CTATos solution. The collected gel composition was SiO_2: 0.033Ti: 0.09 CTATos: 0.35 TPAOH: 79.9 H_2O. The mixture was stirred continually for 2 hours at 60 °C and then loaded into a 250 ml Teflon-lined steel autoclave where the gel mixture was pre-aged for 2 days at 35 °C. The final mixture was heated in autoclave under static condition at 175 °C for 48 hours. The as-synthesized products were collected by filtration, washing, and drying. To remove the templates, the products were finally heated under air for 6 h at 550 °C. Noted that when hybrid materials containing Al atom, the Al source was $Al(OPr)_3$. The obtained product was named MZ-ZSM5-175-2, which reflected the experimental conditions and gel compositions.

4.3 Result and discussion

4.3.1 Synthesis of MCM-41 involved by TMA –FS-AT-x series

The synthesis of MCM-41 involved by TMA at 175 °C as a function of crystallization time was investigated. The powder X-Ray diffraction patterns of calcined samples were shown in figure 4.1 (left), typical of MCM-41 hexagonal cylinder packing structure. All the samples exhibited the intense (100) diffraction peak and some high index peaks, indicating that the mesostructure was maintained after the high temperature postsynthesis treatment even at 185 °C for 2 days. For sample FS-AT-175-2, XRD patterns showed three easily distinguished (100), (110) and (200) peaks, exhibiting high structure ordering. When the hydrothermal treatment was prolonged to 5 days or the hydrothermal temperature was increased to 185 °C, the intensity of peak (100) gradually decreased, implying the lower mesostructure ordering. Another observed phenomenon was that the d_{100} value with crystallization time and temperature was kept unvaried, showing that unit-lattice expansion has the maximum value up to 6.2 nm.

Typical N_2 adsorption isotherm of sample FS-AT-175-2 in figure 4.1 (right) showed a well developed step in the relative pressure range 0.45-0.6 characteristic of capillary condensation (filling) into uniform mesopores. The isotherm also exhibited a H1 hysteresis loop which is characteristic of MCM-41 materials with pores larger than 4.0 nm. Inset figure showed a narrow pore size distribution from BJH method, indicating the high quality of MCM-41 silica.

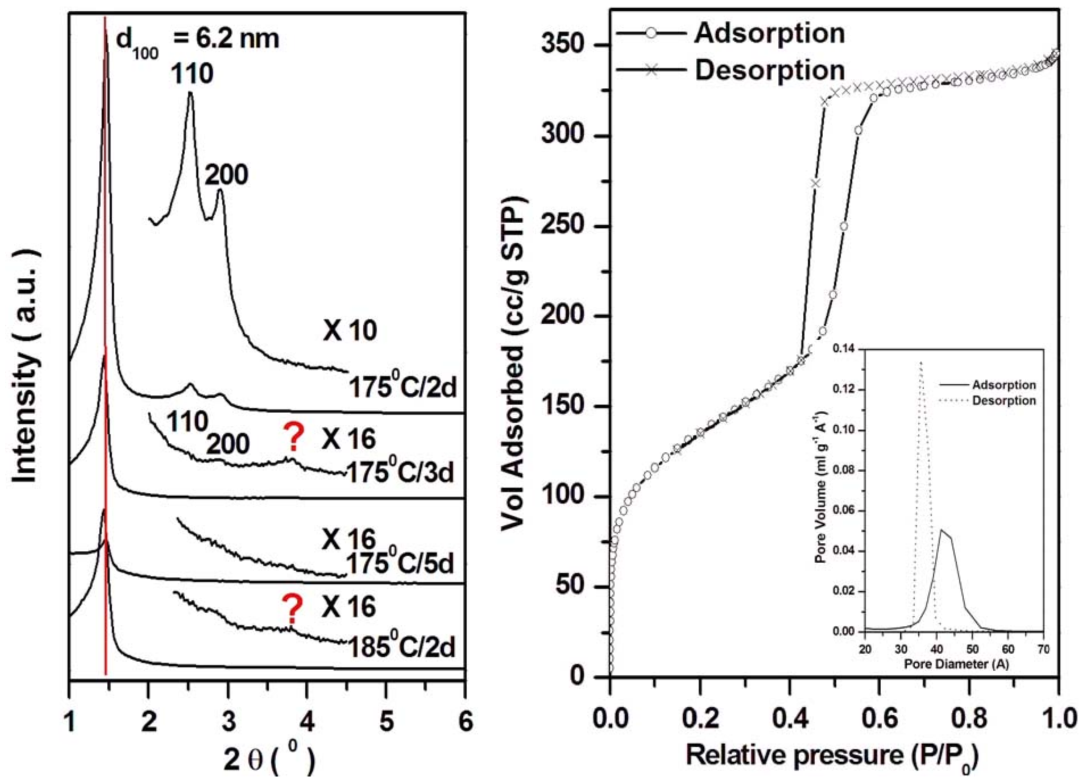

Figure 4.1 XRD patterns of sample FS-TMA-X-2 series synthesized at high temperature (left) and N_2 adsorption-desorption isotherm of FS-TMA-175-2 synthesized at 175ºC for 2d (right).

The textual properties synthesized at high temperature were listed in table 1. When the temperature increased, the pore wall thickness was significantly increased. The most striking aspect was that pore wall thickness for sample FS-AT-175-2 was up to 2.5 and 2.8 nm derived from BDB method and BJH methods[15], respectively. The thickest wall of which was much larger than the 1.0 nm for samples previously synthesized at mild conditions. It was worthy noting that the sample FS-AT-185-2 exhibiting high ordering from XRD patterns did not show any N_2 adsorption, implying that the pore entrance was blocked due to the rapid deposition of silica at high temperature.

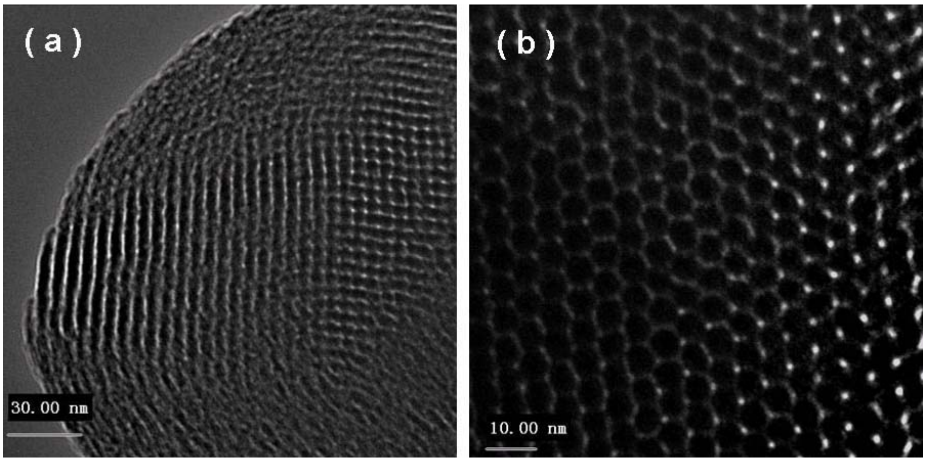

Figure 4.2 TEM observations for sample FS-TMA-175-2.

Table 4.1 Effect of reaction temperature on texture properties of FS-AT series

Sample Name	a_0 (nm)	S_{BET} ($m^2 g^{-1}$)	V_{total} ($cm^3 g^{-1}$)	D_{BJH} (nm)	D_{BDB} (nm)	t_{BJH} (nm)	t_{DBD} (nm)	S_{meso} ($m^2 g^{-1}$)	V_{meso} ($cm^3 g^{-1}$)
FS-AT-155-2	4.86	953	0.97	3.86	4.40	1.75	1.21	520	0.57
FS-AT-165-2	5.37	490	0.50	4.30	4.40	1.90	1.80	347	0.38
FS-AT-175-2	6.07	487	0.53	4.26	4.49	2.75	2.52	240	0.27

Note: t is the mean pore wall thickness, and D is pore size calculated from BDB and BJH theoretical model using desorption and adsorption branch, respectively, Smeso and Vmeso are primary surface area and pore volume of primary mesopores using cylindrical model calculation.

Figure 4.2 showed typical TEM micrographs obtained for FS-AT-175-2. A clear honeycomb structure can be seen with distance between the pore centers of about 6.0 nm in agreement with d_{100} value observed by the XRD patterns. The particle morphology showed the elongated or rod-like particles and did not exhibit the distinct change with temperature and crystallization time.

The most interesting characterization came from FT IR measurement in figure 4.3, which frequently used to collect the information about atomic-level ordering in crystalline zeolites [16-18]. For sample FS-AT-175-2 invoved by TMA molecule, IR exhibited three bands over the range 1000-400 cm^{-1}, 568, 604 and 687 cm^{-1}, that have been assigned to framework vibration associated with five-membered, double-four-membered (D4R) and six-membered rings

[16], respectively, indicating some pore wall ordering (better called semi-crystalline pore wall framework). It was importantly note that conventional MFI structure zeolite was composed of primary structure units mentioned above. Therefore, MFI structured zeolite seems the promising candidate to investigate the synthesis of crystalline hybrid materials, even though the wide-angle XRD pattern did not exhibiting the characteristic of conventional MFI zeolite [14].

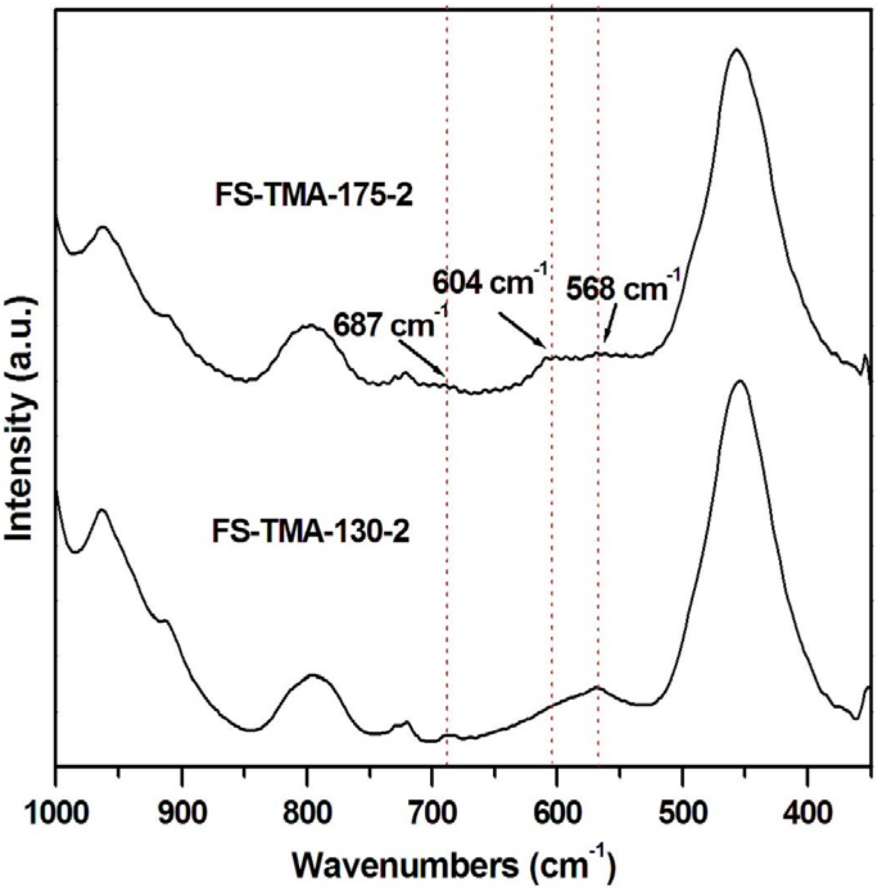

Figure 4.3 FTIR spectra of FS-AT-x-2 (x = 130 and 175 °C) showing the mesoscopic and framework ordering in silica-surfactant mesophases using TMAOH as base source.

4.3.2 Synthesis of MCM-41 involved by TEA

The synthesis recipe was similar with that of FS-AT-175-2, except that TMAOH as base source was changed into TEAOH (tetraethylammonium hydroxide). The low angle XRD patterns in figure 4.4 also showed the typical structure of MCM-41 silica. The most interesting was that, after calcination, the d_{100}/d_{110} value decreased from 1.72 to 1.68, implying the deviation of the standard hexagonal symmetry of MCM-41. The fact that, after TEA^+ molecule was exchanged into the channel at high temperature, which also observed by Corma et al.[19], the decrease of g parameter ($g=V/a_0l$) due to the increase of surfactant head area (a_0) led to the formation of intermediate mesophase with small curvature ($g<1/3$), such as SBA-2 and SBA-1 [20]. The change of intensity ratio between (110) and (200), opposite to that of MCM-41, also identified this deviation. This is the reason that surfactant with larger head volume as template often gives rise to the formation of SBA-1, 2, 6, 7, 16 mesophases. This interesting phenomenon needs further studies in the near future.

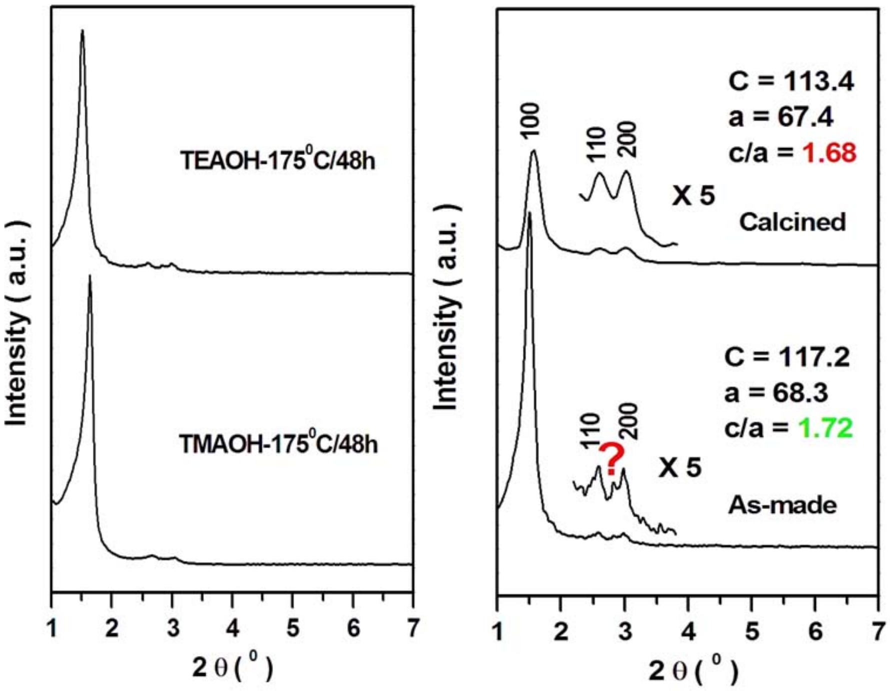

Figure 4.4 XRD patterns of mesophase silicas synthesized using different base sources (left) and XRD patterns of hypothetical SBA-2 mesophase ($p6_3/mmc$ symmetry) before and after calcination (right)

The same characterization by FT IR spectrum was used to identify the evolution of mesopore wall framework in figure 4.5 [16-18]. Compared to that of

FS-AT-175-2, multiple bands for sample FS-TEA-175-2 was observed in a range of 1000-450 cm^{-1}. Similar to assignment of sample FS-AT-175-2, the bands centered at 550, 615 and 645, 710 cm^{-1} were attributed to the vibrations from the five-membered, double-four-membered (D4R) and six-membered rings, respectively, the shift of which was assigned to the slight change of local environment of the pore wall frameworks [18]. New bands centered at around 585 and 740 cm^{-1} remained unclear. This observation agreed that the composition of head group of surfactant species influenced the local molecular ordering of inorganic oxide-mesoporous frameworks reported by Stucky and coworkers [16]. Thus, by precisely tuning the experimental parameters, true crystalline hybrid materials by solid-solid transformation using surfactant as a cotemplate could be realized.

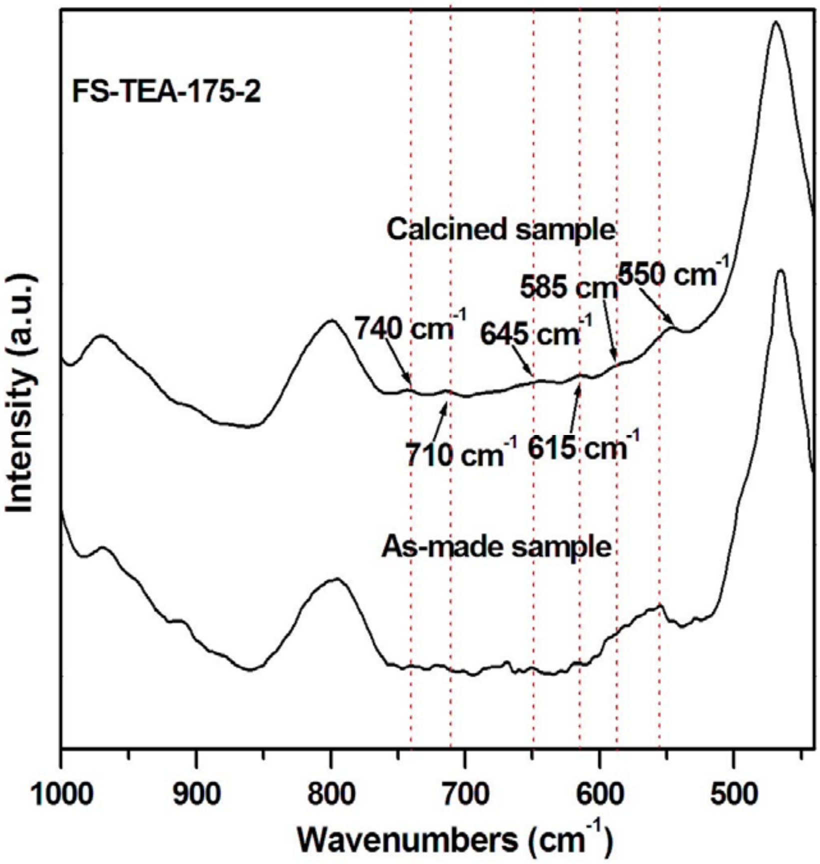

Figure 4.5 FTIR spectra of FS-TEA-175-2 showing the mesoscopic and framework ordering in silica-surfactant mesophases using TEAOH as base source

4.3.3 Synthesis of hybrid materials with hierarchical porosity involved by TPA (tetrapropyl ammonium ions)

Based on the results and discussions above, this synthetic strategy was extended to crystalline hybrid materials involved by TPA^+ ions. Unfortunately, the low-angle XRD patterns did not showed the characteristic peaks of MCM-41 silica in figure 6, indicating that, in the presence of TPA^+ ions, the traditional MFI structure zeolite was more easily formed due to the strong structure directing effect, instead of mesoporous silica. Thus the templating effect between CTA^+ and TPA^+ worked in a competing, rather than a cooperative manner [11]. However, for sample MZ-TS-175-2 (MZ is the abbreviation of mesoporous zeolte, TS means Titanium silicate, same nomenclature rule was applied to the following sample) containing Ti atom, the wide-angle XRD showed the observable difference in figure 4.6 and 4.7. The b-oriented MFI structure was synthesized under current experimental conditions [21-25], and lamellar phase can be observed before calcinations.

Herein, it should be mentioned that, in XRD experiment, the investigated zeolites lied on the test plate with probability. If the thinner in b-direction of zeolites crystals, the more possible of the crystals which located at the test sample plate with its (0k0) crystal face perpendicular to the incident X-ray. In this case, the XRD patterns of zeolite sample exhibited the higher intensity of (0k0) face. The operation for preparing the test sample influenced occasionally the measured XRD relative intensity of different growth directions as exhibited in figure 4.6 (b). Thus, at least one recurrent test for each sample was done.

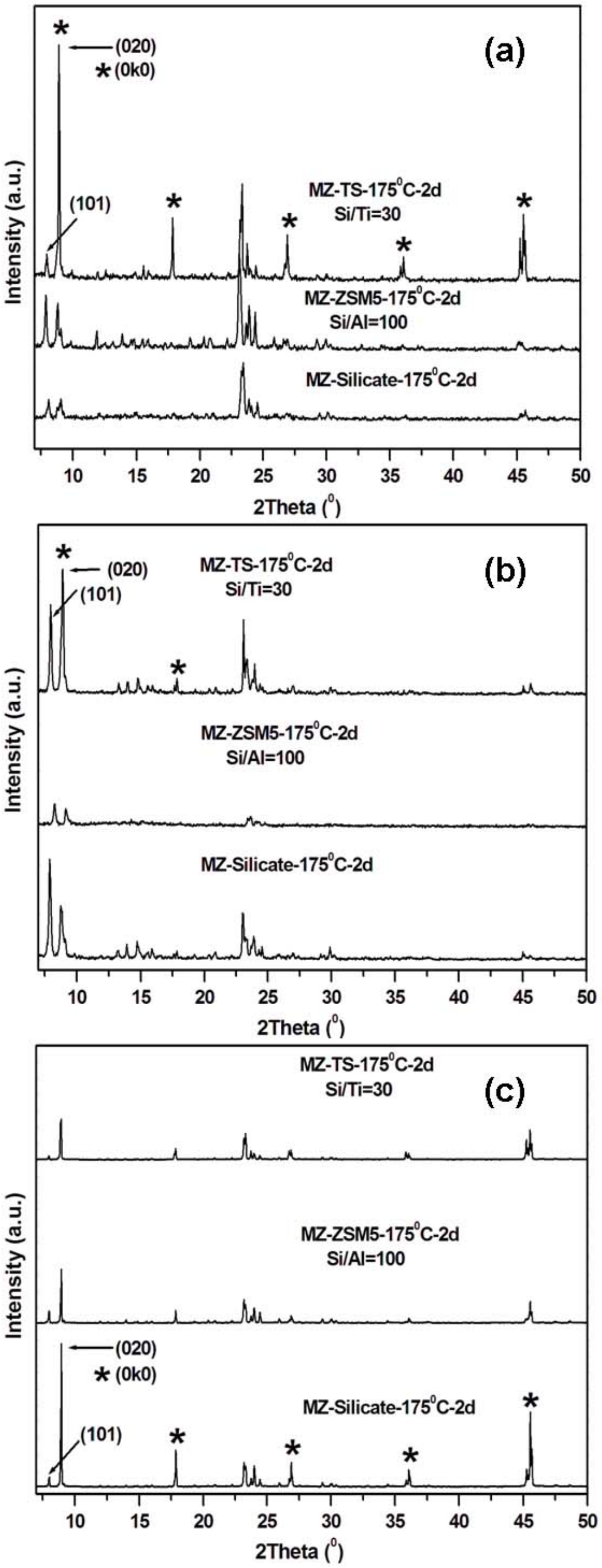

Figure 4.6 High angle XRD patterns of as-made (a), calcined (b) and pellet shaped (c, prepared using IR pelleting machine) hybrid materials containing different heteroatoms.

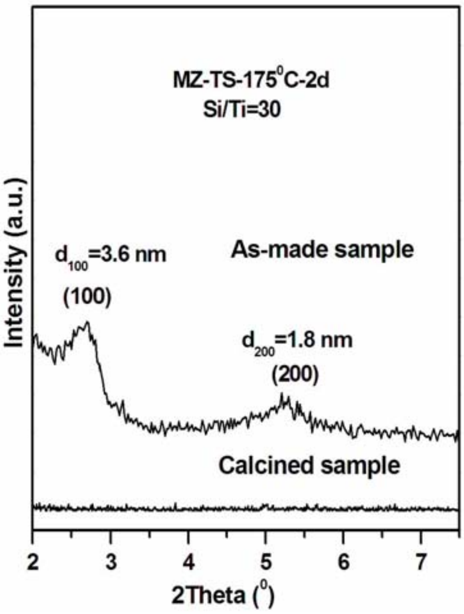

Figure 4.7 Low angle XRD patterns of hybrid materials containing Ti atom synthesized using CTATos and TPA as co-template.

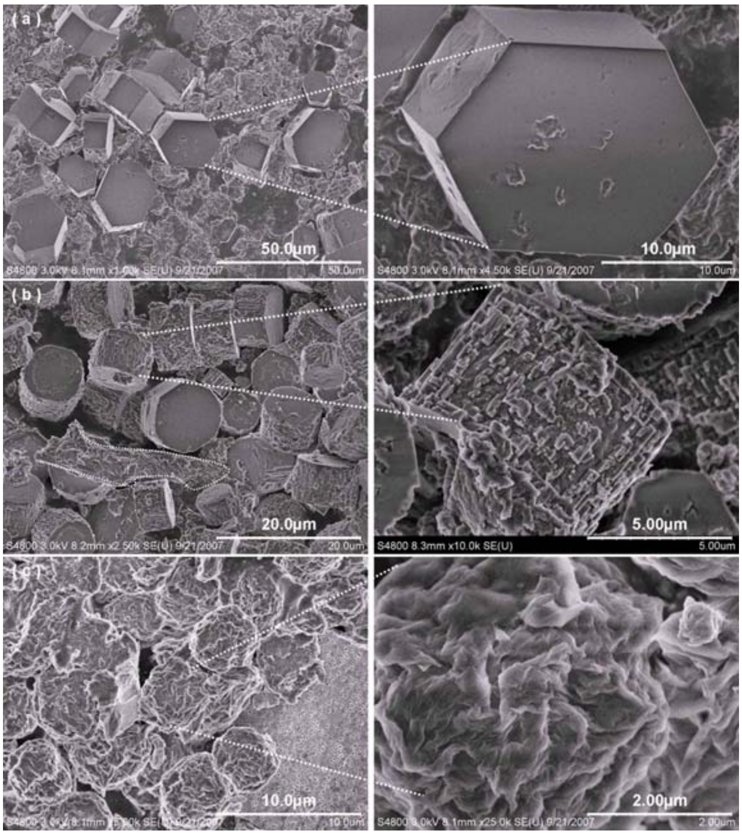

Figure 4.8 SEM images showing the morphology of as-made hybrid materials containing different heteroatoms: (a) pure silicalite-1 with typical coffin-shaped particle, (b) Si/Al = 100 with disk-shaped particles, (c) Si/Ti =30 with globular particles and rugged surface.

SEM images in figure 4.8 showed the influence of the incorporation hetroatoms including Al and Ti atom on the morphology of hybrid materials. Only the hybrid materials containing Ti atoms exhibited pure globular particles with rugged surface, differing from the hybrid materials containing Al atom and free of metal with prism shaped morphology [21-25]. Moreover, the close examination by SEM for sample MZ-TS-175-2 containing Ti atom displayed the existence of macrocavities on the bulky amorphous silica, indicating that hybrid materials were synthesized via the different mechanism as exhibited by Serrano et al[26]. Serrano proposed that, based on the observation by SEM and TEM, the presence of macrocavities indicating the crystallization of the titaniumsilicate zeolites took place via a nonconventional mechanism governed mainly by solid-solid transformtions.

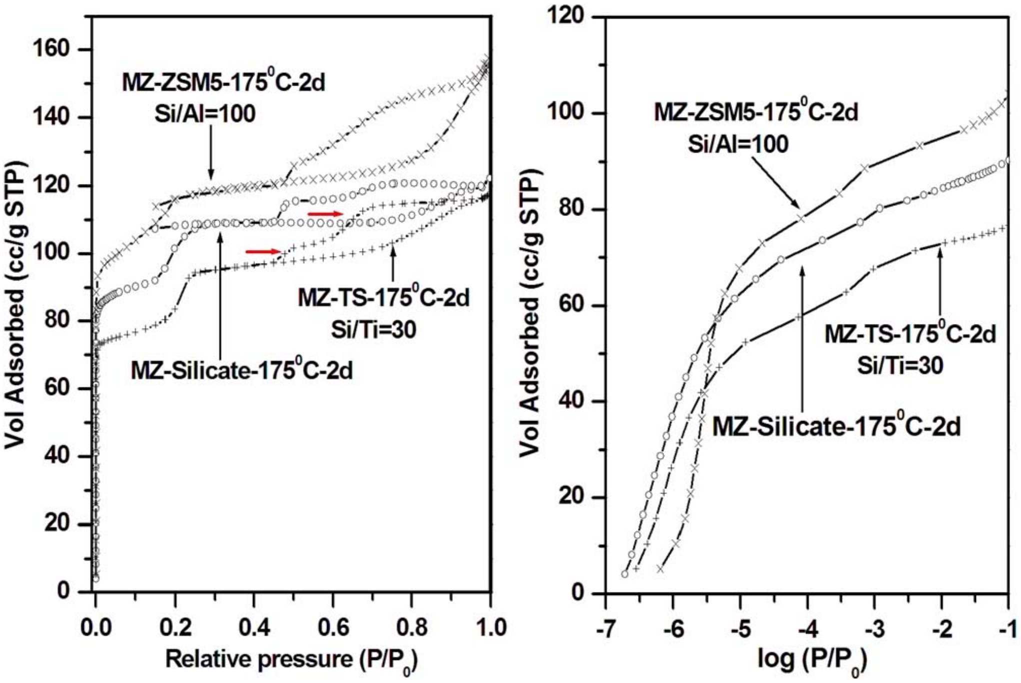

Figure 4.9 N_2 adsorption-desorption isotherms of calcined hybrid materials containing different heteroatoms.

N_2 adsorption isotherms gave much more in formations on the pore structure in figure 4.9. The complexity of nitrogen adsorption and desorption isotherms showed the presence of hierarchical porosity for these serial of hybrid materials It should be mentioned that, three samples showed typical steep nitrogen uptakes in a very low relative pressure, indicating the presence of micropores. Most interestingly, desorption branch exhibited two obvious steps in a range of relative pressure 0.4-0.7, indicating the presence of slit pores. The texture properties of these samples were list in table 4.2. The surface area and pore volume are larger than that of convention MFI structure zeolite.

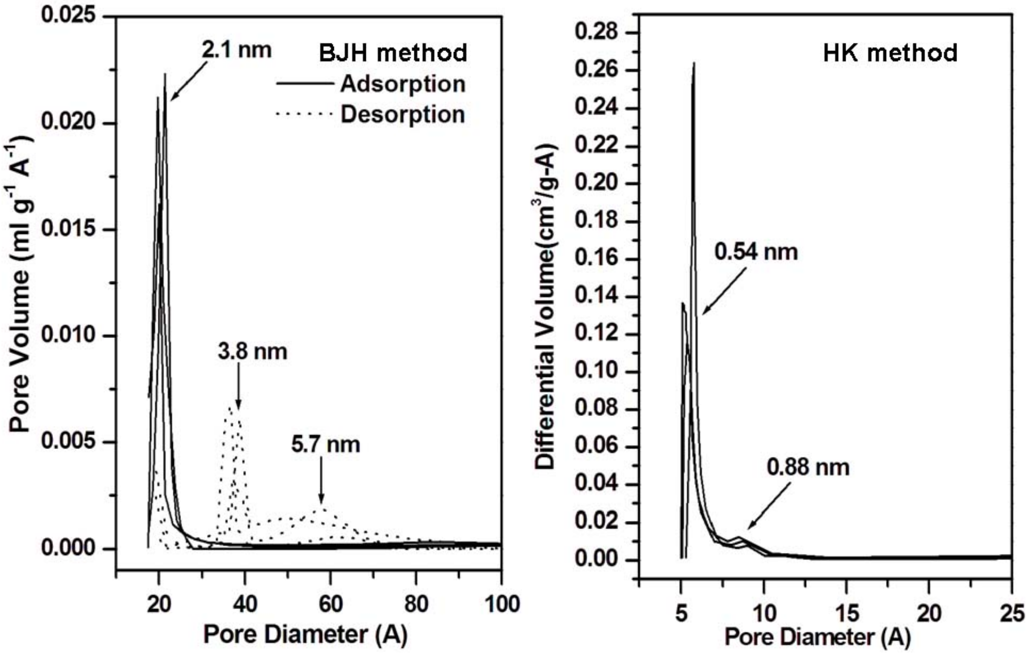

Figure 4.10 Pore size distributions of hybrid materials containing different heteroatoms synthesized using CTATos and TPA as co-template; BJH (left) and HK (right).

Figure 4.10 exhibited the BJH and HK pore size distribution of hybrid materials containing different heteroatom synthesized using C_{16}TATos as co-template. The most interesting thing was that, the BJH plot of pore size distribution showed a well-defined mesopores centered at 2.1 nm without correction, because the BJH method usually underestimated the mesoporous pore size. However, HK plot that was often used to evaluate the pore size distribution for microprous zeolites, did not exhibit this peak, implying that the steep adsorption did not correspond the pore filling. About the assignment of this adsorption centered at the relative pressure 0.1-0.25 is in debate [27-28]. As elucidated by Thommes, the hysteresis loop and associated steps at the relative pressure 0.1-0.25 reflected a phase transformation from a disorded (liquid-like) adsorbate state to a more ordered (solid-like) adsorbate state. Hence, these steps were not associated with any filling of empty pore space, which is consistent to our conclusion. What is the origin for this interesting phenomenon? It should be mentioned that this unusual nitrogen phase transformation was mainly attributed it to the crystal size, the incorporation of the different metal atoms and the ratio between Si and metal atom [27]. Based on current experimental results, unambiguously, the formation of higher restricted nitrogen phase or the more drastic molecular rearrangement of adsorbed nitrogen was resulted by the presence of defects which was confirmed by BJH plot and HK plot. This discovery confirmed that, for pore structure characterization, the complementary techniques are needed to give the definitive conclusion.

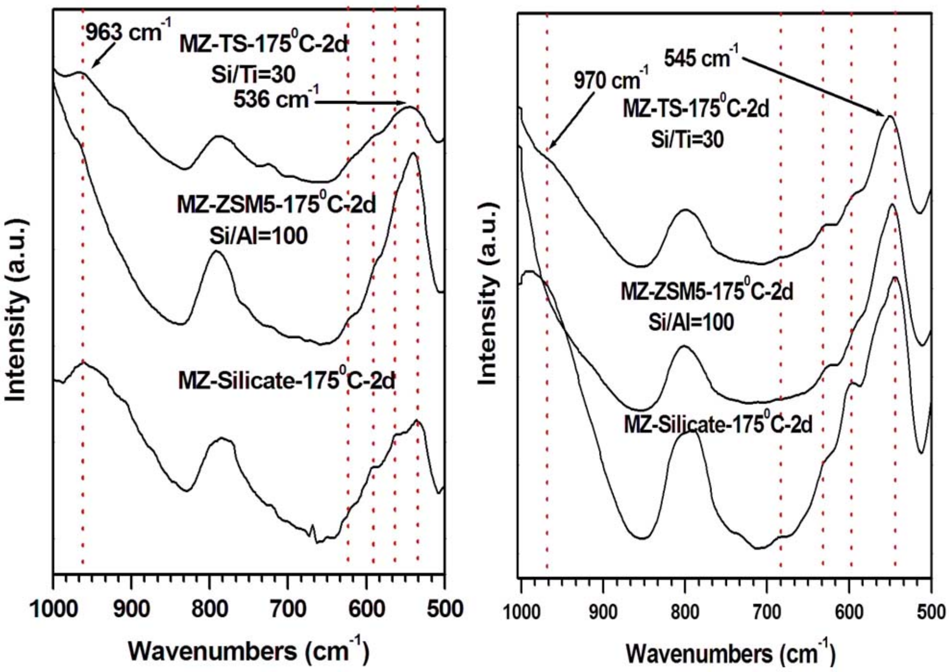

Figure 4.11 FTIR spectra of hybrid materials containing different heteroatoms synthesized using CTATos and TPA as co-template.

Figure 4.11 showed the FT IR spectrum of hybrid materials of both before and after calcinations. For sample MZ-TS-175-2, FT IR spectrum presented a band at about 960 cm^{-1} that was assigned to the asymmetrical stretching vibration of [SiO$_4$] units linked to Ti atoms, indicating tetrahedral coordinated Ti was incorporated into the pore framework [29-31]. A strong, prominent band at approximately 545 cm^{-1} in zeolite is characteristic of five-membered ring T-O-T structures [18]. Moreover, the appearance of the multibands in a range of 1000-400 cm^{-1} indicated the presence of the fragments of primary structure unit due to the semicrystalline nature of pore wall or incomplete crystallization of microporous zeolites in current system [16-18].

4.3.4 Synthesis of crystalline hybrid materials containing Ti atom involved by TPA

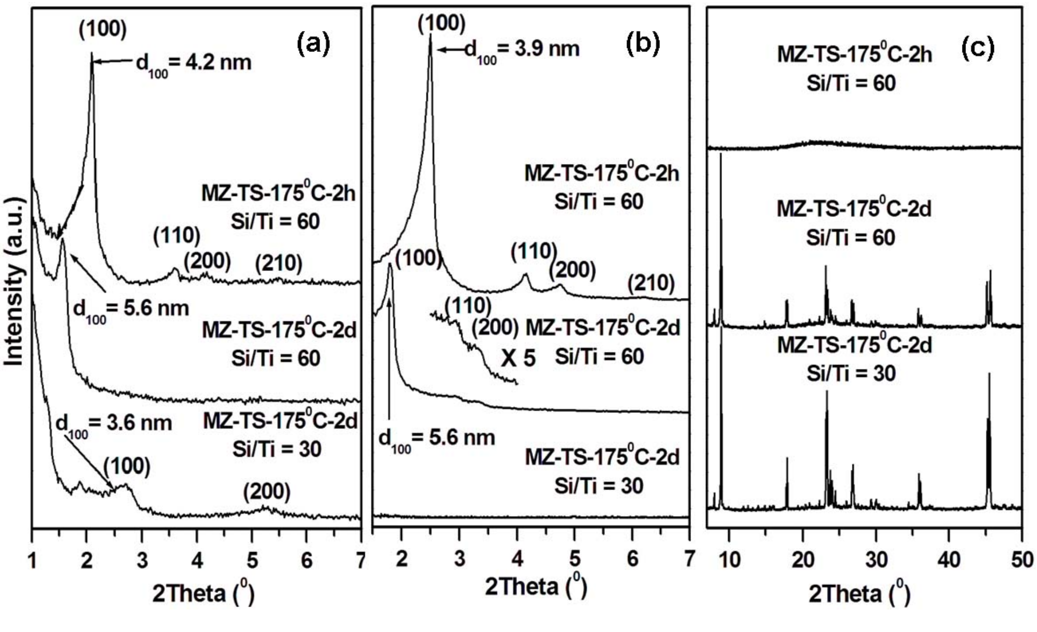

Figure 4.12 Low angle (a and b) and high angle (c) XRD patterns of hybrid materials containing Ti atom synthesized using CTATos and TPA as co-template: a) and c), fresh samples, b), calcined samples

To investigate the zeolite crystallization, several samples have been synthesized under current experiment conditions. The low angle XRD pattern of sample crystallized for 2h showed four resolved peaks of MCM-41 silica indexable as (100), (110), (210) and (210) reflections in a *p*6*m* space group, indicating well-ordered hexagonal MCM-41 (figure 4.12 (a) and (b)). When the crystallization lasted 2 days, sample exhibited three readily distinguished peaks and high d_{100} value up to 5.6 nm due to the pore expansion. However, if the molar ratio of Si/Ti decreased from 60 to 30, at the same crystallization conditions, the obtained solid exhibited lamellar phase, indicating that high Ti loading limited the formation of hexagonal phase [32]. To following the evolution of pore wall structure, wide-angle XRD patterns were also recorded after various crystallization times in figure 4.12 (c): at the initial stage, XRD patterns only showed one broad peak, indicating the mesoporous silica was completely amorphous, with no peaks related to the crystalline phase; after the crystallization for 2 days, the main reflections matched well with the typical pattern of the MFI topology, implying the formation of hybrid materials particles via solid-solid transformation mechniam. However, one can not definitively conclude that the mesoporous wall was composed of molecular ordering MFI zeolite, because numerous studies showed that, even the physical mixture of conventional microporous zeolite and MCM-41 silica gave similar XRD patterns in a full range [7-8].

It was important to note that the predominant b-oriented hybrid materials, was synthesized when the crystallization was extended for 2 days at 175°C in the presence of Ti atom, as shown in figure 4.12 (c). However, hybrid materials containing Al atom and free of metal atom synthesized using the same procedure, did not exhibited the prominent (0k0) lines (figure 4.6) in a wide-angle range, and low-angle XRD patterns did not show any reflections typical for mesoporous structure. This significant difference indicated the different crystal growth mechanism. To our knowledge, the synthesis of b-oriented MFI zeolites required the special conditions, such as, space limitation [21] or tailored structure directing agent [22-25]. In this study, the fact that the MCM-41 mesoporous structure was maintained even at high crystallization temperature for 2 days could be a result that these crystals were trapped in the confined space and were forced to grow in the direction of the available open space. Moreover, the competing adsorption between CTA^+ and TPA^+ molecules on silicate surface should affect the preferential growth of hybrid materials because of the stereo-hindrance of long hydrophobic tail of surfactant as a template for MCM-41 silica. The space-limited growth of hybrid materials involved by surfactant indicated that the synthesis of hybrid materials containing Ti atom was formed via the solid-solid transformation mechanism [26, 33-35], instead of a widely-accepted solution-mediated transformation [9, 11].

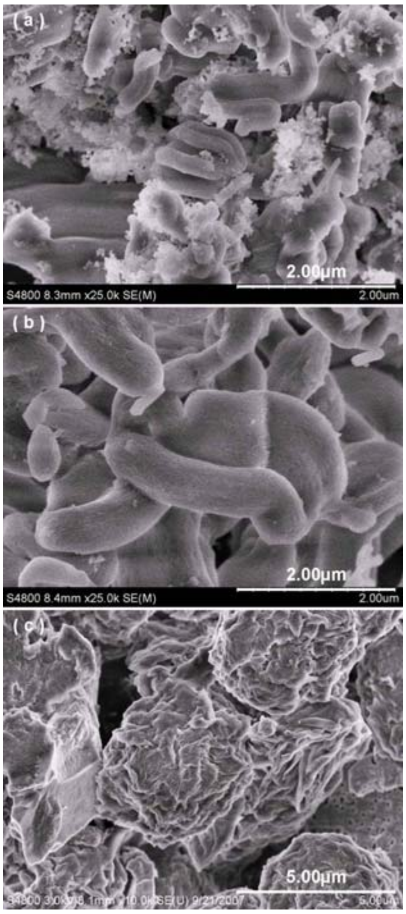

Figure 4.13 Morphology evolution observed using SEM by controlling different experimental conditions, (a) ZM-TS-175°C-2h, Si/Ti= 60; (b) ZM-TS-175°C-2d, Si/Ti= 60; (c) ZM-TS-175 °C -2d, Si/Ti= 30.

Varied the crystallization time, the current mesoporous zeoltes (figure 4.13) showed a distinct change in morphology from fiber-like particles typical for MCM-41 to globular particles with rugged surface, differing from the coffin-shaped morphology of conventional MFI structure zeolite [21-25]. The hybrid materials exhibited globular morphology with rugged surfaces, which could attribute to the faster molecular transport at the external surface.

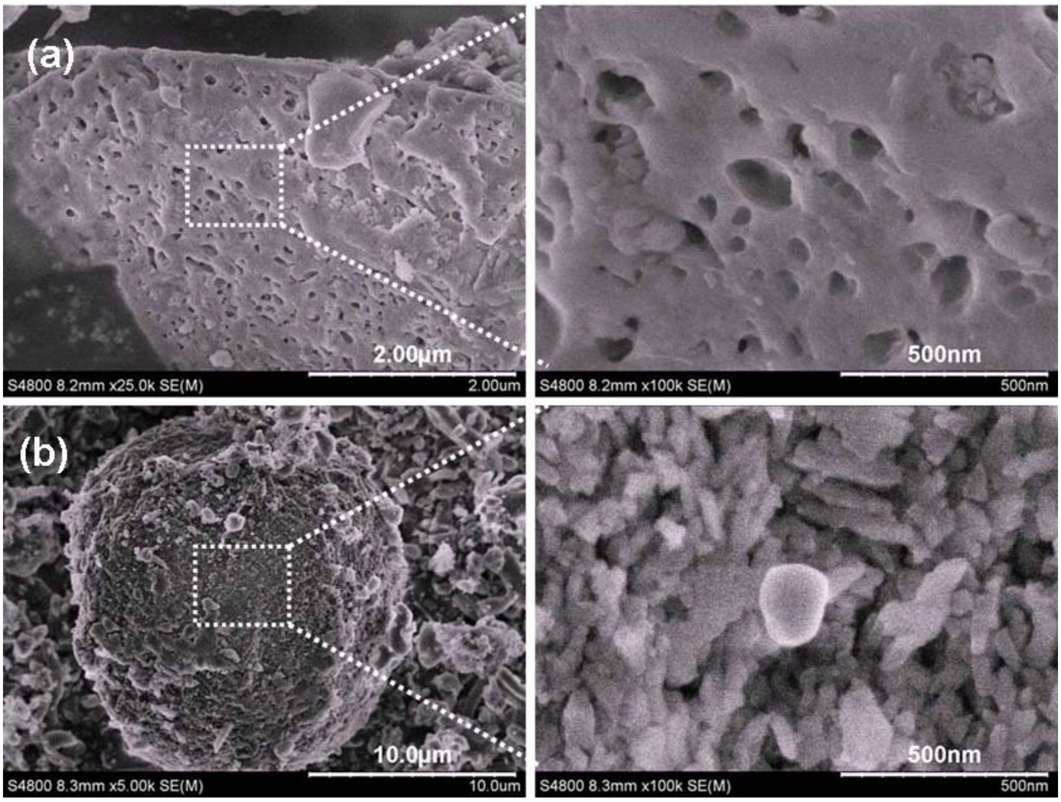

Figure 4.14 SEM images of calcined hybrid materials containing Ti atom synthesized using CTATos and TPA as co-template (Si/Ti=30): a) well facteded particle (rare phase), on the left, zoom of the region indicated by the dot lines, and b) particles of typically 15 μm, on the right, zoom of the region indicated by the dot lines.

To further prove the formation mechanism of hybrid materials containing Ti atom, a close SEM observation on samples with different crystalline degree was performed (figure 4.15). Firstly, the initial mesophase disappeared with crystallization time, leaving many craters (or 50-200 nm in diameter) on the surface of bulky amorphous MCM-41 silica in figure 4.14 (a). Secondly, the globular particles with rugged surface were built with randomly oriented fiber and spherical particles as showed in figure 4.15 (b). In addition, it should be importantly mentioned that the shape and size of spherical particles matched perfectly with that of surface craters as exhibited in figure 4.14 (a). All these results showed that mesoporous MFI zeolite crystallization, in the presence of Ti atom, followed a solid-solid transformations that allowed the amorphous MCM-41 silica to be reorganized into crystalline structure without being completely dissolved, quite similar to that proposed by Serrano et al. for the explanation of the synthesis of TS-1 and TS-2 conventional zeolit [26, 35]. It should be noted that, when aluminum was incorporated, SEM images (figure 4.8) showed the typical hexagon-shape zeolite crytals, implying that hybrid materials containing Al atom were formed though the solution-mediated crystallization mechanism, as suggested by Ryoo et al. [10]

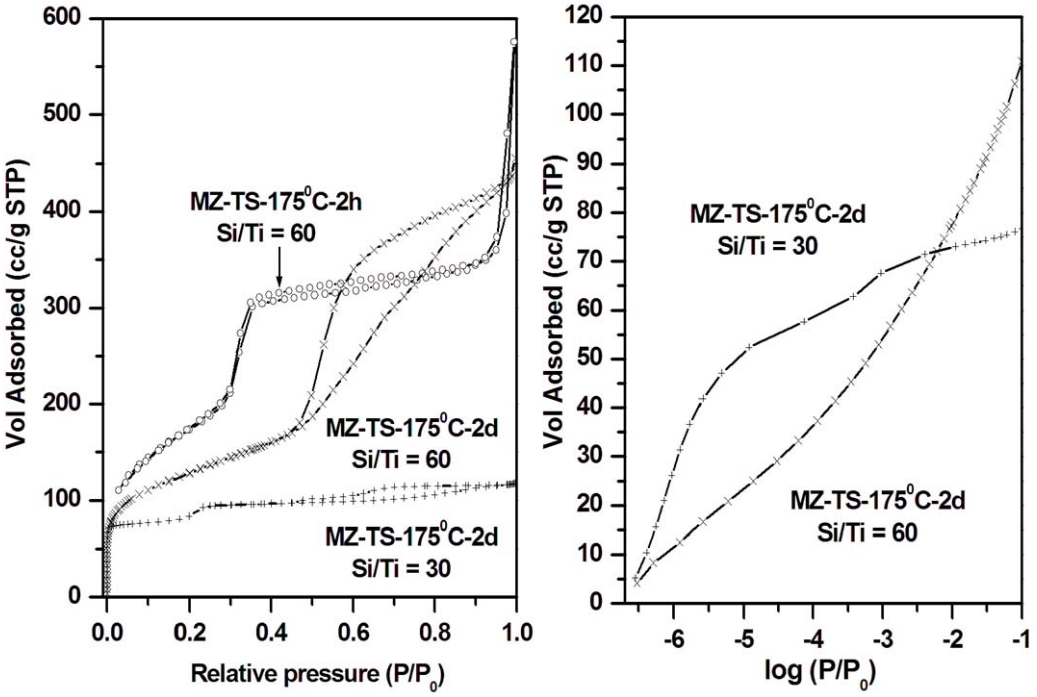

Figure 4.15 N_2 adsorption-desorption isotherms of calcined hybrid materials containing Ti atoms: (left) full isotherms, (right) low pressure range in logarithmic scale.

N_2 adsorption isotherms in figure 4.15 showed a gradual structure evolution after varied crystallization time. The initial phase exhibited a type IV isotherm with a narrow distribution of mesoporous diameter centered at 3.5 nm calculated using BDB mehod from desoprtion branch [22]. When further heating to 2 days, the mesopore diameter increased to 4.1 nm as expected, due to the pore expansion via postsynthesis treatment. This sample did not show the steep adsorption step in a very low relative presseure, indicating the obtained sample was uinformly mesoporous nature without physical mixed MFI structure zeolite. Whereas, when the Si/Ti decreased to 30, low pressure isotherms showed an obvious steep N_2 uptakes at $P/P_0 = 10^{-6}$. Moreover, the complexity of N_2 adsorption isotherm strongly implied the presence of hierarchical porosity associated with the presence of the defects or the packing voids due to the lateral fusion between two layers after calcinations [27, 28].

Table 4.2 Texture properties of hybrid materials using CTATos and TPA as co-template

Sample Name	Si/Al or Ti	Crystal. time	d_{100} (nm)	S_{BET} ($m^2 g^{-1}$)	V ($cm^3 g^{-1}$)	D_{BJH} (nm)	D_{BDB} (nm)	t_{BJH} (nm)	t_{BDB} (nm)
MZ-TS-1	60	2h	3.86	673	0.89	2.65	3.52	1.81	0.94
MZ-TS-2	60	2d	5.57	457	0.67	6.45	4.13	-	2.30
MZ-TS-3	30	2d	3.60	284	0.18	-	-	-	-
MZ-Silicate	∞	2d	-	337	0.19	-	-	-	-
MZ-ZSM5	100	2d	-	401	0.24	-	-	-	-

Note: t = a/(3)1/2 – D/2 is the mean pore wall thickness, and D is pore size calculated from BDB and BJH theoretical model, respectively

Further investigations based on the FT IR and DR UV-visble characterization shed the light on formation mechanism of current hybrid materials via the nonconventional solid-solid transformation. IR spectroscopy, an important tool for characterizing zeolite phases, was used to differentiate between the atomic-level in crystalline zeolite and the amorphous nature of mesoporous materials [16-18]. The appearance of a band at 550 cm^{-1} and 960 cm^{-1} characterized by the FT IR spectra after 2 hours of crystallization, typical of pentasil zeolites and commonly observed in Ti-containing zeolite, respectively, indicated the formation of crystalline products. The band at 550 cm^{-1} was absent in mesoporous materials synthesized at 175 ℃ for 2 hours, implying the lack of the atomic-level ordering in the silica framework. The more detailed examination on the IR bands over the range 500-1000 cm^{-1} showed multiple bands, 594, 630, 686 cm^{-1} in figure 16, which were attributed to various ordered silicate framework structure. The presence of additional bands at 570 and 781 cm^{-1}, especially for hybrid materials with Si/Ti molar ratio equal to 60, was due to the band shift dependence of five ring vibrations on the dimension of nanophase silicate as elucidated by other authors [18], indicating that the pore wall of hybrid materials was gradually transferred into MFI structure framework via solid-solid transformation mechanism as a function of crystallization time.

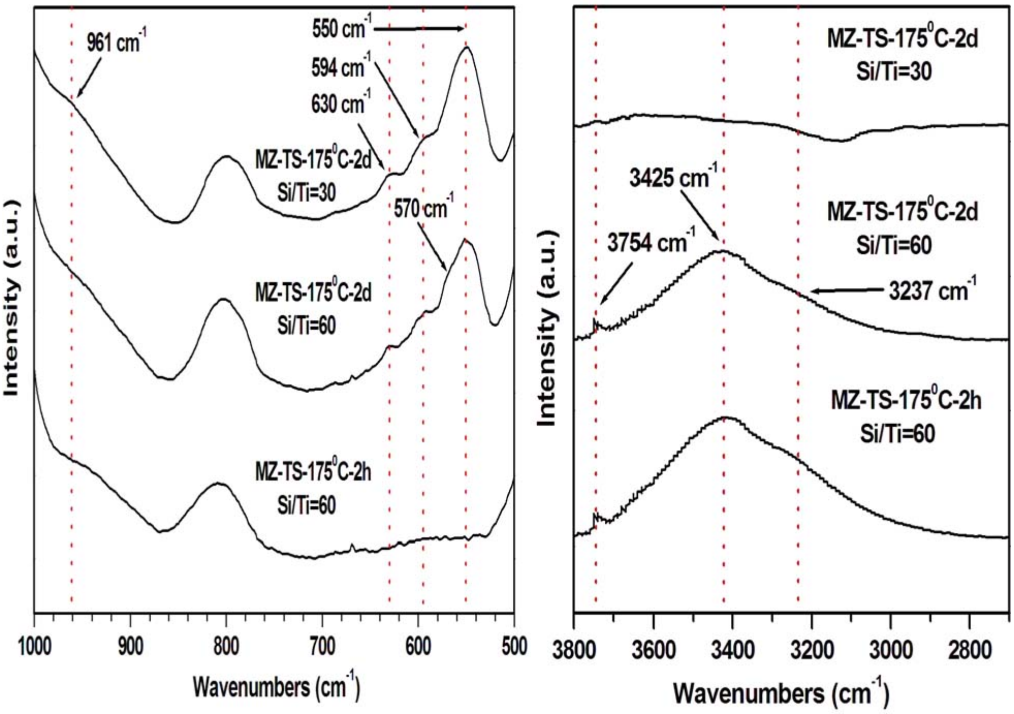

Figure 4.16 FTIR spectra of hybrid materials containing Ti atom synthesized using CTATos and TPA as co-template.

The most interesting was that, from the application viewpoint, if precisely controlled the Ti loading and crystallization time, UV-visble in figure 4.17 showed a narrow band centered around 220 nm with a shoulder at about 270 nm, for instance, sample MZ-TS-175^{0}C-2d with Si/Ti ratio equal to 60. These results indicated most of the Ti atoms were present in tetrahedral positions, while the signal around 270 nm observed by one of us [29-31], has been assigned to the presence of five-coordenated titanium atoms linked to four Si-O groups and an OH$^-$ group, the negative charge being compensated for by CTA$^+$ and TPA$^+$ cations as exhibited by thermalgravimetric analysis (figure 4.18), further confirming that, during the solid-solid transformation, surfactant was not expelled, thus the templating role was maintained.

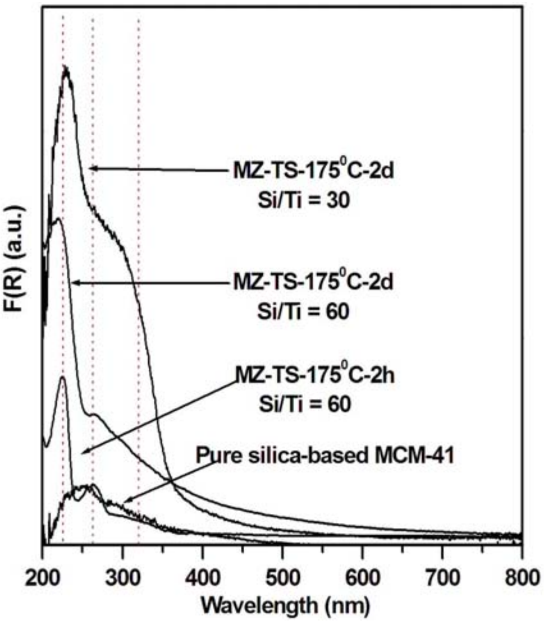

Figure 4.17 Diffuse reflectance UV spectra of as-made hybrid materials containing various loadings of Ti atom and autoclaved for 2 days or 2 hours; the noisy bottom line corresponds to pure silica based MCM-41 prepared without TPA.

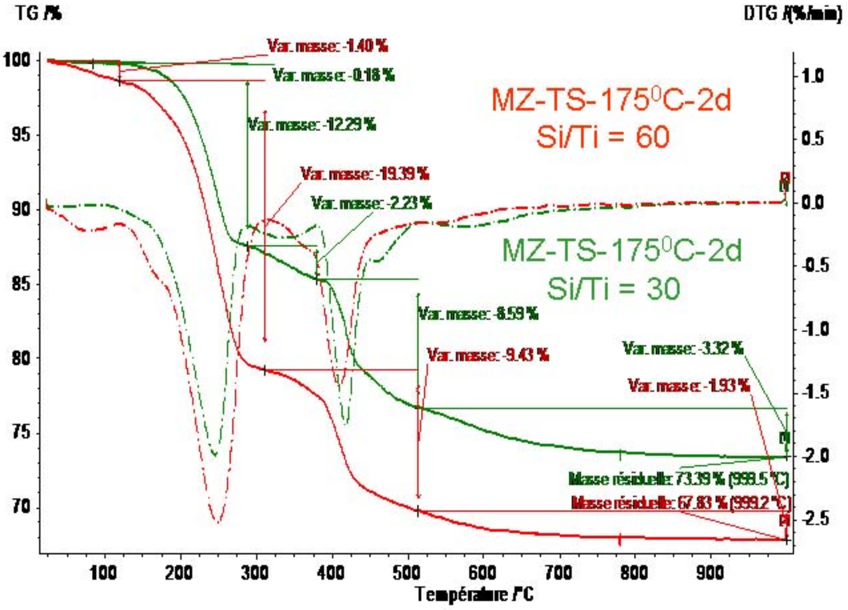

Figure 4.18 Thermogravimetric analysis curves of as-synthesized MZ-TS-175^{0}C-2dwith different Si/Ti molar ratio; full line for weight loss provided in percentage, broken lines for first derivative of weight loss:upper line for Si/Ti= 30, bottom line for Si/Ti= 60.

4.4 Conclusion and perspective

4.4.1 Conclusion

In summary, sufficient evidences exhibited that Ti-containing MFI zeolite with mesoporosity was synthesized through a non-conventional mechanism governed by solid-solid transformations. These results indicated that solid-solid transformations could occur even when starting from clear solutions, not limited to high dense systems as exhibited by Davis et al. The synthesis principle developed in this present work created a good starting point for rationalizing the phenomena during the genesis of micro- and mesoporous materials from starting amorphous gels, and bridged the gap between microporous and mesoporous materials by combining the best of both worlds. Furthermore, these b-oriented MFI zeolites with hierarchical porosity may find application as advanced materials in various fields, especially membrane reactors, membrane separation and photocatalysts etc.

4.4.2 Perspectives

(1) The role of Titanium during the solid-solid transformation should be further investigated.

(2) The current synthetic strategy is extended into other zeolite with different topology structure including BEA, MEL and LTA etc.

(3) The test on the chemical reactivity for organic reaction involved by bulky molecules in the presence of H_2O_2 is ongoing.

4.5 References

(1) Corma, A., *chem. Rev.* **1997**, *97*, 2773.

(2) Ozin, G. A., Kuperman, A.; Stein, A. *Angew. Chem. Int. Ed.* **1989**, *28*, 359.

(3) Vaudreuil, S.; Bosmina, M.; Kaliaguine, S.; Bonneviot, L. *Adv. Mater.* **2001**, *13*, 1310

(4) Beck, J. S.; Vartuli, J. C.; Roth, W. J.; Leonowicz, M. E.; Kresge,C. T.; Schmitt, K. D.; Chu, C. T. W.; Olson, D. H.; Sheppard, E. W.; McCullen, S. B.; Higgins, J. B.; Schlenker, J. L. *J. Am. Chem. Soc.* **1992**, *114*, 10834.

(5) On, D. T.; Kaliaguine, S. *Angew. Chem. Int. Ed.* **2001**, *40*, 3248; *Angew. Chem. Int. Ed.* **2001**, *113*, 3348.

(6) On,D. T.; Kaliaguine,S. *J. Am. Chem. Soc.* **2003**, *125*, 618; *J. Am. Chem. Soc* **2004**, *126*, 14324.

(7) Zhang, Z.; Han, Y.; Xiao, F.-S.; Zhao, D. *J. Am. Chem. Soc.* **2001**, *123*, 5014.

(8) Liu,Y.; Zhang, W. Z.; Pinnavaia, T. J. *J. Am. Chem. Soc.* **2000***,* *122*, 8791.

(9) Cundy, C. S.; Cox, P. A. *Chem. Rev.* **2003**, *103*, 663.

(10) Kirschhock, C.; Kremer, S.; Vermant, J.; Tendeloo, G.; Jacobs, P. A.; Martens, J. A. J. Chem. Eur. **2005**, *11*, 4306.

(11) Choi, M.; Cho, H. S.; Srivastava, R.; Venkatesan, C.; Choi, D. H.; Ryoo, R. *Nature Mater.* **2006,** *5*, 718.

(12) Wang, H.; Pinnavaia, T. J. *Angew. Chem. Int. Edn.* **2006,** *45*, 7603.

(13) Yang, P.; Zhao, D.; Margolese, D. I.; Chmleka, B. F.; Stucky. G. D. *Chem. Mater.* **1999**, *10*, 2813.

(14) Mokaya, R. *Chem. Commu.* **2001**, 1092.

(15) Galarneau, A.; Cambon, H.; Di Renzo, F.; Fajula, F. *Langmuir* **2001**, *17*, 8328.

(16) Christiansen,S. C.; Zhao, D. Y.; Janicke, M. T.; Landry, C. C.; Stucky, G. D.; Chmelka, B. F. *J. Am. Chem. Soc.* **2001**, *123*, 4519.

(17) Naik,vS. P.; Chiang, A. S. T.; Thompson, R. W.; Huang, F. C. *Chem. Mater.* **2003**, *15*, 787.

(18) Kirschhock, C. E. A.; Ravishankar, R.; Verspeurt, F.; Grobet, P. J.; Jacobs, P. A.; Martens, J. A. *J. Phys. Chem. B* **2002**, *106*, 3333.

(19) Corma, A.; Kan, Q.; Navarro, M. T.; Perez-Pariente, J.; Rey, F. *Chem. Mater.* **1997**, *9*, 2123.

(20) Huo, Q. S.; Margolese, D. I.; Stucky, G. D. *Chem. Mater.* **1996**, *8*, 1147.

(21) Li, S.; Yan, Y. *J. Am. Chem. Soc.* **2004***, 12*6, 4122; *J. Am. Chem. Soc.* **2004***, 126*, 10732.

(22) Yu, H.; Wang, X.; Long, Y. Micropor. Mesopor. Mater. 2006, *95*, 234

(23) Mabande,T. P.; Ghosh, S.; Lai, Z.; Schwieger W.; Tsapatsis, M. *Ind. Eng. Chem. Res.* **2005**, *44*, 9086

(24) Phiriyawirut, P.; Magaraphan, R.; Jamieson, A. M.; Wongkasemjit, S. *Micropor. Mesopor. Mater.* **2003**, *64*, 83

(25) Jelfs, K. E.; Slater, B.; Lewis, D. W.; Willock, D. J. *Stud. Surf. Sci. Catal.* 2**007,** *171*, 1685.

(26) Serrano, D. P.; Uguina, M. A.; Ovejero, G.; Van Grieken, R.; Camacho, M. *Microporous Mater.* **1996,** *7*, 309.

(27) Tao, Y. S.; Kanoh, H., Kaneko, K. *Adv. Mater.* **2005**, *17*, 2789.

(28) Yang, Z. X.; Xia, Y. D.; Mokaya, R. *Adv. Mater.* **2005**, *17*, 2791.

(29) On, D. T.; Lonic, L.; Bonneviot, L. *Chem. Commu.* **1996**, *3*, 299.

(30) On, D. T.; kliaguine, S.; Bonneviot, L. *J. Cata.* **1995**, *157*, 235.

(31) Lonic, L.; On, D. T.; Solomykina, S.; Echchahed, B.; beland, F.; Moulin, C. C.; Bonneviot, L. *Stud. Surf. Sci. Catal.* **1996,** *101*, 611

(32) Solberg, S. M.; Kumar, D.; Landry, C. *J. Phys. Chem. B* **2003**, *107*, 1853.

(33) Derouane, E. G. *Appl. Catal.* **1981**, *1*, 101.

(34) Tsapatsis, M.; Lovallo, M.; Davis, M. E. *Microporos Mater.* **1996**, *5*, 381.

(35) Uguina, M. A.; Serrano, D. P.; Ovejero, G.; Van Grieken, R.; Camacho, M. *Zeolites,* **1997,** *18*, 368.

Chapter 5 Design of the bio-inspired catalyst on a molecular scale using 'molecular stencil patterning' technique

5.1 Introduction

Homogenous catalysis is associated with well defined active sites and excellent control on selectivity. However, separation, recovery and reuse of homogeneous catalyst are difficult in comparison to heterogeneous catalyst. Nature shows us that prearrangement of some functions near the active site of metalloproteines favours selectivity and activity, even under mild reaction conditions.[1] In order to tune site activity and favor substrate access, mesoporous silica with tailored porosity described in chapter 3 can be used to mimic the metalloprotein skeleton of natural biological system (scheme 5.1).[2] Their internal surface can easily be functionalized by incorporation of organic groups by either grafting organosilanes on surface silanol[3] of the pre-formed structure, or by co-condensation of the organotrialcoxysilanes and silica precursors in the sol-gel synthesis [4].

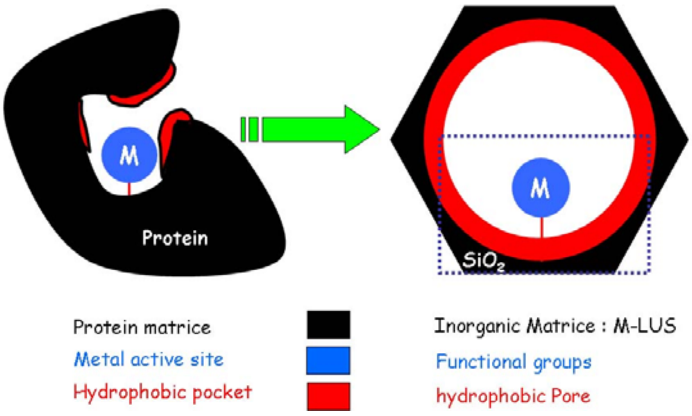

Scheme 5.1 bio-inspired anaology between enzyme and heterogeneous catalyst.

When multifictionalization is at stake, one has to deal not only with their own distribution but also with the relative vicinity of each function. Although molecular imprinting and voluminous function protected sequential synthetic strategy could achieve site-isolated functional groups on the silica surface with controlled distance,[5-11] these methods led to low loading and to inhomogeneous site distribution in the porous solid. One of us proposed a new strategy to synthesize bioinspired catalyst using novel technique of surface engineering called 'molecular stencil patterning'.[12-13] This is processed via sequential grafting, the principle of which is based on retention or partial displacement of the templating surfactant (scheme 5.2). In this method, TMS groups were used as isolated function to control the distance between the functional groups, and chloropropyldimethylsilyl (CPDMS) was the tethers for further derivatization towards functionalities of interest.

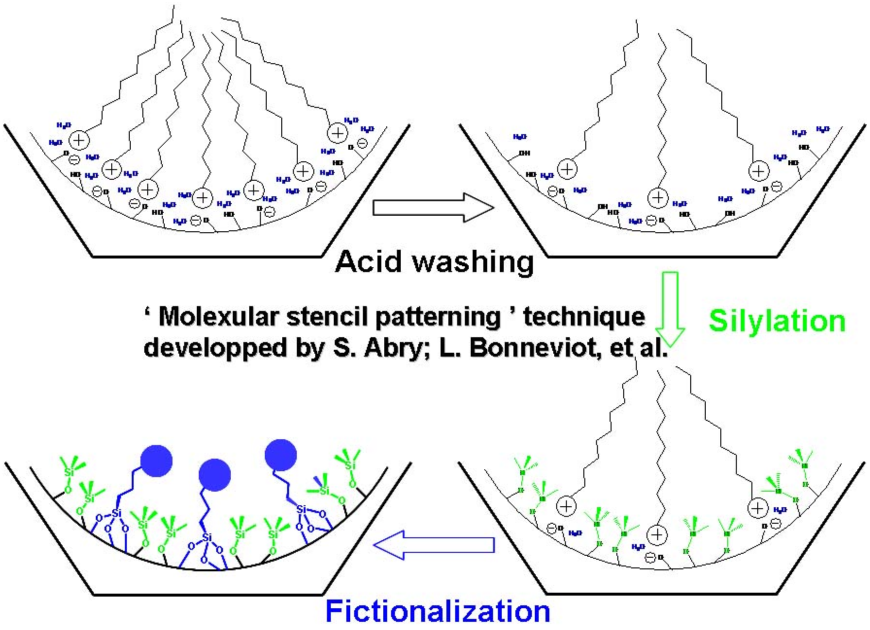

Scheme 5.2 Synthetic route based on the so-called 'molecular stencil patterning'

The surfactant plays here both roles: (i) patterning from coulombic repulsion and, (ii) stencil from surface protection-deprotection. Nevertheless, the fact is that, when more complex or sterically hindered functions were introduced in the first step of this approach, larger organic functions could be accumulated at the entrance of the mesopores, leading to the pore clogging. Another problem is the possibility of none-uniform distribution of CTA^+ due to the entanglement of the long hydrophobic chains. Further improvement for this technique is clearly useful.

As described in chapter 3, TMA^+ ions could replace all the surfactants in the mesopores, herein, TMA^+ ions were used as protecting groups. Compared to the CTA^+ ions, TMA^+ molecules have smaller size, which provides much more space for large molecule diffusion. Moreover, due to the strong electrostatic repulsion interaction, TMA^+ ions should also self-organize homogeneously onto the channel surface. The key step is the complete TMA exchange for CTA^+ ions before starting the sequential grafting reactions. Current improved synthetic strategy is as follows: first, the siloxane (monopod $[(CH_3)_3Si]_2N$ and bipod $[(CH_3)_2Si(CH_2)Si(CH_3)_2]_2N$) used as isolation hydrophobic groups is grafted on the channel surface after TMA^+ partial removal, then the protecting TMA^+ ions are removed. To probe the isolation of the function grafted in second place, AAPTMS ((3-aminoethyl)-amino-propyltrimethoxysilane) is chosen owing to its complexation properties. Cu^{2+} ions knwn to form the stable 1:1 and 2:1 complexes with AAPTMS on amorphous silica is used to reveal local molecular arrangment.[14] The proposed improvement 'molecular stencil patterning' technique in based on the substitution of CTA by TMA protecting group and the used of a bipodal siloxane as diluting function.

UV-visble, EPR (electronic paramagnetic resonance), FT-IR and elemental analysis suggests that active species are possibly binuclear Cu complexes with only a single hydroxo bridge, similar to that of EPR detectable dimer [Cu (Ⅱ)···Cu (Ⅱ)] analogues in biological system.[15, 16] Moreover, it is proposed that intermediate enviroment between types $(4NO)_{xy}$ and $(2NO)_{xy}$ around copper are more likely than the expected $(4N)_{xy}$ type due to partial protonation of the ethylene diamine moieties even in the presence of Cu^{2+} ions. A dynamic equilibrium between different coordination types of copper is taking place depending both on the Cu counterions (Cl^- and ClO_4^-) and on the surface morphology of mesoporous silica. This current synthetic strategy will allow us to develop metallic sites with a spectral characteristics that ressembles that of ‘enzyme metal center’ and that should hopefully ‘biomimic’ its activity.

5.2 Experimental section

5.2.1 Synthesis

5.2.1.1 Synthesis of MCM-41 silica

LUS-1 and L-LUS were synthesized using the recipe described in chapter 4. Pore diameters are 3.7 and 4.5 nm, respectively. To distinguish these two samples, for the larger pores sample, the name of sample was started with the big letter ‘L’.

5.2.1.2 Synthesis of LUS-TMA silica

Ion exchange of LUS containing surfactants was performed in a 100 mL two neck bottom-round flask in the following way:1.0 g as-made LUS-1 was taken, then 0.67g TMABr (3 equi. To surfactant) in 40 ml 95% technical ethanol was added, the mixture was stirred for 15min at 313 K, and then filtrated and washed two times using ethanol and acetone, respectively. The obtained solid was dried at 353 K over night. This process was repeated 3 times. The sample was name LUS-TMA.

5.2.1.3 Controlled removal of TMA^+/ or CTA^+ ions by acid washing

40 ml of ethanol solution containing desired amount of 1.0 M HCl and 1.0 g as-made LUS with CTA^+ or LUS exchanged by TMA^+ ions were mixed at room temperature, then stirred at 313 K for 1 hour, and solid obtained was washed and filtrated with ethanol and acetone for 3 times, respectively. Finally, sample was dried in the oven at 353 K overnight.

5.2.1.4 Controlled trimethylsilylation using the monopod-TMS or bipod-TMS

The LUS-TMA (or CTA) sample partially covered by TMA or CTA (1.0 g) was dried at 403 K under vacuum for 5 h. After cooled to RT and under argon, dry cyclohexane (40 ml) and HMDSA (10 ml, 4.6×10^{-2} mol) were added to the solid under argon atmosphere. The mixture was stirred 1 h at room temperature and then refluxed for 16 h at 353 K. The partially silylated solid, LUS-TMA (or CTA)-Sn, was finally washed with cyclohexane, acetone and ethanol for 3 times, and dried in the oven under air at 353 K overnight. In the name of sample, Sn means the silylation degree, and subscript n, i.e. 1, 2 and 3 correspond the 25%, 50% and 75% coverage of TMS. For instance, in ideal case, if 50% TMA^+ or CTA^+ ions as protecting molecules was removed by acid washing, the produced space should be covered by TMS groups.

5.2.1.5 Ethylenediaminepropyl (AAP) functionalization

Partially silylated LUS-TMA-Sn sample (1.0 g) was first washed using slightly excessive HCl (1.1 equiv) ethanol solution, the recovered sample after washing was dried at 353K overnight. Then the obtained sample was activated under vacuum at 403 K for 5 h. After cooled to RT and saturated by argon, dry toluene (40 ml) and AAPTMS (9 ml, 4.2×10^{-2} mol) were added to the solid under argon atmosphere. The mixture was stirred 1 h at room temperature and then refluxed for 16 h at 383 K. The obtained sample was finally washed toluene, acetone and ethanol for 3 times, and dried in the oven under air at 353 K overnight. To fill the void after the incorporation of AAP function, the above synthesized sample was silylated again using HMDSA as capping agent. The final sample was named LUS-Sn-AAP. The similar synthetic method was performed to synthesize the LUS-Sn-MPTMS (mercaptopropyltrimethoxysilane) and the LUS-Sn-APTMS (aminopropyltrimethoxysilane). It should be mentioned that the challenge here is to maintain as much as possible the TMS groups when introducing the AAP moieties. Thus, the control of reaction conditions was really important.

5.2.1.6 Cu complexation

1.0 g solid was activated under vacuum at 403 K for 5 h. After cooled to RT under Ar flowing atmosphere, an excess amount of $CuCl_2$ in anhydrous ethanol (0.05 M 15.0 ml, pH=2~3) or $Cu(ClO_4)_2$ in THF solution was added into 50 ml round bottom flask, and stirred at RT for 15 min. Note that the concentration of Cu^{2+} and $Cu(OH)^+$ are equal at a pH equal to the pKa of 7.3. The solid obtained was washed and filtrated with ethanol or THF solution for 3 times corresponding different copper counterion, respectively, and the filtrate was light green. Finally the solid was dried at 313 K for 3 days.

5.2.2 Characterization

5.2.2.1 ***UV-visible*** *spectrum* was recorded at room temperature in a range of 200-850 nm on a Beckman 5240 UV-visible spectrophotometer. Cu^{2+} and AAPTMS were mixed in 1:1 and 2:1 molar ratio using ethanol as solvent, then obtained solution was measured.

5.2.2.2 EPR spectra were collected on a Bruker series spectrometer, working at 9.4 GHz (X band) with 100-kHz field modulation and supplied with a variable-temperature accessory in the range 293-77K. The components of the g tensor have been measured with respect to a DPPH sample (g=2.0037).

5.3 Result and discussion

5.3.1 TMA⁺ ion exchange

In our early developed ‘molecular stencil patterning’ strategy, the surfactant plays two functions: (ⅰ) patterning from coulombic repulsion and, (ⅱ) stencil from surface protection-deprotection [13]. More recently, we found that, due to diffusion limitation, in the presence of voluminous surfactant as protecting molecules, the succedent grafting often caused the aggregation of organic functions (even smaller trimethylsilane groups) near the pore entrance. Therefore, the rational assembly of different organic functions keeps the pipe dream. This drawback greatly limited the wide use of this thechnique to synthesize multifunctional catalysts.

In the chapter 3, we have shown that it was possible to replace all the surfactants with TMA$^+$ molecule. Herein, we carefully studied this possibility and the influence of exchange times on pore structure, because the small TMA$^+$ ion can be also used the protecting molecule like surfactant. The difference between CTA$^+$ and TMA$^+$ molecule shown in scheme 5.3 and scheme 5.4 is that TMA molecules has small size, thus the bulky functional molecules could be easily diffusoned in the pore channel .

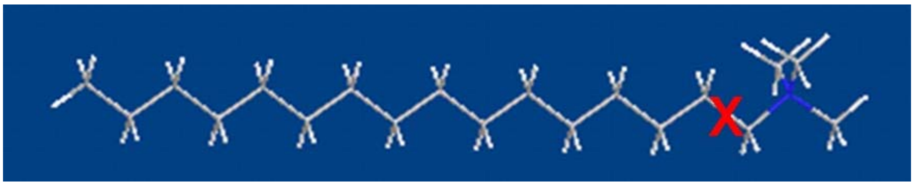

Scheme 5.3 Cetyltrimethylammonium ion (CTA+) with a longer tail used as template reagent in [S$^+$I$^-$] type synthetic pathway of MCM-41 silica.

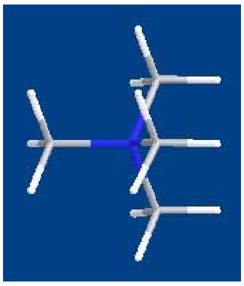

Scheme 5.4 Tetramethylammonium ion (TMA+) without longer carbon chain used as exchange molecule.

Figure 5.1 showed the FT IR spectra of sample continuously exchanged by TMA ions. After 2 times exchange, the adsorption band centered at 2958 and

2870 cm^{-1}, corresponding to the CH_3 and CH_2 stretching in long hydrocarbon chains of the surfactant (CTA^+) disappeared, which implies the complete removal of surfactant. Concomitantly, the four new adsorption bands positioned at 3040, 1490, 1400 and 950 cm^{-1}, assigned to CH_3 stretching, CH_3 bending, CH_3 stretching and C-N stretching of TMA^+ molecule, respectively, can be easily distinguished. A close examination was exhibited that the relative intensity of 1490 cm^{-1} peak began decreasing after 4 times exchange, indicating the lost of TMA^+ ion because of the replacement of proton ions in solution. It should be mentioned that all the samples was normalized according to the adsorption intensity of peaks at about 460 cm^{-1}. Thus three times exchange was thought best.

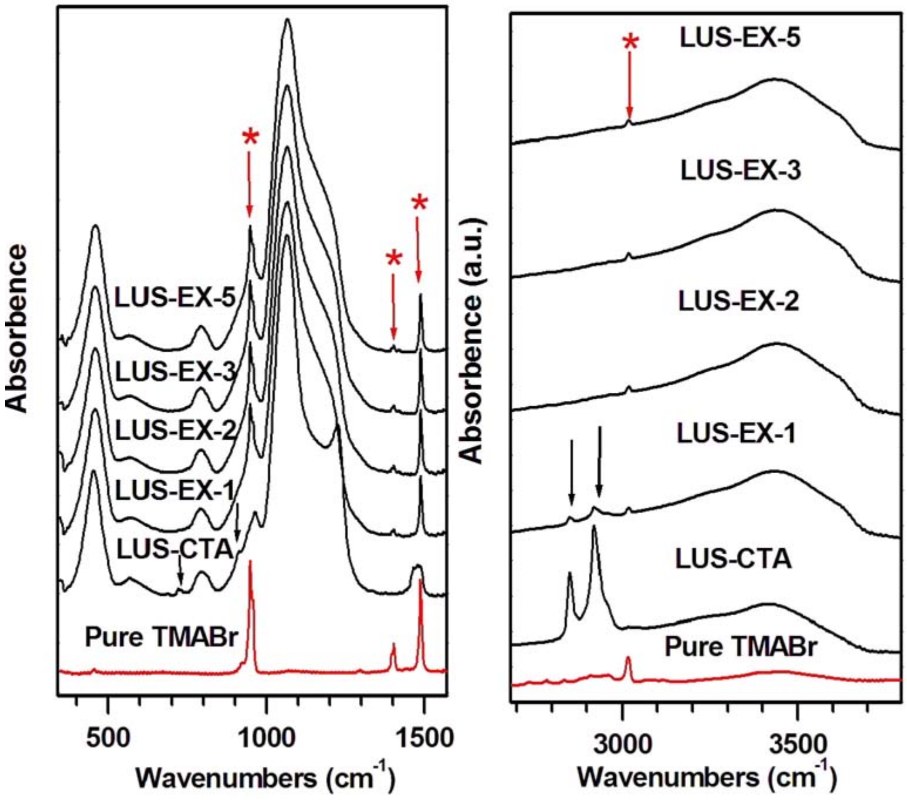

Figure 5.1 FT IR spectra of LUS-1 sample exchanged by TMA^+ cations, EX stands for abrevation of ‘exchange and the last number for the number of exchange operations.

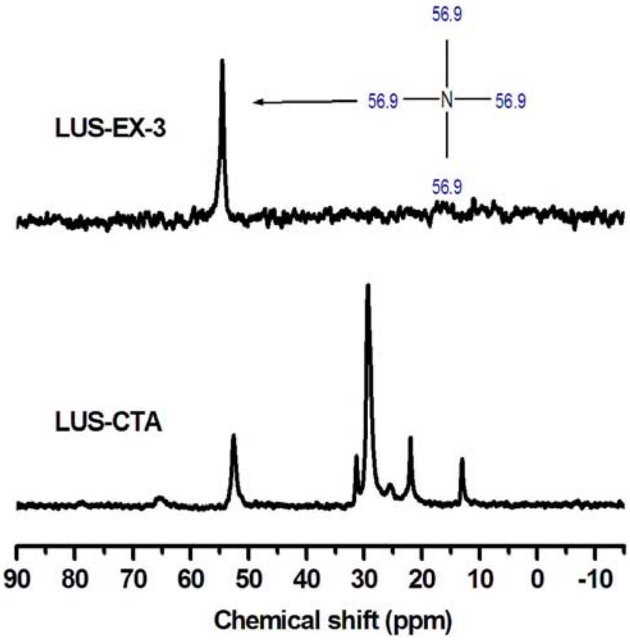

Figure 5.2 ^{13}C CPMAS spectra of LUS-1 samples exchanged 3 times by TMA$^+$ cations.

^{13}C CPMAS spectrum (figure 5.2) only showed one chemical species centered at around 57 ppm after three times exchange run, this result was well consistent with that of IR, meaning complete replacement of CTA molecule by small TMA molecules. Thermalgravimetric analysis also supported the above observation (Figure 5.3, left): after 3 times exchange, the weight loss in a range of 423-723 K which corresponded to the decomposition of organics in the mesopores almost remained constant. To further evidence our result, elemental analysis was performed, and the result was summarized in table 5.1.

Table 5.1 Elemental analysis of LUS-1 and LUS-EX-3

Sample	C	H	N	S	SiO_2	C/N	N/Si
LUS-1	33.0%	6.7%	1.9%	0.35%	51.5%	20.00 (19.0)	0.16
TMA@LUS	8.62%	3.2%	2.3%		70.9%	4.37 (4.0)	0.14

The elemental analysis showed that C/N molar ration (4.37) was slight larger than that of TMA$^+$ molecule, indicating the presence of other organic residue, such as ethanol from solvent, organic counterion from template and CTA^+ molecule. It should be mentioned that the molar ratio of N/Si decreased after ion exchange process. This further confirmed the formation mechanism of mesoporous silica by $[S^+nX^-(1-n)I^-]$ reported early by our group [17, 18], the counterion of surfactant was involved this mechanism. About 15% CTA^+ was interacted with silanol groups (SiOH) via surfactant counterions, such as Br^- and Cl^-, instead of silanote (SiO^-). Thus the current value of N/Si (0.14) less than 0.16 is reasonable.

The XRD patterns in figure 5.3 (right) exhibited four 4 feature peaks of mesoporous silica, indicating the high ordering of mesoporous structure. It should be mentioned that technical ethanol (95%) was best solvent for ion exchange process. If using water as solvent, the pore structure was partially collapsed. Similar result was reported by Martins et al [19].

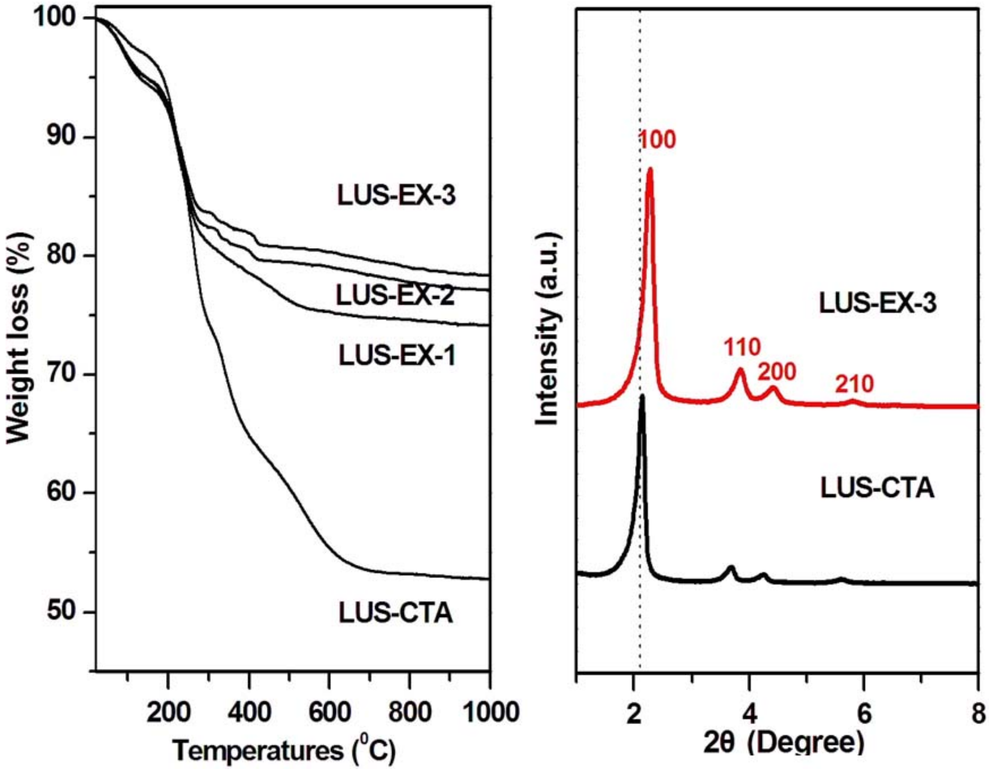

Figure 5.3 TG analysis (left) and XRD patterns (right) of LUS-1 sample exchanged by TMA^+ cations, EX stands for abrevation of ‘exchange and the last number for the number of exchange operations.

In summary, the quantitative replacement of CTA^+ by TMA^+ ions in the mesoporous pore is possible through the careful control of reaction conditions, and the structure ordering of mesoporous silica was maintained after 3 time recycle exchange. The complete replacement of CTA molecules by TMA molecules and maintance of pore structure are requisite for the sequential grafting involved by organic silane and functional groups, herein trimethylsilane (TMS as isolated functions) and (3-aminoethyl)-amino-propyltrimethoxysilane (AAPTMS as probe molecules).

5.3.2 Controlled trimethylsilylation using the monopod-TMS

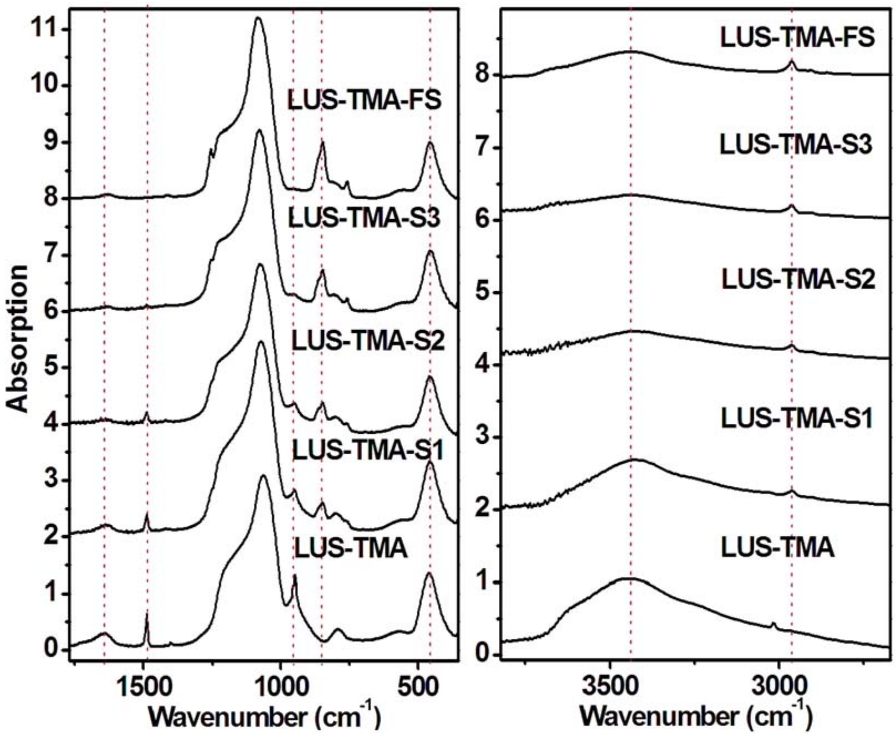

Figure 5.4 FT IR spectra of LUS-1 samples using TMA^+ (cetyltrimethylammonium) as a patterning molecule via the controlled silylation (in Sn, n stands for the percentage of total TMA^+ molecules removel by 1.0 M HCl in ethanol

Previous result showed that FT IR was a good quantitative method to investigate the relative concentration of special organic. Controlled silylation was performed on the series of LUS-TMA-Sn sample. In figure 5.4, IR spectrum showed the typical adsorption bands of Si-CH_3 stretching centered at about 850 cm^{-1}, indicating the incorporation of TMS groups. Moreover, the significant decrease of adsorption bands centered at 1600 cm^{-1} and 3400 cm^{-1}, assigned to OH stretching and bending of H-bond water, respectively, indicated that TMS can tune the surface hydrophobicity of mesoporous silica. As shown in figure 5.5, with HCl/TMA^+ ratio increasing, the concentration of TMA^+ ions linearly decreased, while the relative intensity of TMS groups step increased, implying that the formed silanol groups (Si-OH) after acid washing was not fully silylated.

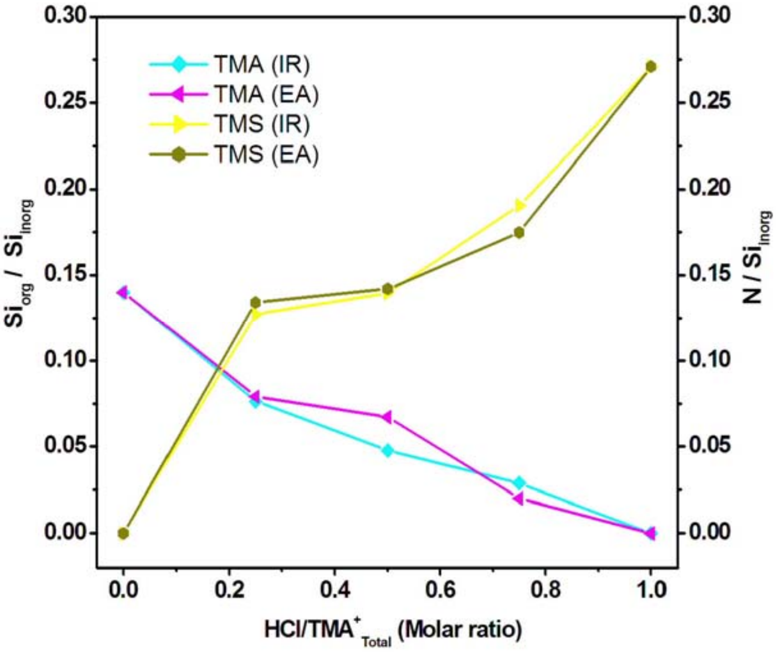

Figure 5.5 Variarion of TMS and TMA concentrations versus the HCl/TMA molar ratio, IR and EA indicate that data were derived from IR spectroscopy and elemental analysis, respectively.

To understand the step increase of TMS coverage, surface coverage of each function has to be taken into account. As already mentioned in chapter 3, TMS covers 0.43 nm^2 with the diameter of 0.70 nm. However, the size of tetramethylammonium (TMA) is about 0.67 nm with a surface coverage of 0.39 nm^2 calculated from Cerius molecular modeling (version 3.5) [13]. In an ideal distribution, assuming a 2D hexagonal compact coverage (scheme 5.5), the site isolation can be foreseen within the 2D hexagonal compact coverage when the TMS/TMA$^+$ molecular ratio is 2/1, i.e. 67% and 33% molecular coverage for each function, respectively. Thus, although the TMA can be controlled removed as a function of HCl concentration, due to the size difference of TMA and TMS molecules, TMS coverage showed the expected step increase, indicating the homogeneous distribution of TMA$^+$ molecules ruled by electrostatic repulsion after controlled acid washing. This technique seemed to be applied to synthesize the multifunctional catalyst with isolated active sites.

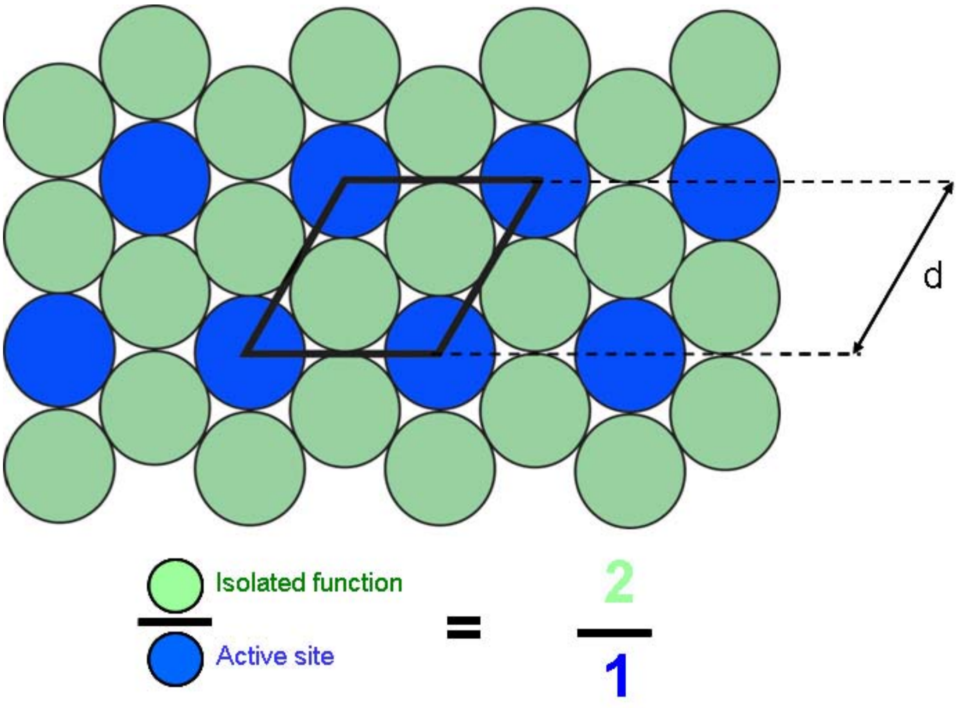

Scheme 5.5 Function isolation in the 2D hexagonal compact layer of functions (one isolated by the other).

In conclusion, patterning has been obtained by trimethylsilylation in presence of the TMA$^+$ molecule whose retention is a key point for the improved 'molecular stencil patterning' technique. In next section, to further prove the feasibility of this technique, site isolation of the second function (AAPTMS) by the first grafted function (TMS) will be elucidated.

5.3.3 Ethylenediaminepropyl (AAP) functionalization and copper complexation

The main objective was to better characterize the distribution of grated units on the surface of the mesoporous silica, depending on the coverage of TMS groups. This is why AAPTMS was chosen, for its ability to form stable 1:1 and 2:1 complexe with Cu^{2+} ions, which could follow the local distribution information of alkoxysilane entities by UV-visible and EPR spectrum [14]. For comparison, $[Cu(AAPTMS)]^{2+}$ and $[Cu(AAPTMS)_2]^{2+}$ complexe solution were prepared.

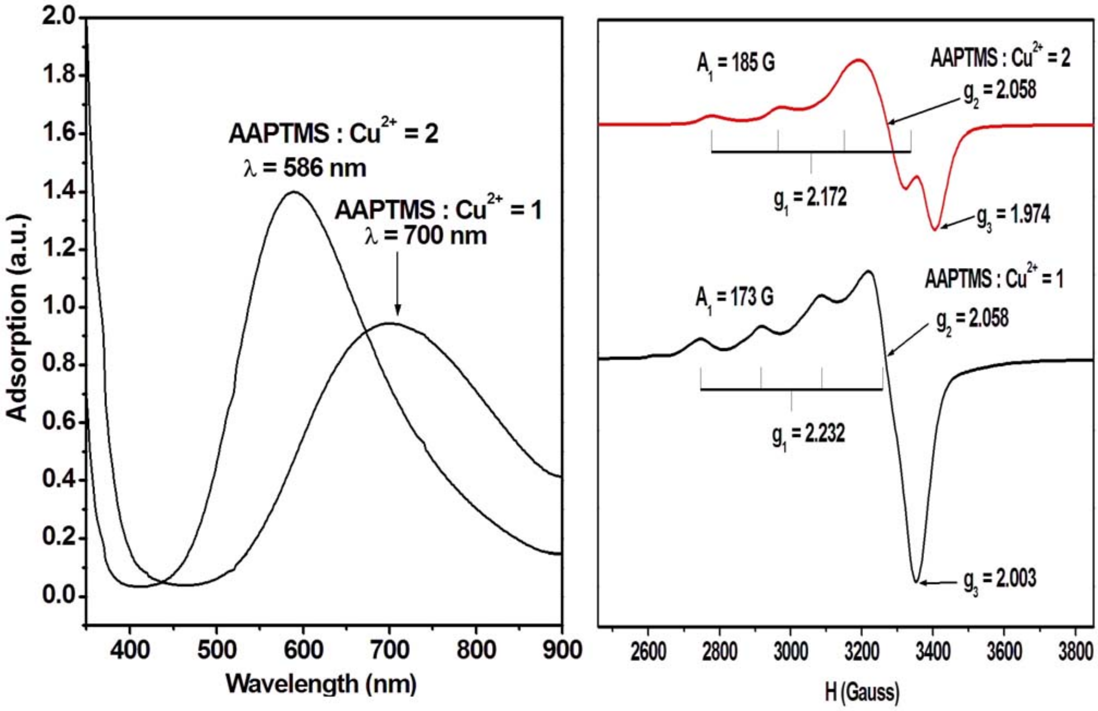

Figure 5.6 UV-visible (left) and EPR (right) spectra of probe molecules AAPTMS-Cu.

Two molecular complexes in ethanol showed their feature characteristic detected by UV-visble and EPR spectrum in figure 5.6. UV-visible spectrum identified two maximum absorption wavelength 586 and 700 nm, corresponding very stable 2:1 and 1:1 complexe in agreement with published values [14, 20], respectively. The EPR spectrum of these two complexes exhibited orthrombic signals in ethanol solution at room temperature. The signal ($g_{//}$ = 2.172 and $A_{//}$=185G) was attributed to the 2:1 complexe, which is consistent to CuN_4 coordination environment. For 1:1 complexe, the signal ($g_{//}$ = 2.232 and $A_{//}$=173G) is assigned to the CuN_3 coordination environment. Unexpectedly, 1:1 complexe in our case exhibited exhibited CuN_3 coordination enviroment, generally in the form of CuN_2, implying only one amino atom of ethylenediamine groups coordinate to Cu.

A point of interest herein is that even simple bidentate ligand ethenediamine can form copper complexes coordinated by polydentate ligand, for instance, N-methyl-N-((6-pivaloyamide)methyl)-N-(2-pyridylethyl)amine(mpppa). When the fumed silica is at stake as support, two Cu species functionalized by organsilane AAPTMS are detected with different EPR siganals, $g_{//}$ =2.27 ($A_{//}$ =181X10^{-4} cm^{-1}) and $g_{//}$ =2.19 ($A_{//}$ =197X10^{-4} cm^{-1}), corresponding to CuN_4 and CuN_2 coordination environment, respectively[14, 20]. These values are in contrast to ours and out of the scope of Peisach and Blumberg type of diagram. According to an up-to-date Peisach and Blumberg type of diagram based on well defined coordination compounds, the EPR parameters of current two species just lie to the range of CuN_4 domains with $A_{//}$ ~190-210 X 10^{-4} cm^{-1} and $g_{//}$ ~2.20-2.16 and CuN_3 domains with $A_{//}$ ~160-190 X 10^{-4} cm^{-1} and $g_{//}$ ~2.21-2.25. The difference of EPR parameters with results reported by litteratures[14, 20] indicates the effect of support on the Cu coordination environment. The details will be discussed in the next part.

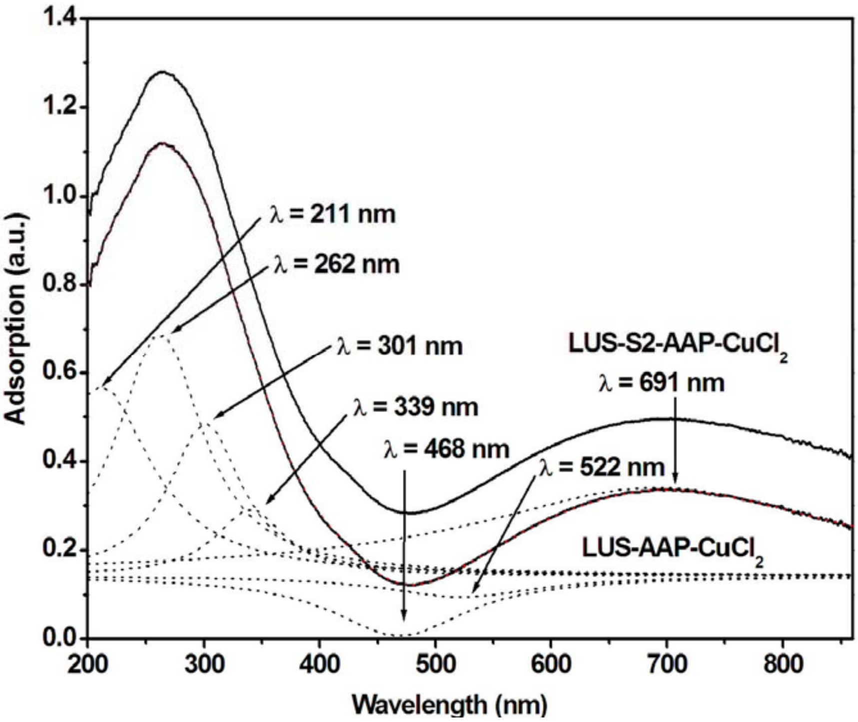

Figure 5.7 UV-vis spectra of LUS-Sn-AAP-CuCl$_2$ series, dot lines are obtained by Lorentzian multipeak fitting.

Table 5.2 Elemental analysis of LUS-1 after Cu incorporation

Sample	C/%	H/%	N/%	Cu/%	N/Cu	C/N
LUS-TMA-S2-AAP	6.23	2.27	1.98	2.48	**3.65**	3.67
LUS-TMA-S1-AAP	8.27	2.91	2.61	3.18	**3.75**	3.70
LUS-CTA-S2-AAP	7.07	2.97	2.28	2.92	**3.57**	3.62
LUS-CTA-S1-AAP	7.71	3.54	2.86	3.50	**3.74**	3.15
LUS-CTA-AAP	7.94	3.39	3.41	5.46	**2.86**	2.72

Then, we systematically study the effect of silylation degree on the site solation trying to achieve a molecular control on both neighbouring and distance. To our surprises, UV-visble spectrum (figure 5.7) of LUS-TMA-Sn-AAP-CuCl$_2$ showed similar adsorption bands independent on the silylation degree. Moreover, the intensity of EPR signal gradually decreased in figure 8, indicating the strong antiferromagnetic coupling (i.e. spin paring) between the two S=1/2 Cu^{2+} ions which is possibly due to their covalent overlap with a bridging ligand [15, 16]. Although elemental analysis (table 5.2) showed CuN_4 coordination enviroment, EPR signal ($g_{//}$ =2.269, $A_{//}$ =162X10^{-4} cm^{-1}) exhibited CuN_2 coordination environment according to Peisach and Blumberg type of diagram, indicating that not all the N atoms in ethylenediamine ligand involved the coordination. As is well konwn that metal aqua ions can act as Bronsted acids, which measns that they can act as proton donors.

In the species distribution digram for Cu(II) in aqueous solutions, the concentations of Cu^{2+} and $Cu(OH)^+$ are equal at a pH equal to the pK_a of 7.3. Note that current Cu^{2+} in ethanol (or THF) solution showed a fairly acidic solution of pH value of about 3. Thus, if the ethylenediaminepropyl (AAP) groups with the weak basicity are present, protonation of amino groups will happen, which lead to the loss of coordination capacity of nitrogen atoms. This answered that the N coordination number was about 4, instead of 2 form EPR characterizations, and also was responsible for CuN_3 coordination environment of the $[Cu(AAPTMS)]^{2+}$ complexes in ethanol solution.

The UV-vis spectrum of this series of samples after Lorentz multipeaks fitting exhibits five adsorption bands: 301 nm, 339nm, 468 nm, 522 nm and 691 nm, indicating the presence of activated oxygen species. Similar UV-vis spectrum was observed by Stark and coworkers for the $[(^{Me,\ Me}cd)_3\text{-}Cu_3(\mu_3\text{-}O)_2]^{3+}$ complexes in the CH_2Cl_2 solution, which was so called T species.

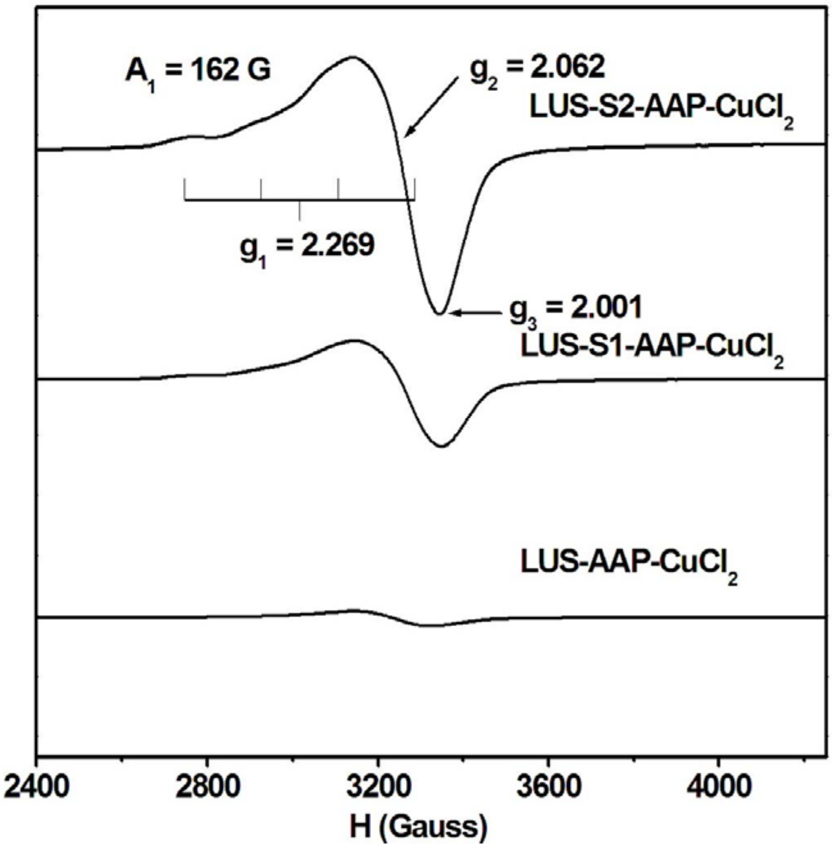

Figure 5.8 EPR spectra of LUS-Sn-AAP-$CuCl_2$ series.

The formation of the T species is dependent on the ligand structure and the initial concentrations of Cu(I) and O_2, and authors concluded that only the least sterically demanding ligands and greater concentration of $[(^{Me,\ Me}cd)_3\text{-Cu (I)(MeCN)}]^+$ preferentially yield T species. However, this is not the case for our series saples in the absence of Cu(I) and oxygen. More recently, quite similar results with our samples were reported by Mou and his colleagues using mesoporous silica as support to immobilize the hydroxo-bridged dinuclear phenanthroline cupric complexe that the absorption band at 350 nm corresponds to the charge-transfer band from the OH→Cu orbital. Further works to define this rare binuclear copper complexes brideged by a single hydroxo group is needed.

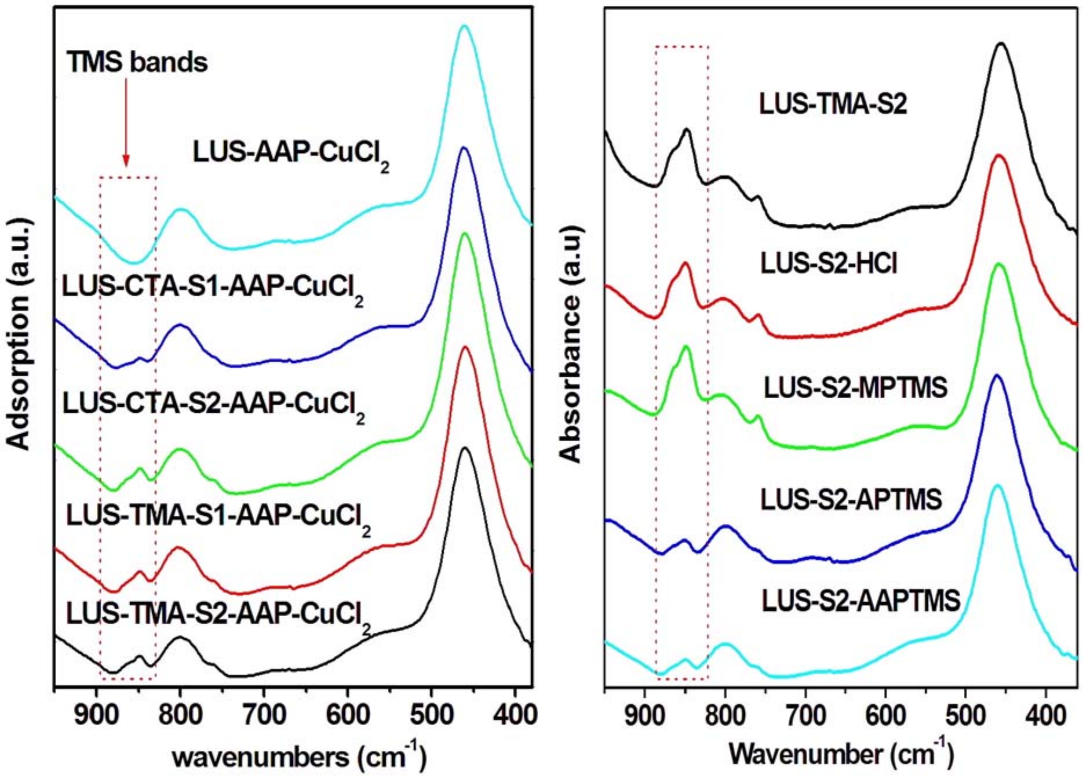

Figure 5.9 FT IR spectra of samples with different organic function incorporations: MPTMS, APTMS, and AAPTMS (= AAP).

Further characterization by FT IR (figure 5.9) exhibited that the stretching band of TMS groups was almost completely lost after the incorporation of AAP functions. It is well known that aminopropyl groups influence the stability of Si-O-Si bond by nucleophilic attack of amine group (-NH_2) [21]. In current case, the same reaction mechanism should be followed. This is correlated to CuN_2 coordination type from EPR measurement, instead of CuN_4 coordination environment, due to the partial protonation of the ligand in relation to the apparent pH of *ca.* 10 of the solid before metallation. Systematic investigation showed that the stability of Si-O-Si depended on the type of incorporated functions. Figure 5.9 in right panel exhibited that, when the mercaptopropyl (-$(CH_2)_3$-SH) was grafted on the pore surface, the density was not changed, while when aminopropyl groups were introduced, most of TMS groups disappeared. Same result was reported by Etienne et al.[21], they found that the chemical reactivity and stability of aminopropyl-grafted silica depended on the pH of solution. Thus the challenge here is to maintain as much as the TMS functions on the channel surface of mesopores when introducing the AAP organic groups.

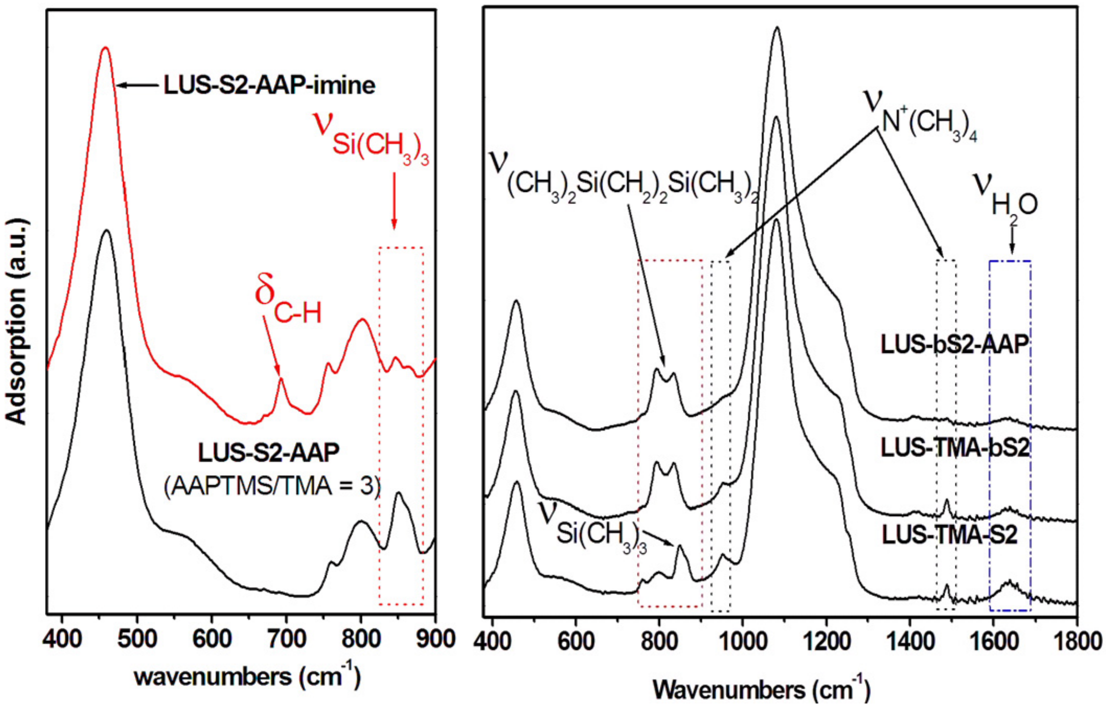

Figure 5.10 FT IR spectra of samples with or without bipodal silane (b for bipodal silane, S2 for 50% TMA removal and TMA for TMA containing materials).

To resolve this problem, according the method reported by Jone et al [22], [3-(trimethoxysilanyl)-propyl]-2-pyridylmethanimine (PMITMs) was synthesized to directly coordinate Cu^{2+} ions, avoiding the nucleophilic attack of amine group ($-NH_2$) on TMS groups. Figure 5.10 in left panel showed the typical stretching δ-CH from benzene cycle, indicating that PMI function have been incorporated into pore channel. However, the density of TMS was little increased, implying PMI groups can still attack the TMS groups. It should be mentioned that, when the grafting reaction took place, we used large quantity of AAPTMS silane (15 molar equivalence to total TMA^+ ions) leading to the pH increase of reaction solution (larger than 10). Inspired by Etienne's work [21], the low pH value is necessary to get long-term stability, we significantly decreased the amount of AAPTMS (3 molar equivalence to total TMA^+ ions) in the reaction system. As expected, most of TMS groups were maintained. For this route, further improvements to keep the density of TMS groups, one is to adjust the pH value less than 7 before the addition of AAPTMS silane; the other way is to shorten the reflux time due to the higher diffusion rate in the current system using TMA^+ ions as protecting groups.

In another route, a new commercial silane (2,2,5,5-tetramethyl-2,5-disila-1-azacyclopentane, *Gelest*, hereafter, it named dipod-silane) was deliberately chosen to tune the surface hydrophobicity. Compared to the TMS with monopod, after grafting, bipod silane should more withstand the attack of AAP functions. IR spectrum in the right panel showed different vibration band centered at 850 cm^{-1}, differing that of monopod TMS groups, which indicated the incorporation of bipod silane. It is interesting to note that the intensity of the bending of H-bond water at 1600 cm^{-1} in bipod silane covered silica is lower than that in monopod TMS grafted silica, indicating much more hydrophobicity (i.e much more silanol groups were consumed using this new silane). Most importantly, after AAP function incorporation, the intensity was maintained, implying bipod silane can resist the attack of AAP function, therefore the problem on the lost of isolated functions, for example TMS groups, can be resolved.

In summary, by carefully controlling the reaction conditions and deliberate choose of bipod silane, isolated functions, such as monopod and dipod siane, can be effectively retained when AAP was incorporated. Dual functionalized mesoporous silica provides an ideal medium to study the accessibility of model molecules in the pore channel and provides new atomisticinsights for understanding the heterogeneous catalysis on a molecule level.

5.3.4 Preliminary investigation on binuclear copper (II) complexes

5.3.4.1 XRD study

XRD patterns in figure 11 showed 3 readily distinguished bands indexing (100), (110) and (200), respectively, implying higher ordering of pore structure after Cu complexation. The only difference of two samples was pore size. The meoporous silica with larger pore 4.5 nm in diameter synthesized via the high-temperature post-synthesis treatment was named L-LUS-CTA (L was the initial letter of 'large').

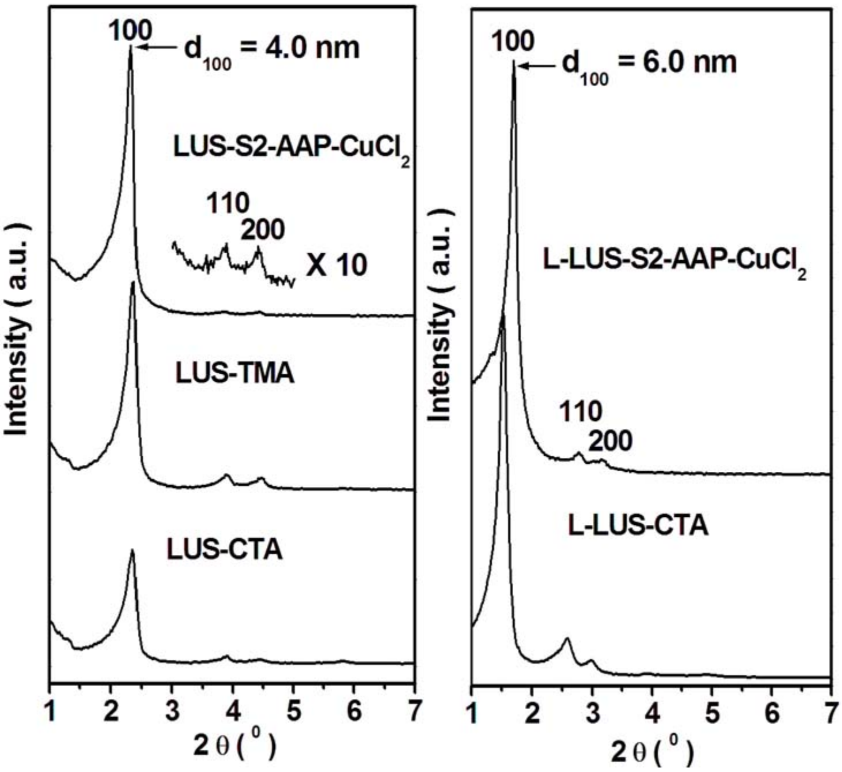

Figure 5.11 XRD patterns of the final samples with different pore size, regular size (left) and large size (right)

5.3.4.2 N_2 adsorption-desorption isotherms

Two samples exhibited the typical IV adsorption isotherm. After functionalization, pore size, specific surface area and total pore volume significantly decreased, indicating that the organic functions were incorporated into the pore channel. Texture properties were summarized in table 5.3.

Table 5.3 Characteristics of the materials porosity

Sample	S_{BET} ($m^2\ g^{-1}$)	V_{total} ($cm^3\ g^{-1}$)	D_{BJH}[b] (nm)	D_{BJH}[c] (nm)	D_{BDB} (nm)
LUS-Calcination [a]	962	0.86	3.3	3.1	3.9
LUS-S2-AAP-$CuCl_2$	505	0.34	2.1	2.0	2.7
LUS-Calcination	672	0.76	4.7	3.7	4.7
L-LUS-S2-AAP-$CuCl_2$	337	0.46	3.5	3.4	4.3

Note: a, the sample was exchanged by TMA^+ molecules, then calcined at 550℃ for 6 hours; BET surface areas and C value were calculated using data over the relative pressure range of $0.05 \le P/P_0 \le 0.16$. V_{total} is single point pore volume at $P/P_0=0.99$. D_{BJH}, D_{BDB}, were pore size determined by corrected BJH method from the adsorption branch (b) and desorption branch of the isotherm (c), BDB method from the desorption branch of the isotherm

However it is interesting to notice two important observations. First, the pore size from BJH and BDB method for sample LUS-S2-AAP-$CuCl_2$ decreased by 1.2 nm, and this value is little larger than the size of AAPTMS of 1.0 nm. For sample L-LUS-S2-AAP-$CuCl_2$, from adsoption branch using BJH method, the pore size decreased by 1.2 nm, however, calculation from the desorption branch in both methods showed the significant decrease of pore size (about 4 Å). The implication of the pore-diameter change is clear because the adsorption branch gives the pore diameter of wide pore region, and desorption branch gives information on the narrow pore region. This further confirmed our previous conclousion: the surface of MCM-41 channel was covered by open micropores, called visually alveoli. The most reasonable explanation is that, initially, the TMS silane were deposited in the edge of alveolus (narrow part of pore channel) and reduced the pore radii in this region by a number corresponding to the size of TMS (about 6-7 Å). When the rest TMA molecules were removed from the alveoli with size about 7 Å, the AAPTMS silane was deposited. Due to the presence of open micropores, the net decrease of mesopore size is 4~5 Å. The sum of both is just the chain length of AAPTMS orgnasilane. Second, from chemical elemental analysis (table 5.4) and

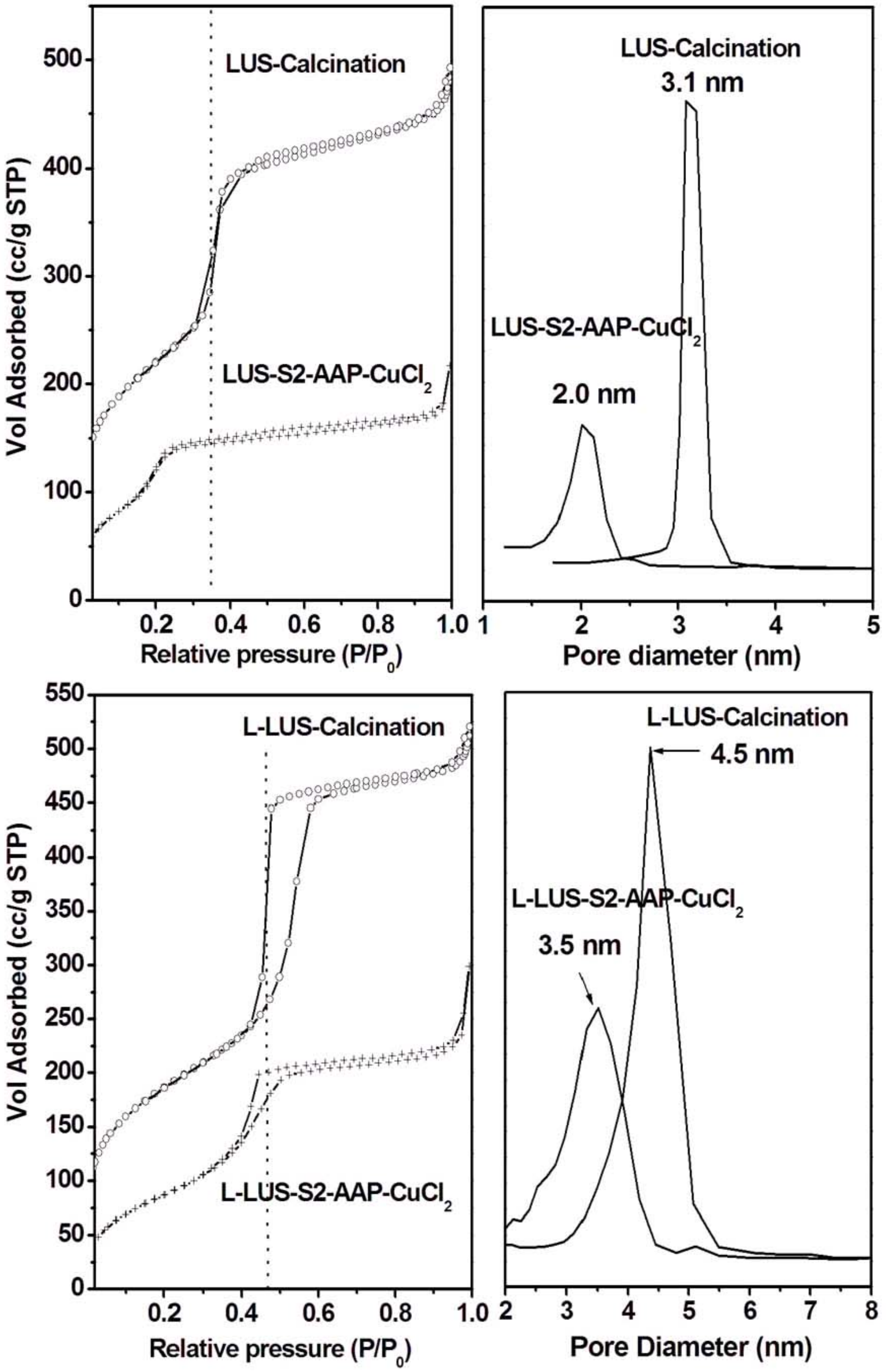

Figure 5.12 N_2 adsorption-desorption isotherms (left) and pore size distribution from BJH method (right) of the final samples.

thermalgravemetrical anslysis (not shown), both samples showed the organic loading, indicating that the decrease of total pore volume from adsorption isotherm should be the same because of the same volume filling. However, the decrease of pore volume for sample LUS-S2-AAP-$CuCl_2$ is almost two times larger than that of L-LUS-S2-AAP-$CuCl_2$. The loss of open micropores (i.e. pore surface becomes smoother) answered this difference and same decrease of pore size calculated from both adsorption and desorption branch.

Table 5.4 Elemental analyses of LUS-1 after Cu incorporation using improved 'molecular stencil patterning' technique

Sample	Cu/SiO_2 mmol/g	Cu (%)	C (%)	H (%)	N (%)	Cl (%)	N/Cu	Cl/Cu	N/Cl	a/b
LUS-S2-AAP-$CuCl_2$	0.64	3.45	9.20	2.08	2.22	2.46	**2.94**	**1.29**	**2.29**	1.56
LUS-S2-AAP- $Cu(ClO_4)_2$	0.52	2.60	8.48	1.95	1.87	2.32	**3.29**	**1.60**	**2.04**	1.86
LUS-bS2-AAP- $CuCl_2$	0.27	1.55	7.20	1.57	1.14	1.29	**3.36**	**1.50**	**2.24**	1.62
L-LUS-S2-AAP- $Cu(ClO_4)_2$	0.27	1.43	8.97	2.08	1.87	1.08	**5.97**	**1.36**	**4.39**	2.06
L-LUS-bS2-AAP- $CuCl_2$	0.33	1.80	8.99	2.05	1.80	2.04	**4.57**	2.04	**2.24**	1.10

Note: a/b stands for the molar ratio between isolated function (TMS or bipod-silane) and organic function (AAPTMS); the Cu loading in unit mmol/g was calculated considering SiO_2 content obtained from weight loss at 1273K with the contribution of the grafted silane.

5.3.4.3 Chemical element analysis

The results of chemical element analysis were listed in the table 5.4. The value of a/b is the number ratio of isolated TMS groups and AAP function in a range of 1- 2 depending on the silylation degree and pore size. The N/Cu molar ratio for the sample with smalle pore size was close to 3, indicating Cu was coordinated by 3 nitrogen atoms. Unexpectedly, for the samples with large pore size, the coordination number is larger than 4.5. Because the maximum number for copper using AAP as ligand is 4, this indicated that Cu complexation environment in confined mesiporous silica was significantly different with that in the solution and on the surface of nonporous silica. Due to the pore confinement effect, and complicated surface chemistry [23], it is possible that only one nitrogen atom of the ethylene diamine (AAP) ligand involved Cu complexation due to the partial protonation of AAP ligands. The loss of coordination by a single protonated aminopyridinyl branch has been already observed in Fe (III) L_5^2 complex where L_5^2 turns from penta coordinated to tricoordinated. Most strong proof is that the XPS spectrum exhibited the presence of positively charged N atom (binding energy= 401.7 eV) in the L_4^2 type DETA ligand, implying the grafting ligand are protonated. Most interesting is that number ration of N/Cl and Cl/Cu exhibited regular change. It should be mentioned that Cl/Cu number ratio is less than 2, implying Cu was coordinated by exogeneous ligands to maintain surface charge balance, most proable hydroxide.

Herein, it is also worth noting that perclorate ion involved Cu coordination. Several investigators have studied Ramin and IR spectra of perchlorate ions. The ClO_4^- ion adopts a regular tetrahedral structure and has nine diiffernent vibrational degrees of freedom. The symmetrical stretching and bending modes are only Ramin active while the assmmetric stretching and bending modes are both IR and Ramin active [24, 25]. These normal modes of vibrations are expected to occur at 928 cm^{-1} (ν_{sym}), 459 cm^{-1} (δ_{sym}), 1119 cm^{-1} (ν_{asym}) and 625 (δ_{asym}), respectively. If the perchlorate ion is involved in the partial covalent bond formation to Cu^{2+} ion, the symmetry will be lowered to $C_2\nu$.The vibrations of the perchlorate anion from FT-IR spectrum (figure 5.13) observed this change: the δ_{asym} specie splits into two occurring at 627 cm^{-1} and 637 cm^{-1}, however, the degeneracy of 1119 cm^{-1} (ν_{asym}) is not distinguished because of the superimpose of Si-O-Si stretching vibration. These assignments are in close agreement with that perchlorate group is semicoordinated to copper. Most interestly, one peak is observed at 1144 cm^{-1} due to the rocking vibration of $–NH_3^+$ [24], confirming that partial amino groups are protonated in current system. To further elucidate the Cu coordination environment, UV-visible and EPR spectrum was performed (table 5).

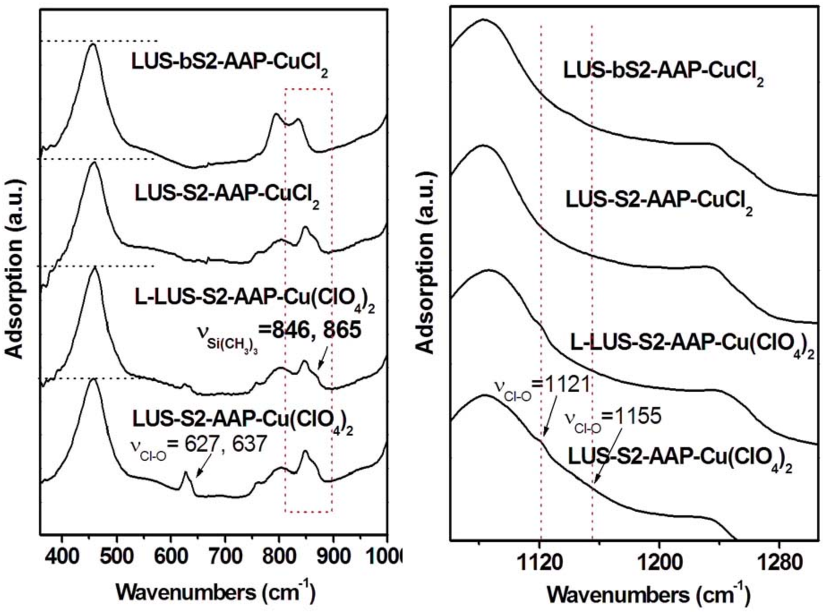

Figure 5.13 FT IR spectra of the materials after sequential graftings and Cu complexation.

Table 5.5 UV-vis and EPR spectroscopic characteristics of the materials after Cu incorporation.

Sample	UV-vis	EPR g and A factors				
	λ, nm	$g_{//}$	$g_{\perp}$	$A_{//}$ (G)	$10^4A_{//}$ (cm^{-1})	R=10^4 ($g_{//}/A_{\perp}$)
LUS-S2-AAP-Cl	261, 299, 352,369, 494, 683	2.232	2.045	176	183	122
LUS-S2-AAP-ClO$_4$	247, 263, 281, 300, 329, 364 560, 669	2.195 ***2.283***	2.017 ***2.017***	239 ***181***	244 ***192***	89 ***118***
LUS-S2-AAP-ClO$_4$^{a}	Same	2.235	1.992	203	213	106
LUS-bS2-AAP-Cl	260, 296, 354, 387 495, 691	2.214	2.008	179	185	120
L-LUS-S2-AAP-ClO$_4$	261, 290, 342, 401 563, 665	2.200 ***2.276***	1.997 ***1.997***	215 ***156***	221 ***166***	100 ***137***
L-LUS-S2-AAP-ClO$_4$^{a}	same	2.201	1.995	188	193	114
L-LUS-bS2-AAP-Cl	262, 300, 349, 426 494, 673	2.194	2.032	188	193	114
LUS-S2-AAP-Cl^b	262, 301, 339, 468, 522, 691	2.269	2.062	162	172	132
2AAPTMS-CuCl$_2$^{c}	586	2.172	2.058	185	188	115
AAPTMS-CuCl$_2$^{c}	700	2.232	2.058	173	180	124

Note: a, EPR was performed at RT, other case was 100 K; b, TMS was partially lost after the introduction of AAP groups; c, Cu complexe was measured in solution at 100K as references.

5.3.4.5 UV-visible absorption spectra study

Due to the complicity of Cu complexe environment like in realistic biology system, the elucidation of UV-visible was divided into two zones, the lower-energy region dominated by transitions from the filled d orbital to the half-occupied $d_{x^2-y^2}$ orbital and the higher-energy region ruled by ligand-to-metal charge transfer (LMCT) transitions [15, 16].

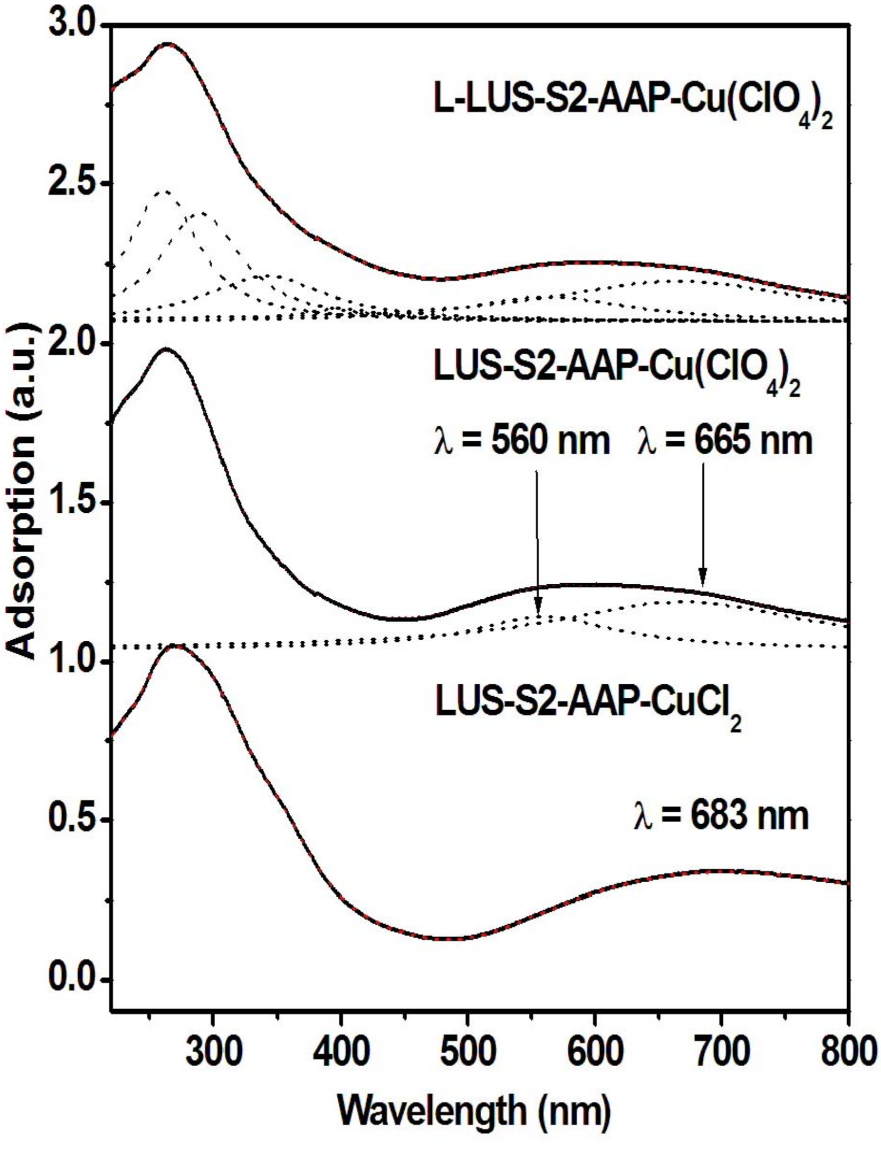

Figure 5.14 UV-vis characterization of LUS-Sn-AAP-$CuCl_2$/$Cu(ClO_4)_2$ series, dot lines are obtained by Lorentzian multipeak fitting.

Since d orbitals are split in energy by the ligand field at the metal center, the associated d→d transitions are sensitive probes of the ligand geometry [16]. In current cases, the most striking aspect was that the Cu incorporated mesoporous silica exhibited the significant color change from violet to blue, only depending the Cu counterion using in compexation reaction, perchlorate (ClO_4^-) and chloride (Cl^-), respectively, further indicating the these anions were coordinated to the copper atom. Indeed, many [Cu^{2+}(ligand)$_4$(anions)$_2$] have been studied having monodentate ligands with N as donor atom.

In these compounds, anions often are weakly bound to the copper atom with distorted octahedron geometry. Using *N*-ethylimidazole and *N*-propylimidazole, Reedijk et al investigated the influence of BF_4^-, ClO_4^-, NO_3^-, Br^- and Cl^- anions on the Cu confirmation geometry, they showed that the geometry of these compounds was tetragonal, because these weakly coordinated ligands and that axial bonding strength increased with the above order [26, 27]. However, Jeannin et al suggested that their complexe Cu^{2+}(ligand)$_4$(NO_3)$_2$ exhibited a distorted square-planar environment, with noncoordinated nitrate ions [28]. It was importantly noted that, Massacesi et al [29] reported semicoordination for NO_3^- like our result derived from chemical elemental analysis, i.e. Cu can be coordinated by a bridging ligand, consitent with IR our observation.

After the treatment using Lorentz multipeak fitting, as done by Jeannin et al [28] and Addison et al [30], for the samples incorporated by $Cu(ClO_4)_2$, one absorption maximum appeared between 500-1000nm, with a shoulder on the high-energy side (figure 5.14). The deconvolution peaks corresponded to 665 and 560 nm, as observed by Jeannin [28]. However, when the chlorine involved the coordination, only adsorption band centered at about 690 nm was observed. According to the LCAO-MO analysis [28], the Cu environment involved by perchlorate was closer to pesudoplanar geometry. The presence of adsorption band centered at 560 nm, on the one hand, showed an increase of the participation of nitrogen p orbital in the ground state ｜$^2B_1$> as suggested by Jennin et al [28], on the other hand, possibly revealed the presence of the mixture Cu coordination environemt on the confined pore channel. This demonstrated that even anion can dramatically change the structure of Cu environment. In the next section, EPR observation further confirmed this conclusion.

In a lower-energy range, due to the possible presence of diverse Cu_2O_2 species, the assignment of ligand-to-metal charge transfer (LMCT) transition bands is a difficult problem [15]. But some common UV-visible features were observed in our samples. In this range, the bands centered at around 260 nm, 300 nm and 350 nm always existed, independent on the anion type, silylation degree and pore size and, in some cases, the bands centered at about 400 nm and 490 nm were observed (figure 5.14).

The most distinguished observation is that, compared to the sample LUS-S2-AAP-$Cu(ClO_4)_2$, the serial of samples LUS-S2-AAP-$CuCl_2$ shows the stronger adsorption bands at 350 nm, which is the characteristic charge transfer band from the OH^-→Cu orbital. The other two peaks may be attributed to the N-, exogenous ligand Cl^-(or ClO_4^- or H_2O or SiO^-) to-Cu, respectively. Now we supposed that Cu^{2+} ions are possibly connected by a hydroxide bridging ligand to form the binuclear complexe, similar assignment was reported by Mou and colleagues [31]. Herein, the hydroide ion provides two basic functions: charge balance ions and coordination ligand group. This sanswers the characterization result by chemical element analysis, in most cases, that the Cl/Cu molar ration is less than 1.5. Much more detailed information on the copper coordination environment can be provided by EPR spectrum.

5.3.4.5 EPR study

The EPR spectrum of the typical samles was recorded at room temperature and 100K (Figure 5.15). The g values reported in table 5.5 are consistent with a distorted copper (II) ion environment. In the left panel of Figure 5.15, g=4 region was presented where the semiforbidden □ms = 2 transitions are contributing, indicating the presence of dinuclear Cu-Cu coupling exchange by the bridgeing ligand hydroxide [32]. The corresponding EPR parameters were summarized in Table 5.5. A closer examination reveales $g_{//}>g_{\square}>2.0023$ in most cases, which is consistent with a $d_{x^{2}-y^{2}}$ ground state and with an elongated square pyramidal or elongated octahedral environment for Cu(II) [28].

It should be importantly mentioned that the dihedral angle between the two N_2Cu planes, denoted as ω, is generally used to estimate the deviation from pure tetrahedral (90°) or square-planar (0°) geometry in Cu^{2+} compexes. The *parameter R* (cm) = $g_{//}/A_{//}$ is a good indication of the distortion magnitude as shown by Jeannin et al [28], and authors studied the variation of *R* value as a function of ω. In a g = 2 region, small spectral changes at room temperature observed for samples involved by chlorine ions, and *R* (cm) was centered at around 120 (ω = 60°), indicating the copper environment is a distorted tetragonal geometry. The samples with perchlorate ions showed the slight smaller *R* value centered at around 110 (ω = 55°) than sample involved by chlorine ions at room temperature, implying the copper coordination inviroment shifted toward the pesudosquare-planar geometry.

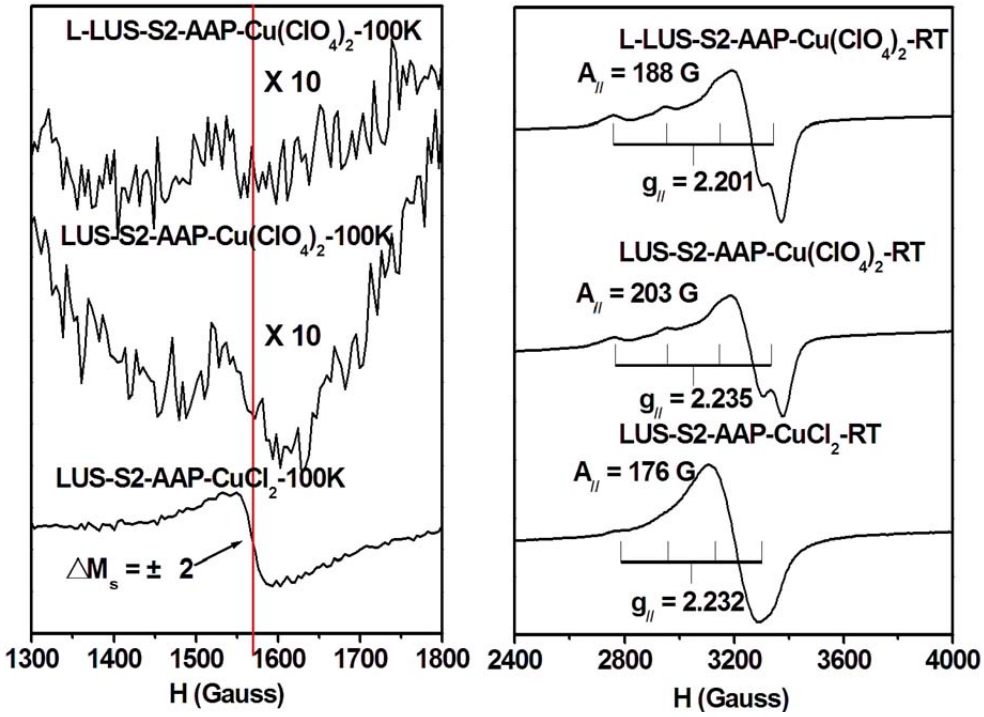

Figure 5.15 EPR spectra of LUS-Sn-AAP-$CuCl_2$/$Cu(ClO_4)_2$ series: half-field resonance (left) and main resonance (right).

The most interesting was that, when EPR measurement was done at 100 K, the samples involved by perchlorate ions displayed two Cu^{2+} tensors in figure 5.16. Especially for sample with smaller pore size, they are easily resolved, one is tensor A with *R* value (ω = 49°), the other one is tensor B with *R* value (ω = 58°). According to an up-to-date Peisach and Blumberg type of diagram, two Cu^{2+} tensors A ($g_{//}$ = 2.195 and $A_{//}$=244 cm^{-1}) and B ($g_{//}$ = 2.283 and $A_{//}$=181 cm^{-1}) were assigned to CuN_4 and CuN_2 coordination environment, respectively [33].

Increasing the measurement temperature, the EPR parameter showed only one signal ($g_{//}$ = 2.235 and $A_{//}$=213 cm^{-1}) corresponding the CuN_3 coordination environment. However, for sample with larger pore size, two set of g parameters are not readily distinguished even at 100 K. After the second derivative, tensor A (*R*, 100; ω = 55°) and tensor B (*R*, 137; ω = 63°) can be observed. Following the same trend, when measurement temperature was increased, only one EPR signal ($g_{//}$ = 2.201 and $A_{//}$=193 cm^{-1}) was observed (table 5.5 and figure 5.16).These results clearly showed the presence of a dynamic equilibrium between both CuN_4 and CuN_2.

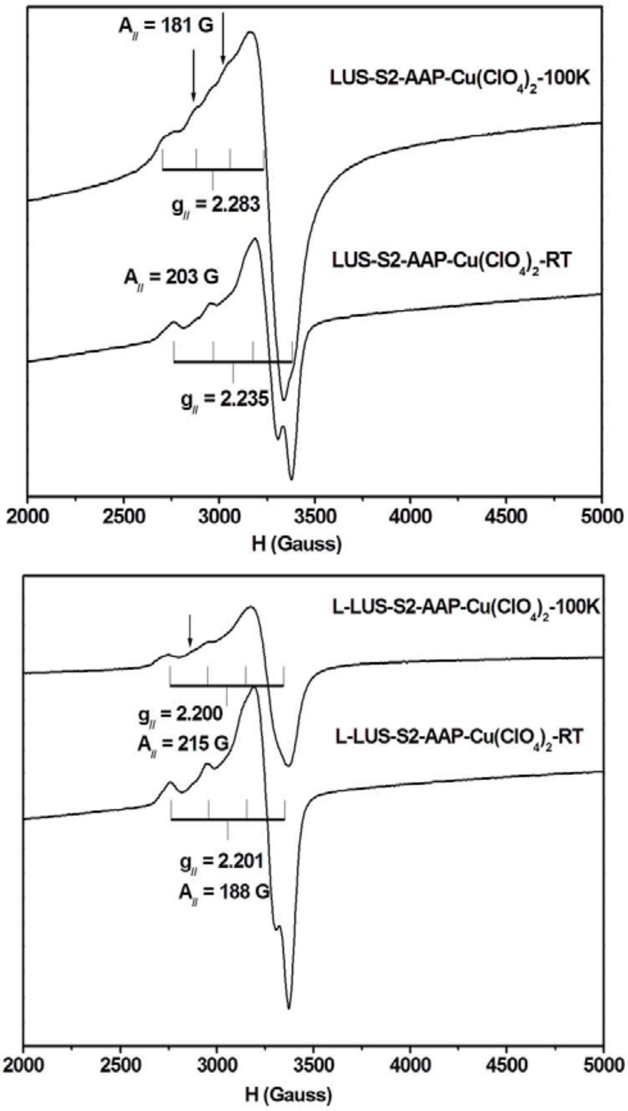

Figure 5.16 EPR spectra comparison between LUS-S2-AAP-Cu(ClO_4)$_2$ and L-LUS-S2-AAP-Cu(ClO_4)$_2$ measured at RT and 100 Ky.

Differing from the Copper complex coordinated by perchlorate anions, Cu complexe involved by chlorine anions only exhibited one EPR signal, which could be assigned to CuN_3 enviroment. There are two possibilities that can be used to explain the dynamic exchange. First, the exchange rate between two copper coordination environments is much faster enough in comparision with the measure time that is about 10^{-8} s for X-band EPR. Second, the exchange never happened. If the first case is true, decresaing the measurement temperature might slow down the exchange process and provoke first a signal broading and then a splitting into two signals. However, this has not been observed down to 100 K (limit of our N_2 cryostat). Thus we believe that this interesting dynamic effect did not occure at all.

In current cases, exchange interaction should be dominant factor for the semiforbidden □ms = 2 transition, because two copper atoms were connected via exogenous hydroxide bridging ligand. Literature also showed that the semiforbidden □ms = 2 transition, typically in noncrytalline Cu complexes, occurred in a case of appropriate bridging molecules connecting two Cu atoms with Cu···Cu distance ~3 Å [34-36]. It should be mentioned that sample involved by ClO_4^- showed very weak intensity at this band due to the semicoordination nature. However, copper complexe coordinated by chlorine ions exhibited strong intensity at low measurement temperature. In some case, a very weak signal even at room measurement temperature could be readily observed. This further confirmed the dynamic equilibrium between two different Cu coordination environments did not happened, and exchange interaction between two coppers was maintained. However, for copper bonded by perchlorate ions did not show any signal at room temperature. It is possible that the exchange passage was blocked due to the loss of the bridging ligand during the exchange process between two different copper species.

Now what is the determining factor to control the exchange between two copper species? The only difference between two series of sample is counterions. Based on the investigation of IR and chemical analysis, the counterions, Cl^- and ClO^{4-} were found acting as exgeneous ligand and counterions of protonated amino groups. Compared to clhloride, perchlorate has stronger hydrogen bonding ability and weaker coordianation ability.

Numerous studies showed that, in the presence of perchlorate ions, copper complexe and some protein structure can readily formed multimensional crystal structure by hydrogen bond interaction [37-39]. Especially, in biological system, the proton transfer in the proimity of metal ions can significantly affect its coordination environment and catalytic activity [39].

The IR spectrum in figure 5.17 was recorded to study the hydrogen-bonding network between amino groups, counterions including Cl^- and ClO_4^-, and water molecule. It is known that aliphatic primary amines salts are characterized by strong absorption between 3200 and 2800 cm^{-1} due to the asymmetric and symmetric $-[NH_3]^+$. Also the $[NH_3]^+$ asymmetric and symmetric deformation wave numbers are expected to fall in the regions 1660-1610 cm^{-1} and 1550-1485 cm^{-1}, respectively [24]. In the present study, the IR bands at 3144 cm^{-1} in broad strong peak is attributed to the $-[NH_3]^+$ asymmetric vibration. The asymmetric deformation band appears as a shoulder at 1632 cm^{-1}. In the $-[NH_3]^+$ group hydrogen atom coordinates with O atom of perchlorate group or chloride ions via hydrogen bonding. These hydrogen bonds are responsible for the lowering of stretching wave numbers due to the weakening of N-H bonds. The water molecule in the crystalline state, three vibration modes are expexted to occur at about 3400, 1620 and 3220 cm^{-1}, respectively [24]. In ths study, two adsorption bands 3424 and 3246 cm^{-1} are observed in the IR spectrum, assigned to the symmetric and asymmetric strectching mode of water molecules, respectively.

Unexpectedly, additional two adsorption bands centered at 3510 and 3351 cm^{-1} are observed after gaussion fitting treatment. This rare case has been reported in some t-amino-alcohols related to methadone and a bonded system system comprising anion, OH, and N^+H functions is proposed, which has feature bands at 3160 and 3570 cm^{-1} assigned to ν_{N^+H} and ν_{OH}, respectively, plus a broad boned absorption near 3350 cm^{-1} due, in part at least, to water of crystallization [40]. Most interestingly, authors found that anion influenced the O-H stretching frequency, well consitent to current observation that ν_{OH} bands shifted from 3510 cm^{-1} to higher wavenumber of 3573 cm^{-1} when counterion was perchlorate. It is worthy note that, in the present study when counterions was changed to perchlorate, the ratio of adsorption intensity between 3510 cm^{-1} and 3350 cm^{-1} dramastically decreased, in line with the UV-vis observation that the absorptionintensity centered at 350 nm was significantly decreased, indicating some hydroxide groups disappeared. It is therefore concluded that a hydrogen bonded system consisting anion, hydroxide and protonated amion groups obtains, and bonding of this type could take the form $–OH\cdots X^{-}\cdots {}^{+}H_3N-$. The proton transfer colud occur along this hydrogen bonding line. Protonation of the bridgeing OH- ions and ensuing proton shuffling are responsible for the observed dynamic behavior by EPR and UV-visible.

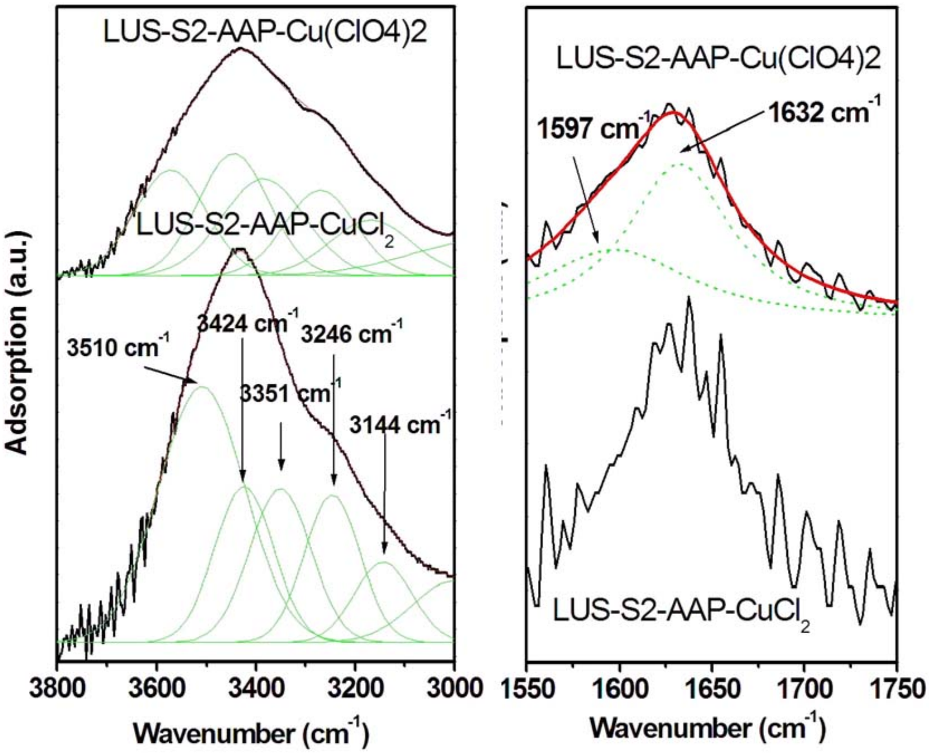

Figure 5.17 FT IR spectra of samples LUS-S2-AAP-$CuCl_2$ and LUS-S2-AAP-$Cu(ClO_4)_2$: O-H and N-H stretching frequency range (left) and deformation range (right).

Based on the characteriztions by chemical analysis, UV-visible, EPR and FT IR, a dynamic equilibrim between both CuN_4 and CuN_2 coordination environment due to the proton shuffling was proposed as showen in scheme 5.6. The exchange rate depends on the distance between two copper atoms, which is the prime requirement. As exhibithed in scheme 5.7, if the pore size is increased, the exchange can not be happened. Most interestingly, when changed the dipod silane as isolated function, chemical analysis show the molar ration of Cl^-/Cu^{2+} close to 2 for sample L-LUS-bS2-AAP-$CuCl_2$. This satisfied with the charge balance, indicating the absence of the exogenous ligands, for instance OH^- ion. This further proved that new bi-pod silane can effectively tune the surface hydrophobicity. Because of the absence of water in pore channel, the bridging hydroxide ions can not be produced.

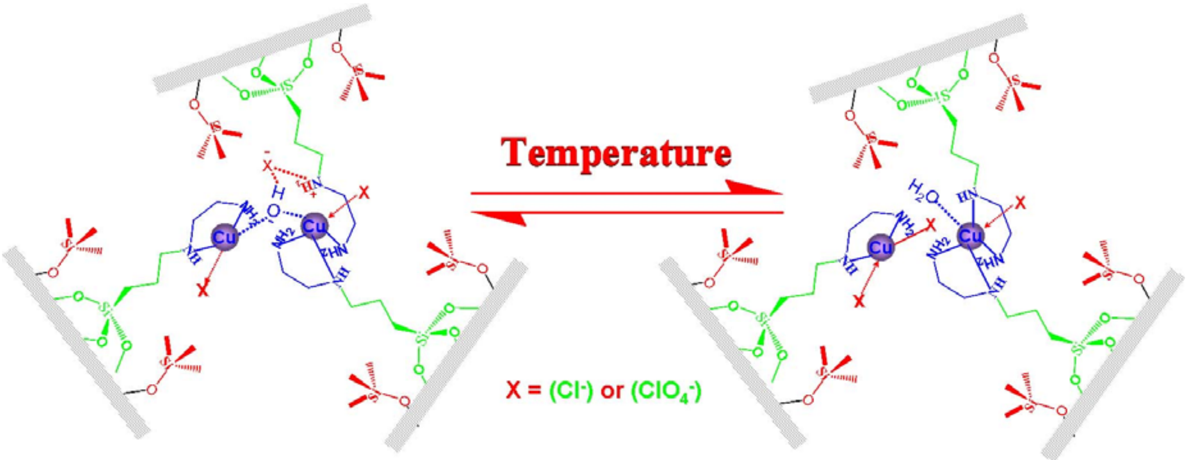

Scheme 5.6 Dynamic equilibrium between both CuN_4 and CuN_2 coordination environment due to protonation of amino groups (inspired from ref. 39).

Besides the pore size effect and suface hydrophobicity, copper counterions and operating temperature also play very important role to control this interesting dynamic behavior.

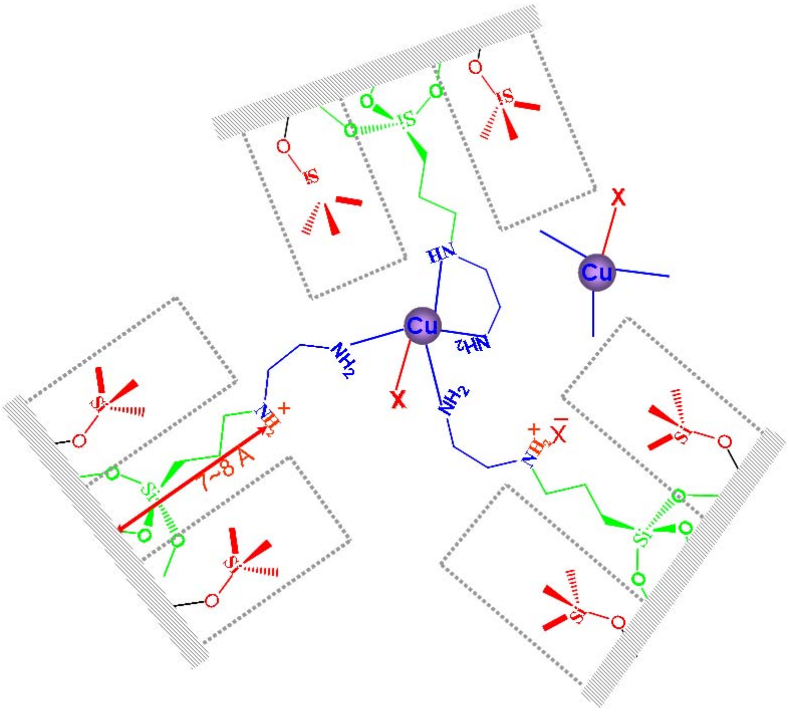

Scheme 5.7 Suggested Cu coordination environment for the complexes formed in L-LUS-Sn-AAP-Cu depending on the silylation degree and mesopore size (or pore geometry), (for clarity, the three AAP ligands are drawn for one Cu site only).

Concerning the copper counterions, due to the stronger hydrogen bonding ability of perchlorate ion than that of chloride, the operartion of intermolecular bonding between perchlorate ion, the bridging ligand hydroxide and protonated amino groups in confined space can be accepted as a reasonable assumption on the basis of the FT-IR evidence presented above (scheme 5.8 (1)). After this step, proton shuffling colud occur within this coordination sphere of binuclear Cu^{2+} ions (scheme 5.8 (2)), then the protonation of the bridging OH^- ion breaks the copper binuclear coordination environment (scheme 5.8 (3)). In the course of the proton transfer, the moderate basicity of the μ-OH^- might allow for a favorable equilibrium between two different copper species, thus EPR and UV-visible showed two distinguished sepecies. However, when chloride ion is at stake as weak hydrogen bonding anions, the intermolecule hydrogen bonding network can not be formed, as a consequent, the protonation of μ-OH^- can not be observed. IR supported this suppose because the ratio of adsorption intensity between 3510 cm^{-1} and 3350 cm^{-1} for sample in the presence of chloride ion is always larger than sample involved by perchlorateion, well consitent with UV-visible observation that the feature absoption at 350 nm for the bridging hydroxide ions can be easily distinguished. Protonation of the bridging hydroxide ions are expected to have much shorter timescales. When operating temperature is decreased, the rate of proton transfer is slow down, i.e., the residence time of proton on the hydroxide ion is extended. The protonation of the bridging hydroxide into water leads to the change of copper conformational geometry as exhibited by EPR at operating temperature 100 K. The water formed by protonation can coordinate to Cu^{2+}, Because aqua ions can act as Bronsted acids, which means that they can acts as proton donors, thus a new bridging hydroxide ion can be resulted (scheme 5.8 (4)). This proton shuffling mechanism is quite similar to that of hammerhead ribozyme where two magnesium ions are connected by a bridging hydroxide ion.

Most recently, this rare Cu (II) coordination chemisty exhibited the strong dynamic effect was only reported most recently by Comba et al using westiellamide (H_3L^{wa}) ligand, as well as its synthetic analogues with [18] azacrown-6 macrocyclic structure as ligand. These compounds H_3L^{wa} and H_3L^1, H_3L^2 and H_3L^3 have an alternating sequence of heterocyclic nitrogen lone pairs and peptide nitrogen donors in a highly preorganized arrangement [41]. The cavity of macrocyclic ligand is just equivalent to the mesopore channel. The similarity of Cu coordination chemistry, in turn, implied that the AAP functions on the surface of mesoporous silica are spatially distributed in well difined organization. This further confirmed that our new and improved ‘molecular stencil patterning’ technique can manipulate the surface and interfacial chemistry on the nanometer scale with multifunctional molecules and groups, which will lead to much more sophisticated catalyst with properties approaching that of the biological counterparts, for example, metalloproteins.

The observation of dynamic effect of current copper complexe supported on mesoprous silica, which was only reported in the biological system, shed a new light to design bioinspired catalyst at the molecule scale.

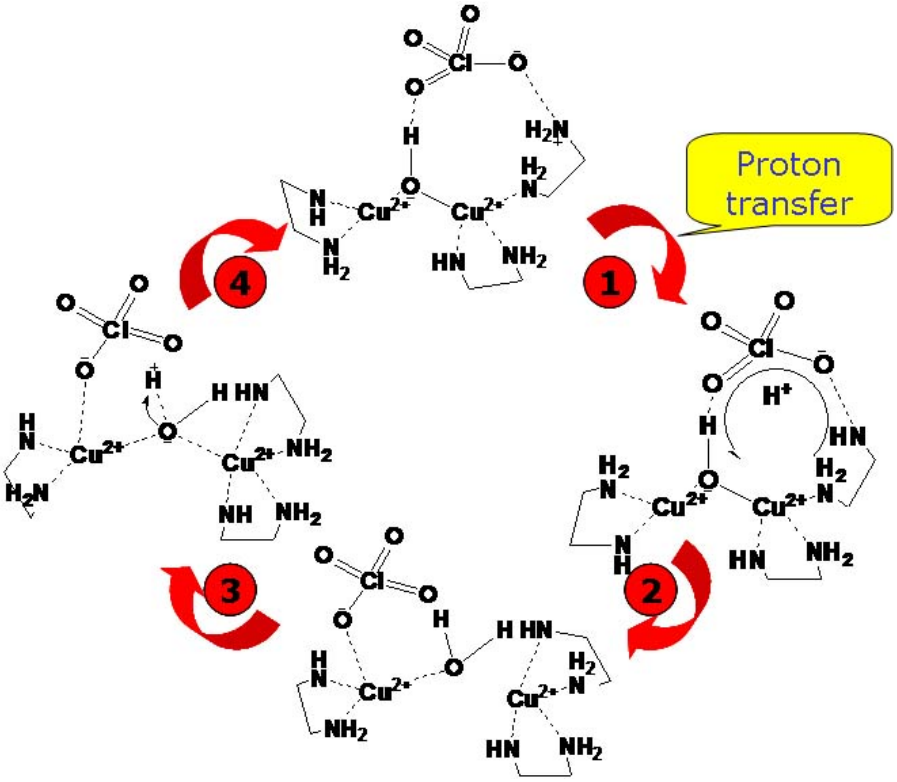

Scheme 5.7 Suggested proton transfer cyclic mechanism to explain the dynamic nature of dinuclear copper complexes supported on the MCM-41 silica (for clarity, only ethylenediamine moities of the grafted funtions are presented in this scheme).

5.4 General conclousion and perspective

5.4.1 General conclusion

Dual functionalization on the surface of mesostructured silica, LUS-1, was investigated here using a novel and improved ‘molecular stencil patterning’ technique. The great challenge was to maintain as much as possible the isolated functions on the surface when introducing the second AAP functions. Most interesting was that the dynamic equlibrium of different Cu coordination environment that has been observed based on chemical element analysis, UV-vis, EPR and FT-IR spectrum. We concluded that, besides the pore size effect and surface hydrophobicity, copper counterions and operating temperature also play very important role to control this interesting dynamic behavior.

5.4.2 Perspectives

(1) The investigation of the Cu coordination environment has shown that some activated Cu-O_2 species were formed. These multifunctional materials will be in a near future used as advanced catalysts for various chemical reactions.

(2) Although the ‘molecular stencil patterning’ technique allows a higher level of control on surface and interfacial chemistry at the molecular scale for multiple functionalization, this sequential grafting method is time-consuming. To avoid this drawback, a new synthetic strategy based on the rational design of templating surfactant may be envisaged.

(3) In this current work, only the influence of pore size on the Cu coordination environment was investigated. Other mesoporous silica with different topology should be tested, for example MCM-48 (cubic *Ia*3*d* symmetry) that possesses better diffusion properties.

(4) Besides Cu based catalysts using our improved ‘molecular stencil patterning’ technique, other metal atoms known for their catalytic properties, such as Fe, Zn and Mn, should be investigated.

5.5 Reference

(1) Gates, B. C. Catalytic Chemistry, Wiley, New York, 1992.

(2) Beck, J. S.; Vartuli, J. C.; Roth, W. J.; Leonowicz, M. E.; Kresge,C. T.; Schmitt, K. D.; Chu, C. T. W.; Olson, D. H.; Sheppard, E. W.; McCullen, S. B.; Higgins, J. B.; Schlenker, J. L. *J. Am. Chem. Soc.* **1992**, *114*, 10834.

(3) Brunel, B.; Cauvel, A.; Fajula, F.; Di. Renzo, F. *Stud. Surf. Sci. Catal.* **1995**, *97*, 173.

(4) Macquarrie, D.J.; Jackson, D.B.; Mdoe, J.E.G.; Clark, J.H. *New J. Chem.* **1999**, *23*, 539.

(5) Wulff, G.; Heide, B.; Helfmeier, G. *J. Am. Chem. Soc.* **1986,** *108*, 1089.

(6) Wulff, G.; Heide, B.; Helfmeier, G. *React. Polym.* **1987**, *6*, 299.

(7) Tahmassebi, D. C.; Sasaki, T. *J. Org. Chem.* **1994**, *59*, 679.

(8) Hwang, K.-O.; Yakura, Y.; Ohuchi, F. S.; Sasaki, T. *Mater. Sci. Eng. C* **1995**, *3*, 137.

(9) Shin, Y.; Liu, J.; Wang, L.-Q.; Nie, Z.; Samuels, W.D., Fryxell, G. E.; Exarhos, G.J. *Angew. Chem. Int. Ed. Engl.* **2000**, *39*, 2702.

(10) Katz, A.; Davis, M. E. *Nature* **2000**, *403*, 286.

(11) McKittrick, M.W., Jones, C. *Chem. Mater.* **2003**, *15*, 1132.

(12) Bonneviot, L.; Badiei, A.; Crowther, N. Patent WO 0216267, 2002.

(13) Abry, S.; Albela, B.; Bonneviot, L. *C. R. Chimie* **2005**, *8*, 741–752.

(14) De Monredon, S.; Pottier, A.; Maquet, J. ; Babonneau, F. ; Sanchez, C. *New J. Chem.* **2006**, *30*, 797.

(15) Mirica, L. M.; Ottenwaelder, X.; Stack, D. P. *Chem. Rev.* **2004**, *104*, 1013.

(16) Solomon, E. I. ; Sundaram, U. M.; Machonkin, T. E. *Chem. Rev.* **1996**, *96*, 2563.

(17) Echchahed, B.; Morin, M.; Blais, S.; Badiei, A.; Bergault, G.; Bonneviot, L. *Microporous Mesoporous Mater.* **2001**, *44-45*, 53.

(18) Badiei, A.; Cantournet, S.; Morin, M.; Bonneviot, L. *Langmuir* **1998**, *14*, 7087

(19) Martins, L.; Bonagamba, T. J.; de Azevedo, E. R.; Bargiela, P.; Cardoso, D. *Appl. Catal. A* **2006**, *312*, 77.

(20) Pinnavaia,T. J.; Lee, J. G. S.; Abedini, M. *Midl. Macromol. Monogr.,* **1980**, *7*, 333.

(21) Etienne, M.; Walcarius, A. *Talanta*, **2003**, *59*, 1173.

(22) Nguyen, J. V.; Jone, C. W.; *J. Polym. Sci. Part A : Polym. Chem.* **2004**, *42*, 1367.

(23) Goettmann, F. ; Sanchez, C. *J. Mater. Chem. 2007*, 17, 24.

(24) Pandiarajan, S. ; Umadevi, M. ; Rajaram, R. K. ; Ramakrishnan, V. *Spectrochimica Acta Part A*, **2005**, *62*, 630

(25) Chen, Y. ; Zhang, Y. H. ; Zhao, L. J. *Phys. Chem. Chem. Phys.* **2004**, *6*, 537.

(26) Welleman, J. A. ; Hulsbergen, F. B. ; Verbiest, J. ;Reedijk, J. *J. Inorg. Nucl. Chem.* **1978**, *40*, 143.

(27) Reedijk, J. *Transition Met. Chem. (Weinheim, Ger.),* **1981**, *6*, 195.

(28) Gouteron, J.; Jeannin, S.; Jeannin, Y.; Livage, J. ; Sanchez, C. *Inorg. Chem.* **1984**, *23*, 3387.

(29) Massacesi, M. ; Ponticelli, G. ; Ramachary, C. ; Krishnan, V. G. *Transition Met. Chem. (Weinheim, Ger.),* **1980**, *5*, 353.

(30) Addison, A. W. ; Carpenter, M.; Lau, L. K. –M.;Wicholas, M. *Inorg. Chem.* **1978**, *17*, 1545.

(31) Lee, C. H.; Wong, S. T.; Lin, T. S.; Mou, C. Y. *J. Phys. Chem. B* **2005**, *109*, 775.

(32) Machonkin, T. E.; Mukherjee, P. Henson, M. J.; Stark, T. D. P.; Solomon, E. I. *Inorg. Chim. Acta.* **2002**, *341*, 39.

(33) Abry, S.; Bonneviot, L. et al. *Chem. Eur. J.* **2008**, in press.

(34) Grigoropoulou, G.; Christoforidis, K. C.; Louloudi, M.; Deligiannakis, Y. *Langmuir,* **2007**, *23*, 10407.

(35) Bencini, A.; bertini, I.; Gatteschi, D.; Scozzafava, A. *Inorg. Chem.* 1978, *17*, 3194.

(36) Eaton, G. S.; Eaton, S. S. In biological Magnetic Resonance; Berliner, L. J., Reuben, J., Eds,; Plenum Press, New York, 1987; Vol, 8, p 339.

(37) Van Albada, G. A.; Van der Horst, M. G.; Mutikainen, I.; Turpeinen, U.; Reedijk, *J. Inorg. Chem. Commu.* **2007**, *10*, 1014.

(38) Sharma, A. K.; Mukherjee, R. Inorganica Chimica Acta, 2008, doi: 10.1016/j.ica.2008.01.047

(39) Hermann, T.; Augffinger, P.; Scott, W. G.; Westhof, E. *Nucleic, Acids Research,* **1997**, *25*, 3421

(40) Casy, A. F.; Hassan, M. M. A. *Canadian J. Chem.* **1969**, *47*, 1587.

(41) Comba, P.; Gahan, L. R.; Haberhauer, G.; Hanson, G. R.; Noble, C. J.; Seibold, B.; Van den brenk, A.L.; *Chem. Eur. J.* 2008, *14*, 4393.

Chapter 6 Summary and Conclusion

6.1. Summary

6.2.1 New insight about pore enlargement: pore enlargement occurs by erosion of this specific rugosity using gel ageing combined with prolonged hydrothermal treatments.

6.2.2 Breakthrough of synthetic concept: MFI structured zeolite with hierarchical porosity can be synthesized via non-conventional solid-solid transformation mechanism in the presence of dual template, zeolite-directing agents and meso-structure directing agents, respectively.

6.2.3 Improvement of synthetic technique: using modified "*molecular stencil patterning*" technique (MSP), true bio-inspired multifunctional heterogeneous catalyst can be synthesized.

6.2. Conclusions

6.2.1. By precisely controlling the experimental parameters, different structured mesoporous silica with tuned pore size and improved hydrothermal and thermal stability can be synthesized. The mesostructured porous silicas of MCM-41 types contains a large fraction of microporous volume (up to 30 %) confined at the mesopore surface as niches that bring a structured surface rugosity. The discovery was driven by the observation that pore enlargement occurs by erosion of this specific rugosity using gel ageing combined with increasing autoclaving treatments. We also made the connection between this rugosity and the templating surfactant head that is indeed imprinted into the surface during the synthesis. This was obtained by specific molecular filling of these niches (or alveoli), using TMA and porosity measurements. Another discovery has been made along the autoclaving study showing that high temperature synthesis of mesostructure porous silicas above 165°C was possible with formation of the 2D hexagonal MCM-41 type of structure. Playing with these high temperature conditions, we reached the thermal conditions for the synthesis of high silica zeolites. TS-1 with the MFI type of structure containing 1 to 3 % of Ti was prepared though soli-solid transformation. In these conditions and in the presence of surfactant and TPA, the ammonium template for MFI, we discovered that not real ordered mesopore was formed. Instead we found out by XRD diffraction that, in the case of TS-1 only, flat crystal can be produced allowing to developing b-oriented layers a very interesting results to develop new zeolite membranes

6.2.2. Organic modification of the solid was also at stake using the "*molecular stencil patterning*" technique (MSP) developed by another student of our group. We have developed a variation of this technique showing that the positively charged surfactant may be exchanged by tetramethyl-ammonium cations quantitatively that, in its turn, can be used as a patterning agent for the MSP technique. Another variation proposed by us included the test for other hydrophobic organosilanes which was found more stable than the trimethylsilane for site isolation (copper was used as an EPR probe for this characterization). Finally preliminary investigation on Cu coordination chemistry was investigated. The rare Cu (II) coordination chemisty exhibited the strong dynamic effect was reported using mesoporous silica as support. These catalysts should be having a good future for environmentally friendly oxidation reaction.

6.3. Future Outlook

6.3.1. The most urgent task is to test the chemical reactivity of already synthesized materials including the hybrid materials and dual functional mesoporous silicas containing the copper complexe.

6.3.2. The great challenge is that how to achieve the synthesis of samples with uniform mesopores in nature, being composed of crystalline zeolite framework. It is also noteworthy that the present synthesis principle, *based on* *solid-solid transformation*, can be successfully extended to the synthesis of hybrid materials with other topology structure, such as MEL and LTA geometry.

6.3.3. The use of enzymatic bio-catalysis could possibly be the start of a new catalytic era, however it is too early to tell due to the difficulty in separation and purification. Bio-inspired and bio-mimetic catalyst is a good alternative. Current work has showed the pore geometry played an important effect on the Cu coordination environment. So far, many pore models of mesostructures with symmetries of *p*6*mm*, *Ia*3*hd*, *Pm*3*hn*, *Im*3*hm*, *Fd*3*hm*, and *Fm*3*hm* have been synthesized, the pore confinement effect of which on the metal geometry configuration and chemical reactivity will be tested in the near future, based on the “molecular stencil patterning” technique.

6.3.4. Although “molecular stencil patterning” technique could obtain a material possessing a surface with site-isolated groups and controlled distance between the grafted functions, the process via sequential grafting using TMA^+ ion as patterning molecule is time-consuming. The challenge is to simply this process in the near future.

Supporting Materials

All the materials used in this thesis including solvent, chemicals, and gases are listed in the following tables.

Solvent: Unless otherwise specified, solvents are not distilled. Indeed, the initial amount of water present in solvents used in the synthesis is low compared to the amount of water remaining in the material. They are kept in a balloon tube Strauss under nitrogen and molecular sieve 4 Å previously dehydrated to 500 °C in order to limit the amount of water in these solvents.

Table 1 the used solvent in this thesis

Solvent	Provenance
Toluene >99,8%	SDS – CarloErba
Acetonitrile >99,5%	SDS – CarloErba
Dichloromethane >99,95% contient un stabilisant (amylène ou éthanol)	SDS – CarloErba
Cyclohexane >99%	SDS – CarloErba
Tetrhydrofuran, extra dry, water<50 ppm	ACRÖS
Acétone >99,8%	SDS – CarloErba
Ethanol technique 96%	Elvetec Services
Ethanol absolu >99%	VWR
Méthanol absolu >99 %	VWR
Eau purifiée	Déionisée par osmose inverse

Reagents:

The main reagents are also summarized in a table below, which are specified their source and possibly their purity. They are not distilled.

Tableau 1 : Reagents used in this study.

Réactifs	Provenance
Ludox HS-40 (40% SiO_2)	Aldrich
Toluène sulfonate de cétyltriméthylammonium ou d'héxadécyltriméthylammonium (CTATos), >99%	Merck
Acide chlorhydrique en solution, 1.0 M and 37%	Acros ou SDS
Triméthylchlorosilane (Me_3SiCl), >98%	Acros
Hexamethyldisilazane >98%	Acros
Hexamethyldisiloxane >98%	Acros
2,2,5,5,-tetramethyl-2,5-disila-1-azacyclopentane, 95%, C.A.S. 7418-19-1 (dipod silane)	Roth – Gelest
1,2-Bis(chlorodimethylsilyi)ethane, 97%	Roth – Gelest
3-aminopropyltriethoxysilane 98%	Roth – Gelest
3-aminopropyltrimethoxysilane 97%	Roth – Gelest
Ethylenediamine N-(propyl trimethoxy silane) 97%	Roth – Gelest
Chlorure de cuivre (II) (2 H_2O) >99%	Acros
Trifluorométhylsulfonate de cuivre (II) >99%	Acros
Copper (II) perchlorate hexahydrate >98%	Acros

Gas:

In the following table is gathered gas we used in this study.

Table 3 gas used in this study

Nature du gaz	Qualité	Provenance	Utilisation	Traitement
Argon	α	Air Liquide	Montages de synthèse	Filtration sur cartouche multifonctions : déshydratation, désoxygénation, déshydrocarburation
Azote	U	Air Liquide	Alimentation ATG	Aucun
Air	Industriel	Air Liquide	Alimentation ATG	Aucun

Acknowledgements

All hardest time long I waited for the harvests with great anxiety, knowing that every small achievement was contributed to the people who ever helped me. In this special time, I want to express my heartfelt thanks to you.

I wish to convey my sincere gratitude to Ms. Yunhua Qian, who is responsible for the program on the cooperation in the field of doctorate training between the ENS Lyon and the ECNU. In the past 5 years, she treated me like her own's children and told me how to behave and walk in society. I am also very much thankful to Dr. Belen Albela and Ludovic Belon for helping me in every possible way through kind and fruitful discussions. I am highly indebted to Prof. Peng Wu, not only for holding me in his group at ECNU, but also personally for many stimulating discussions and valuable guidance throughout the course of my thesis.

I am much thankful to Dr. Veronique Dufaud who helped me a lot during my saty at Lyon. Special thanks to prof. Yimeng Wang who drew a lot of valuable time to read my thesis and provide invaluable guidance and constructive criticism to help me finish the writing of my thesis.

It gives me great pleasure to thank my colleagues, Dr. Virginie Latoure, Dr. Nicola Crowther, Dr. Sebastien Abry and Dr. Stephanie Calmettes, and Dr. Reine Sayah and Dr. Benjamin Jarry, and Steven, and Anissa, Bendjeriou, and Wenjuan for their helpful hand, sympathetic ears and making the lab feel like a family. I would like to express my appreciation to all my Chinese colleagues and friends, and major for the wonderful time I had with them. It gives me great pleasure to thank my old friends Weihe Zhang, Jiguo Nie, Xinyu Yu, and Zebao zheng from whom I have received unfailing support and encouragement during many years of studies that they have shown to me in their own special way. I also take this golden opportunity to convey my sincere thanks to Mr. Jean-Louis, Mr. Jean-Matas and Ms. Nadine who helped a lot in my registration, room reservation, and other related issues.

My heartfelt thanks are due to all other scientific and non-scientific staff of the Labo de chimie (UMR5182) in Lyon and Shanghai key lab of green chemistry and chemical processes in Shanghai for their valuable help and cooperation during my thesis.

The thesis could not have been completed without the continuous love and support from my family. Their steadfast faith in my capability has always spurred me to go ahead, especially in difficult times. No words of admiration can be adequate to express my feelings towards my dear wife, zhengfang Song, for her endless love, respect, constant encouragement, and being the voice of wisdom.

Finally, my thanks are due to Government of France and Rhone-Alpe region, for awarding the research fellowship to carry out my research work and to submit me this work in the form of a thesis for the award of PhD degree.

Time goes fast! You can get anything that you want, but only for time, we can do nothing; with time while away, a lot can be changed, but happy time and memory we experienced together and deep friendship we build will last forever. Because of your kindness, unselfish help, and open & warm discussion in Science, I had really happy time in Lyon in the past three year!

Kun Zhang

后记

教学科研一直是自己的梦想，喜欢象牙塔内这种安静、平和，充满活力而又不失理性的氛围，可以踏踏实实的静下心去做一点自己喜欢的事情：读书、看文献、思考如何做科研，与年轻一代一起感受时代的脉动，共享经历和知识，那是何其快乐的一生。踏入师大的那一刻，这个梦想就跟着起飞了。我们会为985几个简单的数字欢呼、雀跃、激动，因为那是每一个华师人的骄傲。作为一个中法联合培养的博士生，每次离开师大都会感到莫名的失落，因为这里有令我尊敬的老师，有为了实现自己的出国梦想一起努力拼搏的同窗，有美丽的丽娃河，…。

非常幸运地成为第二届中法班学员，更加幸运的是成为上海市绿色化学与化工过程绿色化实验室的一员，成为世界分子筛专家、中国绿色化学奠基人何鸣元院士和第一届国际介观分子筛会议的发起人法国里昂科学高师资深教授Laurent BONNEVIOT联合指导的博士研究生。尽管国籍不同，但是两位导师求真、务实和创新的科学理念却如出一辙，他们对科学的孜孜以求必将深深地影响我的一生。特别感谢两位导师把我带进了科学的殿堂，进入与社会和经济生活息息相关的绿色催化这个世界化学研究的前沿。

两位导师的言传身教让我知道了如何做科研，如何做系统和深入的科研。知道了化学的***“链式反应”(paper after paper)，***知道了做科研的简单道理：what happened？What can we learn**?** Furthermore，what can we do**?** 面对一个科研问题我们会从上午9点讨论到晚上9点，中午食堂吃饭我们一路小跑过去，因为十几分钟后食堂就要关门。令人惊讶的是第二天早晨，经过仔细思考以后，导师会直接到我的办公室追问更加详实的实验细节，然后给出一连窜的解释，下一步试验如何改进，紧张有序的日子就是这样不知不觉的流逝了。我喜欢跟导师一起工作，一起实验、修烘箱、洗EPR（顺磁共振谱）的管子，一起换钢瓶，聆听导师讲述自己亲身经历的科学小故事。这样我可以直接近距离的观察导师如何做实验，如何解决问题，如何做创新性的科学研究；并从这些细节里知道了很多科研关键词：“boss’s eye”、“patience”、“details”、“why not ”等等；也知道了做化学一定要时刻注意“量”的概念；同时真正体会到他们除了做科研，还把指导学生、与学生分享知识作为乐趣。从Channel (孔道，自己博士论文研究的主要对象) 的一端到达另一端，经历过了黑暗，才能欣赏到里面的风景，才能完成从底物到产物的转变。很显然两位导师

“催化”了这个反应。

由衷的感谢钱老师的帮助以及何老师的接收，使我在博士答辩以前就能顺利地找到自己喜欢的工作，留在华师大，留在绿色化学与化工过程绿色化重点实验室，与学生一起分享自己亲身经历的“Sientific Story”,并借助于绿色化学化工过程绿色化重点实验室（985 **工程“绿色合成化学与合成技术”科技创新**）这个强大的科技平台，把自己在里昂科学高师学习和积累的知识做更加系统和深入的研究，去追寻和实现自己的下一个梦想。